Femtosecond photoelectron spectroscopy for observation of chemical reactions

Dissertation

zur Erlangung des akademischen Grades eines
Doktors der Naturwissenschaften (Dr. Rer. Nat.)
im Fachbereich Naturwissenschaften
der Universität Kassel

Oksana Graefe

Kassel
Juni 2005

Contents

Chapter 1

Introduction

An outstanding dream in science is to obtain knowledge on processes on the most fundamental level. Elementary chemical processes take place on a scale which is inaccessible for our eye. Vibrations and rotations of the atoms in the molecule, the geometric change or dissociation of a molecule occur on the femtosecond time scale (1 femtosecond is 10^{-15} s). Therefore, these phenomena require the observation methods which are comparably fast.

The development of laser techniques made the observation of the intramolecular phenomena feasible. New developments in laser technology provided us with lasers of femtosecond pulse durations. A typical femtosecond laser can produce laser pulses with a duration of several femtoseconds in the visible spectrum. Femtosecond laser spectroscopy has, for the first time in human history, provided us with the tools to study molecular quantum dynamics in real time.

With this new technique it became possible to make a direct observation of fundamental dynamical processes in molecules. The importance of this development could be compared with the step from macroscopical to microscopical level. Therefore A. H. Zewail received the Nobel Price in chemistry in 1999. With this wall breaking invention the research area called *Femtochemistry* [1] was founded.

Conventional spectroscopy is focused on the investigation of the single molecular and atomic terms and levels. The central object of investigation in femtochemistry is not a stationary state, but a *wave packet*.

A wave packet is a coherent superposition of a set of stationary wavefunctions. A single molecular wavefunction is not spatially localised and reveal no movement. The wave packet has a well-defined (group) velocity and position, which is analogous to moving classical object with atomic resolution. Thus, a time-dependent molecular dynamics is obtained as a result.

Pump-probe techniques are used to study molecular dynamics. In a pump-probe experiment two femtosecond laser pulses interact with the ensemble of molecules. The first laser *pump* pulse of several femtoseconds has a broad energy bandwidth due to uncertainty principle. It excites several molecular rovibrational levels simultaneously, creating a vibrational wave packet. The time-delayed second laser pulse provides a momentary picture of a molecular motion with high temporal resolution. A full "movie" of molecular motion is achieved by an accurately timed series of these probe pulses. The pump-probe signal detected can be laser induced fluorescence, photoelectron or ionic signal etc.

Within a short time the ultrafast pump-probe spectroscopy has become an effective tool to study molecular dynamics in simple systems [1-4].

While first experiments concentrated on the observation of a wave packets, it was realised that the ultrafast laser techniques provided scientists with a means to study complex *electronic dynamics* in molecules. It includes such non-adiabatic processes as internal conversion, predissociation and vibrational relaxation.

The experiments started with pioneering works of Zewail [5-7] on NaI provided the study of non-adiabatic dynamics for a case when Bohr-Oppenheimer approximation breaks down. The investigation is continued in experiments on NaK [8] and polyatomic molecules [9-11]. The main detection method in the experiments so far was the ionisation with ions detection.

The disadvantage, inherently connected with this method, namely, inability to identify all ionisation pathways is circumvented in photoelectron pump-probe spectroscopy. The released electrons are analysed with regard to their kinetic energies. It was shown [12], that this method features the molecular dynamics with a sub-Ångström spatial resolution and femtosecond time resolution.

The task of the present thesis is to study the nuclear and electronic dynamics of molecules using pump-probe femtosecond spectroscopy together with the detection of the kinetic energies of the released photoelectrons. Several aspects are emphasized here:

- On the model system of the Na_2 molecule we demonstrate the ability of photoelectron spectroscopy to differentiate ionisation pathways arising several dynamical processes;
- On the example of the $2^1\Sigma_u^+$ state of Na_2 molecule we show the utility of the wave packet to map local non-adiabatic changes along the internuclear coordinate. Na_2 is a simple molecule, well-studied experimentally and theoretically, yet its electronic structure is complicated. Particularly, the double minimum $2^1\Sigma_u^+$ state formed by an avoided potential crossing, reveals changes of the chemical nature (from covalent to ionic) with the internuclear distance [13]. The ability to map the electronic dynamics along internuclear distance with photoelectron spectroscopy will be shown;
- We develop a method to disentangle the electronic and dynamical (i.e. vibrational) structure in the molecule on the model of the $2^1\Sigma_u^+$ double minimum state;

The thesis is organised in a following way.

The second chapter gives a concise description of molecular quantum dynamics, the wave packets and the pump-probe detection scheme. The second part of the chapter introduces the necessary properties of the involved Na_2 states and their molecular orbital structure. In

chapter three the experimental apparatus is introduced. It includes the laser technique, molecular and atomic beam apparatus and time of flight methods. The pump-probe experiments demonstrating the ability of the photoelectron spectroscopy to map the vibrational dynamics on several potentials of the Na_2 molecule are shown in the chapter four. Chapter five presents the experiment on the double minimum $2^1\Sigma_u^+$ state of Na_2. The method of determination of the internuclear-dependent of the internuclear distance dependent photoionisation dipole moment is presented. Finally, results obtained in the thesis and future perspectives are given in the chapter six.

Chapter 2

Theory

The chapter introduces the concepts of the molecular dynamics. Furthermore, the creation and the propagation of the wave packets and methods of the femtosecond pump-probe spectroscopy to observe the wave packets are presented. The ionisation as a detection method to probe the molecular dynamics is considered.

The second part of the chapter gives the essential information on Na_2 molecule, its $2^1\Sigma_u^+$ double minimum state orbitals and those of the ionic states. Ionisation from the $2^1\Sigma_u^+$ state is reviewed in the frames of the orbital correlation method.

2.1 Molecular description

The theory of diatomic molecules is extensively described in [14,15]. Here we present a brief overview of the physical background needed for the discussion of the results of this thesis.

Consider a diatomic molecule in the absence of an external field. The time evolution of the molecule is governed by the time-dependent Schrödinger equation:

$$i\hbar\frac{\partial}{\partial t}\psi(\boldsymbol{R},\boldsymbol{r},t)=\hat{H}\psi(\boldsymbol{R},\boldsymbol{r},t), \tag{2.1}$$

where ψ is the wavefunction of the molecule, the coordinates of the wave function are the internuclear separation coordinates $\boldsymbol{R}$ and the coordinates $\boldsymbol{r}$ of the electron manifold in the molecule, $\hat{H}$ is molecular Hamiltonian.

In the absence of an external perturbation $\hat{H}$ is time-independent and therefore the molecular wavefunction $\psi(\boldsymbol{R},\boldsymbol{r},t)$ can be divided into a coordinate-dependent part and a time-dependent phase:

$$\psi(\boldsymbol{R},\boldsymbol{r},t)=\psi_{mol}(\boldsymbol{R},\boldsymbol{r})e^{-\frac{i}{\hbar}Et}. \tag{2.2}$$

The stationary wavefunctions $\psi_{mol}(\boldsymbol{R},\boldsymbol{r})$ of a molecule are obtained by solving the time-independent Schrödinger equation [15]:

$$\hat{H}_{mol}\psi_{mol}(\boldsymbol{R},\boldsymbol{r}) = E\psi_{mol}(\boldsymbol{R},\boldsymbol{r}) \tag{2.3}$$

with eigenfunctions E. The Hamiltonian $\hat{H}_{mol}$ includes the nuclear-nuclear, nuclear-electron and electron-electron interaction terms:

$$\hat{H}_{mol} = \hat{T}_e(\boldsymbol{r}) + \hat{T}_N(\boldsymbol{R}) + \hat{V}_{ee}(\boldsymbol{r}) + \hat{V}_{NN}(\boldsymbol{R}) + \hat{V}_{eN}(\boldsymbol{R},\boldsymbol{r}) \tag{2.4}$$

and can be separated in the so-called *adiabatic representation* into two parts:

$$\hat{H}_{mol} = \hat{T}_N(\boldsymbol{R}) + \hat{H}_{el}(\boldsymbol{R},\boldsymbol{r}), \tag{2.5}$$

where

$$\hat{T}_N = -\frac{\hbar^2}{2\mu}\nabla_R^2 \tag{2.6}$$

is the nuclear kinetic energy operator which includes all differential operators with respect to the nuclear coordinates $\boldsymbol{R}$, and

$$\hat{H}_{el} = \underbrace{-\sum_{i=1}^{N}\frac{\hbar^2}{2m_e}\nabla_{r_i}^2}_{\hat{T}_e(\boldsymbol{r})} + \underbrace{\sum_{i,j=1(i\neq j)}^{N}\frac{e^2}{4\pi\varepsilon_0|r_i - r_j|}}_{\hat{V}_{ee}(\boldsymbol{r})} + \underbrace{\frac{e^2Z^2}{4\pi\varepsilon_0 R}}_{\hat{V}_{NN}(\boldsymbol{R})} \underbrace{-\sum_{i=1}^{N}\frac{e^2Z^2}{4\pi\varepsilon_0\left|\boldsymbol{r}_i - \frac{\boldsymbol{R}}{2}\right|} - \sum_{i=1}^{N}\frac{e^2Z^2}{4\pi\varepsilon_0\left|\boldsymbol{r}_i + \frac{\boldsymbol{R}}{2}\right|}}_{\hat{V}_{eN}(\boldsymbol{R},\boldsymbol{r})} \tag{2.7}$$

is the electronic part which depends only parametrically on $\boldsymbol{R}$ and includes the electron kinetic energy $\hat{T}_e(\boldsymbol{r})$, electron-electron repulsion $\hat{V}_{ee}(\boldsymbol{r})$, the nuclear-nuclear repulsion $\hat{V}_{NN}(\boldsymbol{R})$ and the electron-nuclear attraction $\hat{V}_{eN}(\boldsymbol{R},\boldsymbol{r})$.

Next, we separate the wavefunction $\psi_{mol}(\boldsymbol{R},\boldsymbol{r})$ into a nuclear part $\varphi(\boldsymbol{R})$ and an electronic part $\chi(\boldsymbol{R},\boldsymbol{r})$ and expand the molecular wavefunction according to:

$$\psi_{mol}(\boldsymbol{R},\boldsymbol{r}) = \sum_n \varphi_n(\boldsymbol{R})\chi_n(\boldsymbol{R},\boldsymbol{r}), \tag{2.8}$$

where the $\chi_n(\boldsymbol{R},\boldsymbol{r})$ are the eigenfunctions of the electronic Schrödinger equation:

$$\left(\hat{H}_{el}(\boldsymbol{R},\boldsymbol{r}) - U_k(\boldsymbol{R})\right)\chi_k(\boldsymbol{R},\boldsymbol{r}) = 0. \tag{2.9}$$

The index k labels different electronic states, the eigenvalues $U_k(\boldsymbol{R})$ describe the potential energy surfaces for every electronic state k. Inserting (2.9) into the time-independent Schrödinger equation (2.3), multiplying with $\langle\chi_k|$ from the left and exploiting orthogonally on the electronic wavefunction yields a set of a coupled equations for nuclear wavefunctions [16]:

$$\sum_{k'}\langle\chi_k|\hat{T}_N|\varphi_{k'}(\boldsymbol{R})\chi_{k'}\rangle + \left[U_k(\boldsymbol{R}) - E\right]\varphi_k(\boldsymbol{R}) = 0, \tag{2.10}$$

where the different electronic states k are coupled through the matrix elements of the nuclear kinetic energy operator. The exact equation (2.10) is however difficult to solve, therefore at this point the *Born-Oppenheimer (BO) approximation* is applied. It is based on the fact that the electrons are much lighter then the nuclei and their velocities are therefore much higher than those of nuclei. The electrons can be considered as moving in the stationary nuclear

configuration. Thus the movement of two sub-systems in the molecule, the nuclei and electrons, is adiabatically separated [17]. This implies that the electronic wavefunctions $\chi(\boldsymbol{R},\boldsymbol{r})$ vary only weakly with the nuclear coordinates and we can make the approximation:

$$\hat{T}_N\left[\varphi_{k'}(\boldsymbol{R})\chi_{k'}(\boldsymbol{R},\boldsymbol{r})\right] \approx \left[\hat{T}_N\varphi_{k'}(\boldsymbol{R})\right]\chi_{k'}(\boldsymbol{R},\boldsymbol{r}), \tag{2.11}$$

where the terms corresponding to coupling of different electronic states through the matrix elements of the nuclear operator $\hat{T}_N(R)$ are neglected.

With this approximation equation (2.10) is reduced to the set of the uncoupled equations:

$$\left[\hat{T}_N(\boldsymbol{R}) + U_k(\boldsymbol{R}) - E\right]\psi_k(\boldsymbol{R}) = 0. \tag{2.12}$$

These are the equations of the nuclear motion within the *k*-th electronic state, having the potential U_k The coupling to other states here is absent and motion of nuclei within each electronic state is independent of other states. This is the base of bare-states representation of potentials.

Thus the solution of the complete molecular movement is split into two tasks. First, the solution of the electronic Schrödinger equation (2.9) for fixed coordinates $\boldsymbol{R}$ which yields the potentials $U_{k,}$ second, the solution of the nuclear equation (2.12) with given potentials $U_{k.}$

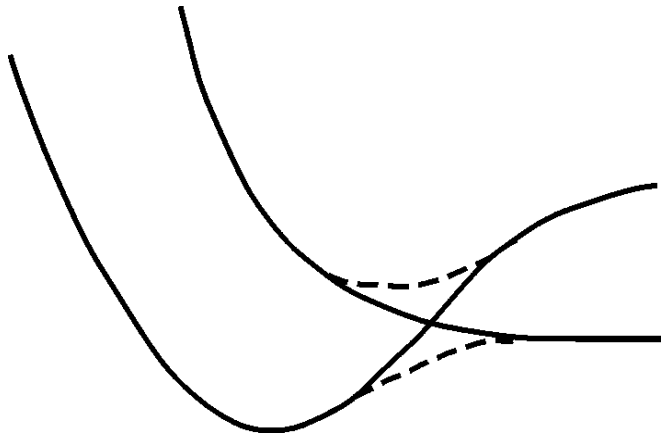

Figure 2.1: Two potential sufaces of a molecule. The full curves show the diabatic basis, whereas the dashed curves show the adiabatic basis. These two formulations differ only at the point where the Born-Oppenheimer approximation fails and the surfaces cross in the diabatic basis.

The BO approximation ignores, for instance, the relativistic effects such as the spin-orbit and spin-spin interactions and is valid when the electronic wavefunctions $\chi_k(\boldsymbol{R},\boldsymbol{r})$ vary weakly with $\boldsymbol{R}$. Then the nuclei move on a single potential U_k. If two potential surfaces strongly mix at some point (this happens when they become degenerate at some particular nuclear configuration, for example at surface or level crossing), the character of the electronic wavefunction varies strongly with $\boldsymbol{R}$, so surfaces can no longer be considered as independent and equation (2.11) is no longer applicable. One can however define a new electronic basis which is again diagonal. This basis is called *adiabatic*, as opposed to *diabatic* which has the non-diagonal coupling terms. Graphically this new adiabatic description appears as an *avoided crossing* of the potential surfaces (Figure 2.1, dashed lines). Although new adiabatic surfaces do not cross, the electronic structure on these potentials can strongly vary or be a singular function of the internuclear distance $\boldsymbol{R}$.

2.2 Pump-probe technique

A powerful tool to study a molecular dynamics and hence chemical reactions in a real time is the femtosecond spectroscopy (see e.g. [1-3]). An effective technique developed is called *pump-probe technique*. The principle of the pump-probe experiment is summarised schematically in the Figure 2.2. Here a first ultrashort laser *pump-pulse* is used to initiate the dynamics of the molecule. A second, *probe-pulse* is applied after some well defined delay time to examine the state of the molecular system. By measuring the response of the molecule as a function of the delay time between two laser pulses the dynamics of the molecule can be investigated. The ultrafast pump-probe experiments were developed in the end of eighties on molecular model systems such as NaI [18], I_2 [19] or Na_2 [20]. Since that, numerous experiments were performed which allow one to make a "movie" of different molecular processes such as wave packet propagation, coherent control, internal vibrational redistribution or structural redistribution [21-23].

The investigated molecule is prepared in the possibly well-defined state $|1\rangle$, usually the first vibrational $v''= 0$ level of the ground electronic state of the molecule. The first laser pulse excites the molecule to the excited state $|2\rangle$. Due to the broad spectral width of the ultrashort laser pulse, it excites several vibrational levels of the state simultaneously. In order to *coherently* excite the vibrational states corresponding to one molecular vibration, the duration of the laser pulse should be less then a vibrational period. After excitation a non-stationary coherent superposition of the eigenstates, called a *wave packet*, starts to evolve. The free evolution of the vibrational wave packet corresponds to the classical vibrational motion of nuclei of the molecule. After a certain delay time Δt, a second laser probe-pulse interacts with the molecule transferring it to the final state $|3\rangle$. The population in the state $|3\rangle$ detected as a function of the pump-probe delay reflects the dynamics in the state $|2\rangle$.

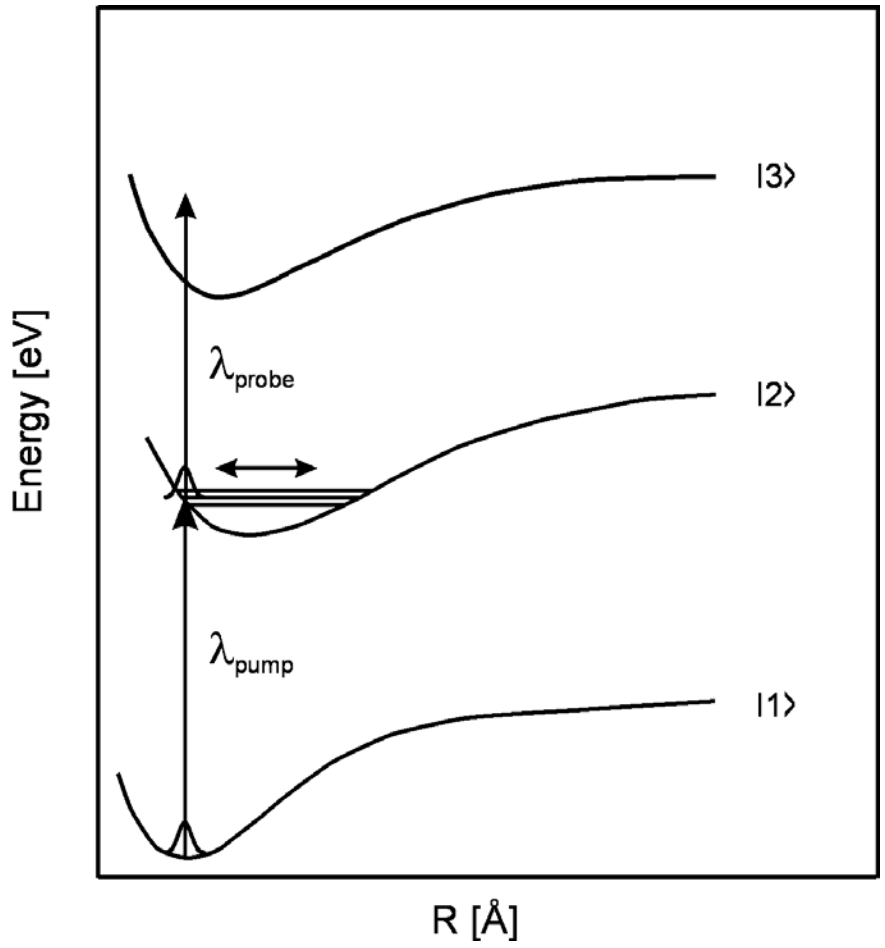

Figure 2.2: Principal potential scheme of the pump-probe experiment. A wave packet in the excited electronic state $|2\rangle$ is created by the pump laser pulse with λ_{pump}. A wave packet is then transferred into a $|3\rangle$ molecular state. The population in the state $|3\rangle$ will be measured.

Several schemes to detect the population in the final state $|3\rangle$ can be applied. One can for instance measure the fluorescence of higher laying neutral states of the molecule [18,24]. Alternatively, transient absorption of the probe photons can be measured [25] or stimulated emission [26,27], if the final state $|3\rangle$ is lower than the state $|2\rangle$. However the interpretation of the experimental results might be very complicated since many excited states in the vicinity of $|3\rangle$ can influence the signal as well. The investigation of the molecular dynamics with these methods is possible only within a short range of internuclear distances determined by Franck-Condon windows.

Another approach is based on the projection of the molecular dynamics onto the ground or excited state of the ion by means of the *photoionisation* [19,20,28]. The second laser can ionise the molecule. In this case the released ions and electrons are measured in the experiment. This scheme has numerous advantages [29]:

- The charged particle detection is extremely sensitive;
- Ionisation is an allowed process at every nuclear configuration since the photoelectron takes the excess energy, therefore any molecular electronic state can be ionised;

- The ground state of the ion is usually much better studied compared to the excited states of the molecule using independent methods like high resolution photoelectron or infrared spectroscopy or by *ab initio* calculations;
- A highly detailed information can be obtained by analysing the outgoing electron with regard to its kinetic energy, angular distribution or spin polarisation;
- Detection of the released ions provides complementary information about the mass distribution of the products.

Numerous experiments applying femtosecond time-resolved techniques with the detection of the yield of the ions [19,20,28] or the photoelectrons [21,30-33] have been performed. Measuring the photoion kinetic-energy averaged yield however does not provide the internuclear distance resolution. Therefore the dynamics in the photoion signal is observed only in cases when the potential scheme of the molecule allows the photoionisation at the certain window of internuclear distances (see, e.g. experiments on NaI [19] and Na_2 [20]).

Detection of the photoelectrons offers an additional experimental parameter (kinetic energy, angle or spin polarisation) in comparison to the averaged photoion yield. The angle-resolved photoelectron signal as a function of time allows to convey information about rotational-vibrational interactions, spin coupling and electronic non-adiabatic processes [34].

In our experiments the angular-averaged, kinetic energy-resolved photoelectrons are detected. The transition probability from the excited state to the ion state is a function of the wave packet's location on the excited potential. Therefore the temporal photoelectron signal generated by the probe laser pulse maps directly the wave packet propagation. For diatomic molecules, for which the participating electronic potentials are known, the kinetic energy of the photoelectrons can be converted into an internuclear distance [31]. The utility of the photoelectron spectroscopy to map the dynamics along the complete relevant internuclear distance range was shown both theoretically and experimentally [31,35-37].

2.3 Laser-molecule interaction

2.3.1 Classical description: difference potential analysis

The analysis of the process is also possible within the classical mechanics framework. The so-called *difference potential analysis* was suggested by Mulliken [38].

First consider the neutral-neutral transition in a molecule. Consider nuclei in two neutral states having the potential energies $U_1(R)$ and $U_2(R)$ and kinetic energies T_{R1} and T_{R2} before and after the absorption of a photon $\hbar\omega$ correspondingly (Figure 2.3). During the transition the Franck-Condon approximation is valid: the nuclei do not change their positions and velocities noticeably. This implies that the transition occurs at a fixed internuclear distance and a constant kinetic energy $T_R(R)$ of nuclei. The total energy conservation during the transition can be written as follows:

$$U_1 + T_R + \hbar\omega = U_2 + T_R \tag{2.13}$$

$$\Rightarrow \qquad U_2(R) - U_1(R) = \hbar\omega\,. \tag{2.14}$$

That is the transition occurs graphically at the intersection of difference potential U_2 - U_1 with the horizontal line at the photon energy $\hbar\omega$.

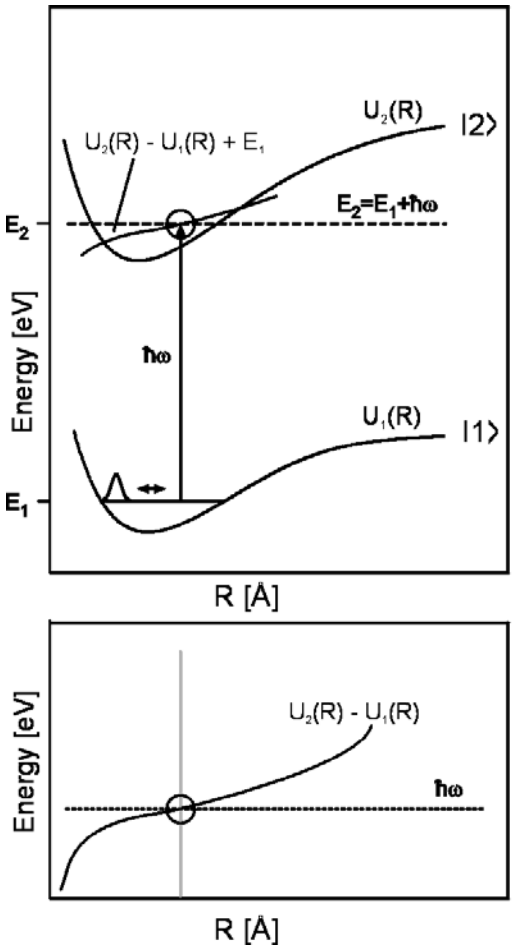

Figure 2.3: Potential scheme for the difference potential analysis for the case of neutral-to-neutral transition. The lower picture shows the difference potential.

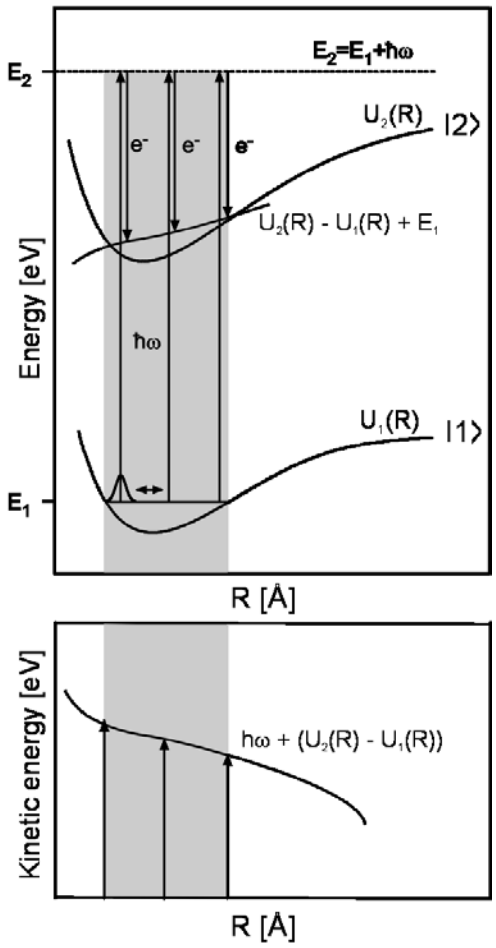

Figure 2.4: Potential scheme for the case of neutral-to-ionic transition. The lower picture shows the kinetic energy of the released electrons.

For the transition between the neutral and ionic states (Figure 2.4) the analysis includes also the kinetic energy of the ejected photoelectron T_e. If the $U_1(R)$ and $U_2(R)$ are the potentials of a neutral and ionic states, the energy conservation gives:

$$U_1 + T_R + \hbar\omega = U_2 + T_R + T_e \tag{2.15}$$

$$\Rightarrow \quad U_2 - U_1 = \hbar\omega - T_e \tag{2.16}$$

That is the transition occurs for those R for which the photon energy is higher than a difference potential. The kinetic energy of the released electrons is given from (2.16) as a difference:

$$T_e(R) = \hbar\omega - (U_2(R) - U_1(R)) \tag{2.17}$$

and hence is dependent on internuclear distance at which an ionisation takes place. Therefore by the detection the kinetic energies of photoelectrons one can get the dynamical information on a wave packet, since electrons with different kinetic energies are formed at different internuclear distances.

2.3.2 Quantum mechanical description

The interaction of the molecule with the laser pulse leads to the time-dependent Schrödinger equation where the total Hamiltonian $\hat{H}$ is a sum of the molecular Hamiltonian $\hat{H}_{mol}$ described by the formula (2.4) and the coupling with the external electric field $\hat{H}_l$:

$$\hat{H} = \hat{H}_{mol} + \hat{H}_l \ . \tag{2.18}$$

Within the dipole approximation the term $\hat{H}_l$ is given by [39]:

$$\hat{H}_l(t) = -\hat{\boldsymbol{d}}\boldsymbol{E_0}\cos\omega t \ , \tag{2.19}$$

where $\hat{\boldsymbol{d}}$ is the dipole electric operator of the molecule and $\boldsymbol{E_0} = E_0(t)\boldsymbol{e}$ is the electric field vector along polarisation $\boldsymbol{e}$. The time-dependent Schrödinger equation for the transition between two states, the ground ψ_0 and the excited ψ_1 in the BO approximation reads:

$$i\hbar\frac{\partial}{\partial t}\begin{pmatrix}\psi_0(t)\\ \psi_1(t)\end{pmatrix} = \begin{pmatrix}\hat{H}_0 & -\mu_{01}E_0(t)\\ -\mu_{10}E_0(t) & \hat{H}_1\end{pmatrix}\begin{pmatrix}\psi_0(t)\\ \psi_1(t)\end{pmatrix}, \tag{2.20}$$

where $\hat{H}_0$ and $\hat{H}_1$ are the Hamiltonian operators which define the dynamics on the states *0* and *1*, $\hat{H}_i = \hat{T}_i + \hat{V}_i(R)$. The *transition dipole moment functions* μ_{ij} are defined as:

$$\boldsymbol{\mu_{ij}}(\boldsymbol{R}) = \left\langle \chi_{kj}(\boldsymbol{R},\boldsymbol{r})\middle|\hat{\boldsymbol{d}}\middle|\chi_{ki}(\boldsymbol{R},\boldsymbol{r})\right\rangle, \tag{2.21}$$

$$\mu_{ij}(\boldsymbol{R}) = \boldsymbol{\mu_{ij}}(\boldsymbol{R})\cdot\boldsymbol{e} \ . \tag{2.22}$$

The transition dipole functions μ_{ij} are, like the potentials, functions of $\boldsymbol{R}$. Their magnitudes determine the overall strength of the electronic transition. The calculation of these functions and especially their coordinate dependence is a challenging task, and therefore, in the most cases, they are replaced by arbitrary constants.

In the perturbative limit the equation (2.20) has the formal solution for the nuclear wavefunction of the excited state 1 in the perturbative limit [15]:

$$\psi_1(t) = -\frac{i}{\hbar}\int_0^t e^{-(i/\hbar)H_1(t-t')}\mu_{10}E_0(t')\cos\omega t'\psi_0(t')e^{-iE_0t'/\hbar}dt' \ . \tag{2.23}$$

The formula can be understood as follows. The system is in a ground electronic state with $v'' = 0$ at time zero. This corresponds to the initial state in a cold molecular beam. The wavefunction evolves till the time t' under the Hamiltonian $\hat{H}_0$ of the ground state. At $t = t'$ the electric field $E(t') = E_0(t')\cos\omega t$ interacts with the molecule with the transition dipole moment μ_{10} and promotes a fraction of the ground-state wavefunction into the excited electronic state, so that the maximum of ψ_1 first increases with the time. The upper state wavefunction ψ_1 is called *wave packet*. It starts to evolve under the influence of the Hamiltonian $\hat{H}_1$ from time *t'* till *t*. When the $E_0(t)$ decays to zero, the promotion from the ground into the excited state stops and ψ_1 travels in the upper state without coupling to the ground state.

More profound insight into the wave packet in the upper state can be obtained when we expand the excited state nuclear wavefunctions ψ_1 in terms of the vibrational eigenfunctions:

$$\psi_1(R,t) = \sum_n a_{1n}(t)\varphi_{1n}(R)e^{-iE_n/\hbar}\,, \tag{2.24}$$

where E_n are the energies of the vibrational levels of the state 1, $\varphi_{1n}(R)$ are the vibrational eigenfunctions of the state 1.

Then the substitution of a (2.24) into (2.20) and solving the equations for the coefficients a_{1n} yields the wavefunction for the upper state [15]:

$$\psi_1(R,t) = -\frac{i}{\hbar}\sum_n \underbrace{\langle \varphi_{1n}|\mu_{10}|\varphi_0\rangle}_{c_n}\varphi_{1n}(R)e^{-iE_n t/\hbar} I(t,\omega,\omega_{n0}) \tag{2.25}$$

$$\Rightarrow \quad \psi_1(R,t) = -\frac{i}{\hbar}\sum_n c_n\varphi_{1n}(R)e^{-iE_n t/\hbar} I(t,\omega,\omega_{n0}) \tag{2.26}$$

with the transition frequencies

$$\omega_{n0} = (E_n - E_0)/\hbar\,, \tag{2.27}$$

the coefficients

$$c_n = \int \varphi_{1n}(R)\mu_{10}\varphi_0(R)dR\,, \tag{2.28}$$

which are in the BO approximation the products of the transition dipole moments and the Franck-Condon factors, and the integrals

$$I(t,\omega,\omega_{no}) = \int_0^t E_0(t')\cos\omega t' e^{i\omega_{n0}t'}dt'\,. \tag{2.29}$$

The interpretation of the wave packet in the upper state is now straightforward. According to (2.26), the wavefunction of the upper state is a sum of the vibrational eigenfunctions weighted with the coefficients c_n containing the molecular properties and the integrals $I(t,\omega,\omega_{n0})$ carrying the information about the laser pulse.

2.3.3 Wave packets

During the interaction of the laser pulse with the molecule several vibrational levels of the upper electronic state are coherently excited due to the spectral width of the laser pulse. The population of the excited vibrational states is dependent on the overlap of the wavefunctions of the ground and the excited electronic states (Franck-Condon Factors) with the envelope $E_0(t)$ of the laser pulse. The shorter the laser pulse, the more vibrational states are excited. The superposition $\psi_1(R,t)$ is coherent due to coherence of the laser pulse. Since the $\psi_1(R,t)$ is not an eigenfunction of the excited-state Hamiltonian, the wave packet starts to move away from the creation point. Right after the excitation the vibrational wave packet is spatially localised. It oscillates in a potential with the classical period [40]

$$T = \frac{2\pi}{\omega} = \frac{1}{\Delta\nu}, \tag{2.30}$$

which is inversely proportional to the frequency spacing $\Delta\nu$ between two neighbour vibrational levels. Since the real potential however is not harmonic, the levels are not equidistant, the level spacing $\Delta\nu$ is decreasing with increasing the number of the level. Hence, every spectral component in the wave packet evolves with somewhat different period, this leads to the dispersion of the initially localised wave packet, after some time the wave packet

is dephased [41]. There is a possibility for the wave packet to regain its shape later resulting in so-called revivals. The revival period is given by the formula [41]:

$$T_{rev} = 2T_a\left(\hbar\frac{\partial\omega}{\partial E}\right)^{-1}, \tag{2.31}$$

where T_a is a classical oscillation period in an anharmonic potential. The revival period contains additional information about the potential $U(R)$. The revival period measured for the $A^1\Sigma_u^+$ state of Na_2 molecule consists T_{rev} = 47 ps [42].

However on timescales on which the dispersion is not yet significant, the movement of the wave packet can be described classically, i.e. as a point mass moving on a potential well of the form $U(R)$.

2.3.4 Ionisation and Koopman's rules

When ionisation is used as a probe step, the second, time delayed laser pulse ionises the molecule at the delay time τ. The final state in photoionisation measurements $\psi_2(R,t)$ includes the quantum states of both the ion and the ejected photoelectron with the kinetic energy E.

Provided the dipole approximation holds, the photoelectron signal can be written within the first-order perturbation theory as [43]:

$$P(\tau,E) = \int \left| I(R,E)\psi_1(R,\tau)\mu_{I1}(R,E)\right|^2 dR \tag{2.32}$$

with the Fourier integral:

$$I(R,E) = \int_{-\infty}^{\infty} e^{i(U_I(R)-U_1(R)-(\omega_2-E))t} E_2(t)dt, \tag{2.33}$$

where E is the kinetic energy of the ejected photoelectron, $\mu_{I1}(R,E)$ is the projection of the transition neutral-to-ion dipole moment operator on the electric field vector defined analogous to (2.22), $E_2(t)$ is the envelope of the probe laser pulse, $U_1(R)$ and $U_I(R)$ are the excited state and the ion potential surfaces. Equation (2.32) is valid for short laser pulses and weak field ionisation. The electron is considered separated from all additional particles and therefore its total energy is equal to its kinetic energy E [44,45].

The interpretation of data usually assumes a constant photoionisation dipole moment $\mu_{I1}(R,E)$ based on the Condon approximation (see, e.g. [35-37]). This picture however neglects the role of the ionisation dynamics itself. Although there are no forbidden transitions, there are so-called propensity rules which can modify the ionisation cross-section [46]. Photoionisation is sensitive to the character of the electronic configuration. This is due to the fact that emission of the electron is a fast process, it occurs without simultaneous reorganisation of the ion core, which is known as a *Koopman's approximation* [46]. Therefore the probability for ionisation into a specific electronic state of the ion (partial ionisation probability) varies strongly with respect to the molecular orbital nature of the investigated electronic state. If the excited state correlates electronically with one state of the ion, which means that ion state orbital configuration can be obtained simply by removing one of the outer electrons, then the photoionisation cross-section is large. If it does not correlate, then ionisation would involve a two-electron process, since another electron must rearrange in order to achieve the ion state orbital configuration. Such a process is not forbidden, but is a lower probability event. Therefore the excited state would preferably be ionised into a state of the ion, which has a similar electronic symmetry.

Consider now a state which undergoes an avoided crossing, i.e. the electronic structure on a potential is changing along the internuclear coordinate. Thus the correlation of the electronic orbitals with the ion state can be different for different regions of the excited potential. This will lead to the photoionisation dipole moment changing with the internuclear distance *R*, and hence, should be reflected in the photoionisation signal. Thus, the time-resolved photoionisation spectra that include ionisation into excited states of the ion can provide a direct measure of the non-adiabaticity of the neutral potential. Hence, the photoelectron spectroscopy is an effective tool to disentangle the nuclear and the electronic motion in the molecule.

2.4 Na_2 molecule

2.4.1 Neutral and ionic states' molecular orbitals

The Na_2 molecule is one of the most explored molecules. Na_2 molecule can be considered, together with other light alkali dimers, as theoretically the simplest after H_2. Experimentally it is easy to handle because of low ionisation level. Na_2 was investigated extensively both theoretically and experimentally (for review see, f.e. Verma et al. [47]). The low-lying states of the molecule were thoroughly explored spectroscopically by Henesian et al. [48], Kaminsky et al. [49], Kaminsky [50] and Kusch and Hessel [51]. The dissociation energy of the ground Na_2 state and the height of the $A^1\Sigma_u^+$ potential were determined with laser fluorescence studies [50], as well as lately the properties of the $C^1\Pi_u$, $(1)^1\Pi_g$ and $(2)^1\Sigma_u^+$ states [52-54]. More recently in [55,56] the high-resolution Fourier transform spectroscopy the parameters of the $2^1\Sigma_u^+$ double minimum state were defined. Na_2 is an attractive object for theoretical studies due to a small number of valence electrons. The Schrödinger equation is reduced here only to a two-electron task. *Ab initio* calculations of few lowest levels of Na_2 were performed in [57,58]. Valance and Tuan [13] used a semi-empirical pseudopotential method to calculate the lowest $^{1,3}\Sigma_{g,u}^+$ state of Na_2 molecule. They also obtained the evolution of dominant molecular orbital configurations of these states. More recently, Jeung [59] reported a theoretical study of 19 low-lying states of Na_2. The calculations were based on a non-empirical pseudopotential method. The calculated adiabatic potential curves are extremely precise and show remarkable agreement with the experiment.

Figure 2.5 shows the scheme of the ground and the double minimum state of the Na_2 molecule and the ground and first excited states of the Na_2^+ ion together with their main electron orbitals.

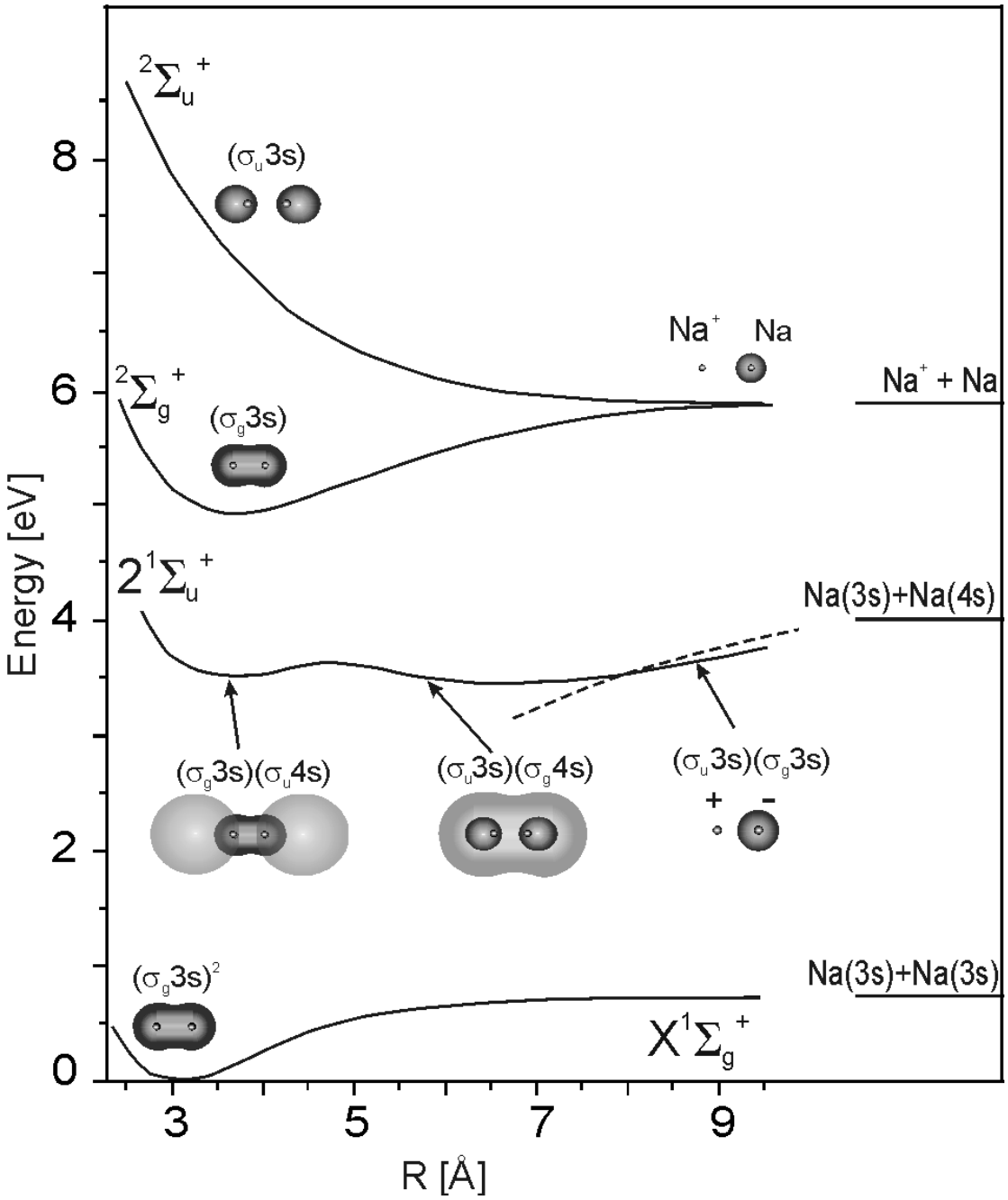

Figure 2.5: Scheme of the lowest $X^1\Sigma_g^+$ state, the double minimum state $2^1\Sigma_u^+$ of the Na_2 molecule and the two lowest $^2\Sigma_g^+$ and $^2\Sigma_u^+$ states of the ion Na_2^+. The molecular orbitals participating in each electronic state are also indicated [60,61]. The orbitals are plotted schematically, without preservation the dimensions.

The ***$X^1\Sigma_g^+$ ground state*** of Na_2 molecule has a minimum at R = 3.1 A. It dissociates into *Na(3s) + Na(3s)* limit at 0.75 eV [51]. The Na_2 molecule has two valence electrons, they occupy the lowest possible molecular orbitals giving the configuration KKLL$(\sigma_g 3s)^2$ of the $X^1\Sigma_g^+$ state [14]. Here K and L indicate the inner shells of the molecule. Both electronic orbitals (σ_g3s) are bound, what leads to a deep minimum of the state. Visually, the molecular orbitals can be indicated schematically by the *probability density distribution* of the electrons. The typical σ_g-orbitals are shown on the Fig. 2.5 [60,61]. The orbitals have the elliptical shape surrounding two nuclei typical for s-symmetry. The electrons spend most of the time between the two nuclei, thus "gluing" them together.

The ***$2^1\Sigma_u^+$ double minimum*** state of Na_2 was first predicted by Valance and Tuan [13] and then quantitatively calculated by Jeung [59]. The state was observed by Cooper et al. [56] using Fourier-transform spectrometry to record laser-excited infrared fluorescence of the Na_2 molecule. A more recent study using two-photon ionisation spectroscopy by Delacteraz and Wöste [62] and Haugstätter et al. [63] confirm these studies. The experiments allowed the observation of tenths of levels in both wells below and above the barrier. There are marked similarities with the predicted potential of the $2^1\Sigma_u^+$ state of Li_2 [64]. Both can be compared with the E, F and G, K states of H_2 molecule [65-67].

The double minimum state arises from an avoided crossing of two diabatic states. The first one gives rise to the inner well and is a Rydberg state dissociating to the Na(3s) + Na(4s) limit at 4 eV. The inner well has a minimum at the internuclear distance of R = 3.69 Å at the energy of E = 3.53 eV [56]. The barrier between two minima lies at R = 4.8 Å. The outer well has the minimum at R = 6.74 Å and E = 3.46 eV [56]. It arises from the second diabatic state, which has considerably ionic character at large distance but its structure changes with internuclear separation. The $2^1\Sigma_u^+$ state dissociates to Na(3s) + Na(4s) so that there are actually two avoided crossings between this pair of the diabatic curves.

Valance and Tuan [13] calculated the weights of the orbitals contributing to the double minimum potential using semi-empirical pseudopotentials. The bond structure and the orbitals are identical to those calculated for the E, F state of H_2 [65]. The main contributing orbitals are indicated in Figure 2.5. The inner well is described by the configuration of the outmost electrons $(\sigma_g 1s)(\sigma_u 2s)$ [13]. It should be noted that this notation, used by authors [13] for simplification and generalisation of calculations, implies hydrogen-like atomic wavefunctions and corresponds to the configuration $(\sigma_g 3s)(\sigma_u 4s)$ of Na_2 molecule. We will use the last notation further. The first orbital $(\sigma_g 3s)$ is analogous to the ground electron orbital of Na_2 and is bonding. We plotted it as an ellipse on the picture. The second one, $(\sigma_u 4s)$ is antibonding, it consists on two ellipses where the electron spends most of the time outside the nuclei, thus pushing them away from each other. The typical form of the σ_u - orbital constructed using [61] is plotted in Figure 2.5. Note that not an overall electron density but only a superposition of two single orbitals is shown in Figure 2.5 without consideration of their interaction. The orbital $(\sigma_u 4s)$ has a higher principal quantum number of $n = 4$. Such an orbital is called Rydberg orbital and has substantially bigger radius, as n is responsible for the distance of an electron from a nucleon (the orbital is shown qualitatively on the picture without maintaining the real dimensions). The electron in the Rydberg state has a weak connection to the core. The bond in the molecule is considered from stability of corresponding ion formed by removing the Rydberg electron [14]. Here the residual electronic orbital $(\sigma_g 3s)$ is bonding, therefore the configuration is bonding one. The lowest levels of the inner well have properties that approach those of Rydberg states (i.e. similar to those estimated for the ground state of Na_2^+).

The outer well has two main orbital configurations: $(\sigma_u 3s)(\sigma_g 4s)$ and $(\sigma_u 3s)(\sigma_g 3s)$ [13]. The first one is a covalent and the latter belongs to an ionic Na^+Na^- configuration. The weight of the $(\sigma_u 3s)(\sigma_g 4s)$ orbital configuration increases in the outer well with the internuclear distance. The first electron remains on a $(\sigma_u 3s)$ antibonding orbital, whereas the second electron occupies excited $(\sigma_g 4s)$ orbital. This orbital is again a Rydberg one with the principal quantum number n = 4. A schematic orbital is shown as an ellipsoid with larger size (Figure 2.5). Although this orbital is a bonding one, the electron on it is weakly connected with nuclei, so the stability of the configuration is mainly defined by another electron, which is an antibonding one. Hence the $(\sigma_u 3s)(\sigma_g 4s)$ configuration is antibonding and is responsible for a covalent repulsion.

Another orbital configuration $(\sigma_u 3s)(\sigma_g 3s)$ has a wavefunction [14]:

$$\psi = N_g N_i [\underbrace{\psi_A(1)\psi_A(2)}_{Na^- Na^+} - \underbrace{\psi_B(1)\psi_B(2)}_{Na^+ Na^-}], \tag{2.33}$$

where N_g and N_i are factors, and A and B indicate atoms, numbers 1 and 2 indicate electrons. It corresponds to the case when both electrons are either at first Na atom or at second one simultaneously. Therefore the configuration represents a pure ionic state Na^+Na^-. However, there is no permanent dipole moment in this ionic state because of continuous interchange between Na^+Na^- and Na^-Na^+ [14]. The weight of the ionic configuration in the potential can be qualitatively seen from the Figure 2.5. We plotted with the dashed line a simple *1/R* ionic potential converging to the Na^+Na^- limit at 5.34 eV[1)]. It follows the double minimum well at the distances $R \sim 7.8 - 8.7$ Å. Thus, the ionicity should play a role at the outer limb of the potential.

The $^2\Sigma_g^+$ lowest ***ionic state of Na_2^+*** has minimum at $R = 3.6$ Å and $E = 4.90$ eV [14]. The electron configuration is $(\sigma_g 3s)$ analogous to that of H_2 [14]. Here one valence electron occupies the bound orbital. The first excited state of the ion is $^2\Sigma_u^+$. The electron here should be on the first excited $(\sigma_u 3s)$ repulsive orbital [14]. At the very large internuclear separation the molecular orbital representation is no longer valid and the electrons may be considered as belonging to the separate atoms. It can be seen from the Figure 2.5, since $^2\Sigma_g^+$ and $^2\Sigma_u^+$ states have almost the same energies at large internuclear separation.

2.4.2 Ionisation of Na_2 molecule and correspondence of electronic states

The ionisation of the $2^1\Sigma_u^+$ double minimum state of the Na_2 molecule was studied in [56,62], and more recently in [62]. A resonant two-photon ionisation spectroscopy was applied in [62] to investigate the double-minimum Na_2 state. Due to ionisation wavelength the experimental scheme includes both bound $^2\Sigma_g^+$ and repulsive $^2\Sigma_u^+$ ionisation channels. The authors [62] observed the Na_2^+ signal from ionisation into the bound ionic state accompanied by Na^+ signal when the laser frequency is large enough to excite the $2^1\Sigma_u^+$ state above the barrier. No ionisation signal from the inner well is detected. As well, no ionisation from the close lying $C^1\Pi_u$ state is detected. It was then speculated that dissociation occurred during the ionisation step and the ionisation into a bound and a repulsive states is favoured at large internuclear distances. However, since authors measured only the total ion signal, the close lying states could obscure their results.

More clear view on the ionisation channels from the $2^1\Sigma_u^+$ state is given in [63] where two-photon ionisation together with kinetic-energy resolved ions measurement was applied. In contrast to [62], the ionisation from the inner well both into the repulsive $^2\Sigma_u^+$ and the bound $^2\Sigma_g^+$ ionic states is observed, probably due to the higher sensitivity of the experiment. The ion signal is higher at larger internuclear distances, indicating the increasing photoionisation dipole moment in the outer well of the $2^1\Sigma_u^+$ potential.

Here we propose a simple qualitative analysis of the ionisation probability from the double minimum well into the bound and repulsive ionic states performed on the basis of the molecular orbital structure of the state. As was already mentioned in the section 2.3.3 of the present chapter, the ionisation can depend drastically on the molecular orbital structure of the

[1)] The ionic curve was calculated as follows: $I(Na) - E_{aff}(Na) + D_e(X^1\Sigma_g^+) + 1/R$, where $I(Na)$ is the ionisation potential of Na and $E_{aff}(Na)$ is the electron affinity of Na.

neutral state. The ionisation probability into a specific ion state will be higher if a given electronic configuration correlates, upon removal of a single electron, with the configuration of a cation. Since the molecular orbital structure changes significantly along the internuclear distance for the $2^1\Sigma_u^+$ state, the ionisation probability may differ a lot for different internuclear distances and for different final ionic states.

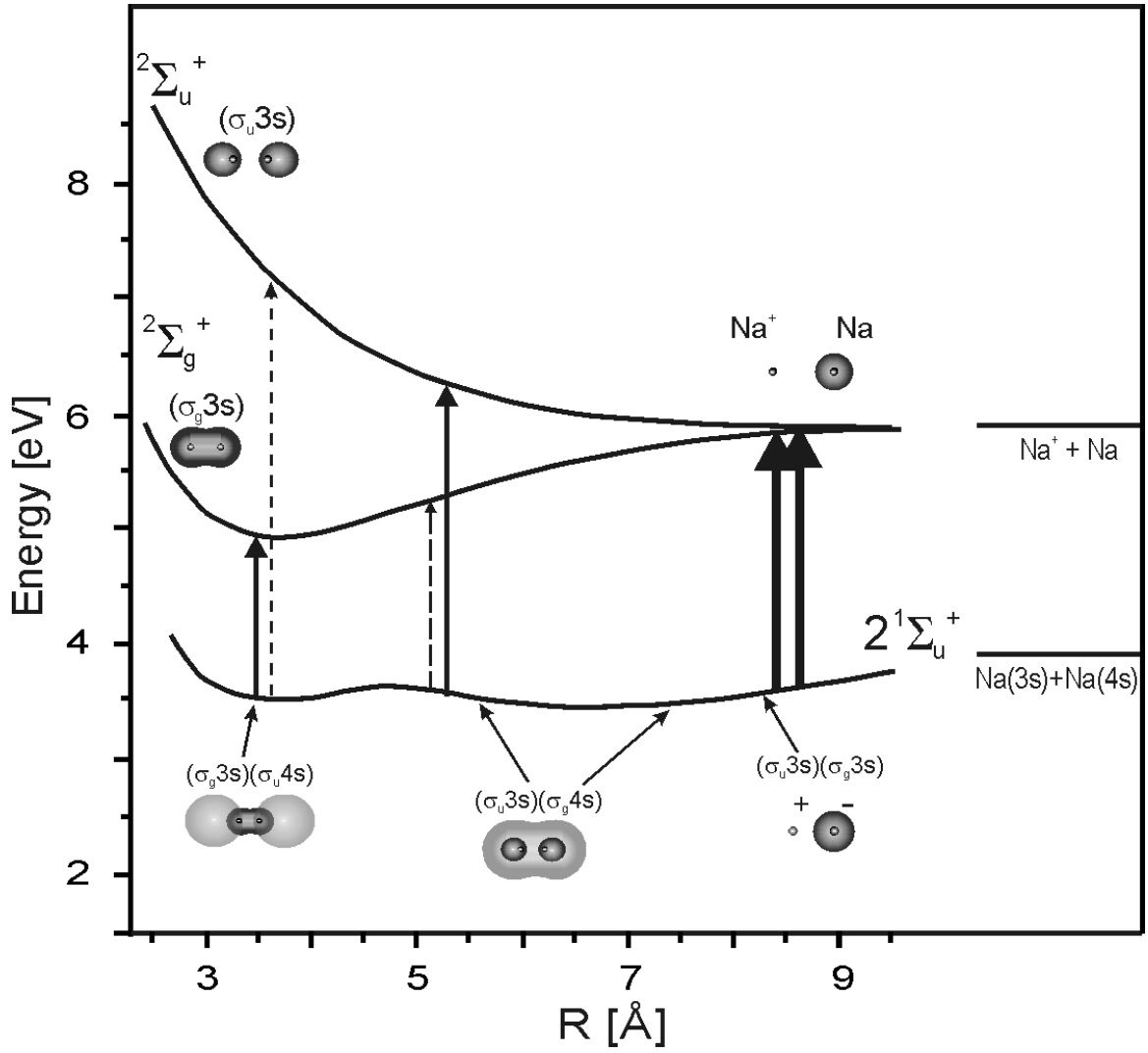

Figure 2.6: Schematic representation of the ionisation probability from the $2^1\Sigma_u^+$ double minimum state of Na_2 into both lowest $^2\Sigma_g^+$ and $^2\Sigma_u^+$ ionic states based on the electronic structure correspondence. The ionisation probability in the inner well of the double minimum is higher for the ionisation into the bound ionic state and lower for the ionisation into the repulsive ionic state. Ionisation in the outer well is increasingly strong with the internuclear distance due to increasing ionic character in the well.

The $2^1\Sigma_u^+$ double minimum state and two lowest ionic states of Na_2 molecule together with their orbitals are shown in Figure 2.6. In the inner well of the $2^1\Sigma_u^+$ state the main orbital configuration is (σ_g3s)(σ_u3s) [13]. Removing of the Rydberg electron (σ_u4s) leads directly to the configuration KKLL(σ_g3s) of the bound $^2\Sigma_g^+$ ionic potential. Since the Rydberg electron is weakly connected with the core, the ionisation probability into a bound ionic state would increase. Since there is no correlation of the orbital structure with the repulsive ionic state structure, ionisation into it would be unfavourable. The next orbital configuration (σ_u3s)(σ_g4s)

becomes significant in the outer well with increasing internuclear distance. It does not correlate with the bound ionic configuration, leading to low ionisation probability into the bound ionic state. Removing the weakly bound Rydberg (σ_g4s) electron leads to a $^2\Sigma_u^+$ ion state configuration, thus the ionisation probability into a repulsive ionic state is higher. An interesting case is the ionic orbital (σ_g3s)(σ_u3s) admixture at higher internuclear distances. Here both electrons are located either at one or at another Na nucleus, thus at every moment one sodium cation has two electrons, another, anion, has no valence electrons. Ionisation here corresponds to removing one of the valence electrons from a Na^- cation, a process called detachment. This process has much higher probability then ionisation of a neutral Na atom [68]. Since at large internuclear distances the Na_2^+ molecule can be rather considered as composed of a weakly interacting Na atom with a Na^+ ion, the ionisation dipole moment should be approximately equal for the bound and repulsive states of the ion.

Summing up, the ionisation probability in the inner well should be higher for the ionisation into the bound $^2\Sigma_g^+$ ionic state and lower for ionisation into the repulsive $^2\Sigma_u^+$ ionic state. At the outer well the ionisation probability increases strongly with the internuclear distance for the ionisation into both bound $^2\Sigma_g^+$ and repulsive $^2\Sigma_u^+$ ionic states due to the increasing ionic character of the double minimum well.

Chapter 3

Experimental set-up

3.1 Overview

The experimental set-up combines the molecular beam technique with femtosecond laser pump-probe methods and a signal registration system, which is capable to detect both ions and photoelectrons. The principle of set-up is summarized schematically in Figure 3.1.

- The high temporal resolution necessary for mapping the molecular or atomic dynamics is obtained by making use of a ***femtosecond laser system***. The femtosecond pump and probe pulses are obtained by a Titan:Saphire laser oscillator and subsequent frequency conversion. The Ti:Sapphire oscillator provides laser pulses with a wavelength of λ = 790 nm and a pulse duration of 12 fs which are amplified in a multipass amplifier. At the exit of the amplifier the laser pulses have a pulse duration of 25 fs, a pulse energy of 1 mJ at the repetition rate of 1 kHz. The frequency conversion of the pulses is performed with an optical parametric amplifier and optical frequency tripler integrated in both arms of Mach-Zender interferometer. The delay between pump and probe laser pulses is set by a stepper motor driven delay line. After that the pump and probe laser pulses are recombined and the collinear pulses are focused with a lens into a vacuum chamber where they orthogonally cross an alkali beam.
- An ***atomic or molecular beam*** is produced by a supersonic expansion of alkali metals heated in an oven. For the production of the molecular beam an additional seeding technique using noble gas (Ar) is implemented. The Na_2 molecules thus obtained are mainly in the ground vibrational level $v'' = 0$, $T_{vib} = 30 - 50K$ [69] and have low rotational temperature $T_{rot} = 5 - 10K$ [70]. This molecular beam technique enables the preparation of species in well-defined initial state thus making the spectroscopic analysis substantially easier. The first pump laser pulse excites molecules and initiates the dynamics. The second, time-delayed probe pulse is used for ionisation of molecules to probe the molecular dynamics.
- Electrons released by the photoionisation are extracted with magnetic fields from the interaction region and their kinetic energies are measured in ***magnetic bottle time-of-flight spectrometer***. It was shown [12] that the measurement of kinetic-energy resolved electrons permits the sub-Angström spatial resolution of molecular dynamics. In addition, the masses of released ions are measured in a linear TOF ion spectrometer. Control of the

experiment is performed by a PC. Results can be obtained as single time-of-flight spectra or as evolution of TOF spectra with varying a pump-probe delay.

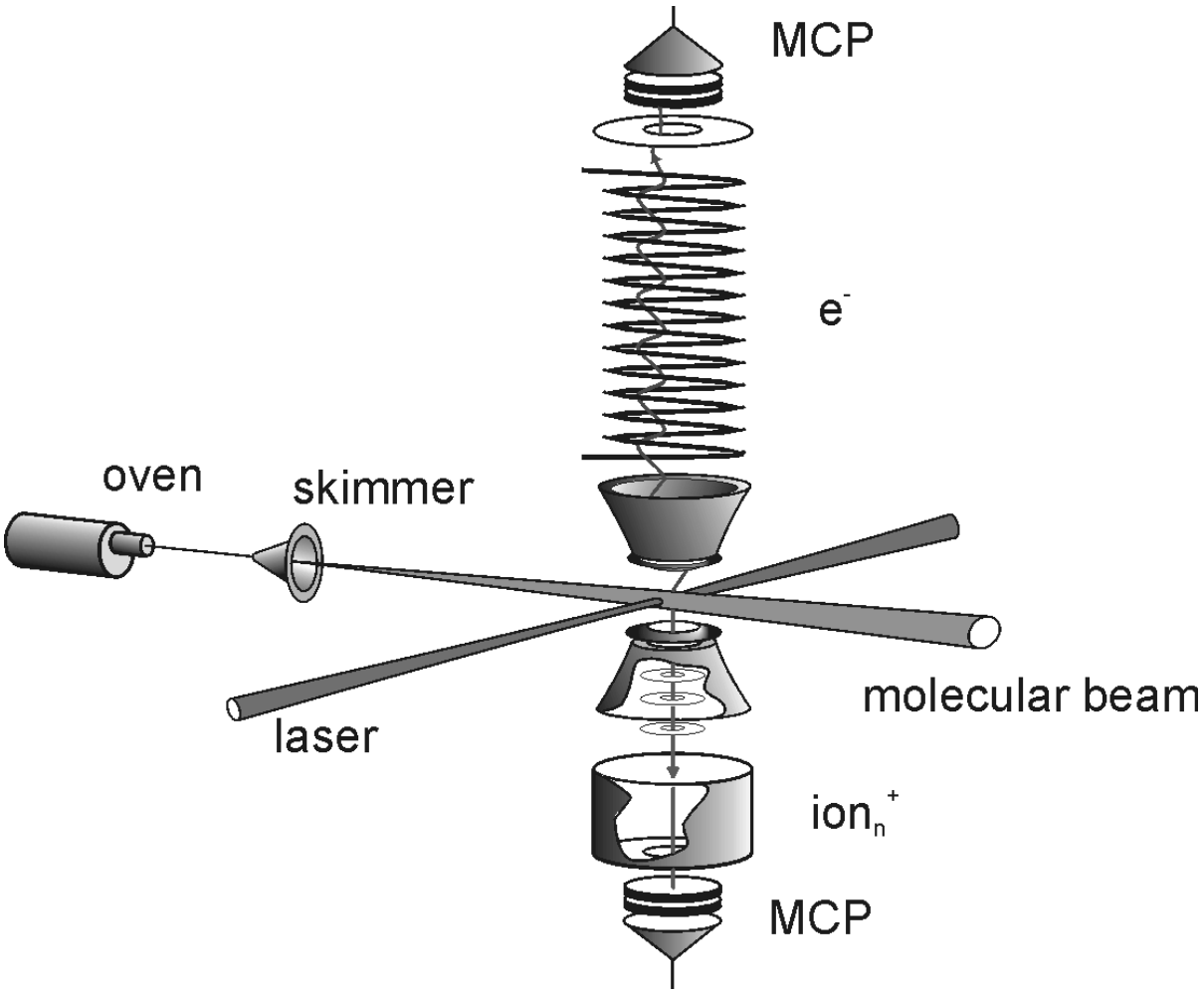

Figure 3.1: Scheme of the pump-probe experimental arrangement.

The following chapter describes each part of experimental set-up in more detail. The second section shows vacuum machine where the molecular beam is obtained, its interaction with femtosecond laser pulses occurs and photoproducts are measured. The third section shows the apparatus, used for the production of the supersonic beam and steering it into the interaction area. It also gives the notion of seeding technique. Next two sections describe the principles of detection of charged particles - ions and electrons - with time-of-flight spectrometers and their experimental implementation. In the sixth section the scheme of the femtosecond laser system is given, and in the following section an overview of used nanosecond laser systems. Finally, in the last section of the chapter the signal triggering and data acquisition system are described.

3.2 Magnetic Bottle Spectrometer molecular beam machine (MaBoS)

3.2.1 Schematic plan of vacuum chambers

The main requirement for the construction of the vacuum apparatus was flexibility, applicability for the investigation of a broad spectrum of substances [70]. The machine is also suited for experiments with corrosive compounds and alkali metals.

Figure 3.2 shows the construction of vacuum chambers and detectors. The basic elements of high vacuum apparatus are two cubes (main and vacuum chamber) made of 15 mm stainless steel (*Nr. 1.4571, VA-TEK*). The foundation is constructed of two 2 meter long tubes. Both chambers are jointed with the foundation using linear ball-bearing so that they can be moved along the tubes separately. This is used for adjustment the oven position and online femtosecond laser lens adjustment. Details of vacuum set-up are described in [70].

The ***oven chamber*** is used for producing the atomic and molecular beams. The set-up for beam consists of the oven, which is placed on the XYZ-manipulator, and the cartridge with the investigated substance placed in the oven.

The XYZ-manipulator was made by *VA-TEK* as a special unit and is used for adjustment the oven position. It allows oven translation in x, y and z directions for up to ±1 cm, and rotation in vertical and horizontal planes up to ±5 degrees.

In the ***main chamber*** there are electron and ion time-of-flight spectrometers and a cold trap for the beam. Both spectrometers are connected through tubes with the chamber for efficient evacuation. The interaction region is pumped through the tube connected to the main chamber. Calibration gas (Xe) is supplied directly to the pole-plate area using 6 mm copper tube. The tube is connected using Gyrolock *(Hoke)* connectors to the Xe bottle (*Messer, Xenon 4.0*). The cold trap is placed in the beam direction. During the experiment the trap is filled with liquid nitrogen and serves also to improve the vacuum (Figure 3.2).

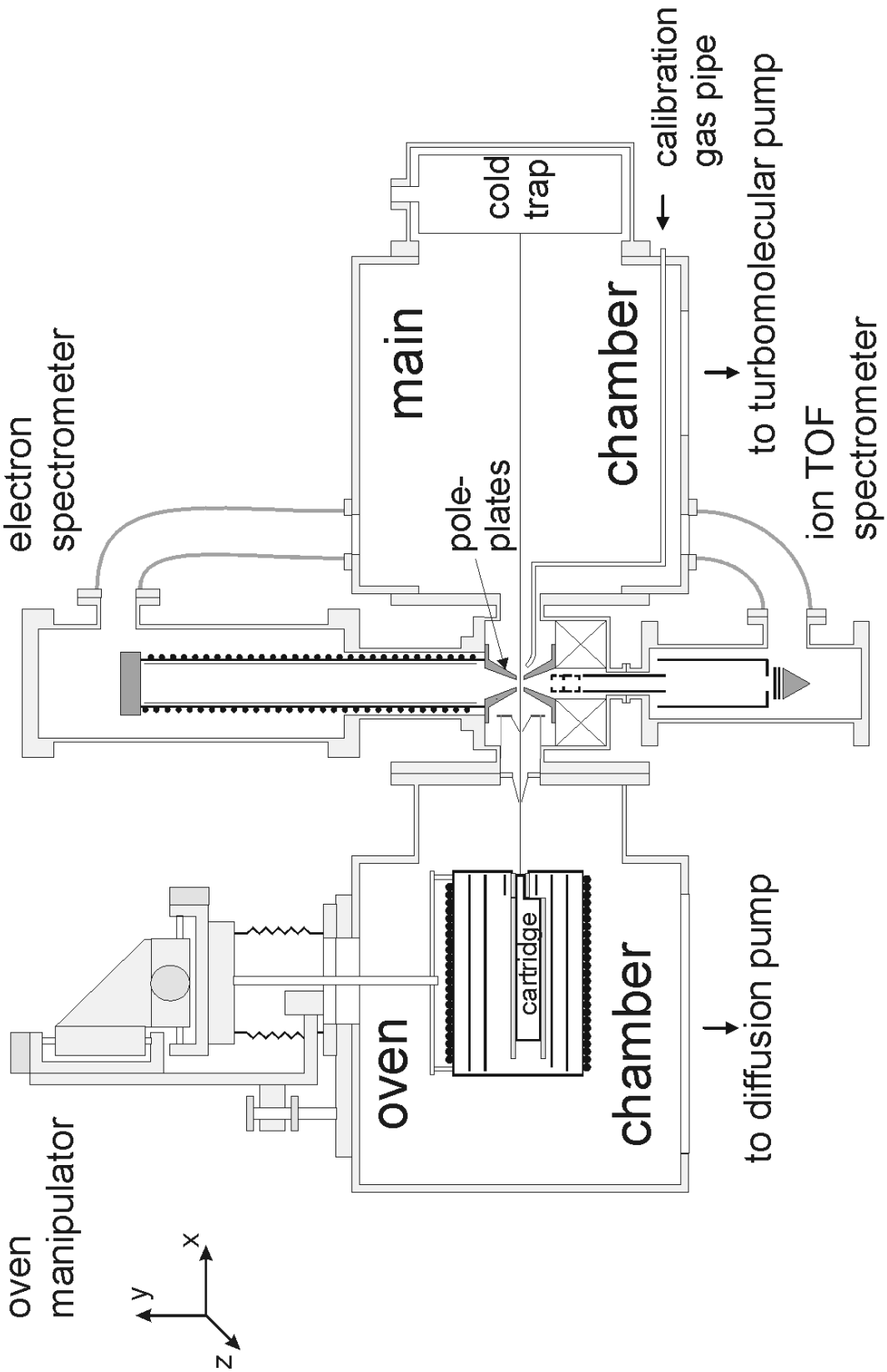

Figure 3.2: Overview of molecular beam apparata. The molecular beam is produced in the oven chamber. Both ion and electron spectrometers are connected to the main chamber. The interaction of laser pulses and molecular beam occurs between the pole-plates of electron spectrometer. A cold trap for alkali beam is placed in main chamber.

3.2.2. Pumps and pressure measurement

The oven chamber is equipped with the diffusion pump (*Varian VHS-10, pumping speed 5300 l/s*). The advantage of diffusion pump, especially useful for seeded beam technique, is its ability to fast pump out a big volume. In the experiments with alkali metals a special mineral pump oil (*Diffilen, Leybold*) is used, which doesn't react with basic agents. A peculiarity of this oil is that it is flammable on open air when hot, so the chamber should be opened only when the pump is cooled down. The backing system for diffusion pump consists of two stages, the Roots pump (*Alcatel RSV 301, pumping speed 83 l/s*) and the oil-sealed vane pump (*Varian CD-1400, pumping speed 18 l/s*).

The main chamber is pumped out with a turbomolecular pump (*Varian V550 969-9049, pumping speed 550 l/s*). The reason for choosing oil-free pump was to avoid the contamination of both spectrometers with pump oil. These oils are objectionable in photoelectron spectrometry, since they can create disturbing contact potentials on the pole plates. The turbomolecular pump is backed by the vane pump (*Varian CD-700, pumping speed 10 l/s*).

The pressure in oven and main chambers is measured by cold-cathode gauges (*Varian 525 Cold Cathode Ionization Gauge*). In addition a Balzers-type gauge (*IKR 010, Schaefer Technologie*) is installed in main chamber. The forevacuum pressure is measured with fast ionisation gauges (*Varian 531*).

Table 3.1 shows the pressure in the chambers for three cases, when a MaBoS machine is ready to experiment and during experiment with Xe and seeded beam (100 μm nozzle):

	Ready to experiment	Exp. with Xe	Exp. with seeded beam
Oven chamber	10^{-7} mbar	10^{-7} mbar	10^{-3} - 10^{-4} mbar
Main chamber	10^{-7} mbar	10^{-5} mbar	10^{-5} mbar
Forevacuum	10^{-2} mbar	10^{-2} mbar	10^{-2} mbar
Ar pressure	-	-	1.5 – 2 bar

Table 3.1. Typical values of pressure in chambers in ready-to-experiment condition, during the calibration with Xe and experiment with seeded beam.

3.3 Production of atomic and molecular beams

3.3.1 Introduction

A molecular or atomic beam is formed when a gas placed in a reservoir flows through an orifice into a vacuum. Liquid or solid substances are first heated, their vapours are spread through the orifice forming a beam. Properties of a beam are determined mostly by the vapour pressure and the shape and diameter of the orifice [71]. The knowledge of the corresponding vapour pressure curve is essential in production of beams. Alkali-metal beams can be produced without a complicated apparatus since their melting and boiling points are low, and their steam pressures are quite high. For example, the melting point for Na and K are 371 K and 329 K respectively. The dependence of their steam pressure [72] for atoms and diatomic molecules is shown in Figure 3.3.

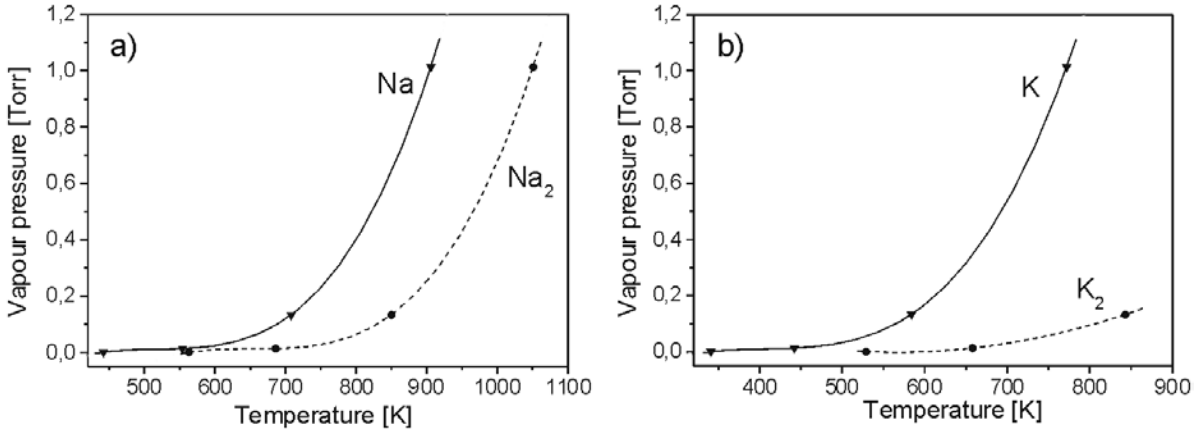

Figure 3.3: The temperature dependence of the steam pressure of a) Na and b) K atoms and diatomic molecules plotted according to data [72].

The influence of vapour pressure and the diameter of the nozzle is defined by the so called Knudsen number [73]:

$$K_n = \frac{d}{\lambda}, \tag{3.1}$$

where d is the diameter of the nozzle, and λ is the mean free path length of particles in the reservoir.

When $K_n \ll 1$ we get an *effusive* beam consisting of particles not interacting with each other. When $K_n \gg 1$ – the beam is *supersonic*, the particles strongly interact with each other and with nozzle walls.

The mean free path length can be expressed as follows:

$$\lambda \approx \frac{1}{\sigma\, n}, \tag{3.2}$$

where σ is cross-section of collisions ($\sigma \approx \sqrt{2}\pi r^2$) and n is particle density in a gas ($n \approx p / kT$).

For ***supersonic beams*** the conduction of the heat from a nozzle walls to a beam can be neglected, so the process of a beam streaming is considered as *adiabatic*. In such a process, since a pressure after expansion into a vacuum chamber may be taken equal 0, the increase of the kinetic energy of the stream is achieved only at the cost of internal energy of the gas, leading to its decrease.

Considering a molecular expansion, one should take into account also internal molecular degrees of freedom:

- vibrational
- rotational
- translational

Since besides elastic also inelastic collisions occur, they lead to an exchange between these energies. Effective cross-sections of these processes are ordered as follows:

$$\sigma(E_{trans} - E_{trans}) > \sigma(E_{rot} - E_{trans}) > \sigma(E_{vib} - E_{trans}). \tag{3.3}$$

Two-body collisions between molecules and atoms lead to a collisional cooling, that is relaxation of internal degrees of freedom. In this case only deepest rotations and vibrations are populated. [74] reported for Na_2 molecules $T_{rot} = 5 - 10K$ (because of efficient rotational-translational transfer), which is close to $T_{trans} = 1 - 5K$. The vibrational temperature is 1-2 orders of magnitude higher – $T_{vib} = 30 - 50K$. According to [74] for an oven temperature 870 K, 83 % of Na_2 molecules are in ground vibrational state ($v'' = 0$), 12 % are in first vibrational state ($v'' = 1$), and 3 % are in $v'' = 2$.

Besides cooling of internal and translational degrees of freedom, a molecular and cluster building occurs in a beam expansion. Many works have been devoted to investigation of Na_2 molecules in a beam. It was shown in [75,76] that already in a pure sodium vapour there are approximately 1-10 % Na_2 molecules. Most of the molecules are formed in gas expansion outside of the nozzle, in three-body collisions. Bergmann et al. showed [76] that the Na_2 formation rate is proportional to a product of a stagnation pressure p_0 in reservoir and nozzle diameter *d*: $p_0^2 \cdot d$, whereas the destruction rate is proportional to $p_0 \cdot d$.

The density of molecules is however small and hot molecules obtained in three-body collisions can be easily fragmented again. An effective cooling occurs in the co-expansion with another noble gas. In this mixture two processes, molecular production and cooling can be separated. This is employed in so-called *seeded-beam technique*.

In the ***seeded beam*** the investigated substance (called a "seed") is mixed in small concentration with an inert gas and expands through a nozzle into a vacuum chamber. The relation of partial pressures of a substance and an inert gas reaches typically values between 1% and 10%. The density of the carrier gas is much higher than that of seed gas. Therefore lots of collisions between seed-gas particles and noble gas atoms occur, whereas the collision rate between seed-gas particles remains low. This leads to an efficient cooling and stabilization of the molecules formed already.

In the case of sodium seeded with argon the argon density is $n = 4.9 \cdot 10^{25}$ atoms/m^3, the collision radius is $r = 11.3 \cdot 10^{-10}$ m [73], the mean free path length λ according to (3.2) is approximately 4 nm. Provided the nozzle diameter of $d = 100$ μm the Knudsen number is $K_n = 2.5 \cdot 10^7$, therefore the beam character is supersonic.

The seeding technique requires powerful vacuum apparatus specially suited to pump high stagnation pressures. To reach low pressure in the vacuum chamber expansion should occur through a nozzle with smallest possible diameter. Handling with small nozzles is a challenge in practice. However, the alkali metals studied here (Na, K) have relatively low melting and boiling points. Thus a considerable vapour pressure (of the order of tenths of mbar) can be reached with not so complicated oven technique.

3.3.2 Na beam implementation

In the Na beam preparation the cartridge filled with sodium is heated in the oven and sodium vapour containing atoms and molecules expands through a small orifice of the cartridge (Figure 3.4). The cartridge is made of *V4A* stainless steel in our workshop and consists of a 15 cm long cylinder chamber with a diameter 3.5 cm. One end is closed with a top. On the other side the cylindrical nozzle chamber is placed. The plate with small nozzle opening is welded on top of the chamber. The shape of the nozzle is cylindrical, the typical diameter used in measurements is 100 or 200 μm, the length of the nozzle channel is 250 μm. The

nozzle orifice ends with a cone (90° opening angle), which has an opening to the outer side of the cartridge. The nozzle plates (*V4a stainless steel*) are produced by *Wetzel Gröbzig Micro Products*. We have compared under the microscope the nozzles made in our workshop using drills and those produced by company and have found that home-made nozzles have an irregular "potato"-shape leading to their clogging or increasing beam divergence. Also, we ordered nozzles made of a special *Nimonic alloy* (90.0 *Goodfellow*) preventing the clogging, however haven't observed a significant difference in beam working time.

The cartridge is filled with about 15 grams of Na (*Merck*). We used sodium of the highest purity (>99%) available at Merck. This amount of Na was enough for approximately 15 days of work with unseeded beam. After that a new cartridge should be filled.

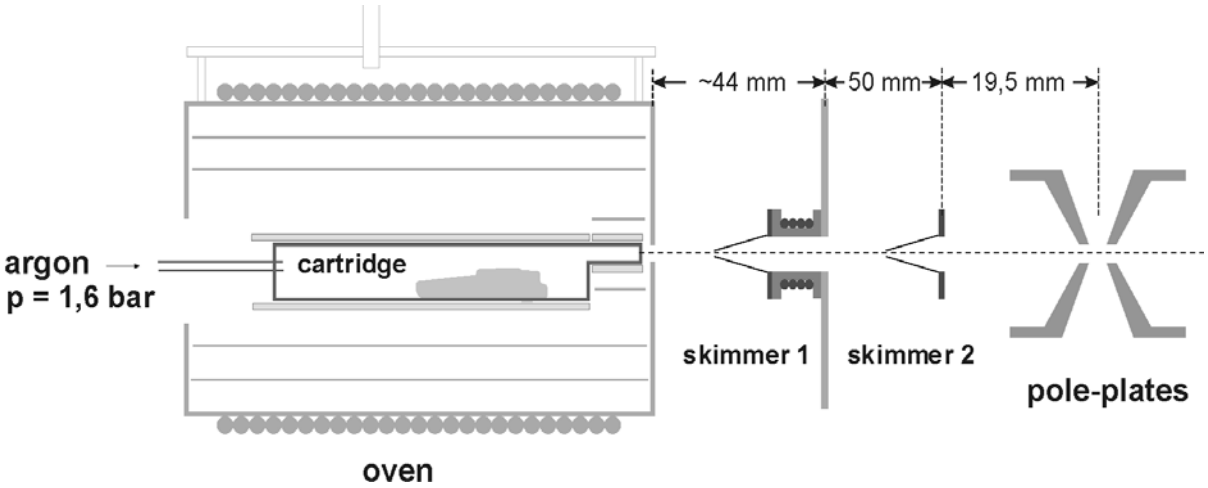

Figure 3.4: Experimental set-up for producing an alkali beam. A cartridge is heated in an oven [77]. Heating elements consist of Ta wires isolated in two ceramic cylinders. To insure the open nozzle its temperature is kept 100 K higher than cartridge temperature. Skimmer 1 separates oven and main chamber and constricts the beam. In order to keep it open, it can be heated. Second skimmer prevents the pollution of pole-plates with alkali particles.

The oven consists of two Al_2O_3 ceramic cylinders (*Alsint 99.7, Haldenwanger*) [77]. Along the cylinders there are holes, through which tantalum wires (*99.9%, d = 0.5 mm, Advent Research Materials*) for heating ($I \leqslant 10$ A) are strained. The cartridge and nozzle chambers can be heated separately. A temperature measurement is accomplished with NiCr-Ni thermocouples (*d = 1.5 mm, Reckmann*). There are steel shield cylinders around ceramics for protection against heat. All the construction is placed into a brass holder cooled with water circuit. Before experiment or after cleaning the oven is adjusted using the XYZ-manipulator.

For collimating the beam the skimmer system is used, as shown on Figure 3.4. The first skimmer (diameter 1.5 mm) is placed on the flange between main and oven chambers and separates them. To avoid its clogging with alkali metals, the skimmer is heated using Ta wire insulated with Al_2O_3 ceramics to about 420 - 450 K, which is well above Na melting point. Since we use in our experiment a magnetic bottle spectrometer, great care was taken to avoid the pollution effects. For this purpose the second skimmer (diameter 1 mm) was built in near the pole-plates to prevent them from pollution with alkali metals. Both skimmers are adjustable in the plane perpendicular to the beam.

The cartridge is typically heated in an oven to T_{cart} = 870 K, the nozzle chamber temperature is always kept approximately 100 K higher in order to prevent nozzle clogging. The Na vapour pressure at this temperature is 0.8 bar (see, e.g. [72]), and the Na_2 vapour pressure is approximately 170 mbar.

In order to obtain a *seeded beam* we slightly modified the set-up. The cartridge is now closed with a top in which the tube for inert gas (Ar) supply is implemented. The top is connected using a flexible metal tube (*Senior Berghöfer*) to the flange tube feedthrough and then to an inert gas bottle placed outside the vacuum chamber. The flexible tube is cooled in front of the flange using water cooling circuit in order to prevent the damage of rubber o-rings. Two valves for coarse and fine gas flow regulation are also built in. In addition a bypass directly to the main chamber provides a proper purge of the gas supply tubes, which is necessary for stable work of the alkali beam. The argon used in the experiment (*Argon 5.0, Messer*) has a purity of >99.999 Vol%. Using a pure inert gas is important to keep the nozzle open during seeding. A manometer (*Landefeld*) is installed on the tube outside the chamber to monitor the Ar partial pressure. A typical Ar pressure during experiment is 1-2 bar.

3.3.3 K beam implementation

The potassium being even more chemical reactive than sodium requires a special additional care in preparation and handling the experiment. The cartridges were charged in the atmosphere of non-reactive gas. In the case of experiments with K atoms it was done in nitrogen atmosphere, and in the case with K_2 molecules – in argon. For experiments with an *atomic beam* we used a 98% potassium from *Merck*. The nozzle diameter was 200 μm.

The working temperatures for the K atomic experiment were T_{cart} = 620 K for the cartridge, T_{noz} = 720 K for the nozzle, and 420 – 450 K for the skimmer.

For experiments with *molecular beam* the major problem was the clogging of the nozzle. There could be several reasons for that. Potassium from Merck still contained some impurities, and since it was stored in a paraffin oil, some oil particles could penetrate into deep layers. Further, in an oven the oil could burn and close the nozzle. Therefore we used more pure potassium 99.95% (*ABCR*) in ampoules. Filling of the cartridge was performed in more inert Ar atmosphere. Normally, the cartridge was filled with one ampoule (5 grams), which was enough for about 10 hours of measurement. The nozzle diameter was 100 μm.

In the K_2 molecular experiment the cartridge was kept at temperature T_{cart} = 630 K, the nozzle at T_{noz} = 700 K and the skimmer at 420 – 450 K.

Another reason for closing the nozzle was impurified argon we used before in Na experiments. Therefore we changed to a Ar 6.0 (*>99.9999 Vol%, Messer*) of higher purity. In addition, in this experiment we heated the argon supply pipe right in front of the cartridge to about 650 K. The Ar pressure was 1-2 bar.

The parameters used during the work with atomic and molecular beams of sodium and potassium are presented in the Table 3.2.

	Na molecular beam	Na molecular seeded beam	K atomic beam	K molecular beam
Oven temperature	870 K	870 K	620 K	770 K
Nozzle temperature	970 K	970 K	720 K	870 K
Ar pressure	-	1-2 bar	-	1-2 bar
Nozzle diameter	200 μm	100 μm	200 μm	100 μm
Beam duration	15 days	~ 24 hours	7 days	~ 10 hours

Table 3.2: Typical parameters of alkali beams.

3.4 Magnetic bottle electron spectrometer

3.4.1 Principle of operation

An electron spectrometer has to fulfil a number of demands. First of all the requirements for a spectrometer include highest possible electron kinetic energy resolution, state-of-the art detection techniques, efficient data handling and data analysis, restriction of pumping systems. It also important to collect all the electrons over a wide a range of initial velocities. This is difficult to achieve with conventional designs of electron energy analysers because the energy resolution deteriorates rapidly as the acceptance angle is increased. These problems have been overcome in "magnetic bottle" spectrometer. It combines a high collecting efficiency (2π sterad for electrons from 0 to 10 eV) [78] with good energy resolution. In this instrument electrons initially emitted in all directions from the region of the laser-matter interaction are formed into a nearly parallel beam using an inhomogeneous magnetic field. The laser focus where the multiphoton ionization takes place is located between the pole-pieces of an electromagnet producing a 1 Tesla magnetic field. The Lorentz force

$$F_1 = ev \times B \tag{3.4}$$

causes each emitted electron to spiral around a magnetic field line. The radius of the orbit (cyclotron radius):

$$r_i = \frac{v \sin \Theta_i}{\omega_i} \tag{3.5}$$

and the angular momentum of the circular motion in the strong field B_i:

$$l_i = \frac{m^2 v^2 \sin^2 \Theta_i}{eB_i}, \tag{3.6}$$

where T_i is the angle between the velocity vector of the electron and the spectrometer axis. Then the electron enters the region of the weak uniform magnetic field of 10^{-3} Tesla. If the variation of the magnetic field along the axis is adiabatic, that is if the magnetic field changes slowly along one loop, then the angular momentum is a conserved quantity. Therefore the angle T_f of the helical motion in the region of low field B_f is given by [78]:

$$\frac{\sin \Theta_f}{\sin \Theta_i} = \left(\frac{B_f}{B_i} \right)^{1/2}. \tag{3.7}$$

The transverse component of the velocity is thus reduced. Since the total velocity is unchanged the longitudinal component increases from v to:

$$v_{zf} = v \left(1 - \frac{B_f}{B_i} \sin^2 \Theta_i \right)^{1/2}. \tag{3.8}$$

The electron trajectories are parallelized in this type of the magnetic field configuration. Even electrons that are initially emitted nearly perpendicularly to the field lines in the high-field region are nearly parallel in the low-field region, having the angle $T_{f,max}$:

$$\Theta_{f,\max} = \sin^{-1} \left(B_f / B_i \right)^{1/2} = 1{,}8°, \tag{3.9}$$

if the field strengths in the two regions are sufficiently different. After the electron beam has been parallelized, the electrons travel in a uniform magnetic field down to a flight tube before being detected. The time-of-flight in the drift tube is:

$$T_{drift} \approx \frac{l_{drift}}{v}\left(1+\frac{B_f \sin^2 \Theta_i}{2B_i}\right), \tag{3.10}$$

thus depends on the electron energy, but because of the parallelization of the trajectories it is almost independent of the initial direction of emission.

3.4.2 Design of apparatus

The magnetic bottle used in our set-up is produced by the company *Applied Laser Technologies*. The spectrometer consists of an ionisation region, a drift tube and a detector (Figure 3.5). The 1 Tesla field is created by an iron yoke and a large coil external to the vacuum. The power supply gives 4 A at approximately 55 V. The cross-sectional area of the iron circuit in the pole-peaces was designed so to provide adiabatical change of the field strength.

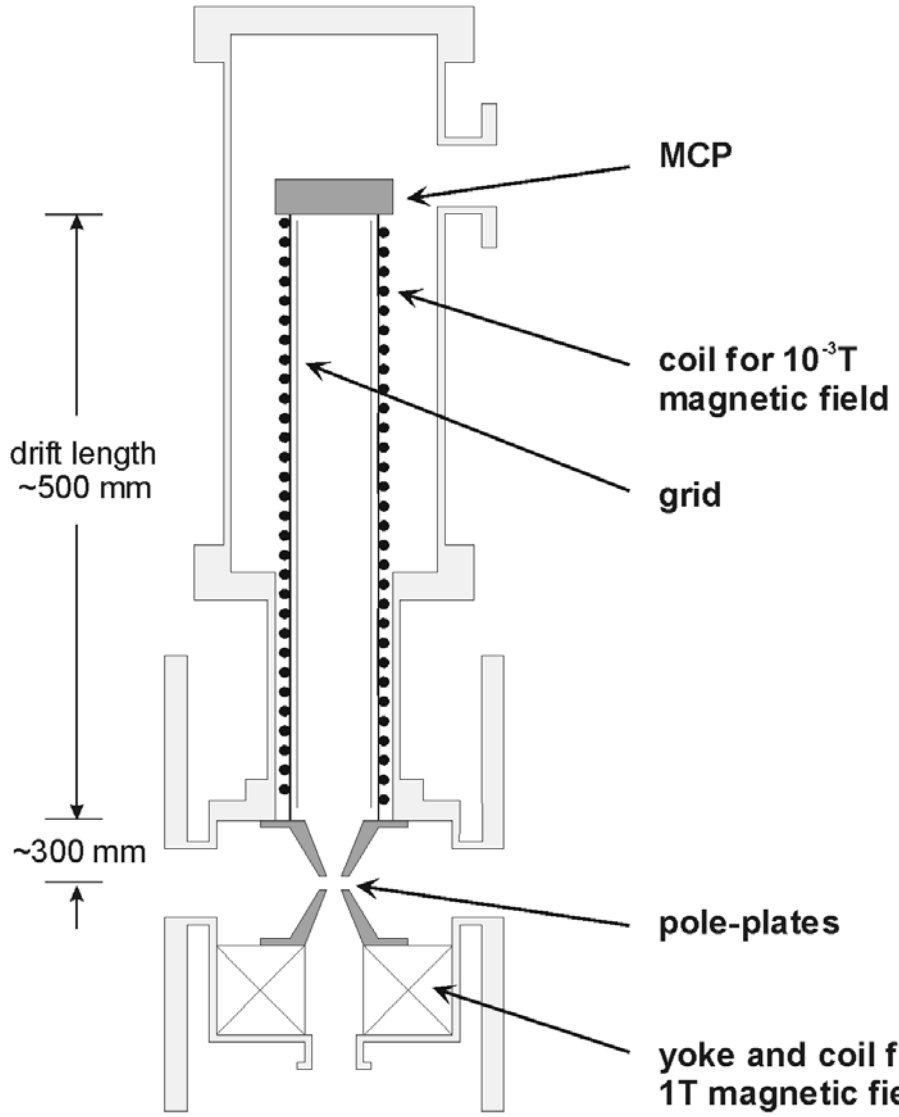

Figure 3.5: Vertical sectional view of the magnetic bottle electron spectrometer. The photoelectrons are created in a volume between pole-plates. The 1 Tesla field formed by an iron yoke and the large coil is used for parallelization of the electron orbits. The 10^{-3} Tesla magnetic field guides electrons to a detector – MCP. Electrons can be retarded or accelerated with electrostatic field created by the grid.

A weak magnetic field of 10^{-3} Tesla is produced in the drift tube (0.5 m) by means of an external coil operated at 2 A, 1 V. The earth magnetic field in the ionisation region and flight tube is compensated using two pairs of mutually perpendicular Helmholtz coils. In the direction of the flight tube the magnetic field generated inside the spectrometer dominates over the earth magnetic field.

Finally, the flight times of the electrons are measured using two microchannel plates in chevron mount (*Hamamatsu F 1094-23S*) as a detector at the end of the flight tube (Figure 3.5).

The electric potential along the spectrometer axis can be adjusted externally by three independent power supplies (see Figure 3.6);

- The pole-pieces are grounded.
- The two electrodes are mounted on top of pole-pieces. Voltages U_1 and U_2 are applied typically to compensate contact potential fields. In our experiments a field-free case was reached by connecting pole-plates to the same voltage ($U_1 = U_2 = U_{pp} = -0.65$ V). Furthermore, [79] reported about covering the pole-pieces with carbon to eliminate charge effects, which however wasn't done in our set-up. Non-equal pole-plate voltages can be used to provide an extraction field such that acceptance angle is increased to 4π sterad, and to extract ions in a direction opposite to electrons.
- the potential applied to a cylindrical grid has two main operation modes. In first mode a fixed retardation of electrons is used to improve the resolution of time-of flight analysis. In the second, used for calibration the TOF axis, the retardation voltage U_g is applied to yield a constant energy resolution.

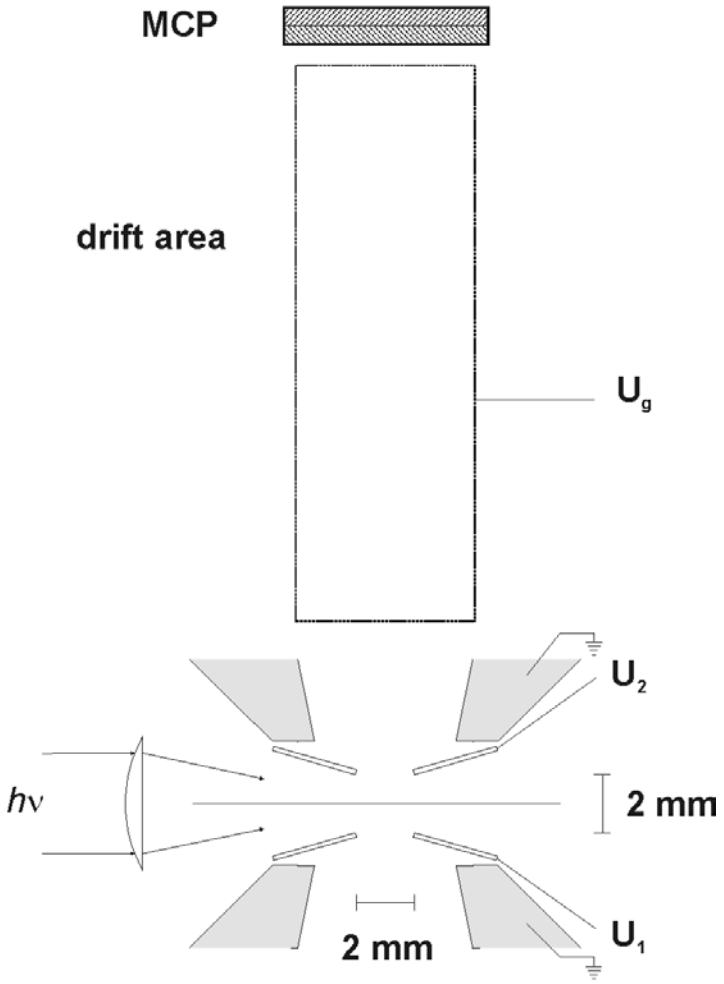

Figure 3.6: Schematic representation of electric potentials applied in magnetic bottle spectrometer. The pole-pieces are grounded. Voltages U_2 and U_1 are applied to upper and bottom electrodes covering pole-pieces. Typically used combination in experiment $U_1 = U_2 = U_{pp}$. A voltage U_g applied to a cylindrical grid is used for retardation or acceleration the photoelectrons.

3.5 Ion time-of-flight spectrometer

In our set-up mass analysis of the formed ions can be a very useful complement to the photoelectron studies. A Wiley-McLaren type spectrometer for measuring ions time-of-flights is shown schematically in Figure 3.7. The voltage applied to the pole-plates of magnetic bottle spectrometer is used to extract ions from the interaction region and force them to move towards the detector. We found an optimal combination of upper- and lower-pole-plate voltages of U_1 = 410 V and U_2 = 390 V. This arrangement corresponds to that one typically used in Wiley-McLaren scheme [80] with the difference that the position and shape of pole-plates cause already the focussing the ions. Because of this, we use the only one lens (U_{EL} = 100 V) as ion optics for parallelization the ions. Two others are grounded (see Figure 3.7). After extraction and parallelization ions are drifting in field-free region (l = 31 cm) until they hit the detector. The detector consists of two MCPs connected in chevron arrangement (*Burle, APD 3025 12/10/12 D STD*). The ions hit the front surface of negatively charged MCP (-2 kV). The released electrons that leave the MCPs have small kinetic energies, therefore they are accelerated towards a positively charged copper anode (U_{anode} = 160 V). The details and construction of ion time-of-flight spectrometer set-up as well as electric schemes can be found in [70].

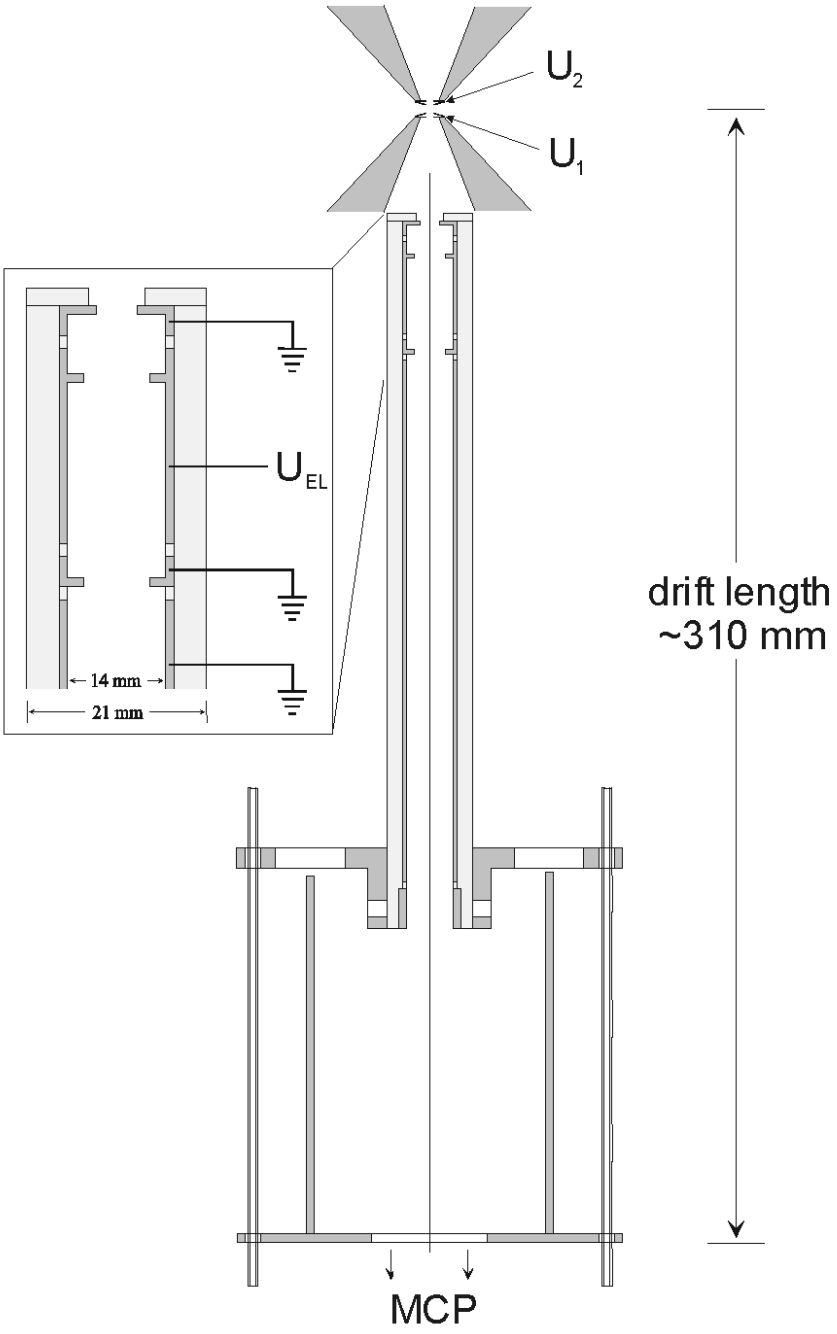

Figure 3.7: Vertical sectional view of the time-of-flight ion mass spectrometer. Voltages U_1 = 410 V and U_2 = 390V are applied to the pole-plates to extract ions from interaction region. Furthermore, ions are parallelized with electrostatic lens (U_{EL} = 100V) and drift in a field-free region towards a detector, which consists of two MCP in chevron arrangement.

3.6 Femtosecond laser system

The femtosecond laser system used in a pump-probe experiment together with wavelength conversion units is scetched in Figure 3.8.

A Ti:Sapphire oscillator (*Femtolasers, Femtosource Scientifis Pro*) [81] is pumped by Nd:YVO_4 pump laser (*Coherent, Verdi V-5*) [82]. The oscillator provides laser pulses with a wavelength of λ = 790 nm, the pulse duration of 12 fs at an energy of 4 nJ at a repetition rate

of 75 MHz. The laser pulses are coupled into a chirped-pulse multipass amplifier (*Femtolasers, Femtopower Pro*) [83]. Before amplification the laser pulses are stretched in time, so their power remains under the destructive threshold of the amplifier crystal. The cooled Ti:Sapphire crystal is optically pumped by a Nd:YLF laser (*B.M. Industries, YLF 621 D)*. The YLF generates pulses at frequency doubling on 527 nm, pulse duration 500 ns, and power 3 to 18 W at 1 kHz [84]. After amplification the laser pulses are compressed in a pulse compressor to 25 fs. The pulse energy after the prism compressor is 1 mJ at a repetition rate of 1 kHz.

Frequency conversion is performed with an optical parametric amplifier (*TOPAS, Light* C*onversion*) and an optical frequency tripler (*HHG, Light Conversion*). They are integrated in each arm of the Mach-Zender interferometer. The beam splitter (60% transmission and 40% reflection) after the output of the amplifier divides laser pulse into two parts. The probe pulse is time delayed with the computer operated moving stage (*SMS, MICOS*).

The optical frequency tripler HHG is used in a pump-probe experiment to obtain a third harmonic of 267 nm. For that two BBO crystals are used. First, the second harmonics is obtained by a frequency doubling (λ = 395 nm). Then the fundamental and the second harmonic are overlapped in a second BBO crystal to form a 267 nm beam by sum frequency mixing. Another prismcompressor is used to compensate dispersion introduced by HHG. The laser pulses obtained on exit of the HHG have wavelength λ = 266 nm. Evaluation of the pulse duration using a transient two-photon absorption in water gives a value of t = 100 fs [85,86].

The TOPAS converts 790 nm, 500 μJ input pulses using parametric fluorescence and difference frequency mixing. The frequency quadrupling of the pulses *(*λ = 1360 nm, t = 30 fs) is performed using two BBO crystals. The pulses at the exit of the TOPAS have a wavelength in the range of λ = 330 - 340 nm and a pulse energy of E = 3 μJ. The divergence of the pulse is compensated with a telescope at the exit of TOPAS.

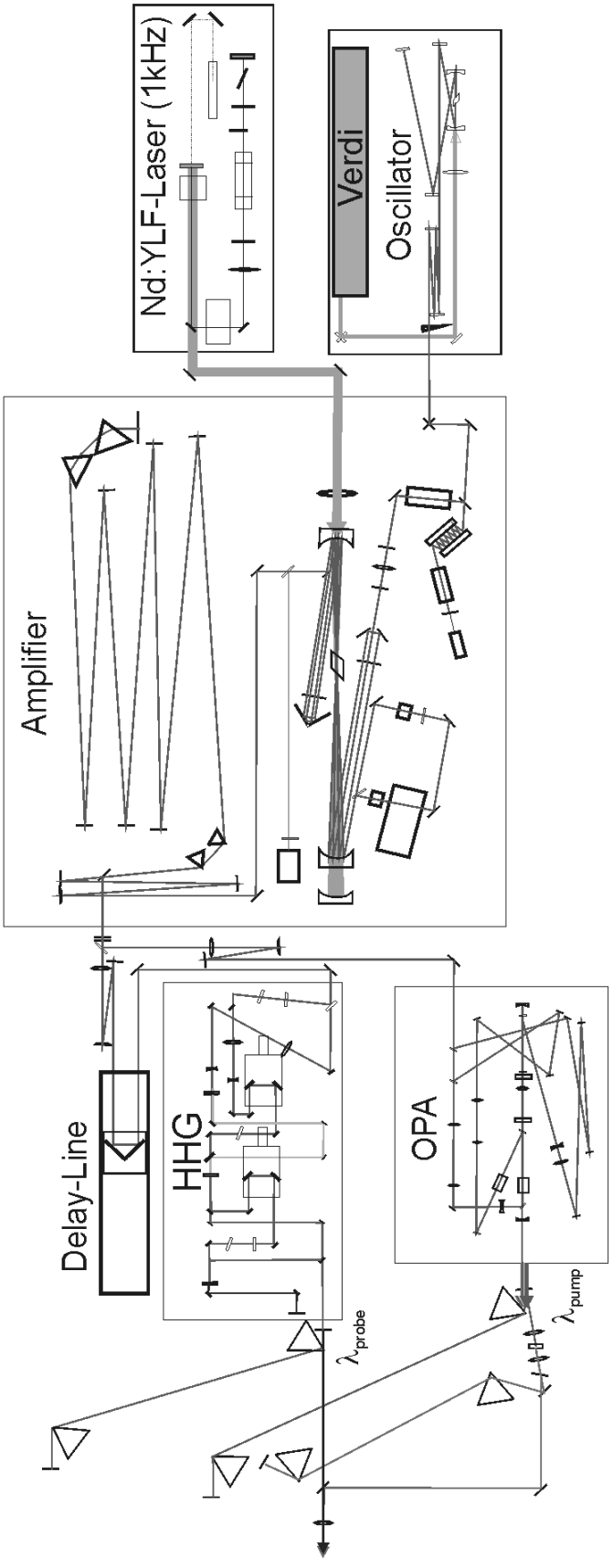

Figure 3.8: The femtosecond laser system consists on: a Ti:Sapphire oscillator *Femtolasers Femtosourse Scientific pro* [13], pumped by a $Nd:YVO_4$ laser *Verdi Coherent* [14]; a multipass amplifier *Femtolasers Pro [15]*, pumped by *BMI Nd:YLF 621-D*; a harmonic generator *Light conversion*; an optical parametric amplifier *Light Conversion TOPAS*.

After recombining both 340 nm and 266 nm beams with a partial beam splitter they are adjusted to be collinear. With the help of a f = 200 mm lens the laser beams are coupled into the vacuum chamber between the pole-plates of the spectrometer.

For the characterisation of the femtosecond laser system the following methods are used:

- spectral distribution of the pump and probe laser were taken with a spectometer (*Stellarnet EPP2000*);
- coarse defining the time overlap of the pump and probe laser pulses in the picosecond time region is made with a streak camera;
- pulse duration measurements of the 340 and 266 nm laser pulses are performed using cross-correlation in Xe. Figure 3.9 [86] shows the corresponding photoelectron spectrum from the ionisation of Xe with 2 photons of 265 nm and 1 photon of 340 nm as a function of the delay between the laser pulses. The evaluation of the cross-correlation curve gives the pulse duration for both pulses $t_{265} \approx t_{340} \approx 48$ fs [86];
- cross-correlation in Xe is also used for precise measurement the temporal overlap of pump and probe pulses. The cross-correlation method is described in details in [86].

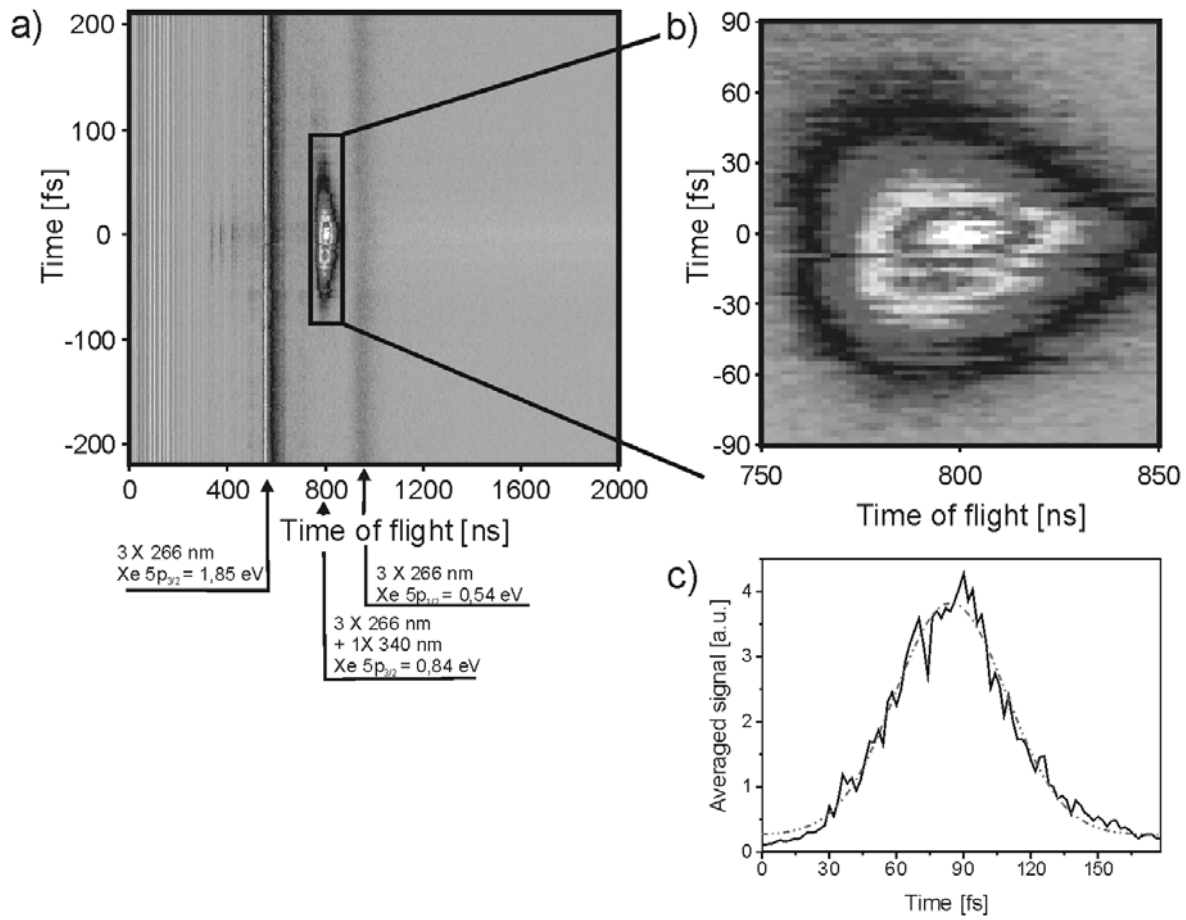

Figure 3.9: Multiphoton ionisation of Xe atoms. a) The measured photoelectron spectrum as a function of delay between λ_{pump} = 340 nm and λ_{probe} = 266 nm laser pulses; b) the enlarged cut of the photoelectron spectrum. c) the averaged two-colour photoelectron signal (solid line) and fitted Gaussian curve (dashed line). The cross-correlation has a FWHM of 58.7 fs, what yields a pulse duration of 48 fs [86].

3.7 Nanosecond laser system

The nanosecond laser system was used for test experiments with both spectrometers, i.e. the calibration of the electron and ion spectra and the characterization the molecular beam.

We used two lasers:

- ***Nd-YAG nanosecond laser*** (*Spectra Physics, Quanta-Ray INDI-30*) provides pulses at 20 Hz repetition rate, 7 ns pulse width. The wavelengths are 1064 nm fundamental, second harmonic 532 nm, third harmonic 355 nm and forth harmonic 266 nm. The 355 nm light has linear polarization parallel to the axis of the electron spectrometer, the 532 nm light has polarisation perpendicular to the spectrometer axis. The laser beam is focused with a lens with the focal length 25 mm into the interaction area.
- ***Dye laser*** (*Sirah, Cobra-Stretch Dye Laser*) pumped by a frequency doubled Nd-YAG laser is used for the calibration of the magnetic bottle spectrometer. The laser gives pulses with 20 Hz repetition rate in the tuning range of dye used in laser. We used Fluorescein 27 (*Sirah*) solved in ethanol + water solution, which gives pulses in the wavelength range of 540-575 nm and a maximum efficiency at 548 nm. The maximum laser energy at 548 nm was approximately 70 mJ.

3.8 Triggering and data acquisition

The triggering for the nanosecond lasers was performed with a photo-diode placed in front of the MaBoS machine. It is lightened by a reflected portion of nanosecond laser beam. The trigger for the femtosecond laser system was a signal, which activates the Pockels cell.

The time-of-flight spectra are taken with a digital storage oscilloscope from the company LeCroy (*LeCroy 9370*). This oscilloscope has an analog bandwidth of 500 MHz and a maximum counting rate of 2 gigasamples obtained by adding the four incoming channels of the oscilloscope.

Two routine procedures were used to acquire measurement data:

- For creating an *instantaneous time-of-flight spectrum* a signal taken with LeCroy was averaged over several thousand laser shots. Averaged spectra were further read by the computer using an IEEE-interface using LabVIEW program *Read_osci.vi*.
- In a *pump-probe experiment* time-of-flight ion or photoelectron spectra are taken as a function of time delay between pump and probe laser pulses. The program controls the motion of the translation stage of Mach-Zender interferometer using a controller (*MICOS SMCbasic*) in given steps. At every position of a delay stage a signal from MCP with the repetition rate of laser system of 1kHz is sent to LeCroy oscilloscope triggered with a signal from a Pockels cell. A signal at LeCroy is averaged typically over 862×2 or 862×4 shots and is then saved with a computer using a National instruments DAQ card (*DAQ-PCI 6034E*). For monitoring the changes in femtosecond laser beam intensity a photodiode using a reflected portion of a beam was used. After finishing a single measurement program moves a delay line to the next position. A software for steering an experiment was written by M. Winter in LabView (version 6.1.1) package and is described in his diploma [86].

  The average time of one scan is approximately 40 minutes for approximately 1500 points along pump-probe delay.

Chapter 4

Vibrational wave packet dynamics in Na_2 states

In this chapter the observation of the vibrational dynamics in the $C^1\Pi_u$ and $7^1\Pi_u$ states of the Na_2 molecule is reported. The utility of the femtosecond pump-probe scheme with kinetic energy-resolved photoelectron detection for the observation of the molecular dynamics will be shown. Further, the ability to distinguish between several ionisation pathways in the scheme with kinetic energy photoelectron detection will be discussed.

4.1 Introduction

Femtosecond pulses available nowadays are shorter than the period of molecular vibrations, so it is possible to excite and probe time-dependent vibrational motion of the molecule. The ability to probe the molecular dynamics with femtosecond laser pulses has been demonstrated with a variety of different techniques in several molecules [1-4].

The use of the energy-resolved photoelectron spectroscopy to probe the molecular dynamics was proposed by Seal and Domcke [44,45] and developed in the theoretical publications by Meier and Engel [36,37,87]. The utility of this technique to monitor the evolution of a vibrational wave packet in a real time was demonstrated on excited states of sodium dimer [31] and sodium iodide [88]. It was shown in [12] that the photoelectron detection enables besides the femtosecond time resolution a sub- Ångström spatial resolution.

Briefly the scheme of the pump-probe experiment for the observation of molecular dynamics can be described as follows. A first femtosecond laser pulse excites a superposition of vibrational levels, a wave packet, in a neutral state of the molecule. The wave packet is the quantum mechanical analogue of the molecular motion. The evolution of this wave packet after some delay is probed by a second laser pulse which ionises the molecule. in the experiment the kinetic energy of the released electrons are measured as a function of a pump-probe delay.

In this chapter the Na_2 molecule is used for observation of the molecular vibrational dynamics in the real time. The choice of Na_2 dimer for our experiment was motivated by several reasons. First, the Na_2 molecule is one of the simplest systems for the theoretical description,

the molecule and its potentials are very well investigated both theoretically and experimentally. Thus it is a suitable system for analysing the ultrafast dynamics. Second, in order to follow the molecular dynamics by creating vibrational wave packets the laser pulse must have a duration less than the vibrational period of the molecule. For this reason alkali dimers and in particular the sodium molecule are experimentally well suited. Because of the weight of the nuclei (for instance 23 at. un. for Na) and the way of potentials the vibrational period of the nuclei in the molecule consists around 300 fs thus being much higher than for instance the vibrational period of the simplest molecule H_2 [89].

In our experiment the kinetic energies of the photoelectrons are detected. Use of the kinetic energy resolved photoelectron spectra enables to disentangle ionisation pathways from different potentials. The vibrational dynamics in several states of Na_2 molecule will be shown.

4.2 Experiment and parameters

In our experimental scheme using $\lambda_1 = 340$ nm pump femtosecond laser pulse and $\lambda_2 = 266$ nm probe pulse the observation of the molecular dynamics in several potentials of the Na_2 molecule is possible.

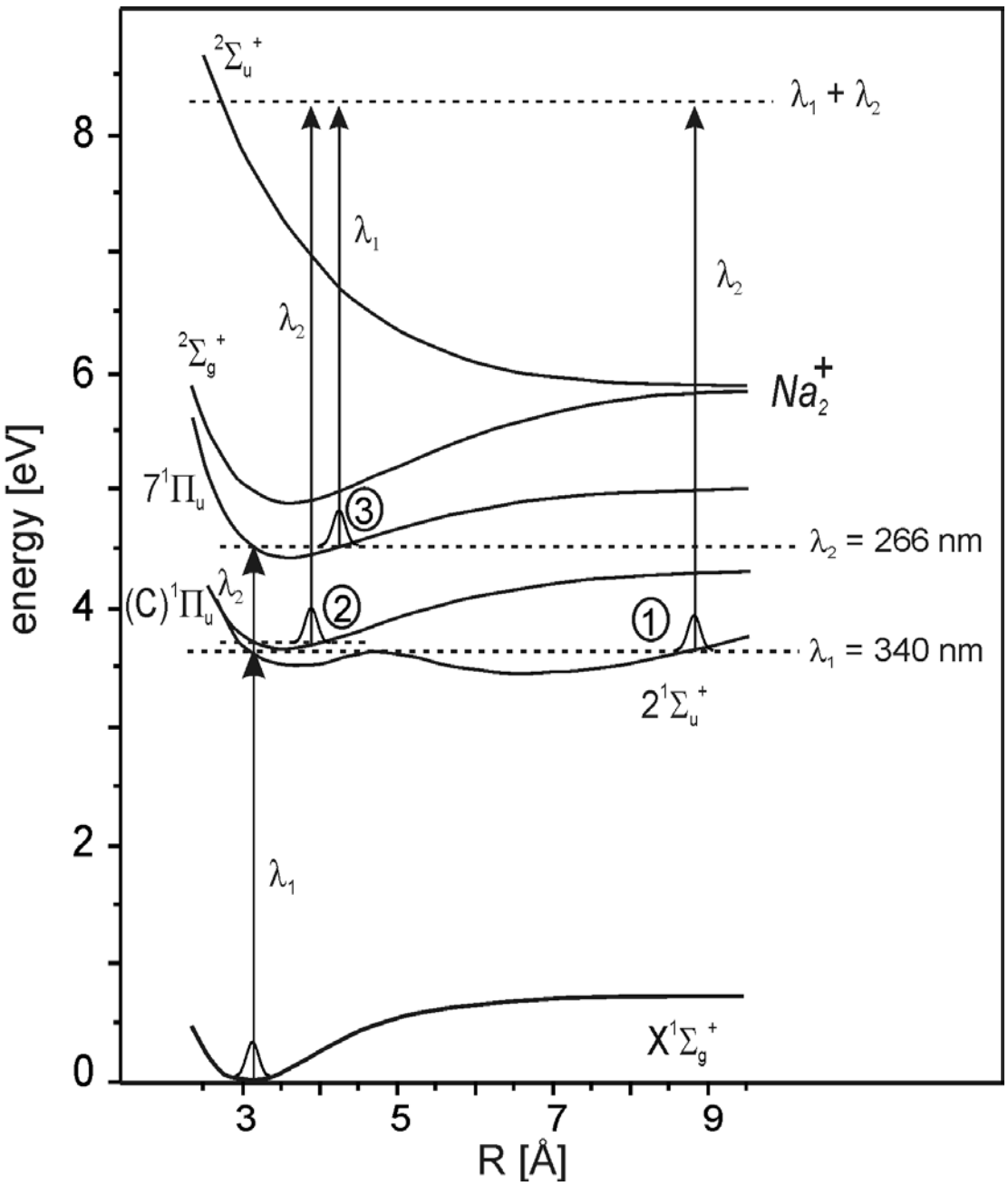

Figure 4.1: Excitation scheme for Na_2 for the two-color experiment pump wavelength of λ_1 = 340 nm and probe wavelength of λ_2 = 266 nm. The dynamics is mapped in several states: (1) – excitation of the $2^1\Sigma_u^+$ double minimum state with λ_1 = 340 nm and ionisation with λ_2 = 266 nm; (2) – excitation of the $C^1\Pi_u$ state with λ_1 = 340 nm and ionisation with λ_2 = 266 nm; (3) – excitation of the $7^1\Pi_u$ state with λ_2 = 266 nm and subsequent ionisation with λ_1 = 340 nm. Ionisation into two lowest ionic states , $^2\Sigma_g^+$ bound and $^2\Sigma_u^+$ repulsive, is possible.

Figure 4.1 shows the scheme of the ground, excited $2^1\Sigma_u^+$, $C^1\Pi_u$ and $7^1\Pi_u$, and ionic $^2\Sigma_g^+$ and $^2\Sigma_u^+$ potentials of Na_2. Process (1) is the excitation of the wave packet in the double minimum state $2^1\Sigma_u^+$ of the Na_2 molecule with the pump wavelength of λ_1 = 340 nm and subsequent ionisation with the probe wavelength of λ_2 = 266 nm. The experiment on this state with slightly different experimental parameters will be discussed in detail in the next chapter. Process (2) is the excitation of the wave packet in the $C^1\Pi_u$ state with the wavelength of λ_1 = 340 nm and subsequent ionisation with the wavelength of λ_2 = 266 nm. The state $C^1\Pi_u$ is energetically close to the double minimum state and can be also excited if the spectral width

of the pump laser pulse is large enough and ionised with the probe laser pulse. The process (3) occurs when the λ_1 = 266 nm laser pulse is used to excite the $7^1\Pi_u$ state and the λ_2 = 340 nm to ionise the molecule. Thus in this case an inverted pump-probe scheme is observed.

The experimental set-up is described in detail in the Chapter 3. The pulses of 790 nm, 25 fs and 1 kH are frequency converted to give the λ_1 = 340 nm, $\Delta\lambda$ = 5.7 nm pump laser pulse and λ_2 = 266 nm, $\Delta\lambda$ = 3 nm probe laser pulse. In the Michelson-type interferometer a variable time delay between two pulses is introduced. The collinear propagating laser pulses are focussed with a f = 200 mm lens into the vacuum chamber where they perpendicularly intersect the molecular beam. The sodium beam is obtained by a supersonic expansion from an oven operating at 870 K through a 200 μm nozzle. The photoelectron spectra are recorded with the magnetic bottle spectrometer and averaged over several thousand laser shots. The pump-probe delay is changed in 30 fs steps. The retardation and pole-plate voltages in experiment are set to U_g = 0.6 V and U_{pp} = -0.65 V respectively.

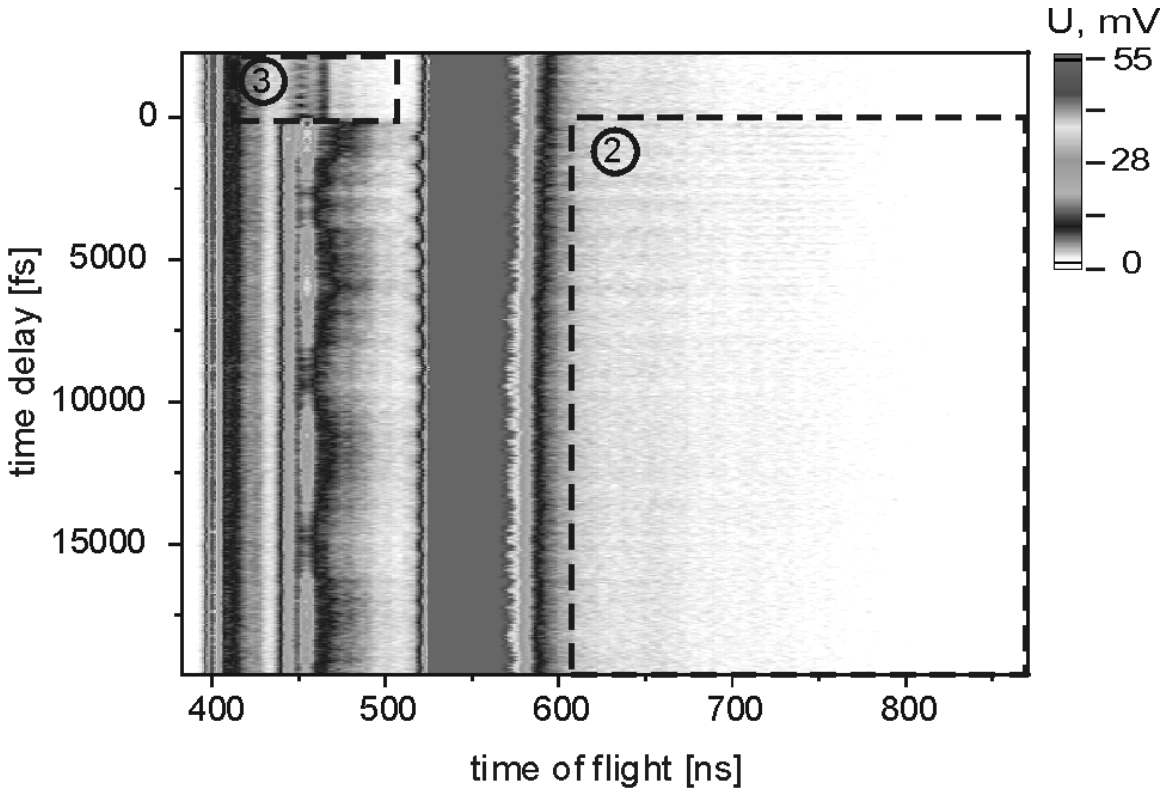

Figure 4.2: Grey scale representation of the pump-probe photoelectron time of flight spectrum. The areas 2 and 3 indicate the molecular dynamics in the $C^1\Pi_u$ and $7^1\Pi_u$ states respectively.

The experimental result is shown in Figure 4.2 and represents a photoelectron time-of-flight spectra as a function of the pump-probe delay in a range of -2 till 20 picoseconds. The spectrum presented is obtained by averaging of the experimental spectra using a Gaussian 3x3 averaging. The time of flight scale calibration is performed using the Na signal present in the spectrum at 400, 450 and 550 ns and calibration using ionisation of Xe with Nd:YAG nanosecond laser. The dynamics from the processes (2) and (3) are also indicated in the figure. Below we discuss these individual contributions to the signal in detail.

4.3 Vibrational dynamics in $C^1\Pi_u$ state

4.3.1 Excitation scheme

The potentials of Na_2 molecule relevant to the experiment are shown in Figure 4.3a. The $C^1\Pi_u$ state has a minimum at the internuclear distance of 3.5 Å at an energy of 3.7 eV. The state is energetically close to the double minimum state of Na_2 molecule, the energy separation between them is ΔE = 0.11 eV. Therefore at a wavelength of λ_1 = 340 nm of the pump pulse it can be excited since the spectral width of the pump pulse is broad enough. As shown on the scheme, the wavelength of λ = 336 nm is required to excite first vibrational levels (v' = 0,1) of the $C^1\Pi_u$ state. Since the excitation spectrum of the pump beam of λ_1 = 340 nm has the spectral width of 5.7 nm, the (v' = 0, 1) levels are excited with the spectral "wings" of the laser pulse. The pump laser pulse creates a wave packet at the inner turning point of the $C^1\Pi_u$ state at 3.2 Å. The wave packet starts to move towards big internuclear distances. After it reaches the outer turning point at 145 fs, it is reflected back, reaches inner turning point again at 290 fs, thus oscillating in the potential. The period of the wave packet oscillation is determined by the energy separation between adjacent coupled levels. In our experiment the energy difference between (v' = 0) and (v' = 1) levels is 115.8 cm^{-1} [90] corresponding to the period of 290 fs. The wave packet moves in the well at the internuclear distances between 3.2 and 3.8 Å.

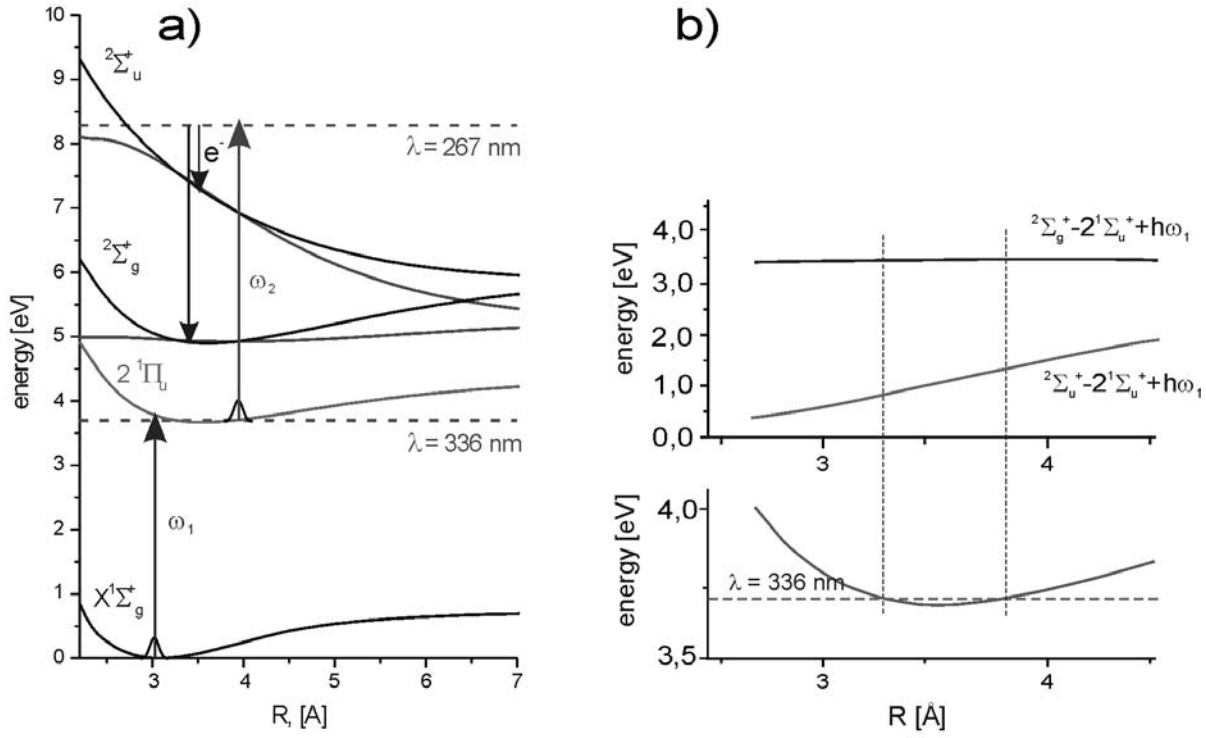

Figure 4.3: (a) Scheme of the $X^1\Sigma_g$ ground, $C^1\Pi_u$ and ionic states [90] of the Na_2 molecule for the λ_1 = 340 nm excitation and λ_2 = 266 ionisation. For the wavelength of λ_1 = 340 nm the first (v' = 0,1) levels of the $C^1\Pi_u$ state are excited. With a probe wavelength of 266 nm the $^2\Sigma_g^+$ bound and $^2\Sigma_u^+$ repulsive states are energetically accessible. (b) Difference potentials for $^2\Sigma_g^+$ and $^2\Sigma_u^+$ ionic states.

The probe pulse of a wavelength of λ_2 = 266 nm ionises the molecule. The photon energy of the pulse is sufficient to reach two lowest ionic potentials, i.e. the $^2\Sigma_g^+$ bound and $^2\Sigma_u^+$

repulsive states. The kinetic energies of the photoelectrons obtained during the ionisation from the $C^1\Pi_u$ state are measured in the experiment. As was shown in the Chapter 2, the kinetic energy of the photoelectrons can be determined using the classical difference potential analysis (formula (2.17)).

The corresponding difference potentials are presented in Figure 4.3b. Photoelectrons with kinetic energies ranging from E_{kin} = 0.7 to 1.2 eV are expected to map the wave packet motion by projecting the $C^1\Pi_u$ state onto the $^2\Sigma_u^+$ repulsive ionic potential. Since the difference potential corresponding to the ionisation into $^2\Sigma_g^+$ bound state is almost flat, all the photoelectrons from the bound state are concentrated on a small interval of kinetic energies around 3.2 eV thus revealing no internuclear distance resolution.

4.3.2 Experiment and results

Figure 4.4 shows a portion of the experimental photoelectron time-of-flight spectrum for the pump-probe delay from -500 till 10000 fs and time-of-flights 600 till 1000 ns. The oscillations at flight times of 720 ns and 950 ns are clearly visible in the measured signal. The oscillation period is 290 fs what corresponds to the wave packet motion in the $C^1\Pi_u$ potential.

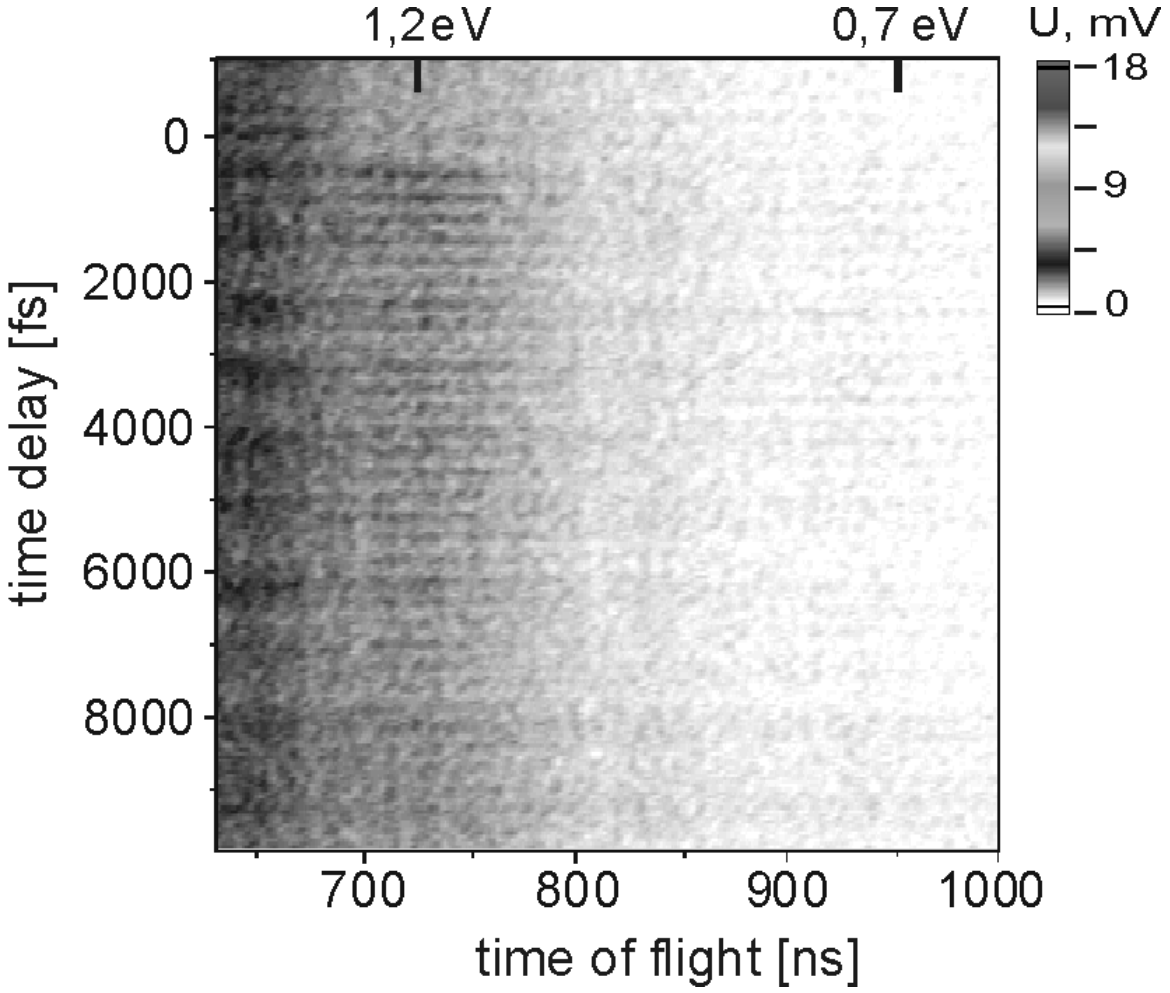

Figure 4.4: A portion of the experimental pump-probe spectra for the delay times -500 – 10000 fs and times of flight within 600 – 1000 ns. The photoelectron energies of 1.2 and 0.7 eV correspond to the wave packet localised at the outer and inner turning points of the $C^1\Pi_u$ well projected onto a repulsive ionic state.

In order to obtain the photoelectron kinetic energies the calibration of the time of flight scale is performed as discussed in the Appendix E. The corresponding photoelectron energies of 0.7 eV and 1.2 eV are also shown in Figure 4.4. Comparison of this energy with the difference potentials shown in Figure 4.3 shows that the photoelectrons released from ionisation into the repulsive $^2\Sigma_u^+$ potential from the wave packet localised at the outer (inner) turning point of the $C^1\Pi_u$ state contribute to the signal at 720 ns (950 ns).

It should be noted that it is impossible in our experiment to map the wave packet dynamics for the complete range of internuclear distances 3.2 – 3.8 Å because of overlapping contributions to the photoelectron signal. The signal at 3.2 eV is overlapped with the signal from ionisation of atomic Na, and the signal at 0.7 – 1.2 eV is overlapped with the signal from the $2^1\Sigma_u^+$ state of Na_2. In addition, the signal from $C^1\Pi_u$ state is weak in comparison to other contributions. Therefore we consider the temporal behaviour of the photoelectrons only at particular times of flight. The ionisation signal at the turning points is significantly higher because of the low velocity and hence a large time spent by the wave packet at these points. According to the difference potential scheme (Figure 4.3a) the inner and the outer turning points projected on the repulsive ionic potential correspond to the electron energy of E_{kin} = 0.7 and 1.2 eV. Cuts of the measured signal along the pump-probe axis performed at these energies (corresponding time of flights are 720 and 950 ns) are shown in Figure 4.6.

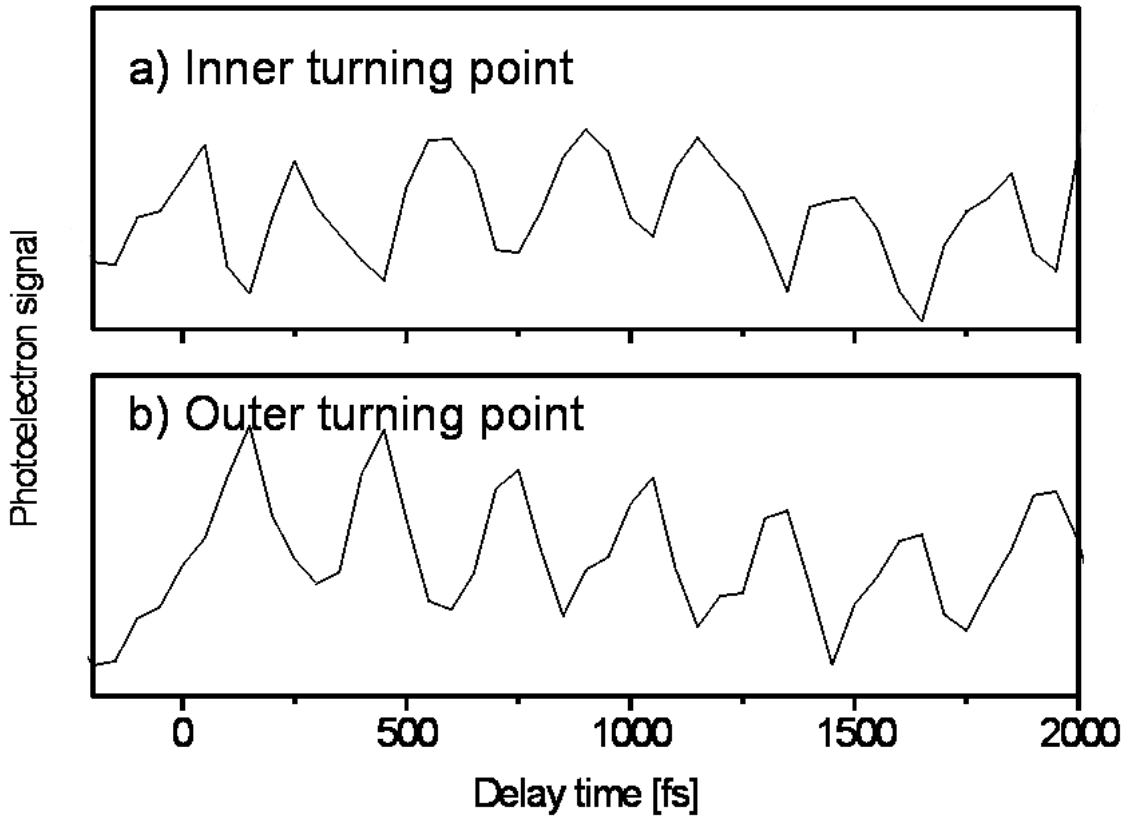

Figure 4.5: Time profiles of the photoelectrons from (a) the inner turning point (repulsive ionic state) at 0.7 eV (950 ns); (b) the outer turning point (repulsive ionic state) at 1.2 eV (720 ns). The photoelectron signals (a) and (b) are clearly shifted by half an oscillation period of 145 fs.

It is visible from the Figure 4.5 that the oscillation starts at t = 0 at the inner turning point (Figure 4.5a) where the wave packet is created and then reaches the outer turning point, where the signal is seen at the pump-probe delay time 145 fs (Figure 4.5b). The signals at 720 and

950 ns are shifted by 145 fs, which is a half an oscillation period. Thus one can derive the phase of the oscillating signal from the kinetic-energy resolved photoelectron spectrum, i.e. at which point on the potential the wave packet is ionised.

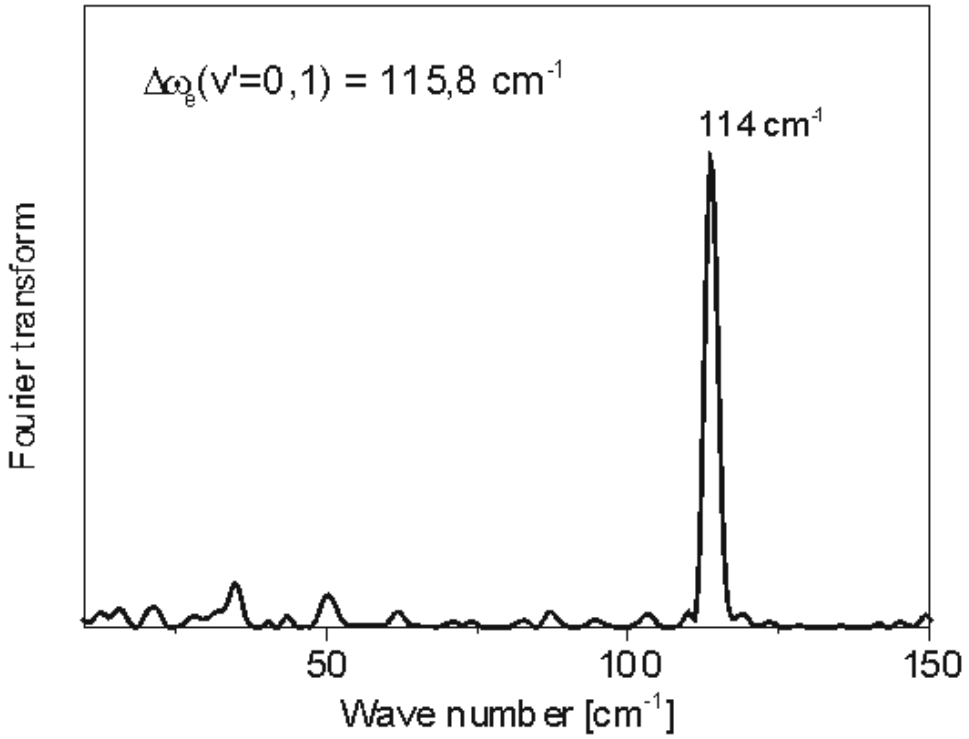

Figure 4.6: Fast Fourier transform of the photoelectron pump-probe spectra at 720 ns. A peak at 114 cm^{-1} corresponds to the wave packet oscillation in a $C^1\Pi_u$ well with a period of 290 fs. This value is close to the value of $\Delta\omega_e$ = 115.8 cm^{-1} [90].

The vertical cut through the fast Fourier transform (FFT) spectrum made at 720 ns (Figure 4.6) shows the signal at 114 cm^{-1} which is close to theoretical value (115.8 cm^{-1}) for the $C^1\Pi_u$ state.

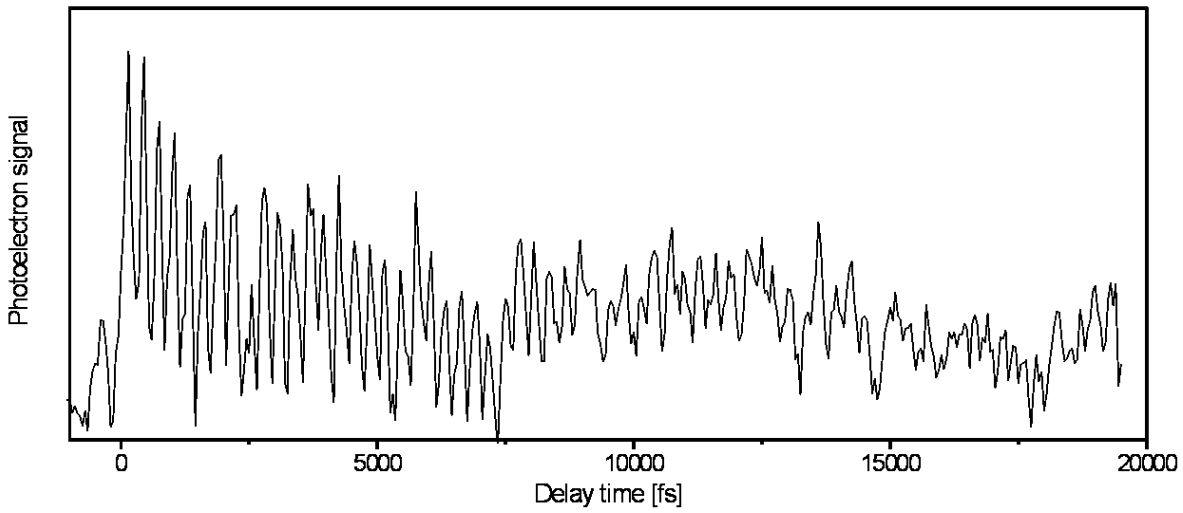

Figure 4.7: Temporal behaviour of the photoelectron signal at 720 ns on a longer time scale of -500 – 20000 fs. The decrease of the oscillation signal is visible after approximately 10 picoseconds.

Consider the long-time behaviour of the photoelectron signal. Figure 4.7 shows the time profile made at 720 ns for delays in a range of 0 – 20 ps between pump and probe laser pulses. The decrease of the maxima of the oscillations is seen and after delay times approximately 10 ps the decrease of a signal. An origin of this effect is the anharmonicity of the $C^1\Pi_u$ potential well. The dispersion of the energy level splitting leads to a spreading of the wave packet on a timescale of several picoseconds. The time when the vibrational wave packet is localised calculated according [42] consists T_{rev} = 25 ps. This time is however beyond our measurement window.

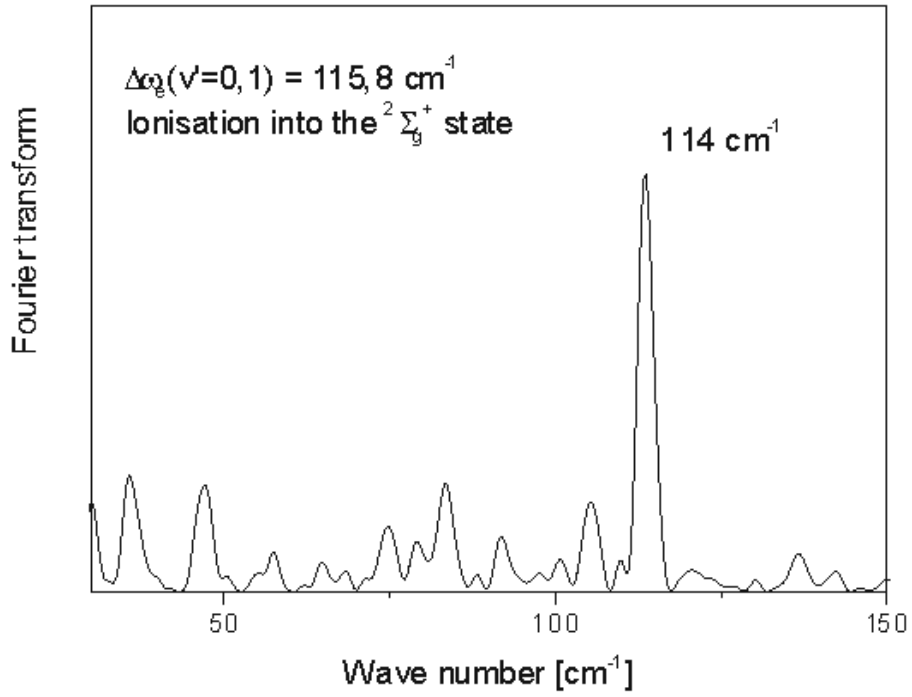

Figure 4.8: Fast Fourier transform of the photoelectron pump-probe spectra at 450 ns. A peak at 114 cm^{-1} corresponds to the wave packet oscillation in a $C^1\Pi_u$ projected onto the bound $^2\Sigma_g^+$ ionic state.

According to the Figure 4.3b we should also observe a strong oscillating signal at the energy 3.2 eV corresponding to the projection of the $C^1\Pi_u$ state onto the bound $^2\Sigma_g^+$ ionic state. A signal arising from ionisation Na atoms with 340 + 266 nm at the energy 3.2 eV is observed. The dynamics from the $C^1\Pi_u$ state here is visible as a weak modulation of the strong atomic signal. Figure 4.8 shows the cut through the fast FFT spectrum performed at 3.2 eV (corresponding to the 450 ns flight time in Figure 4.2). A peak at 114 cm^{-1} is visible, which corresponds to the wave packet oscillation in the $C^1\Pi_u$ state.

4.4 Vibrational dynamics in $7^1\Pi_u$ state

4.4.1 Excitation scheme

The potentials of Na_2 molecule relevant to the experiment for excitation with a λ_1 = 267 nm pump pulse and λ_2 = 340 nm probe laser pulse are depicted in Figure 4.9a. The $7^1\Pi_u$ state has a minimum at 3.7 Å with energy of 4.5 eV. The first femtosecond laser pulse with a wavelength of λ_1 = 266 nm excites the $7^1\Pi_u$ state at the equilibrium position of the $X^1\Sigma_g^+$ ground state of 3.1 Å corresponding to a lowest vibrational level (v'' = 0) of electronic

ground state. The wave packet created at the inner turning point of the $7^1\Pi_u$ state at time zero starts to oscillate within the potential well sampling the range of internuclear distances between 3.1 Å and 4.8 Å during its evolution. The oscillation period of the wave packet motion is 100.3 cm^{-1} for the central vibrational level of (v' = 14) [90].

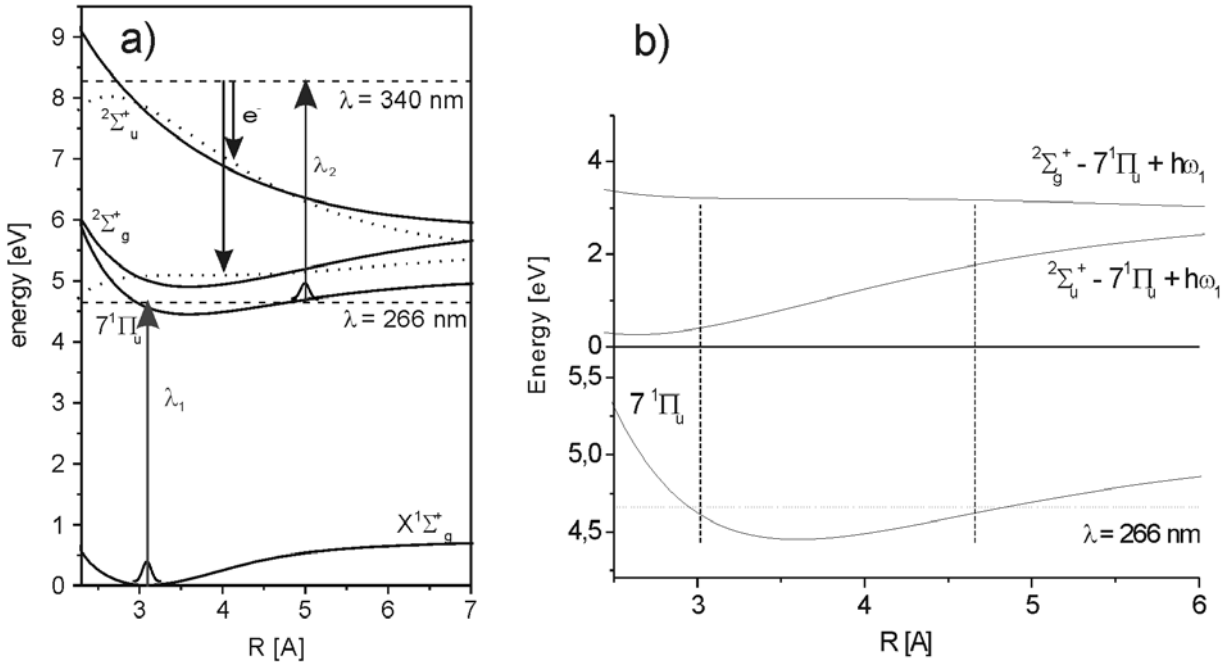

Figure 4.9: (a) Potentials of the Na_2 molecule according to [90] for a wavelength of λ_1 = 266 nm pump pulse excitation and a wavelength of λ_2 = 340 nm probe pulse ionisation. The first laser pulse of a wavelength λ_1 excites a wave packet in the $7^1\Pi_u$ state which is ionised by the second pulse of a wavelength λ_2. Electrons from ionisation into the $^2\Sigma_g^+$ bound and $^2\Sigma_u^+$ repulsive ionic states are released. (b) Corresponding difference potentials for $^2\Sigma_g^+$ and $^2\Sigma_u^+$ ionic states.

The ionisation of the wave packet is performed by the second, time-delayed laser pulse with a wavelength of λ_2 = 340 nm. The difference potential for ionisation into the repulsive $^2\Sigma_u^+$ and the bound $^2\Sigma_g^+$ ionic states are shown in Figure 4.9b. Photoelectrons with energies 3.2 eV are obtained from ionisation into the bound ionic state. Photoelectrons with energies in the range of 0.5 till 2.0 eV result from ionisation into the repulsive ionic state. Strong signals from ionisation of a wave packet sampling the inner and the outer turning points are expected, like for the C state, at the energies of 0.5 and 3.2 eV (inner turning point) and 2.0 and 3.2 eV (outer turning point).

4.4.2 Experiment and results

Figure 4.10 shows a portion of the time-of-flight pump-probe spectra for a range of delays -2000 – 500 fs between pump and probe lasers and a range of 420 - 500 ns time of flight of photoelectrons. Here the order of pump and probe laser pulses are reversed compared to the previous experiment, i.e. the λ_1 = 266 nm laser pulse comes first and excites the Na_2 molecule, and then the λ_2 = 340 nm pulse ionises it. Therefore the pump-probe times are "negative". Oscillations are visible at the flight time of 450 ns. Calibration of the time-of-flight axis yields the energy of 3.2 eV corresponding to this flight time.

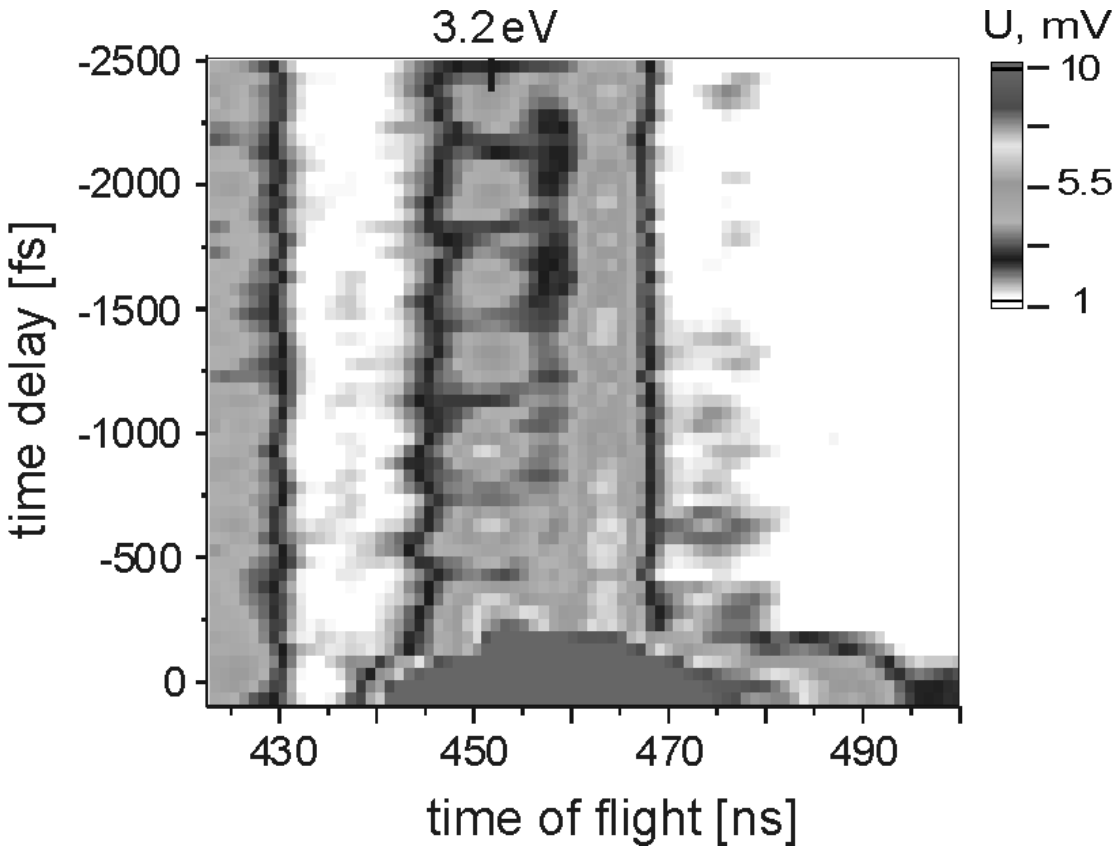

Figure 4.10: A portion of the experimental spectrum for the delay times -2500 – 100 fs and times of flight 600 – 1000 ns. The kinetic photoelectron energy of 3.2 eV corresponds to the wave packet in the $7^1\Pi_u$ well projected onto the bound ionic state.

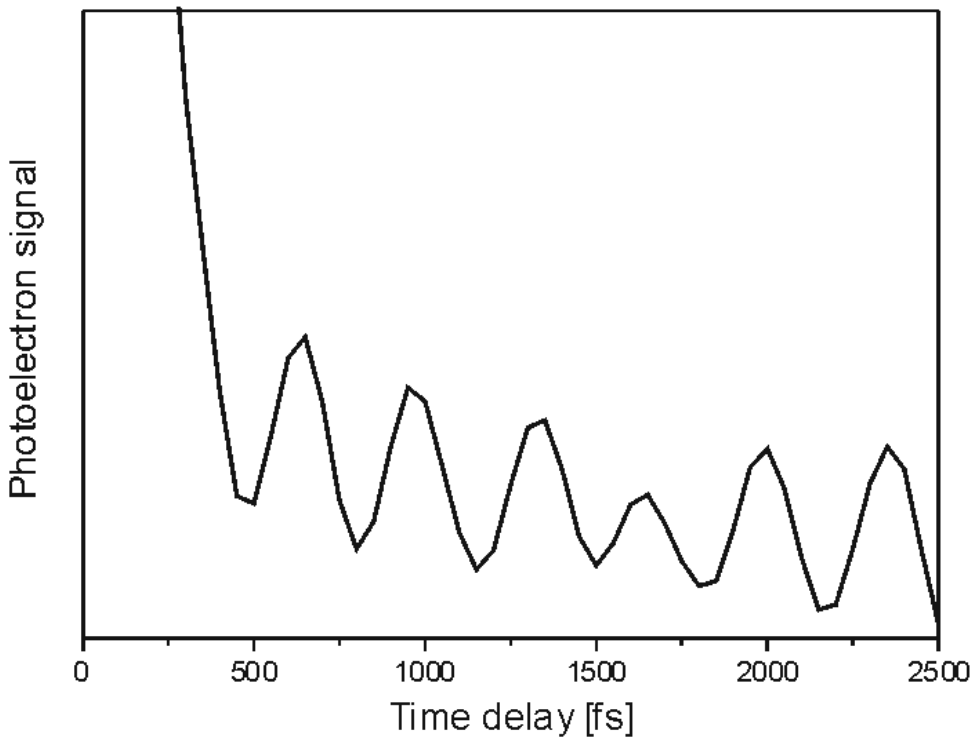

Figure 4.11: Time profile of the photoelectron signal at 450 ns. The period of the oscillations is 340 fs. A first minimum is visible at -500 fs, corresponding to a 1.5 ^{x} oscillation period. The next maximum is at the delay time of -680 fs.

A cut along the pump-probe delay axis at 450 ns is shown in Figure 4.11. The period of the oscillations is 340 fs. The difference potential for the bound ionic state in Figure 4.9b is flat. This implies that photoelectrons of all energetically accessible internuclear distances sampled by wave packet are mapped onto same energy interval of 3.2 eV. Thus no internuclear distance resolution is obtained from the kinetic energy analysis. However, we can differentiate the phase of the oscillation from the experimental signal. First two maxima in Figure 4.11 are difficult to recognise because of interference with the Na atomic signal arising at this energy at time zero. A minimum in the signal occurs at the pump-probe time around -500 fs which is equal to a 1.5 ^{x} oscillation period. At this time the wave packet is localised at the outer turning point of the $7^1\Pi_u$ potential. The next maximum is at the delay time of -680 fs. The wave packet is localised in the inner turning point at this time. Hence the electrons from the bound ionic state mapping the inner turning point of the $7^1\Pi_u$ state are seen in the experiment.

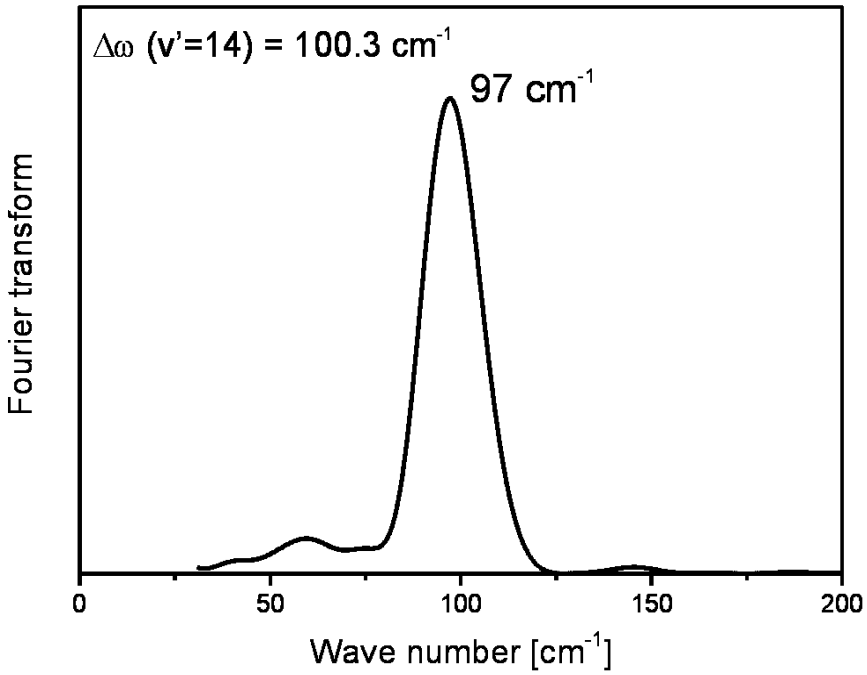

Figure 4.12: Fast Fourier transform spectrum of the pump-probe signal at 450 ns. A peak at 114 cm^{-1} corresponds to a wave packet oscillation in a $7^1\Pi_u$ well with a period of 340 fs and is close to the theoretical value of $\Delta\omega_e$ = 100.3 cm^{-1} [90].

A section through the fast Fourier transform spectrum performed at the flight time 450 ns, as shown in Figure 4.12, shows a peak at 97 cm^{-1}, which corresponds to a 340 fs oscillation period in the $7^1\Pi_u$ state and is close to the theoretical value (103.1 cm^{-1}) [90].

Oscillations with the period of 340 fs should be visible in the experimental signal at the energies of 0.5 and 2.0 eV. This signal arises from the ionisation into a repulsive ionic potential. However this signal is not observed in the measured data. A possible explanation could be that the photoionisation probability for the ionisation into the repulsive $^2\Sigma_u^+$ ionic state is lower than the photoionisation probability for ionisation into the bound $^2\Sigma_g^+$ ionic state.

4.5 Conclusion

Experiments on the observation of the wave packet motion in the $C^1\Pi_u$ and $7^1\Pi_u$ states are presented in this chapter. We were able to unravel several dynamical contributions to the photoelectron signal arising from different potentials and ionisation pathways. This is an advantage of the kinetic energy resolved photoelectron spectra in comparison with ion detection where the signal is the sum of all the sources. The analysis of the temporal behaviour of the photoelectron signal at a certain kinetic energy provides information about the phase of the wave packet motion, i.e. the particular place of the potential which is sampled by the photoelectron signal.

Chapter 5

Electronic structure dynamics in Na_2 double minimum state

In the previous chapters we presented the experiments on the observation of the dynamics in different states, e.g. quantum beats on the spin-orbit states of Na atoms or the vibrational wave packet motion in several states of the Na_2 molecule. In this chapter we will show how the wave packet can be used to probe the changes of the *electronic* structure in the molecule. An ideal candidate for this experiment is Na_2 $2^1\Sigma_u^+$ state, for which electronic changes of the chemical bond along internuclear coordinate are predicted. Since photoionisation together with energy-resolved electron detection has proven to be sensitive to such changes [46], a femtosecond pump-probe photoelectron spectroscopy experiment on the Na_2 double minimum state is performed to directly observe the electronic structure evolution in a molecule.

5.1 Introduction

Femtosecond time-resolved photoionisation is a widely used technique to probe ultrafast atomic and molecular dynamics. Its utility to map the vibrational and rotational motion have been proven for the simple molecules [1,2,91]. The knowledge of the *R*-dependence of the transition dipole moment for a neutral-to-ionic transition $\mu(R)$ is crucial for the interpretation of such pump-probe experiments. So far in most of the theoretical descriptions of time-resolved photoelectron and photoion experiments the ionisation probability is treated internuclear distance *R*- and photoelectron energy *E*-independently [36,37,87,92]. Moreover, such dependencies are not well known for diatomic molecules, since the quantum chemical calculations of the dipole moments require high computational capacities.

However, generally, the neutral-to-ion dipole moment is not constant in molecular systems in which the probed state is characterised by non-adiabatic coupling of the electronic and the vibrational motions. The adiabatic separation between electronic and vibrational motions in a molecule, based on a Born-Oppenheimer approximation, is valid when the nuclear kinetic energy is negligible (see Section 2.1 of the Chapter 2). Its breakdown is due to motion of the

atoms and occurs at the intersections or near intersections of potential energy surfaces having different electronic configurations. Prominent examples of such systems are the A state of the NaI molecule and $2^1\Sigma_u^+$ state of the Na_2 molecule.

The necessity to include into consideration the variation of the dipole moment with internuclear distance in calculations was suggested in [93]. The studies of Zewail and co-workers [7] on NaI highlighted the role of *R*-dependent process at avoided potential crossings. Subsequent work using two-color pump-probe measurements on the NaI A 0^+ state [88] employing photoion and photoelectron detection showed a strong variation of ionisation cross-section from a NaI A 0^+ potential changing its bond character from a covalent to an ionic, such that ionisation is greatly enhanced in the ionic region of the potential. In a subsequent experiment using a resonant transition step at intermediate internuclear separation [94], authors concluded an *R*-dependence of the photoionisation efficiency of this intermediate state. Furthermore, the changing with internuclear distance bonding character of the A 0^+ potential of NaI was used to study the interferences between the direct versus indirect ionisation of the NaI molecule [95]. The direct electron ejection of a NaI molecule at small internuclear distances where the potential is covalent is superimposed by a scattering of the electron on the Na^+ ion in the regions where the potential is ionic thus leading to structure in the photoelectron spectrum. A theoretical investigation of the influence of non-adiabatic effects on the photoelectron energy- and angle-resolved photoelectron spectra studied on example of NaI A state are presented in [96]. Authors investigated such non-adiabatic effects as the bifurcation of the wavepackets as it moves through the potential crossing and intramolecular electron transfer.

The role of a geometry-dependent photoionisation dipole moment $\mu(R)$ in femtosecond pump-probe experiment was investigated in other systems such that NaK, K_2 and Na_2 using ion detection. For instance, the wave packet dynamics in the Rydberg $B^1\Pi_u^+$ state of K_2 molecule was studied by Schwoerer et al. [97]. In this work the experimental results were explained by linear variation of the dipole moment with *R* and a second indirect ionisation pathway via autoionised Rydberg states. Also linear variation of $\mu(R)$ for ionisation of the $B^1\Pi_u^+$ state of K_2 was suggested in [98]. However the authors could not differentiate between the higher ionisation probability at large internuclear distances and the second ionisation pathway – in their case a doubly excited neutral state.

The ultrafast photoionisation dynamics of NaK molecules in the $C^1\Sigma^+$ state was investigated by pump-probe spectroscopy in [8]. The potential has an ionic Na^+K^- character at the outer turning point, therefore a decreasing electronic transition dipole moment for ionisation into lowest ionic state correlating with $Na + K^+$ dissociating limit was suggested in this work. Another pathway via neutral, Rydberg or doubly excited states, again could not be excluded by the authors due to the ion detection scheme. This is a general problem of the schemes based on ion detection the signal is averaged over all kinetic energies thus individual ionisation channels of the ionisation signal cannot be identified.

The non-adiabatic dynamics and the electronic structure of excited states in polyatomic molecules was investigated in details in [9-11] using photoelectron spectroscopy. These works emphasise the role of the electronic structure correlations for several states of the cation to probe the non-adiabatic dynamics reflected in the transient photoelectron spectrum.

The $2^1\Sigma_u^+$ double minimum state of the Na_2 molecule arises from an avoided crossing of two diabatic states, and hence the electronic structure changes rapidly along the internuclear distance. Thus a strong variation of $\mu(R)$ is theoretically predicted for the Na_2 $2^1\Sigma_u^+$ state [37,99-102]. In a two-color 340 pump and probe experiment ions from the outer turning point

were detected to obtain spectroscopic information on the Na_2 double minimum state [103]. Using kinetic energy time-of-flight mass spectroscopy in a one-color (341.5 nm) pump-probe scheme [104] the dynamics of the wave packet on the Na_2 double minimum state was mapped. In that experiment the repulsive $^2\Sigma_u^+$ ionic state was not energetically accessible from the complete inner well and therefore the ionisation probability could not be measured for all internuclear separations sampled by the wave packet. Applying time-resolved photoelectron detection in another one-color (340 nm) pump-probe experiment, the bound ionic $^2\Sigma_g^+$ was used to monitor the wave packet dynamics over the whole range of possible internuclear distances [105]. Analysis of the data in frequency domain has shown that the ionisation at the outer turning point is favoured but no direct comparison with time domain simulations was performed. Theoretical wave packet studies on this state focussing on effects of excitation/ionisation with chirped femtosecond laser pulses [106] were reported in addition.

In a theoretical investigation by Arasaki et al. [99] the internuclear distance dependent photoionisation amplitudes in the double minimum $2^1\Sigma_u^+$ state of Na_2 are included into the calculations of the transient photoelectron spectra. The excitation scheme used in calculations is shown in Figure 5.1. A first laser pulse of wavelength λ_1 = 337 nm, 120 fs pulse duration excites a wavepacket in the $2^1\Sigma_u^+$ double minimum state, which is then ionised by a second, time-delayed laser pulse of λ_2 = 544 nm wavelength. The energy of the probe photon is just above the ion dissociation limit thus only the ionic ground $^2\Sigma_g^+$ ion state is energetically accessible.

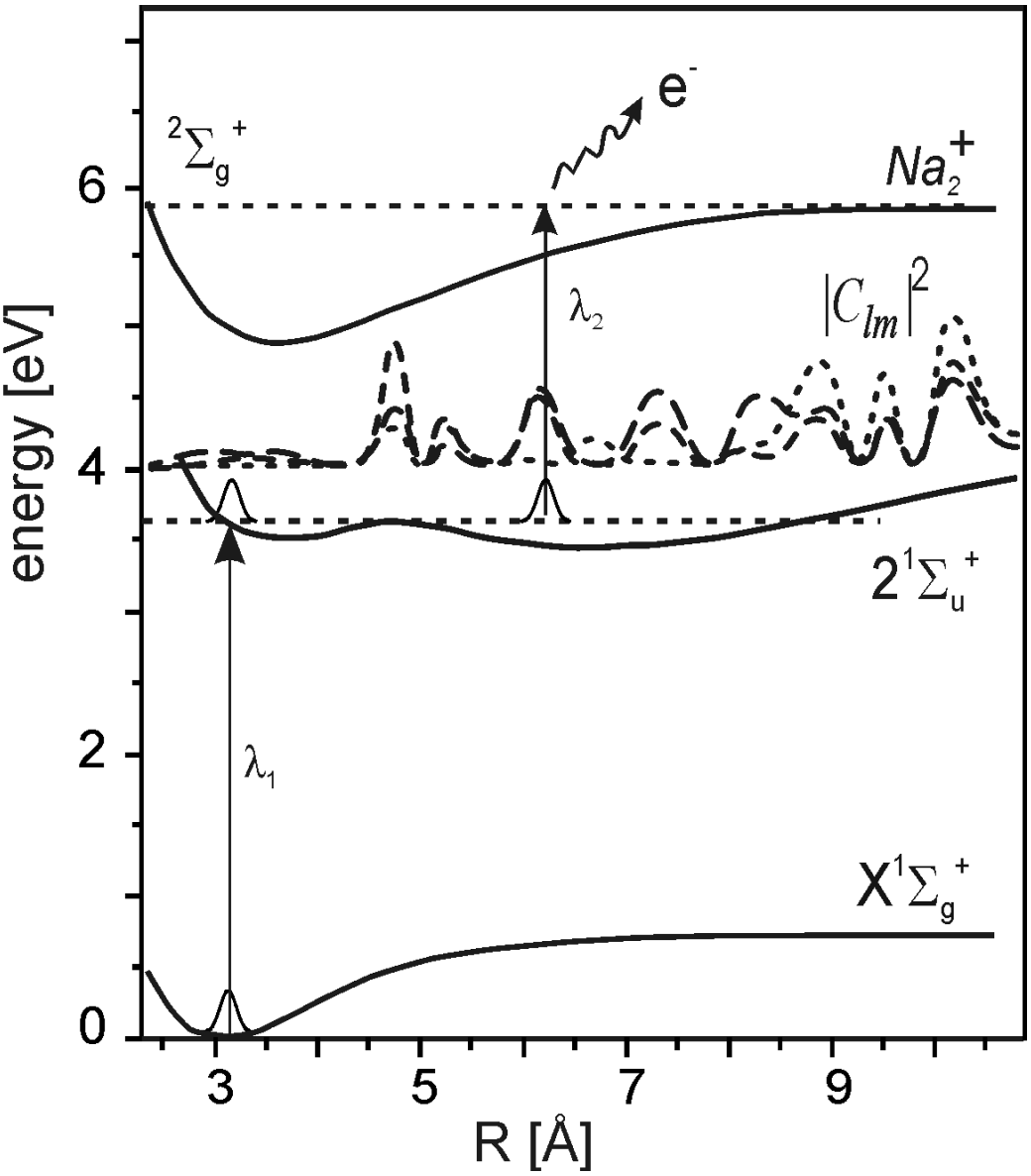

Figure 5.1: Potential energy surfaces of Na_2. A pump pulse of 337 nm wavelength excites the molecule slightly above the barrier. With a probe pulse of 544 nm only the ionic ground state is accessible. The photoionisation amplitudes $|C_{lm}|^2$ are superimposed.

In order to obtain the coupling of the matrix element between the excited $2^1\Sigma_u^+$ and ionic $^2\Sigma_g^+$ states the wavefunction of the ion state was considered as a product of an Na_2^+ ion wavefunction and a photoelectron orbital $\phi_k^{(-)}$. The last one was expanded in its partial components ψ_{klm}. The photoelectron signal is then proportional to the coefficients of this expansion, $|C_{lm}|^2$. The coefficients $|C_{lm}|^2$ are dependent on the internuclear distance R and the radial components of the wave functions ψ_{klm} of the outgoing electron and provide the underlying dynamical information needed to describe the photoionisation of Na_2 molecule by the probe laser. Figure 5.1 shows these coefficients as a function of the internuclear distance for polarisation vectors of the pump and probe pulses parallel to the molecular axis and for a photoelectron energy of about 0.6 eV. Several important features are visible. Around the inner Rydberg potential well of $2^1\Sigma_u^+$ state the $|C_{lm}|^2$ amplitudes have near-vanishing values in a range to the left of the potential barrier thus revealing a region where no ionisation takes place. The $|C_{lm}|^2$ coefficients change rapidly in the barrier area where the avoided crossing occurs. The large magnitude of the $|C_{lm}|^2$ around the barrier will have a strong influence on the

signal as the wave packet moves through this region. The pronounced oscillatory behaviour of the coefficients at large internuclear distances arises from the change of the electronic structure towards the outer well, where the wave function acquires a significant ionic character. Such behaviour should arise quite generally in nonadiabatic regions of potential surfaces.

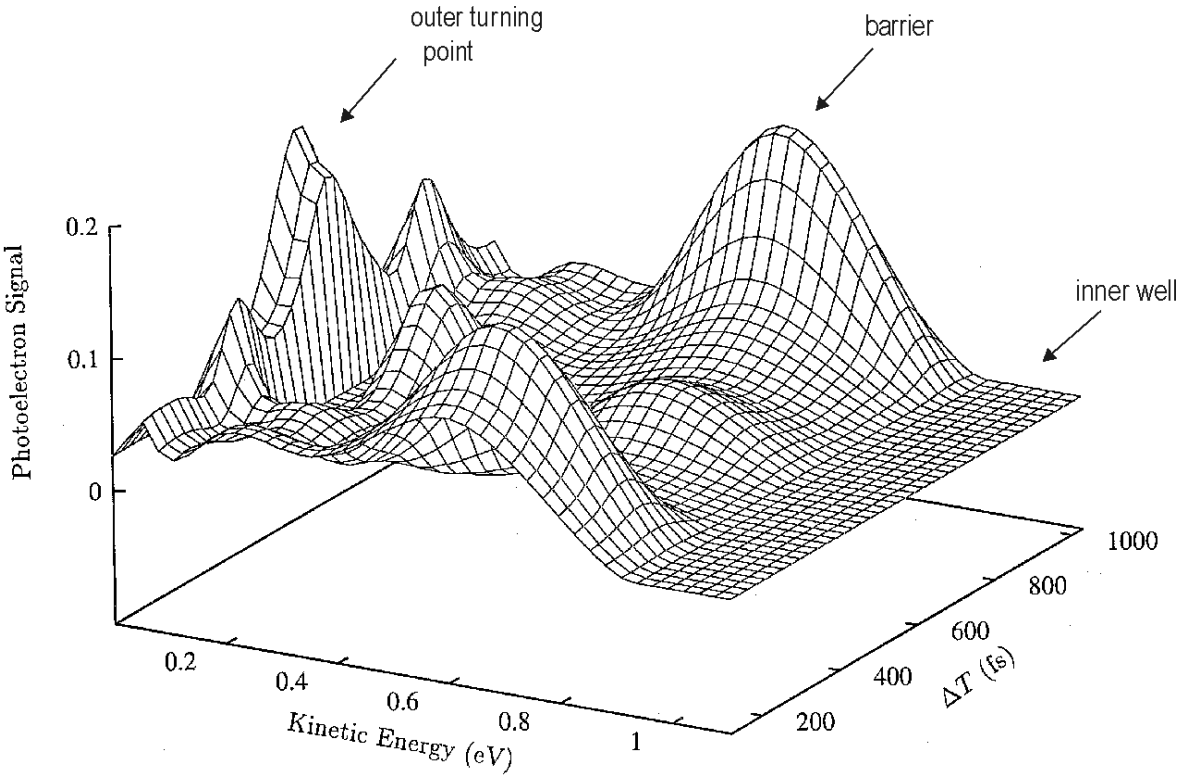

Figure 5.2: Photoelectron signal from [99] as a function of kinetic energy and pump-probe delay for a wavepacket at the top of the barrier and parallel polarization of the pump and probe pulses.

Figure 5.2 shows the photoelectron distribution as a function of the delay time for the probe laser pulse polarisation parallel to that of the pump laser pulse. Almost vanishing ionisation coefficients in the inner well region lead to a very small photoelectron signal at 1 eV whenever the wave packet hits the "depleted" region. The large values of the dynamical coefficients sandwiching the barrier region and the slow wave packet motion at the barrier result in a strong peak at about 0.6 eV. A peak at a very low photoelectron energy is seen around Δt = 600 fs when the wave packet hits the outer turning point and where only electrons with low kinetic energy can be ejected.

5.2 Idea of the experiment

Figure 5.3 shows the relevant potentials of Na_2 for the experiment. The change of a chemical bond of the $2^1\Sigma_u^+$ double minimum state from a covalent at small internuclear distances to ionic at large distances should lead to a measurable dependence of the photoionisation probabilities on internuclear distance. The detection of the kinetic energy resolved electrons enables to resolve the internuclear distance and hence should reflect the change of the photoionisation probability.

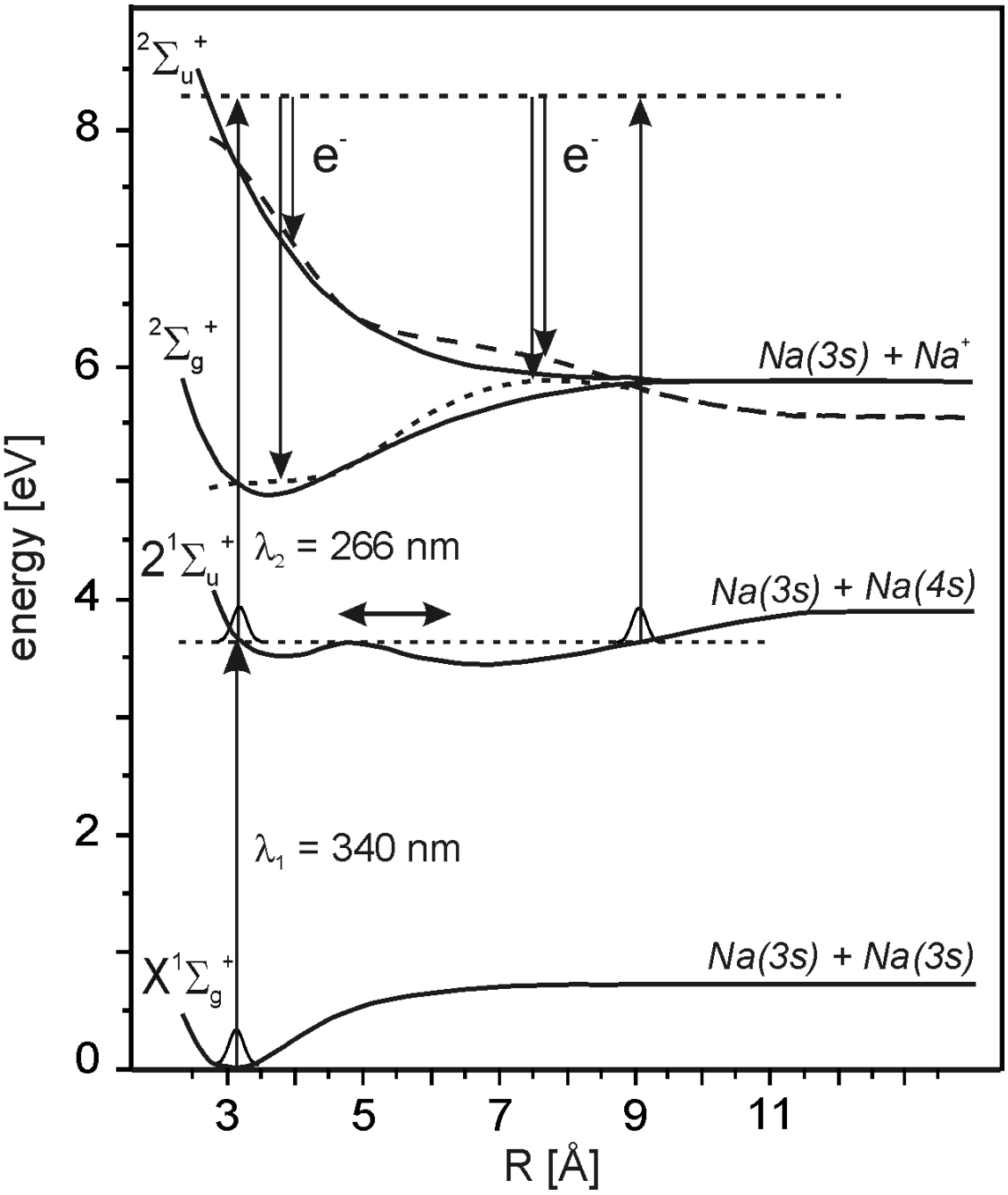

Figure 5.3: Potential energy curves of Na_2 molecule for λ_1 = 340 nm excitation and λ_2 = 266 nm ionisation. A pump pulse of λ_1 excites the wavepacket above the barrier of the $2^1\Sigma_u^+$ state. The wavepacket probes the internuclear distances 3 – 9 Å. A probe pulse of λ_2 ionises molecules. Kinetic energies of the photoelectrons from $^2\Sigma_g^+$ bound and $^2\Sigma_u^+$ repulsive ionic states are measured.

In our experiment we use a two-color pump-probe scheme, as shown in Figure 5.3. A first femtosecond laser pulse of a wavelength of λ_1 = 340 nm creates the wave packet in the double minimum state. The time evolution of the wave packet is then probed by the second, time-delayed laser pulse of wavelength of λ_2 = 266 nm, which ionises the molecule. The kinetic energy of released photoelectrons as a function of pump-probe delay is measured in the experiment.

The excitation wavelength is chosen so that vibrational levels with nonvanishing wave functions in the complete double minimum well are excited. Hence the wave packet maps the

whole region of internuclear distances between 3 to 9 Å without significant disturbances and reflections at the barrier into the inner well, thus making this excitation case suitable for mapping the evolution of electronic structure in the complete double well potential. A good overlap of the Franck-Condon factors with the pump pulse gives high intensities in the signal [107].

With the choice of the ionisation wavelength the complete wave packet motion in the $2^1\Sigma_u^+$ potential well can be mapped with photoelectron signal. The photon energy of the probe pulse is enough to reach both lowest $^2\Sigma_g^+$ bound and $^2\Sigma_u^+$ repulsive states of the Na_2^+ ion. Thus the wave packet motion can be projected simultaneously onto two states. Another aspect of the two ionisation continua is that the partial ionisation probabilities, i.e. ionisation into a specified ionic states, can differ significantly with respect to the molecular orbital nature of the investigated state [10].

Since the kinetic energy-resolved photoelectron spectra reveal directly the ionisation pathways, competing ionisation processes can be identified in this scheme.

5.3 Wave packet evolution

The calculation of the wavepacket propagation is performed using the split operator technique described in [108]. Detailed calculations for Na_2 molecule with the parameters relevant for the experiment are summarised in [107]. A pump λ_1 = 340 nm, 35 fs FWHM laser pulse prepares a wave packet in the inner turning point of the double minimum state at the internuclear distance of R = 3.1 Å, corresponding to the equilibrium position in the Na_2 ground state $X^1\Sigma_g^+$ ($v'' = 0$). The propagation of a wavepacket for the first 3.5 ps is shown in Figure 5.4a. The photon energy of the pulse is chosen so to be larger than the height of the barrier. Figure 5.4b shows the relevant Franck-Condon factors.

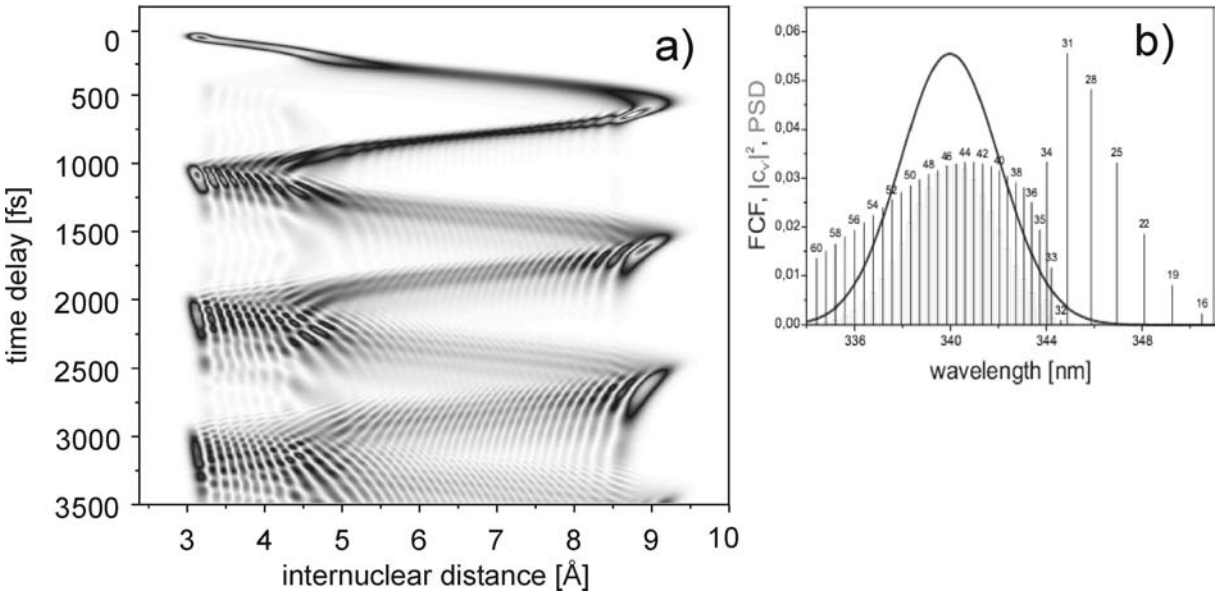

Figure 5.4: a) Calculated temporal evolution of the wave packet in the Na_2 $2^1\Sigma_u^+$ state for λ_{pump} = 340 nm, 35 fs FWHM excitation from the ground $X^1\Sigma_g^+$ ($v'' = 0$) state. b) Franck-Condon factors for the $X^1\Sigma_g^+$ ($v'' = 0$) – $2^1\Sigma_u^+$ (v') transitions superimposed by the normalised pump laser spectrum from [107]. The numbers indicate the values of v'.

Due to the large bandwidth the laser pulse excites a large number of vibrational states, centred at $v`= 45$ (see Figure 5.4b). The states belonging almost solely to the complete well are excited, although a small contribution from the tunnelling wavefunctions $v`= 31$ and 32 is present [107].

The wave packet oscillates within the complete potential well with a period of 1 picosecond in accordance with energy level spacing of approximately 32 cm^{-1} at $v`= 45$ [107]. The wave packet dynamics shows strong peaks at the inner and outer turning points and is spread in the regions in between. The broadening of the distribution at intermediate internuclear distances is due to the high kinetic energy of the nuclei on a relative flat potential. The recompression occurs when the wave packet decelerates at the turning points. Thus reflecting the longer time spent by nuclei in these points. Thus strong peaks arise at turning points. The peaks from the outer turning points are shifted by half an oscillation period (500 fs) from those from inner turning points. The dispersion of the wave packet velocity, that is the different kinetic energy for different components is responsible on the bending structure of the edges at inner and outer turning points (i.e. at internuclear distances 3, 9 Å and time delays 500, 1000, 1500 fs and so on), when slower components arrive the turning points at correspondingly longer times. This effect is also seen at the barrier at $R = 4.7$ Å, where the wave packet "piles up", that is the fast components are retarded at the barrier being overtaken by slow components (see classical analysis in [107]). The large number of excited vibrational states is responsible for the interference of components with different beating frequencies inducing the quantum interference pattern seen in the bottom part of the Figure 5.4. The wave packet dephases rapidly within several oscillation periods. This effect was discussed in details in [42].

The calculations neglected the rotational motion, which occurs on a much longer timescale because of much lower rotational energy levels spacing, and considered the molecule in the ground vibrational initial state. According to [72] a molecular beam is not perfectly cold, at the production temperature of $T = 870$ K approximately 12 % of the molecules are in the first vibrationally excited state $v`` = 1$. However, as was shown in [107], although the Franck-Condon distributions are different, the wave packet distribution is surprisingly similar to the case of $v`` = 0$, thus providing no significant changes in the analysis of the experimental results.

5.4 Photoelectron spectra: classical difference potentials analysis

The second, time-delayed laser pulse ionises the Na_2 molecule. The kinetic energy of the electrons released is measured in our experiment. The analysis of the ionisation process is also possible within the classical mechanics framework, by the use of the difference potential analysis, suggested by Mulliken [38]. Here we consider a classical analogue of a wave packet – a mass point moving along an anharmonic molecular potential well (see Section 2.3.1 of the Chapter 2).

The difference potential analysis of the photoelectrons in a double minimum state includes several features:

- First, the photon energy of a probe pulse ionising the molecule is enough to reach two lowest ionic states: a lowest bound $^2\Sigma_g^+$ and a first excited $^2\Sigma_u^+$ states. The corresponding difference potentials yielding the kinetic energies of the photoelectrons calculated according the formula (2.17) are shown in Figure 5.5a.

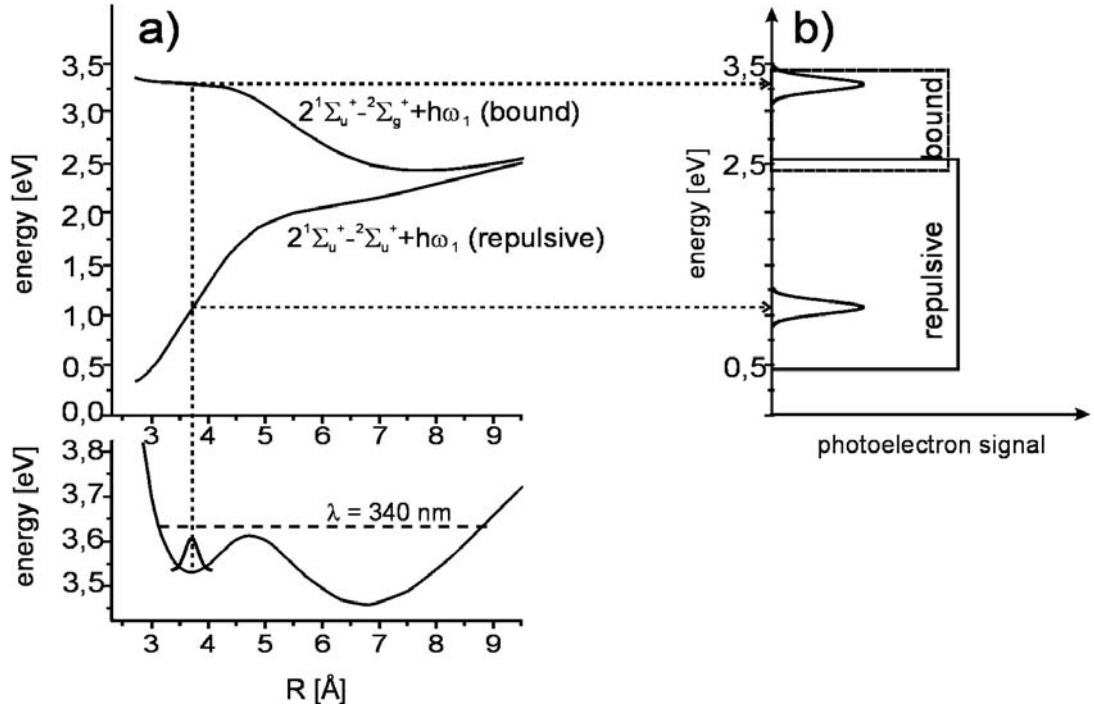

Figure 5.5: (a) Difference potentials for the $^2\Sigma_g^+$ bound and the $^2\Sigma_u^+$ repulsive ionic states according to the formula (2.17). The dashed line indicates the energy of the central excited level above the barrier; the dotted lines indicate the kinetic energies of the electrons from ionisation at a particular *R*.. (b) Expected kinetic energies of the signal. The rectangles indicate the energy ranges for electrons from two ionic states. Note that the kinetic energy spectra for the bound and repulsive ionic potentials overlap at 2.5 eV.

- One can see from Figure 5.5a that the ionisation of a molecule at the inner turning point of the double minimum potential yields photoelectrons with a kinetic energy of 0.5 eV for *repulsive* ionic state. The photoelectrons from the barrier have a kinetic energy of 1.9 eV, and from the outer turning point a kinetic energy of 2.6 eV. Thus, the complete range of internuclear distances is projected monotonously onto the repulsive difference potential yielding photoelectrons with energies in the range of 0.5 – 2.6 eV. This is shown in Figure 5.5b. Analogous, for the *bound* ionic state, the photoelectrons from the inner turning point have E_{kin} = 3.3 eV, and from the inner turning point E_{kin} = 2.4 eV. Thus, as seen in Fig. 5.5b, the electrons from the bound state with energies E_{kin} = 3.3 - 2.4 eV map the complete energetically accessible double minimum well.
- The difference potentials at large internuclear distances approach the same limit, thus implying that the photoelectrons from the outer turning point are formed with the same kinetic energies for both ionic states E_{kin} = 3.3 eV.
- The difference potential for the bound ionic state is non-monotonous having a minimum at large internuclear distances. As a consequence, the relation between the internuclear distance and kinetic photoelectron energy is then non-monotonous around the outer turning point.

- Generally, the most detailed mapping of the wave packet is obtained for those regions where the difference potential is the steepest. The difference potential for the repulsive ionic state is steep at small internuclear distance (R = 3 - 5 Å) and almost flat for R = 5 – 9 Å. The difference potential for bound ionic state is flat for small R = 3 – 5 Å and steep for R = 5 - 8 Å. Hence the inner well of the double minimum potential is mapped with higher spatial resolution with photoelectrons from the repulsive ionic state and the outer well with electrons from the bound ionic state.

5.5 Photoelectron spectra: quantum mechanical calculations

Quantitative information on the photoelectron signal is obtained however only in quantum mechanical approach. Figure 5.6 shows the kinetic-energy resolved, angle averaged photoelectron spectra for a λ_2 = 265 nm, 40 FWHM ionisation laser pulse calculated in [107] using first order perturbation theory for ionisation based on Fourier techniques [36]. For the sake of visibility the spectra are shown separately for the ionisation into the bound $^2\Sigma_g^+$ and into the repulsive $^2\Sigma_u^+$ ionic states. The calculation was made assuming constant photoionisation dipole moment for ionisation into both ionic states.

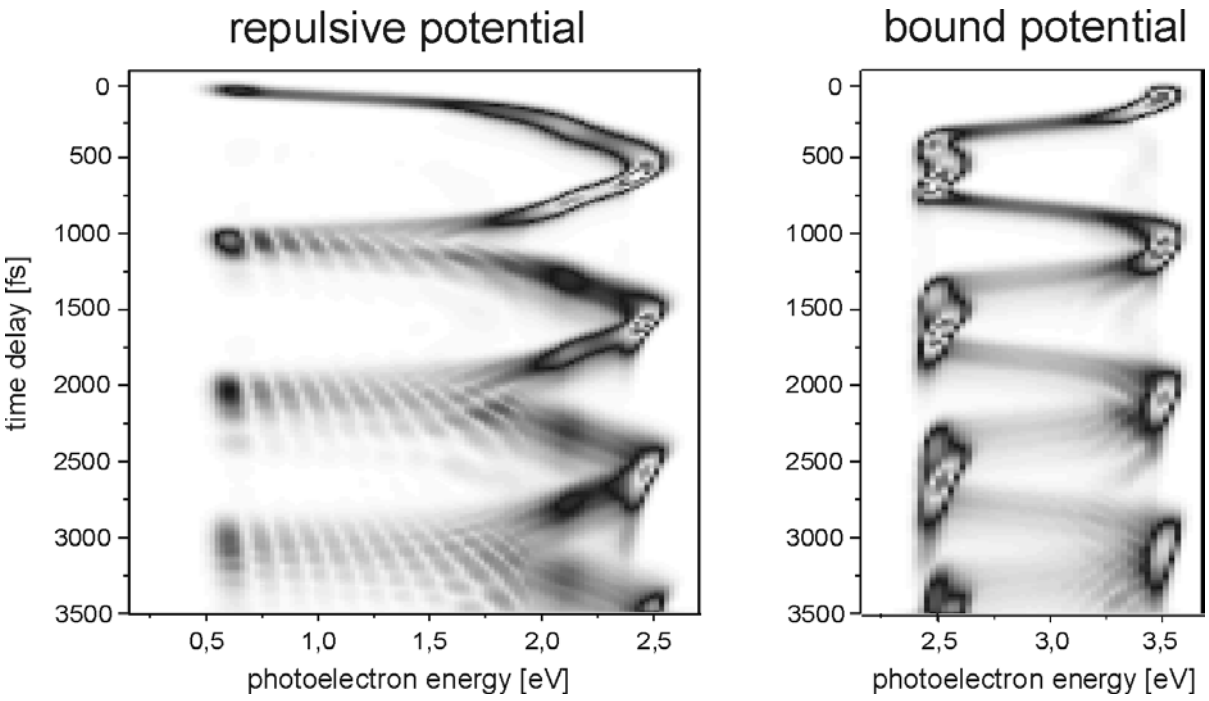

Figure 5.6: Calculated photoelectron signal for the first 3.5 picoseconds for ionisation with λ_{probe} = 265 nm, 40 fs FWHM laser pulse. For convenience the signals from the $^2\Sigma_u^+$ repulsive and from the $^2\Sigma_g^+$ bound ionic states are shown separately.

The wave packet evolution is clearly visible in both photoelectron spectra. The bound state electrons arise in the energy range of 2.5 – 3.3 eV, but because of non monotonic behaviour of the difference potential the complete inner well is projected on a small kinetic energies region around 3.3 eV, thus disabling a detailed spatial resolution for R = 3 - 5 Å, on the other hand giving the benefit in the signal intensity. The signal from 3.3 till 2.5 eV maps the outer well. Another peculiarity arises when we compare the motion of the wave packet close to the outer turning point with the photoelectron signal at the corresponding delay times. The electron signal first follows the wave packet towards small energies, but then shifts to higher

energies before the wave packet reaches its turning point. This is explained by non-monotonous way of the difference potential at large distances (see Fig. 5.5a).

On contrary, the electrons from the repulsive state map the inner well with high spatial resolution and the barrier of the double minimum potential (E_{kin} = 0.5 – 2.1 eV), however the signal intensity here is low. The effect of dynamical compression at the barrier is also clearly visible in the signal.

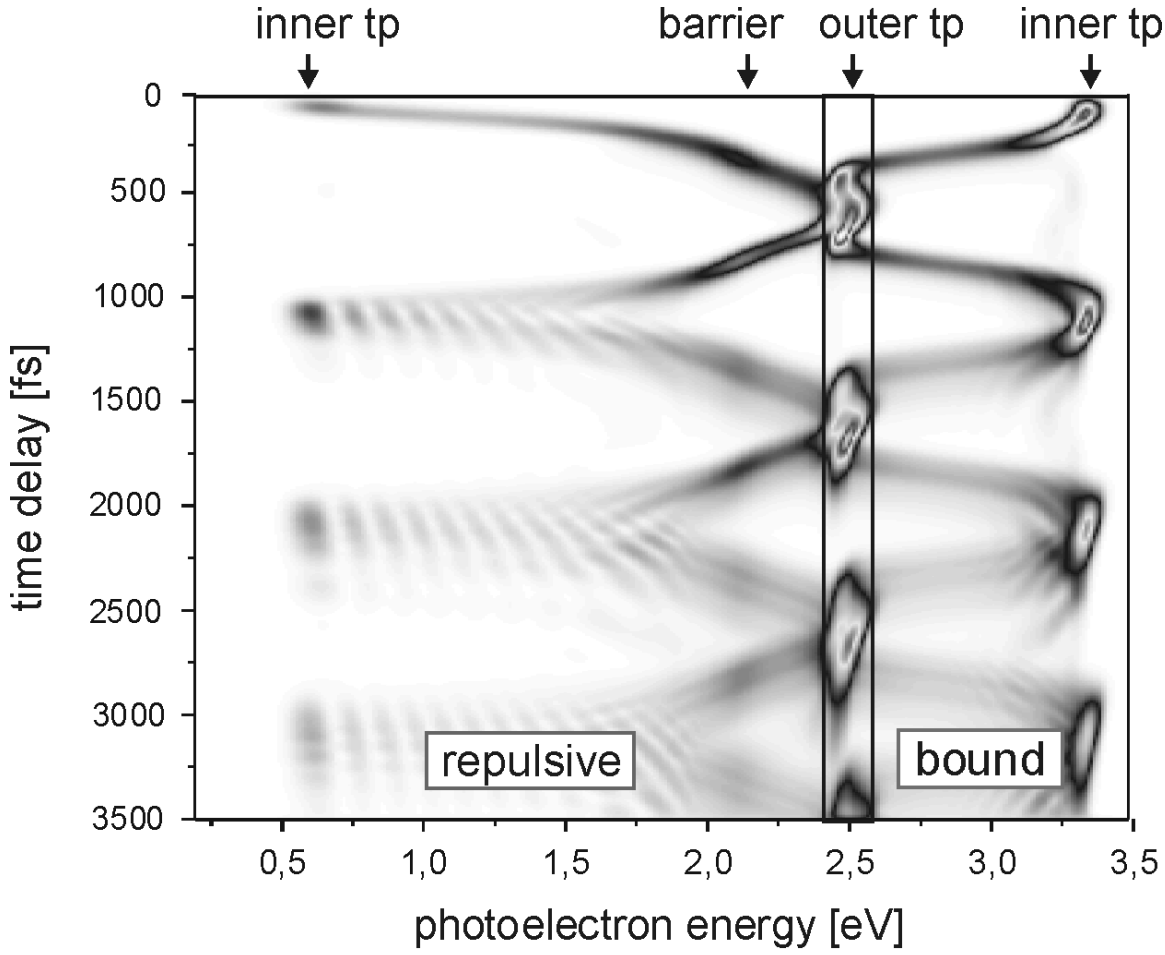

Figure 5.7: Calculated photoelectron kinetic energy spectrum obtained by superposition of two spectra depicted in Figure 5.6. The positions for inner and outer turning points are also indicated. Note that the spectra from bound and repulsive ionic states overlap at E_{kin} = 2.4 – 2.6 eV, corresponding to the outer turning point of the $2^1\Sigma_u^+$ state of Na_2.

The united photoelectron spectrum obtained by the superposition of spectra from both ionic states is shown in Figure 5.7. One can see, that spectra overlap in a small region of kinetic energies of E_{kin} = 2.4 – 2.6 eV, where the photoelectrons map the outer turning point.

Strong peaks in the photoelectron signal appear whenever the wave packet hits either the outer or the inner turning point.

5.6 Experimental results and data processing

5.6.1 Experimental set-up and parameters

The two-colour experiment includes a pump laser beam which excites the molecules and a probe femtosecond laser beam which ionises the Na_2 molecules. A Ti:Sa oscillator produces pulses with a wavelength of λ = 785 nm, t = 10 fs and 1 kHz. The amplified pulses are frequency converted giving a λ_1 = 340 nm, E = 0.6 μJ and 4.7 nm FWHM pump and a λ_2 = 266 nm, E = 0.4 μJ and 3.0 nm FWHM probe laser pulses. The spectra of both laser pulses are shown in Figure 5.8.

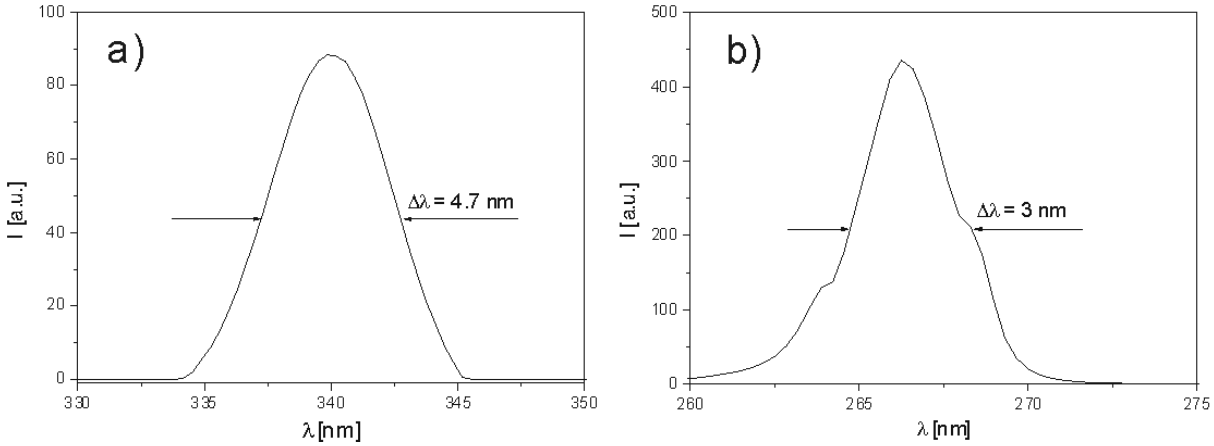

Figure 5.8: (a) Spectrum of the λ_1 = 340 nm, 4.7 nm FWHM pump laser pulse. (b) Spectrum of the λ_2 = 266 nm, 3 nm FWHM probe laser pulse.

The pump and the probe laser beams are propagating collinear and are focussed with a f = 250 mm lens into a vacuum chamber where they intersect a Na_2 molecular beam. The polarisation of both pulses is collinear with the spectrometer axis. The delay between pulses ranged from –5 till 30 ps in 30 fs steps. The sodium beam is obtained in a seeded beam set-up. The oven- and nozzle-temperatures are T_{oven} = 870 K and T_{noz} = 970 K correspondingly. The nozzle diameter is 100 μm. The Ar seed gas with a partial pressure of 1.6 bar is supplied to the cartridge with sodium. The pressure in an oven chamber consists 10^{-4} mbar. The photoelectron spectra are detected with magnetic bottle spectrometer. The signal from the spectrometer is taken with LeCroy and averaged over several thousand shots. The spectra at the output of LeCroy are read by computer using an IEEE-interface. Experimental photoelectron time-of-flight spectra are recorded for every delay between pump and probe laser pulses.

5.6.2 Experimental results

Figure 5.9 shows a grey scale representation of a “raw” time-of-flight photoelectron spectrum. The measured spectrum is a 2D-distribution, in which a photoelectron flight time distribution is recorded as a function of delay between the pump and the probe laser pulses.

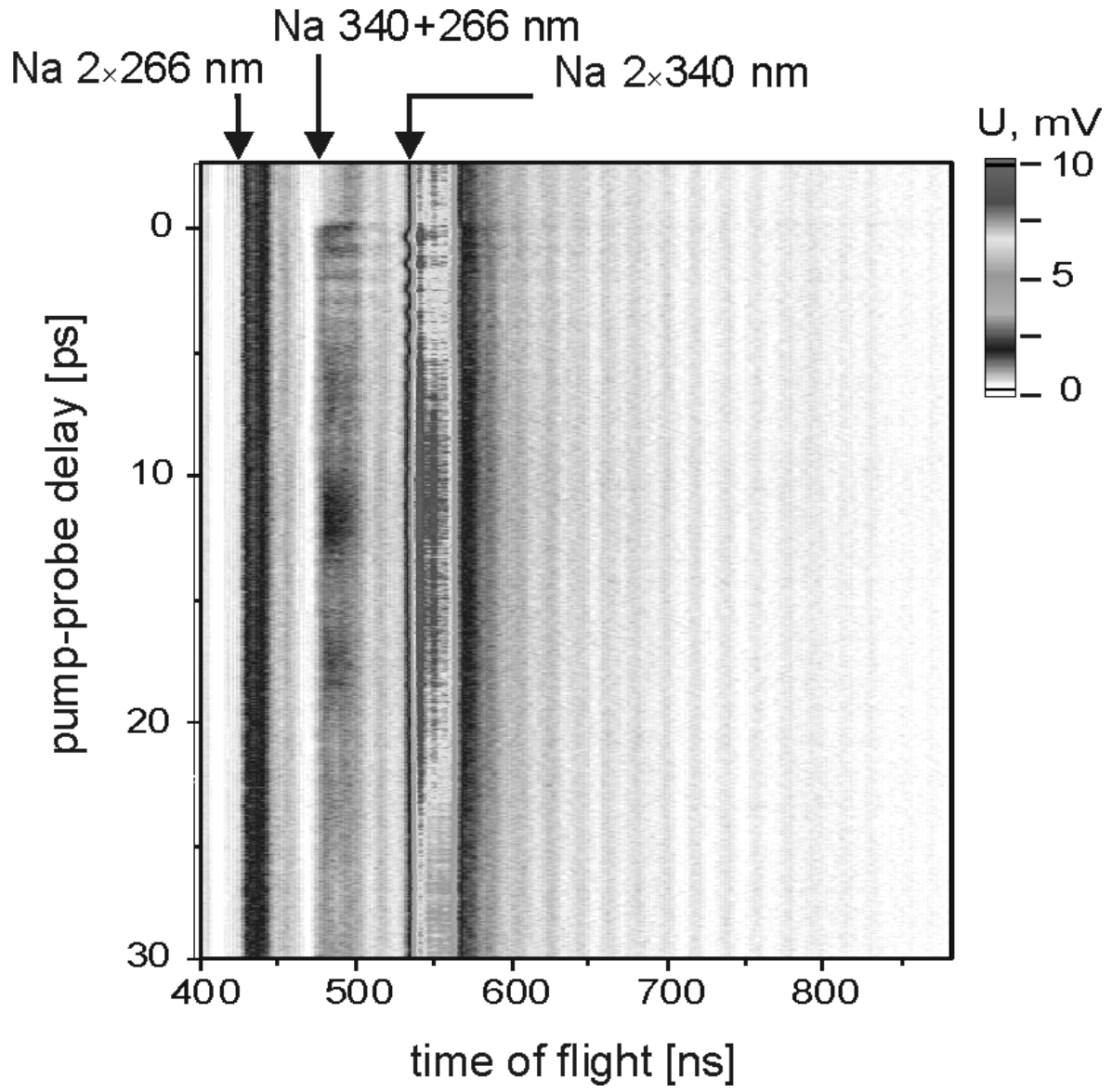

Figure 5.9: Measured time-of-flight photoelectron spectrum as a function of delay between pump and probe laser pulses. Arrows indicate the signals from ionisation of Na atoms with two photons of λ_1, two photons of λ_2 and $\lambda_1 + \lambda_2$.

Along the abscissa axis the flight time of the photoelectrons is measured. The flight times, dependent also on the voltage applied to the grid U_g, are chosen to fit the ranges of dynamics (i.e. the kinetic energy in a range of 0,5 – 3,5 eV) in the double minimum state. The flight time in experiment ranges from 200 to 900 ns.

The delay time between pump and probe laser pulses ranges from -5 till 30 picoseconds. Considering the vibrational oscillation to take 1 ps, the complete measurement maps several tens of oscillations. The time resolution is 30 fs. Negative pump-probe times ($t < 0$) mean that the λ_2 = 266 nm laser beam comes first and excites the Na_2 molecule whereas the λ_1 = 340 nm probe beam is used for ionisation of Na_2. According to the Na_2 excitation scheme no excitation of double minimum $2^1\Sigma_u^+$ state should occur at the λ_2 = 266 nm wavelength, therefore no dynamics is seen in the spectrum. At the time zero the pump λ_1 = 340 nm and the probe λ_2 = 266 nm laser pulses overlap, therefore the ionisation of Na_2 $2^1\Sigma_u^+$ state occurs at the equilibrium 3.1 Å position of the ground $X^1\Sigma_g$ state of Na_2 corresponding to the creation of a wave packet at the inner turning point of the double

minimum state. Measurements at times $t > 0$ correspond to the excitation of the $2^1\Sigma_u^+$ state with λ_1 = 340 nm and time-delayed ionisation with λ_2 = 266 nm to map the molecular dynamics in a double minimum state.

In order to extract the physical information from the "raw" time-of-flight spectra, the several contributions to the signal are considered and eliminated:

1. The measured signal contains an independent on a pump-probe delay background TOF signal due to uncompensated contact potentials on the pole-plates arising after some hours of work with alkali metals; often this includes the oscillatory along the TOF axis structure in the time-of-flight scan, or accordingly stripes along the delay axis in the pump-probe scan good visible in Figure 5.9, which do not vanish completely after the pole-plate voltage compensation;
2. The variation of the pump-probe signal is not solely due to a molecular dynamics. There are apparatus contributions from temporal changes of properties of the femtosecond laser system and the molecular beam. This gives rise to additional time modulation of the signal;
3. Since the Na atoms are still present in a sodium beam (the Na:Na_2 relation in a beam is is 2:1), the stationary time-independent signal arising from the ionisation of Na with λ = 340 and 266 nm is present in a spectrum. The Na signal is also used for the calibration procedure described below;
4. The dynamical changing of the time signal arising from a fine structure splitting of Na atoms is present in the measured scan at delay times $t > 0$ for time of flight at about 470 ns. We minimise it in the experiment first by seeding the sodium beam with Ar and hence the decreasing the portion of Na atoms, and second by detuning the excitation wavelength from the 3s – 4p resonance at 330 nm;
5. The dynamics from other states of the Na_2 molecule can influence the signal. This will be discussed in the Section 5.4 of the present chapter.

Therefore the signal processing proceeds in the following steps. First, we discuss these individual contributions to the signal and their elimination. This includes the choice of the window of interest for subtraction, the subtraction of stationary background signal and the averaging of the signal. Then the calibration of the signal, i.e. the conversion the TOF axis into the kinetic energy axis will be performed. Further the choice of the areas for cuts along the pump-probe axis and the kinetic energy axis will be discussed. The signal processing and the results visualisation of the results are performed using the LabView 6.1 programming package. The programs used in this chapter are summarised in the Appendix F.

5.6.3 Background subtraction and averaging

The instability of the signal coming from the apparata, e.g. the laser system and the molecular beam, define the choice of the area for subtraction, and the method of background signal subtraction.

The changes in the laser system have the contributions from the amplifier (< 3-5 %) and the laser beam position instability occurring on a scale of few hours, that is longer than a measurement, and are related to temperature fluctuations. The major contribution of the signal variation however is due to the instability of the seeded molecular beam. During the time needed for one measurement, which is approximately 40 minutes, the signal changes can achieve 30 %, as is seen from the Figure 5.9. Therefore for the analysis of the experimental

results in the time domain, we have chosen the area of subtraction spectrum ranging from -100 till +3500 femtoseconds pump-probe delay.

The subtraction is performed in the following way. For the composition of the spectrum to subtract the program searches for the minima in the selected area along the pump-probe delay. The area selected is a cut through a delay axis averaged over 524 till 538 ns. Photoelectron spectra corresponding to the local minima along time delay are extracted and an average spectrum for the pump-probe delay area from -100 till 3500 fs is obtained. This TOF spectrum used for the subtraction is shown in Figure 5.10.

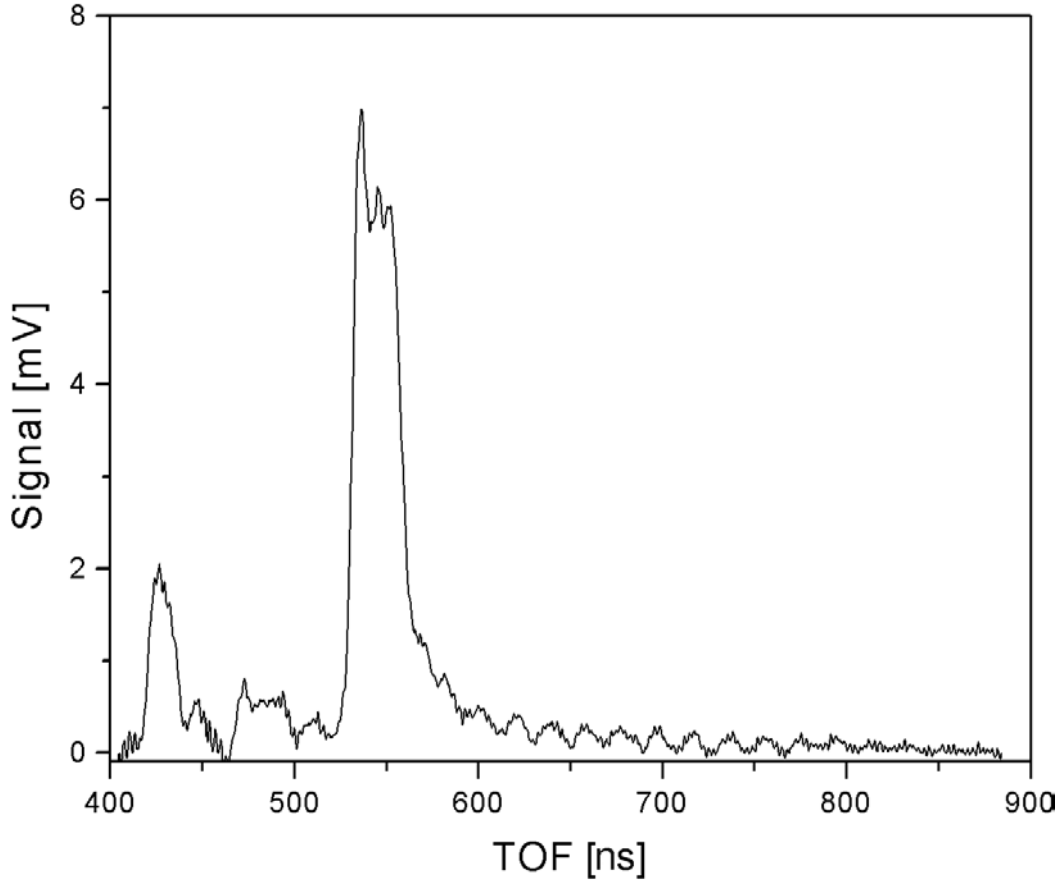

Figure 5.10: The photoelectron time-of-flight spectrum for the subtraction of the signal from the measured signal shown in Figure 5.9. The spectrum is obtained by selecting the time-of-flight spectra corresponding to local minima along the pump-probe delay for delay times 524 till 538 ns. The spectrum is the average of them.

The signal obtained by subtraction of the spectrum shown in Figure 5.10 from the initial signal, is presented in Figure 5.11 and contains mostly the dynamical information from Na_2.

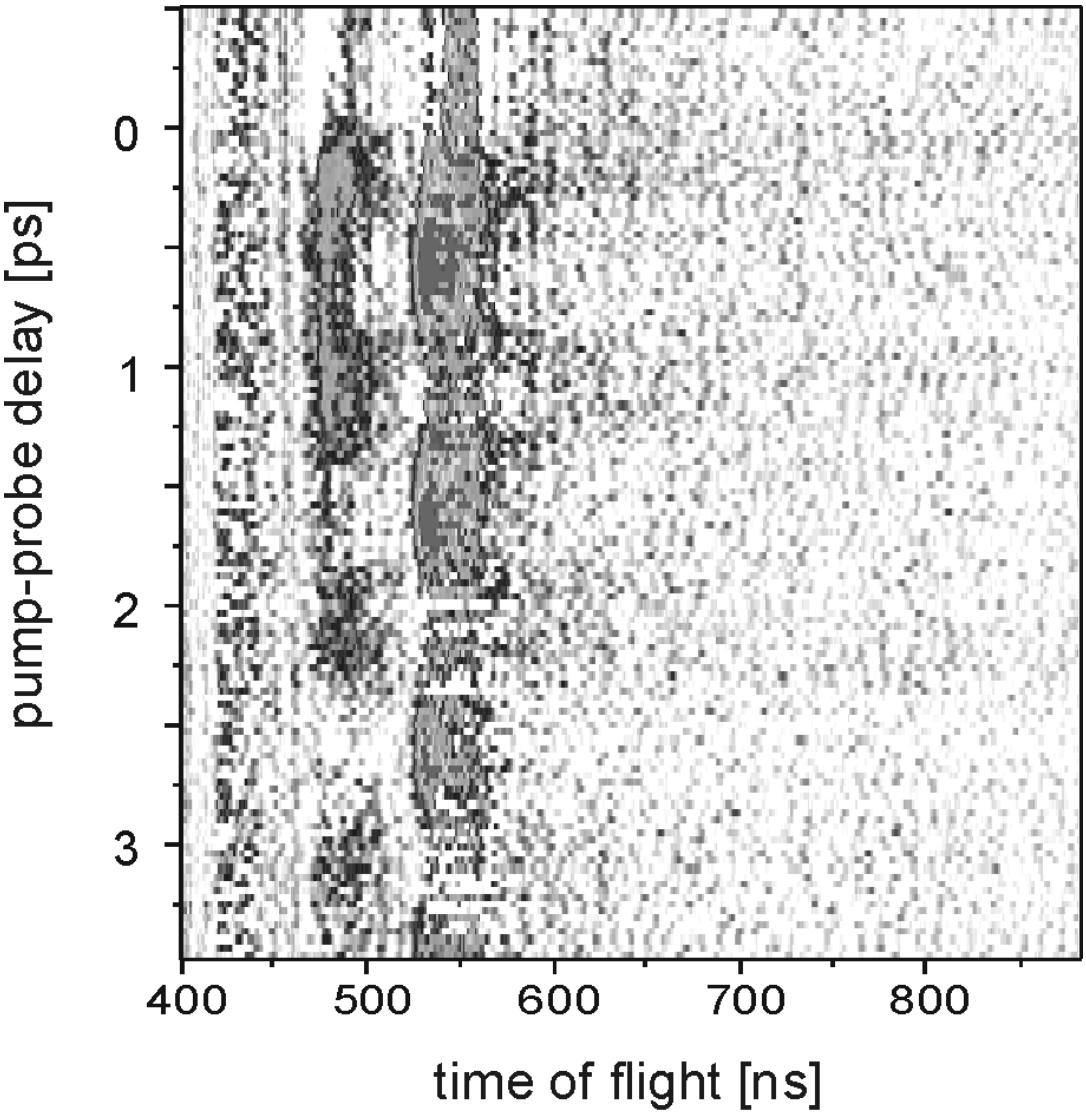

Figure 5.11: Photoelectron spectrum obtained by subtraction of the spectrum shown in Figure 5.10 from the measured signal depicted in Figure 5.9.

After that the spectrum is averaged using a Gauss 3x3 averaging filtering, in which each point of the signal is replaced by the average of itself and its neighbouring pixels. This neighbourhood is multiplied by a set of Gaussian integer weights. Eventually, 10 times smoothing along the time-of-flight axis is performed in which every point in a signal is replaced with a weighted mean value of its neighbours including itself. The final signal is shown in Figure 5.12.

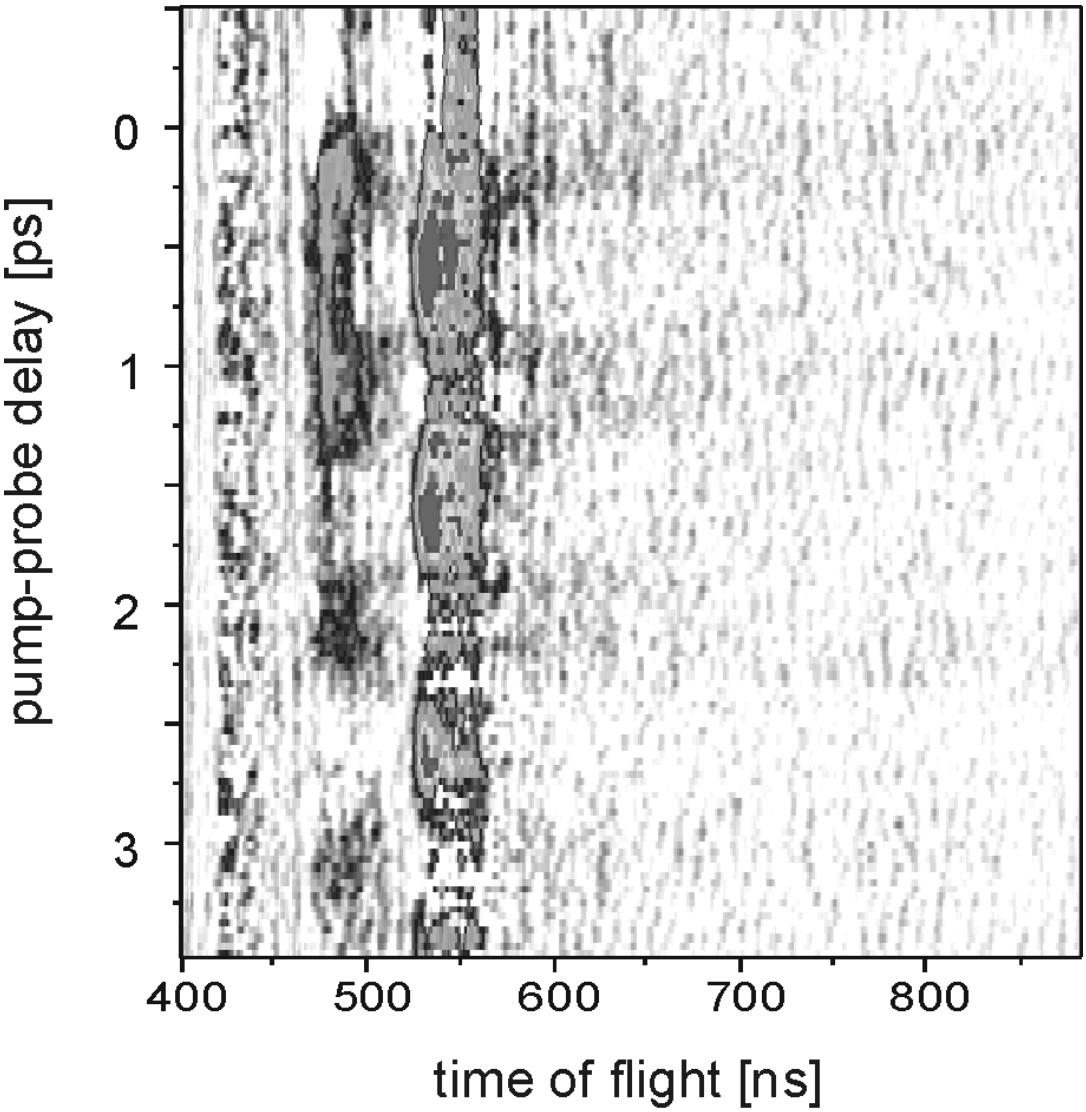

Figure 5.12: Photoelectron spectrum obtained by Gaussian 3x3 averaging and subsequent 10 times smoothing along the TOF axis of the spectrum depicted in Figure 5.11.

5.6.4 Calibration of the signal

The general calibration procedure using both nano- and femtosecond laser systems is described in Section E.6 of the Appendix E. However, this procedure includes two separate kinetic energy ranges calibrated either with nanosecond laser or with femtosecond laser. This fact can lead to a high calibration uncertainty for the small kinetic energies (0.5 – 2.5 eV). Therefore, the following calibration procedure is performed:

- First, the calibration using the signal from ionisation of Xe with Nd:YAG laser and the signal from the ionisation of atomic Na with femtosecond laser pulses is used. The points taken for the calibration are 1.85 eV and 0.54 eV from the ionisation of Xe with λ = 355 nm of Nd:YAG laser and 2.15 eV, 3.17 and 4.18 eV from ionisation of atomic Na with λ_1 = 340 and λ_2 = 266 nm of femtosecond laser (see Figure 5.9). The procedure is described in the Appendix E, Section E.6. Figure 5.13 shows the calibration curve. The calibration points are shown with squares.

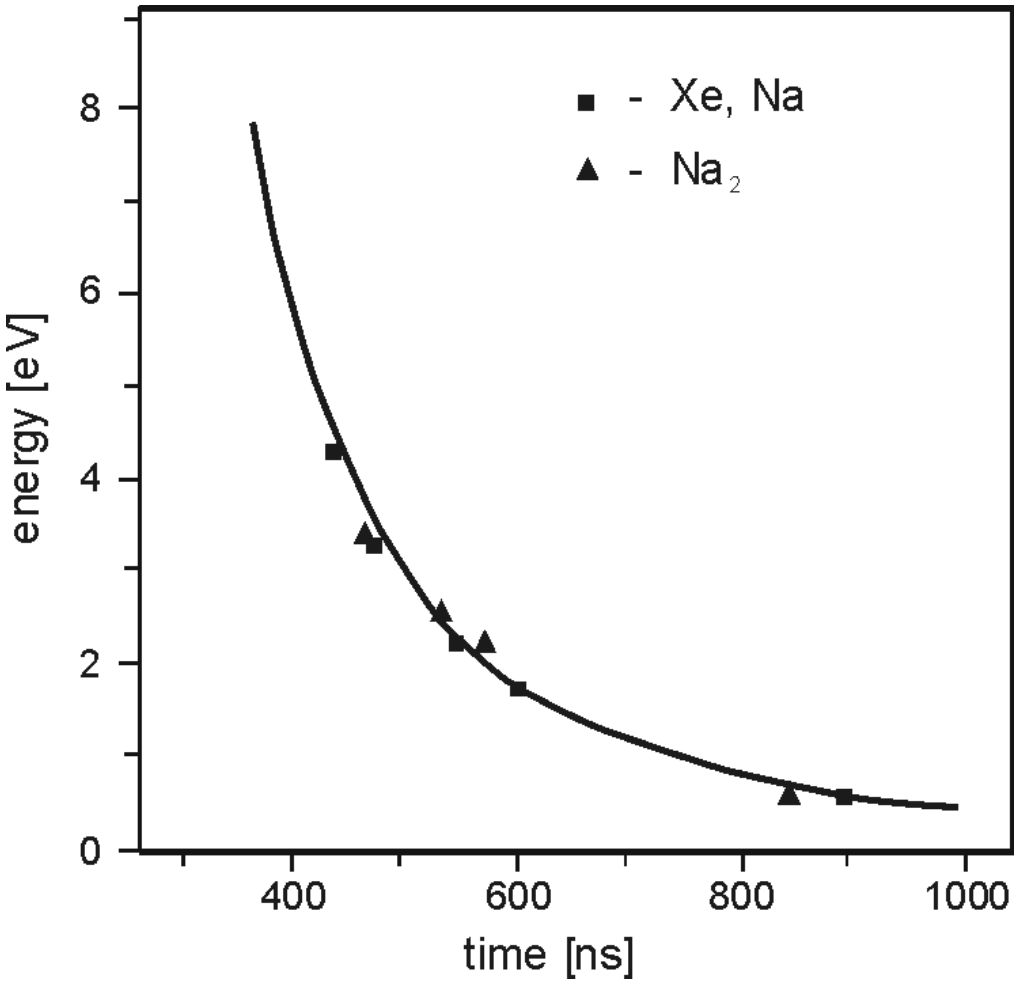

Figure 5.13: Calibration curve for U_g = 1 V using the signal from ionisation of Xe with Nd:YAG laser and the signal from the ionisation of atomic Na with λ_1 = 340 and λ_2 = 266 nm femtosecond laser pulses. Squares show the calibration points. Triangles show the signal from the ionisation of the dynamical evolution of the wave packet on the $2^1\Sigma_u^+$ double minimum state.

- In order to perform a more correct calibration, new points should be used in the area of kinetic energies of 0.5 – 3.5 eV. These points can be the signal from the dynamical evolution of the wave packet on the double minimum state. It includes the signal from the inner turning point of the double minimum potential projected onto a repulsive state, calculated to be at 0.5 eV (presumably the signal at 850 ns in Figure 5.11), from the outer turning point of the $2^1\Sigma_u^+$ state projected on both bound and repulsive state giving photoelectrons with the same energies of 2.46 eV (530 ns), from the inner turning point of the $2^1\Sigma_u^+$ state projected onto a bound state giving 3.31 eV electron energy (480 ns) and from the barrier at 2.15 eV (590 ns). In order to prove if the signal at these time of flight arises indeed from the ionisation of the wave packet on the double minimum state, we plotted these points on the calibration curve (triangles in Figure 5.13). The points fit to the curve satisfactory.
- Finally, a new calibration is performed using the signal from the ionisation of Na and Na_2 with the λ_1 = 340 nm and λ_2 = 266 nm of the femtosecond laser. The points taken for the calibration together with their photoelectron kinetic energies are summarised in a Table 5.1.

Source	Ionisation wavelength, λ	Electron energy, E_{kin}
Na	340 nm	2.15 eV
Na	340 + 266 nm	3.17 eV
Na	266 nm	4.18 eV
Na_2, inner turning point, $^2\Sigma_u^+$	340 + 266 nm	0.5 eV
Na_2, barrier, $^2\Sigma_u^+$	340 + 266 nm	2.15 eV
Na_2, outer turning point	340 + 266 nm	2.46 eV
Na_2, inner turning point, $^2\Sigma_g^+$	340 + 266 nm	3.31 eV

Table 5.1: Kinetic energies used for the calibration of the time-of-flight scale. Electrons from ionisation of Xe atoms with 355 nm of YAG laser, Na atoms with 340 nm and 266 nm of femtosecond laser and electrons from the double minimum dynamics are used.

The calibration curve for the grid voltage relevant for the experiment U_g = 1 V and the coefficients of a fit series (see formula E.9) are shown in Figure 5.14.

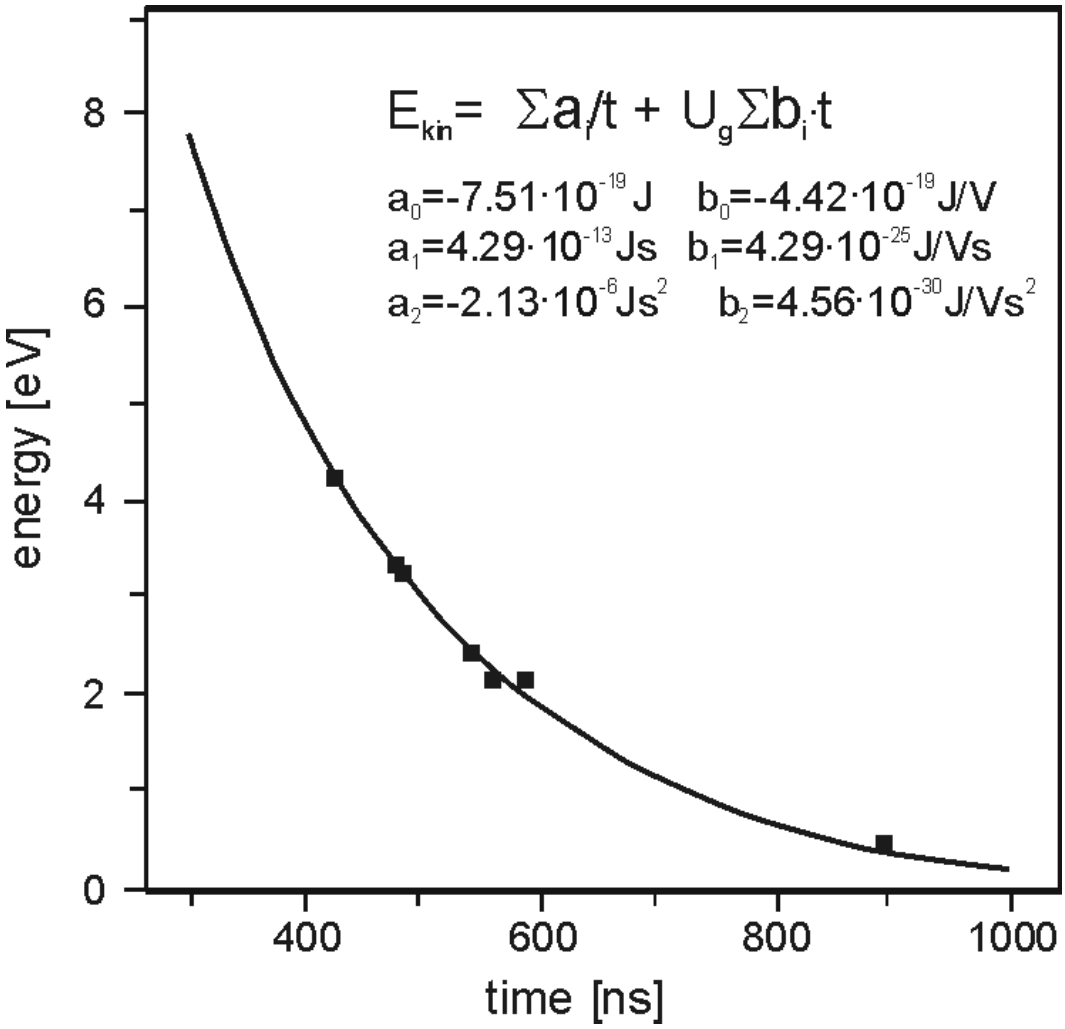

Figure 5.14: Calibration curve for U_g = 1 V used in experiment. Also shown are the coefficients a_i and b_i of the least squares fit.

Finally, in addition to a TOF-to-kinetic energy axis conversion a Jacoby transformation was applied to a photoelectron signal (see formula E.14) in order to convert also the signal intensity. The final photoelectron kinetic energy spectrum after calibration is shown in Figure 5.15.

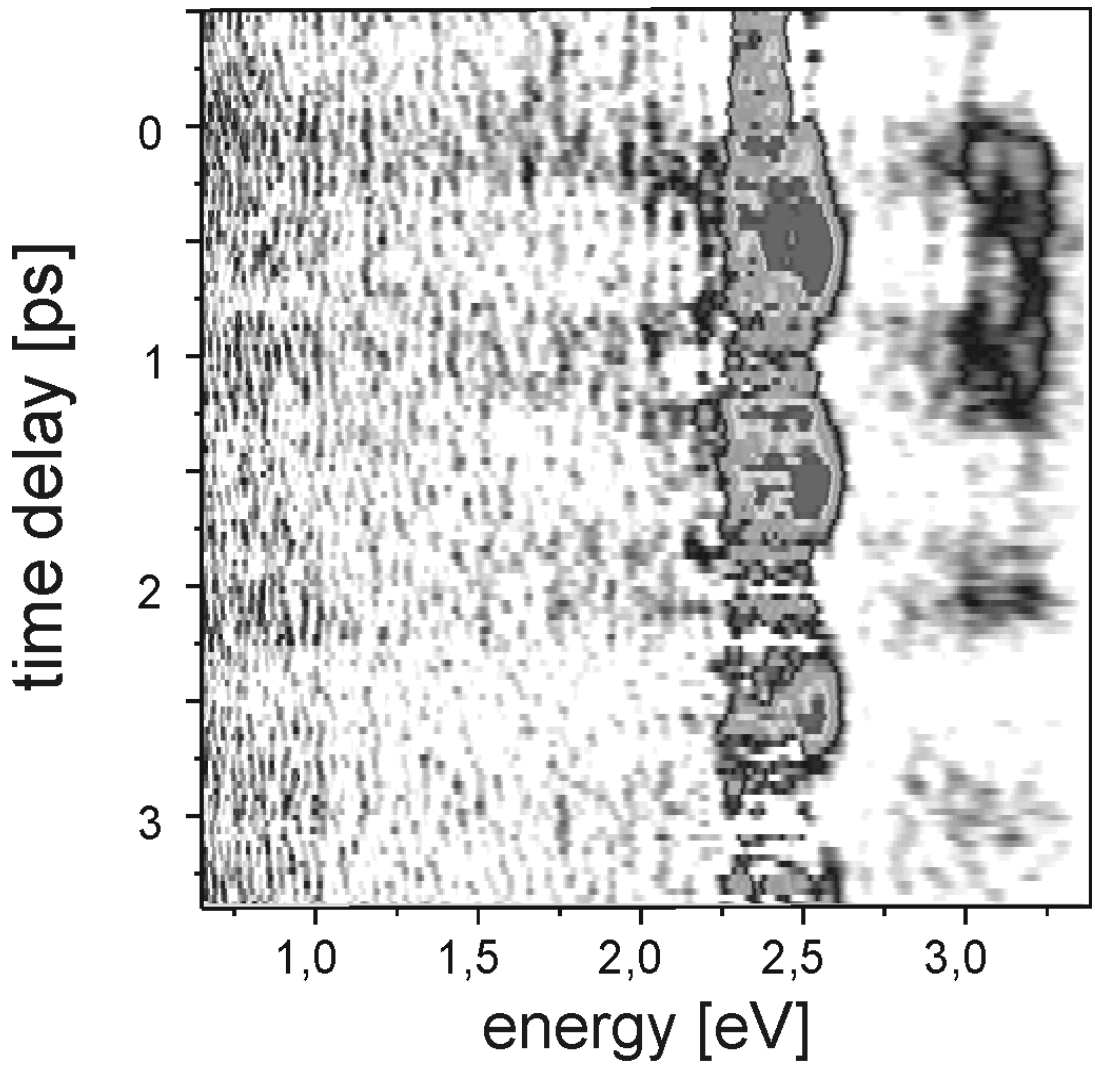

Figure 5.15: Experimental kinetic energy spectrum obtained by the calibration of the time-of-flight spectrum shown in Figure 5.12. A portion of the spectrum for delay times t = –0.5 – 3.5 ps and E_{kin} = 0.4 – 3.6 eV is shown.

5.6.5 Cuts along the energy axis and delay time axis

In order to enhance the visibility of results and to compare with calculations cuts along both axes of the experimental scan were performed.

Firstly, a cut along the energy axis, representing the time-of-flight spectrum at a certain delay between pump and probe laser pulses, was made. The spectrum was averaged for the delay times from 533 till 1533 fs, that is over one period of oscillation of a wave packet in a double minimum well. After that it was smoothed over 50 pixels of 0.5 ns, i.e. 25 ns. The spectrum is shown in Figure 5.16.

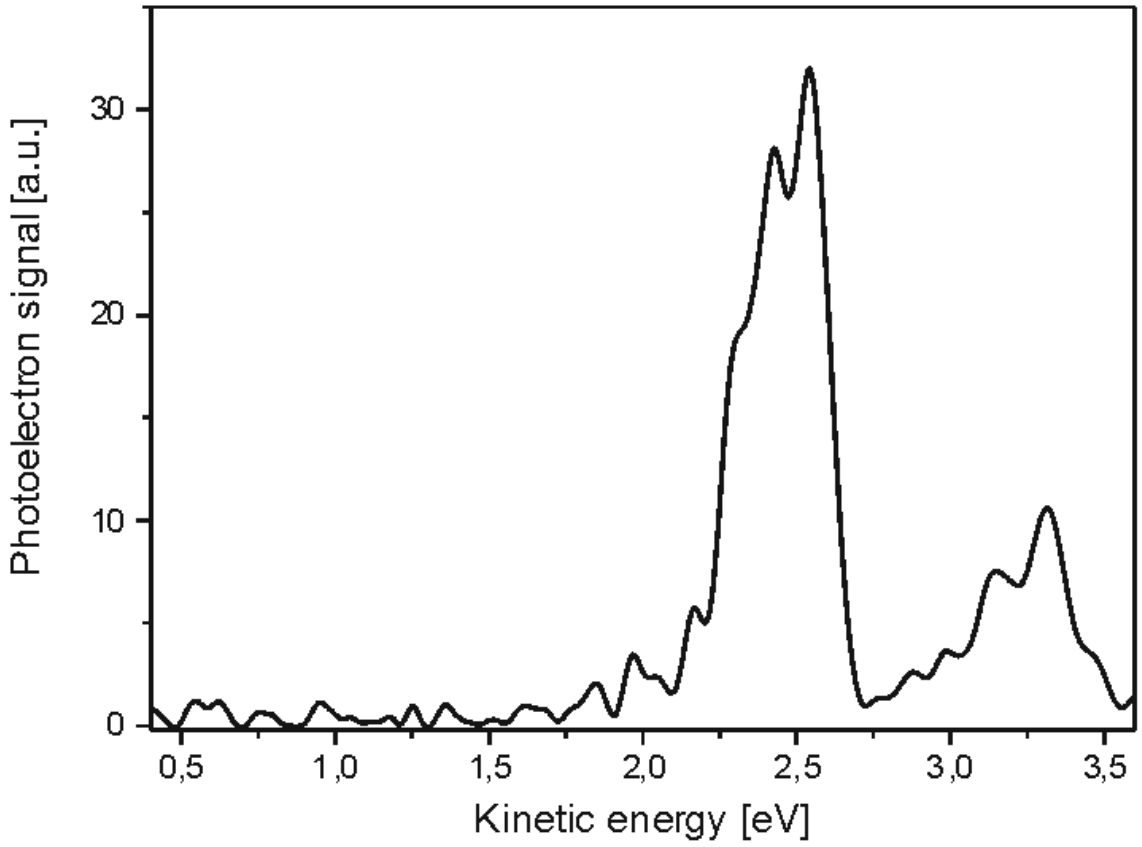

Figure 5.16: A cut along the energy axis representing a photoelectron kinetic energy spectrum averaged over one period (533 – 1533 fs) of the oscillation in the double minimum state and smoothed over 25 ns with respect to time of flight axis.

Secondly, several cuts of the experimental scan were made along the pump-probe axis. The cuts represent the temporal behaviour of the photoelectron signal at a certain electron kinetic energy. Remembering from the difference potentials analysis that the photoelectrons with certain kinetic energy correspond to a certain internuclear distance, one can see, that the cuts reflect the temporal behaviour of the wave packet at certain regions of the double minimum potential reflected onto either the bound or the repulsive potential.

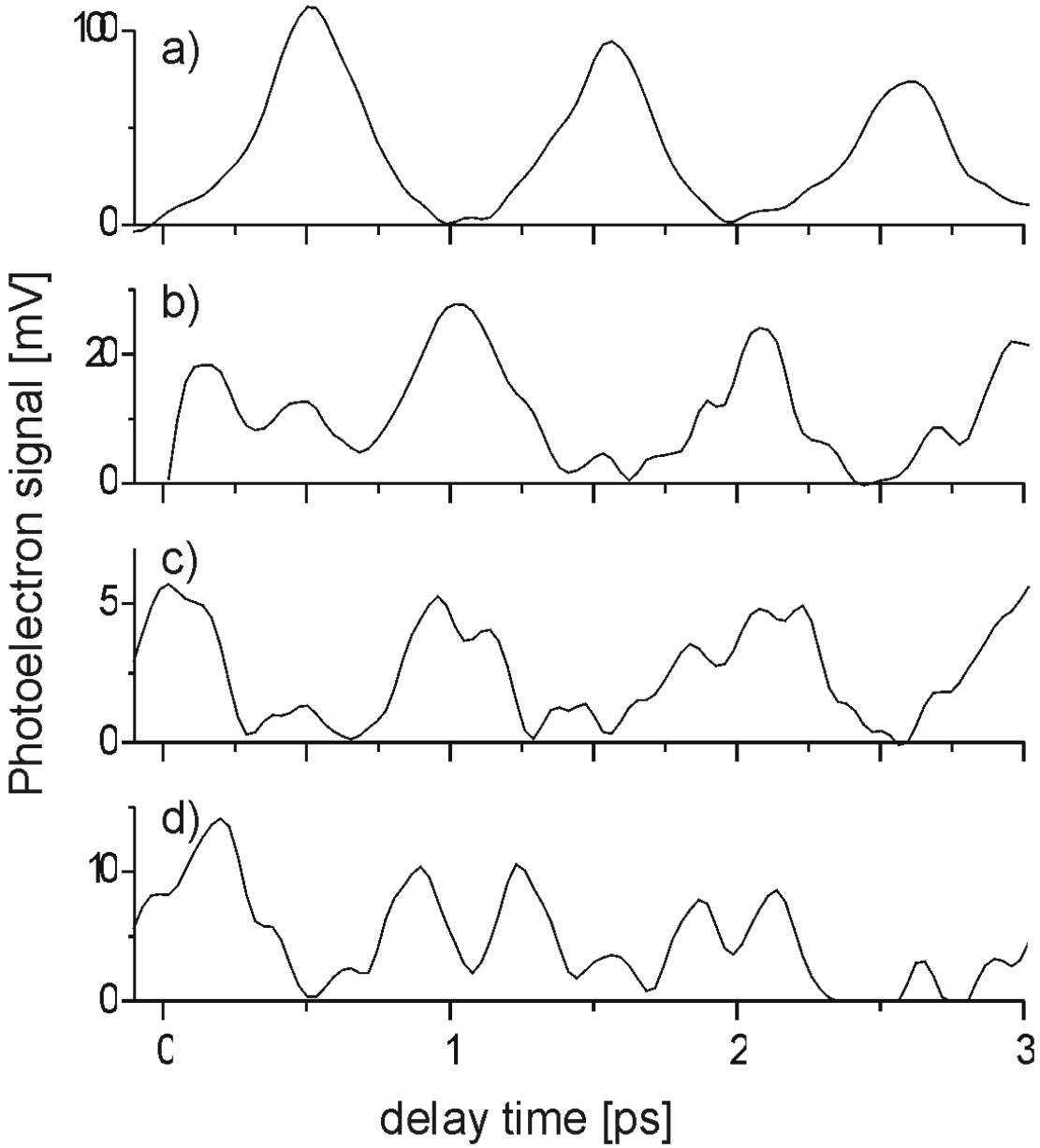

Figure 5.17: Measured time profiles of the photoelectrons from (a) the outer turning point (both ionic states) at 2.4 – 2.6 eV, (b) the inner turning point (bound ionic state) at 3.2 – 3.4 eV, (c) the inner turning point (repulsive ionic state) at 0.4 – 1.5 eV and (d) the barrier (repulsive ionic state) at 1.8 – 2.0 eV.

Figure 5.17 shows cuts along pump-probe delay for several energy intervals. Figure 5.17a is taken at photoelectron kinetic energies of 2.4 till 2.6 eV, which corresponds to a wave packet located in an inner turning point (~3.1 Å) of the double minimum potential projected onto the bound ionic state. Figure 5.17b shows a signal averaged over 3.2 till 3.4 eV kinetic energies of the photoelectrons. From the difference potential analysis this corresponds to the outer turning point (~9 Å) of the double minimum. Since the difference potentials coincide at these internuclear distances, photoelectrons both from the bound and the repulsive ionic potentials are mapped. In Figure 5.17c the photoelectrons from the projection of the inner turning point onto a repulsive ionic state are mapped. The signal is averaged for E_{kin} = 0.4 till 0.15 eV. Finally, Figure 5.17d shows the photoelectrons from the barrier. The spectra are averaged

over the kinetic energies from 1.8 to 2.0 eV which corresponds to internuclear distances of ~ 5 Å projected onto a repulsive ionic state.

5.7 Dynamical information: vibrational wave packets

First, we concentrate on the dynamical information obtainable from the experimental data. The analysis of the experimental results can be performed in the time domain and in the frequency domain.

The photoelectron spectrum for the first 3.5 ps time delay between pump and probe laser pulses is shown in Figure 5.18. To enhance the visibility of the measured signal the kinetic energies for "classical electrons" is superimposed as a white line. For this purpose, classical trajectory calculations are performed to model the wave packet motion and the corresponding photoelectron energies are obtained by projecting the movement onto difference potentials [109].

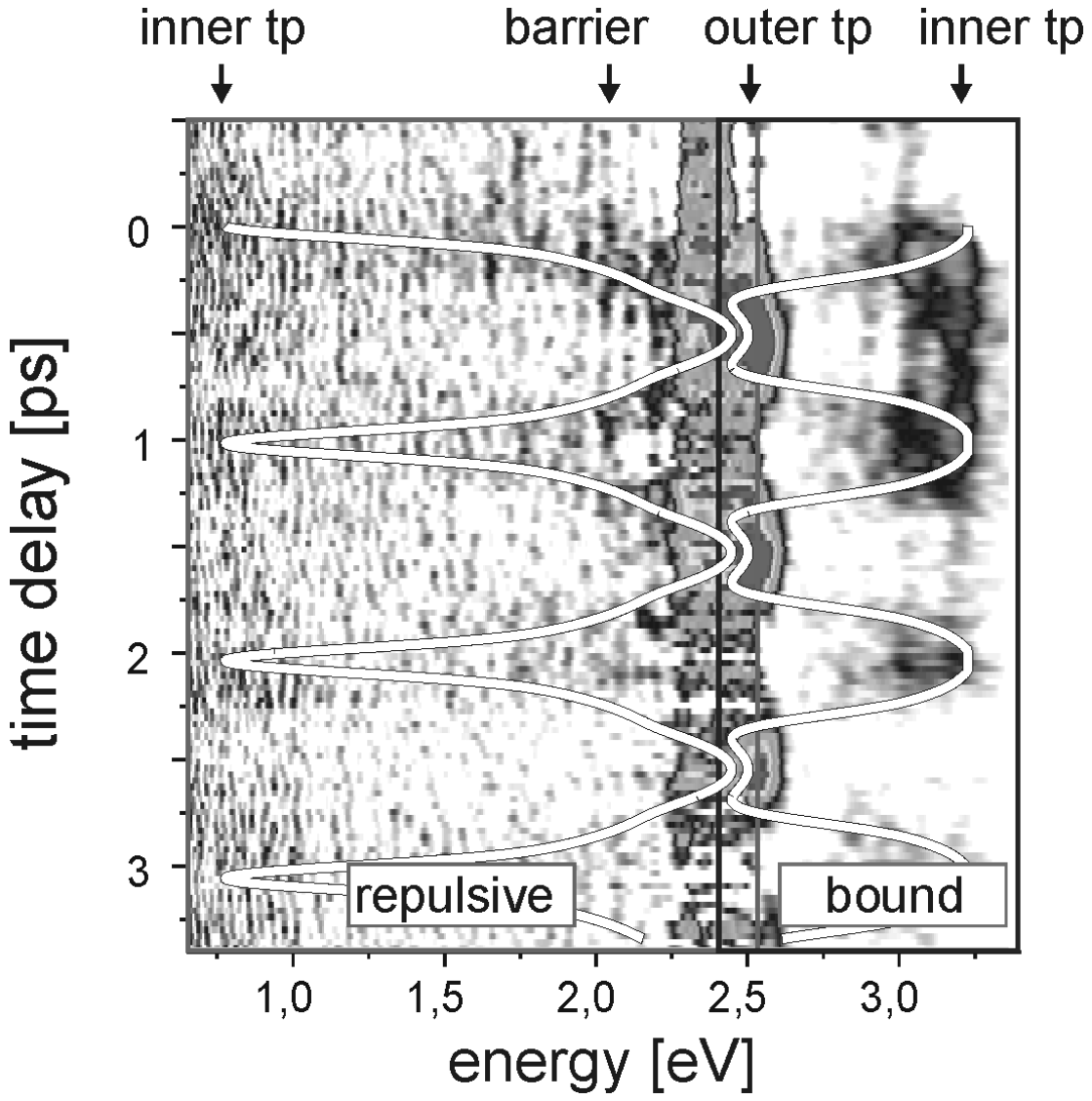

Figure 5.18: Measured photoelectron kinetic energy spectrum after signal subtraction and calibration. The "classical electrons" trajectories are also shown obtained by solving the Newton equation for the mass point starting to move in the $2^1\Sigma_u^+$ potential at 3.1 Å and subsequent calculation of kinetic energies using difference potential depicted in Figure 8.5. In addition the kinetic energy areas for electrons from bound, repulsive ionic states, and energies for inner, outer turning points and barrier are indicated.

The wave packet motion is clearly visible for both, bound and repulsive, ionic potentials. At a zero delay time between pump and probe pulses electrons are generated at the inner turning point (R = 3.1 Å). This corresponds to the kinetic electron energies of 0.4 and 3.5 eV for the repulsive and bound ionic state respectively. Then the electron signal follows the wave packet moving towards big internuclear distances. A dynamical enhancement of the wave packet at the barrier is seen around 2 eV on the repulsive state. This dynamical effect is not visible for the bound ionic curve, since the corresponding difference potential is almost flat between 3 and 4.5 Å (see Figure 5.5), all electrons from this interval are mapped onto a kinetic energy of approximately 3.3 eV. The dynamical compression at the barrier at 2 eV recurs twice per period. At 500 fs, when the wave packet arrives at the outer turning point, the kinetic energies of the photoelectrons from both ionic states coincide at 2.5 eV. The complex structural shape of the observed photoelectron at 2.5 eV, 500 fs, mentioned in Section 5.5 (see, f.e., Figures 5.6 and 5.7), leads to a strong enhancement of the signal at these points. The oscillations are repeatedly observed with a period of 1 ps, in accordance with the energy level spacing of 32 cm^{-1} for v`= 45 [107].

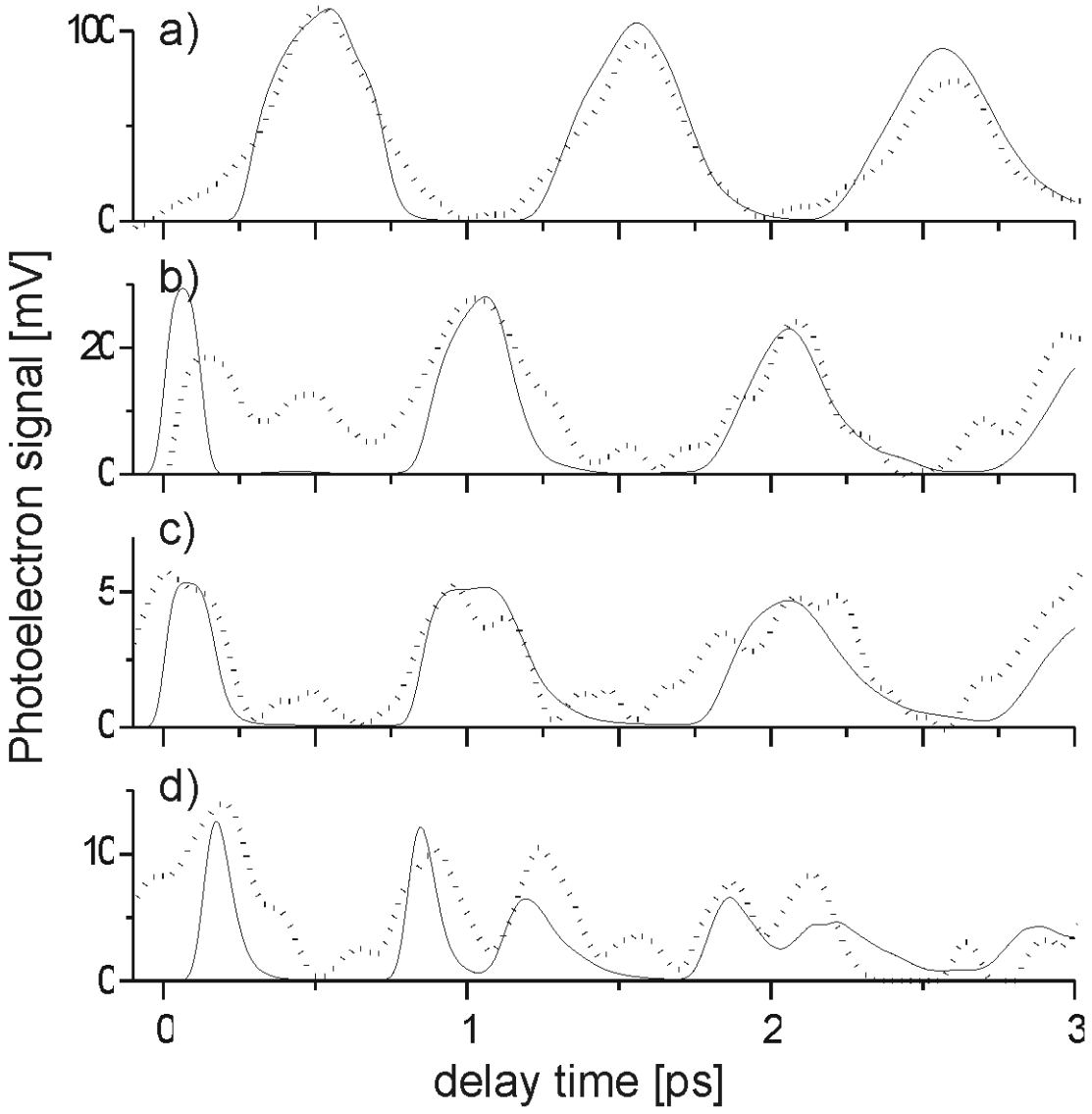

Figure 5.19: Measured (dots) and calculated (lines) profiles of the photoelectrons from a) the outer turning point (both ionic states); the inner turning point (bound ionic state; c) the inner turning point (repulsive ionic state); d) the barrier (repulsive ionic state).

In order to illustrate the phase shift between electrons from the outer turning point, the inner turning point and the barrier, sections along the pump-probe delay axis were taken at the respective kinetic energies of the measured photoelectron distributions, as described in the section 5.6, and compared with the corresponding calculated signals, as shown in Figure 5.19. The calculated profiles were normalised to the peak height of the measured profiles.

Measured and calculated profiles are in excellent agreement for the electrons generated at the outer turning point (Figure 5.19a). Here the signal-to noise ratio is the best due to localisation of the wave packet (see Figure 5.7) and due to the overlap of kinetic energies for bound and repulsive ionic states. Even when the measured signal is close to the noise limit, as is seen for the photoelectrons from the repulsive ionic state at the inner turning point (Figure 5.18c), the measured and calculated signals agree reasonably well.

The oscillations of the photoelectrons from the outer turning point (Figure 5.19a) and the inner turning point (Figure 5.19b and c) are clearly shifted by half a period (500 fs). Therefore the ionisation pathway, i.e. whether the electrons are ionised at the inner or outer turning point, can be unambiguously identified. Moreover, the good agreement of the measured signal with the calculation confirms that no measurable contributions from other competing ionisation channels are present. In the region of the barrier the photoelectrons monitor the twofold reccurence of the wave packet leading to an oscillation at twice the oscillation frequency as seen in Figure 5.19d.

5.8 Determination of electronic changes along the internuclear coordinate by measurement of the ionisation dipole moments

In order to determine the dependence of the ionisation dipole moment on the internuclear distance the measured photoelectron spectra are averaged over one oscillation period (533 – 1533 fs), as described in the section 5.3 (Figure 5.16), and compared with the calculated photoelectron signal averaged over the same time interval. The calculated photoelectron spectra are convoluted with a resolution of 0.2 eV. For the determination of the experimental error the time-integrated photoelectron signals for two energy windows at 2.1 – 2.7 eV (outer turning point) and 2.8 – 3.5 eV (inner turning point mapped by electrons from the bound well) are compared for different time windows. The choice of the time window in our case introduces less than 10 % variation of their ratio. This value is used for the further error analysis of the ionisation dipole moment.

Generally, the ionisation dipole moment can be a non-monotonous function of internuclear distance, as predicted, for instance in [99] for Na_2 molecule. There are techniques developed recently, allowing the direct extraction of the energy- and coordinate-dependence of the ionisation dipole moment via matrix inversion from the photoelectron spectra [43]. However, in our case this technique is not applicable, first, because of the fact that the photoelectrons from two different potentials are mapped onto the same kinetic energy region (i.e. electrons with 2.4-2.6 eV from the bound and the repulsive ionic states at the outer turning point), therefore the direct extraction of the dipole ionisation moment function is impossible. Second, a serious limitation of the quantitative data analysis via matrix inversion is provided by the low signal intensity at small photoelectron kinetic energies, where the signal level approaches the noise level. Therefore, instead of inversion, we proceed as following: several simple functions of the ionisation dipole moment are included in the calculated photoelectron signal. The calculations will be compared with the experimental photoelectron spectrum. The obtained dipole moment functions are discussed from the point of view of their physical meaning.

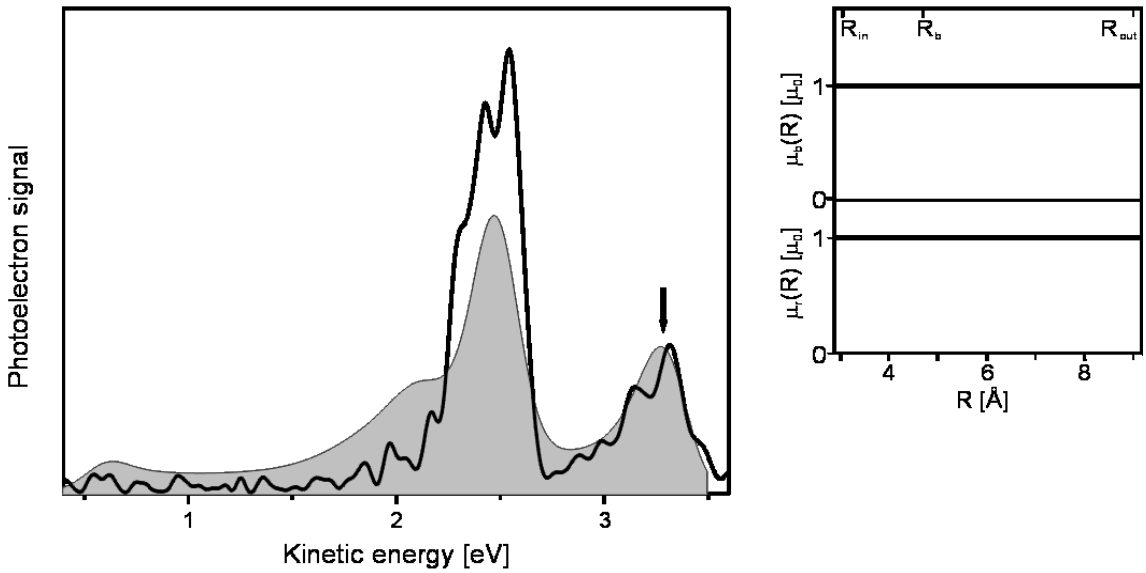

Figure 5.20: Measured (bold) and calculated (light grey) photoelectron spectra averaged over one oscillation period (533 – 1533 fs) (left). A constant photoionisation dipole moment $\mu_b = \mu_r = \mu_0$ was assumed in the calculated signal (right).

First, we start with a case, where we assume a constant, i.e. R-independent ionisation dipole moment of equal magnitude for both ionic states, i.e. $\mu_b = \mu_r = \mu_0$. Figure 5.20 shows the averaged calculated and measured photoelectron spectra. The value of μ_0 is adjusted in the calculated signal to fit the photoelectrons from the bound ionic state at 3,3 eV (shown with an arrow). It is clear from the comparison that the photoelectrons from the repulsive ionic state at inner turning point and barrier (in the area 0.5 – 2.1 eV) are overestimated in the calculated signal, whereas the photoelectrons at the outer turning point (around 2.5 eV) are underestimated.

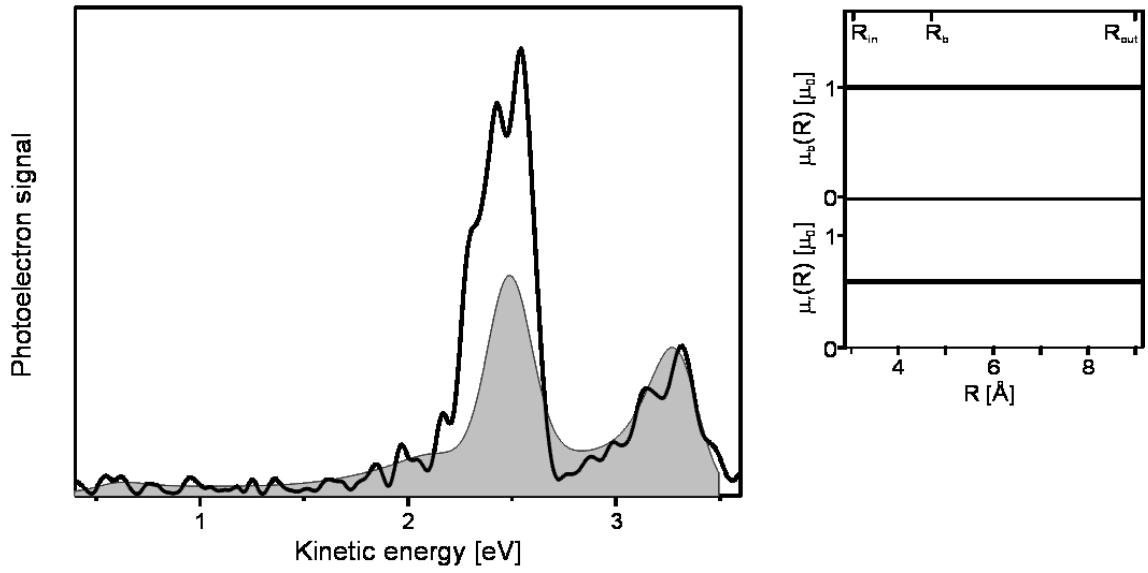

Figure 5.21: Measured (bold) and calculated (light grey) photoelectron spectra averaged over one oscillation period (533 – 1533 fs) (left). Constant photoionisation dipole moments $\mu_b = \mu_0$ for the ionisation into the bound ionic state and $\mu_r = 0.59\mu_0$ for the ionisation into a repulsive ionic state are used in the calculated signal (right).

In the next step, we shall assume a constant dipole moment for both potentials, but reduce the photoionisation dipole moment for the ionisation into the repulsive ionic state to fit the measured signal at the barrier. The calculated signal assuming $\mu_r = 0.59\mu_0$ is shown in Figure 5.21. Obviously, the calculation does not reproduce the measured signal at 2.5 eV, where electrons from the outer turning point are detected. Therefore one can assume that the ionisation probability is increasing at the outer turning point. To model this observation, we assume first a linear increase of the dipole moments for the ionisation into the repulsive and the bound well.

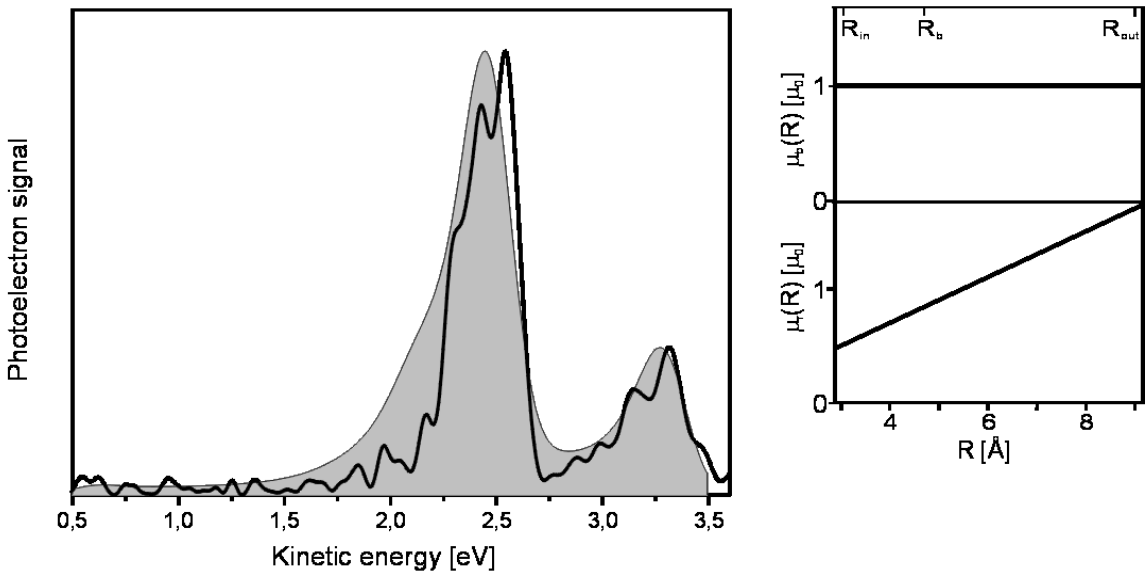

Figure 5.22: Measured (bold) and calculated (light grey) photoelectron spectra averaged over one oscillation period (533 – 1533 fs) (left). Constant photoionisation dipole moment $\mu_b = \mu_0$ for the ionisation into the bound ionic state and linear increasing $\mu_r = (0.20\text{Å}^{-1}R + 0.17)\mu_0$ for the ionisation into the repulsive ionic state are used in the calculated signal (right).

Figure 5.22 shows the calculated photoelectron spectrum with μ_b = const and $\mu_r = (0.20\text{Å}^{-1}R + 0.17)\ \mu_0$. The coefficients of $\mu_r(R)$ are chosen to fit the signal at the outer turning point. It is visible, that the increase of the photoelectron signal at the outer turning point for the repulsive ionic well leads to an overestimation of the calculated signal at the barrier region of 1.5 – 2.2 eV.

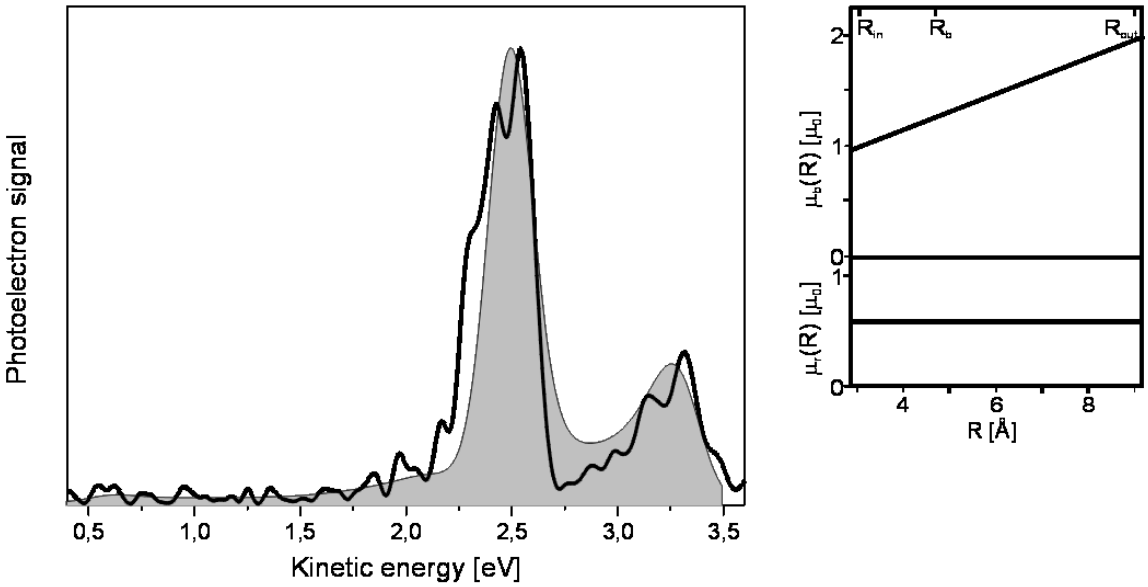

Figure 5.23: Measured (bold) and calculated (light grey) photoelectron spectra averaged over one oscillation period (533 – 1533 fs) (left). A linearly increasing photoionisation dipole moment for the ionisation into the bound ionic state $\mu_b = (0.16\ \text{Å}^{-1}R + 0.50)\mu_0$ and constant for the ionisation into the repulsive ionic state $\mu_r = 0.59\mu_b$ are used in the calculated signal (right).

A linear photoionisation dipole moment for the ionisation into the bound ionic state is depicted in Figure 5.23. The dependence of $\mu_b = (0.16\ \text{Å}^{-1}R + 0.50)\mu_0$ was obtained by fitting the calculated signal to the measured at 2.5 eV. The calculation and the experimental spectrum agree satisfactory.

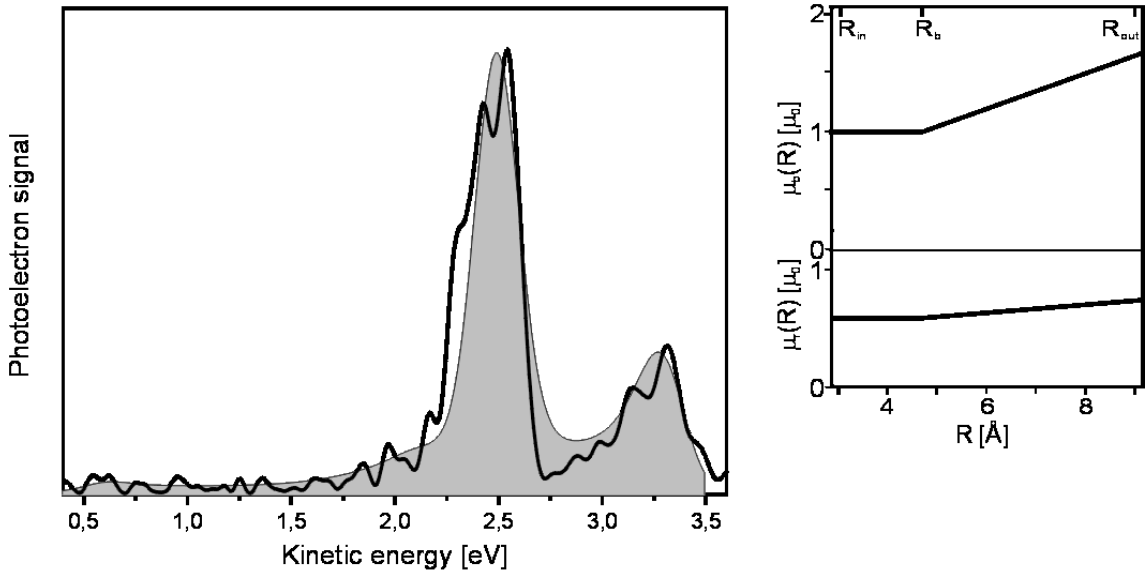

Figure 5.24 Measured (bold) and calculated (light grey) photoelectron spectra averaged over one oscillation period (533 – 1533 fs) (left). Functions of the dipole moments μ_b for the ionisation into the bound ionic state and μ_r for the ionisation into the repulsive ionic state used in the calculated signal are constant in the inner well (3.1 – 4.7 Å) and increase linearly in the outer well (4.7 – 9 Å) (right).

Let us consider next the case of photoionisation dipole moments consisting of two different functions for ionisation into both bound and repulsive states: the dipole moment for ionisation from the inner well of the double minimum is constant and in the outer well is linear

increasing, starting from the barrier at 4.7 eV. The calculated photoelectron signal is depicted in Figure 5.24. For the inner well (i.e. for 3.1 – 4.7 Å) the dipole moments μ_b and μ_r from Figure 5.21 were adapted. A linear increasing ionisation dipole moment for the outer well for the repulsive state was chosen to fit the signal around the barrier with a slight increase at 2.0 - 2.2 eV. Next, a linear dipole moment for the ionisation into a bound well at distances 4.7 - 9 Å was fitted to match the signal at 2.5 eV. The dipole moments thus obtained are:

$$\mu_b = \begin{cases} \mu_0, R < 4{,}7\text{Å} \\ (0.14\text{Å}^{-1}R + 0.32)\mu_0, R > 4.7\text{Å} \end{cases}$$

$$\mu_r = \begin{cases} 0.59\mu_0, R < 4.7\text{Å} \\ (0.03\text{Å}^{-1}R + 0.43)\mu_0, R > 4.7\text{Å} \end{cases} . \qquad (5.1)$$

It is visible from the Figure 5.24 that the calculated signal fits to the measured satisfactory. Moreover, upon comparison of Figure 5.23 and Figure 5.24 both functions of the dipole moment fit the measured data within the experimental error.

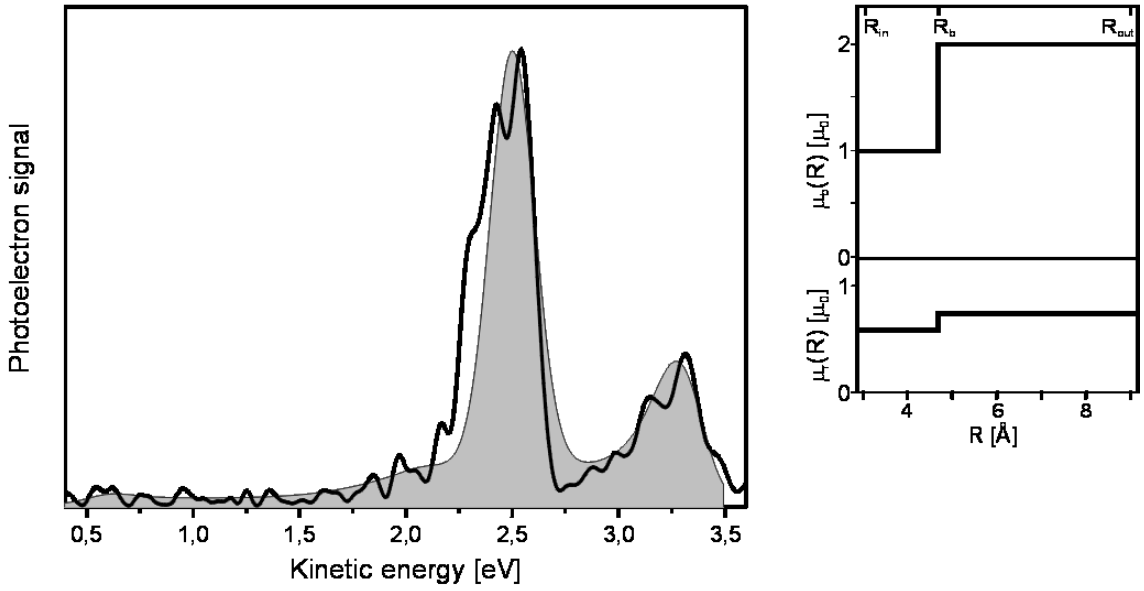

Figure 5.25: Measured (bold) and calculated (light grey) photoelectron spectra averaged over one oscillation period (533 – 1533 fs) (left). Functions of the photoionisation dipole moments μ_b for the ionisation into the bound ionic state and μ_r for the ionisation into the repulsive ionic state used in the calculated signal represent a Heaviside function $\mu(R) = \mu\ T(R - R_b)$ (right).

Finally, we describe the last case of the photoionisation dipole moment into both bound and repulsive ionic states represented by a Heaviside function, shown in Figure 5.25. Good agreement with experimental results was found for the following values:

$$\mu_b = \begin{cases} \mu_0, R < 8.5\text{Å} \\ 2\mu_0, R > 8.5\text{Å} \end{cases}$$

$$\mu_r = \begin{cases} 0.59\mu_0, R < 8.5\text{Å} \\ 0.74\mu_0, R > 8.5\text{Å} \end{cases}, \quad (5.2)$$

where the ionisation dipole moments increase only at the outer turning point (8.5 – 9 Å). Note that the values of dipole moment (5.2) at the outer turning point at 9 Å are not equal to those in equation (5.1).

From comparison of the calculated and experimental results in Figures 5.23, 5.24 and 5.25 is visible that all the three suggested models for the ionisation dipole moment match the experimental data well within the experimental error. The difficulty in differentiation between them arises from (a) the overlap of the signal from to different sources onto the same kinetic energy at 2.3 – 2.5 eV which does not allow direct analysis of the separate ionisation ways and (b) the low signal to noise ratio at small kinetic energies of 0.5 – 2.0 eV. That is why we will concentrate now on the question of the physical interpretation of the models.

As described in detail in the Chapter 2, the electronic structure of the double minimum well evolves with internuclear distance leading to an *R*-dependence of the ionisation probability. Indeed, comparing the experimental signal (Figure 5.20) with the theoretical one, we assume that the ionisation cross-section is higher at the outer turning point. First we estimate roughly the dependence of the ionisation dipole moment on the internuclear distance based on physical considerations. In the inner well and the barrier region the Na_2 molecule can be considered as covalent, whereas at larger internuclear distances at the outer well limb the bond is rather ionic. A difference between the probability of ionisation from these regions can be illustrated using the simple analysis adopted from [94]. The ionisation cross-section in the covalent region can be approximated by the ionisation cross-section of a sodium atom, which is of the order of 0.1 Mb [110]. At large internuclear distances, i.e. in the Na^+Na^- ionic region, the ionisation can be approximated by the cross section of the photodetachment of the electron from the Na^- ion. The photodetachment cross-section is of the order of 1.5 Mb for a photon energy of E = 4 – 5 eV [68]. Thus the ratio between the ionisation dipole moment in covalent and ionic regions can be estimated as:

$$\frac{\mu_{ionic}}{\mu_{covalent}} = \sqrt{\frac{\sigma_{Na^-}}{\sigma_{Na}}} \approx \sqrt{15} \quad (5.3)$$

These considerations provide a physical picture for the observation that the signal at the outer turning point is higher than at the inner turning point.

Next, an analysis of the favourable ionisation of the Na_2 double minimum state into the bound $^2\Sigma_g^+$ ionic state compared to the ionisation into the repulsive $^2\Sigma_u^+$ ionic state was performed in Chapter 2. It was found that the ionisation from the inner well of the $2^1\Sigma_u^+$ double minimum potential would be rather advantageous into the bound ionic state. This explains the lower ionisation dipole moment for the repulsive state at small kinetic energies, shown in Figure 5.21. Second, the ionisation probability in the outer well is increasing with increasing the ionic character of the bond both for the ionisation into the bound and the repulsive ionic states. In addition, as was determined in the Chapter 2, Section 2.3.1, in the outer well (i.e. where the orbital configuration $(\sigma_g 3s)(\sigma_u 3s)$ is ionic) the ionisations into both $^2\Sigma_g^+$ bound and $^2\Sigma_u^+$ repulsive ionic states are *one-electron processes*, i.e. removing of one electron can lead both to $^2\Sigma_u^+$ repulsive and $^2\Sigma_g^+$ bound ion orbital configurations without remained orbital

structure rearrangement. In this regard the ionisation dipole moments used in Figure 5.23, although reproducing the experimental data properly, are disadvantageous compared to those presented in Figure 5.24 and 5.25, since they represent the preferable increasing of the ionisation probability only into one of the ionic state.

Finally, to answer the question if the dependence of the ionisation dipole moment is stepwise (Figure 5.25) or linear (Figure 5.24), we consider the calculations of the weight of the ionic orbital configuration in the outer well of the $^2\Sigma_u^+$ potential. According to calculations for Na_2 [13] and for H_2 molecules [111] the weight of the $(\sigma_g 3s)(\sigma_u 3s)$ configuration, and hence the ionic character of the bond, is smoothly increasing in the outer well of the potential with increasing internuclear distance. This picture corresponds to the case depicted in Figure 5.24, where both ionisation dipole moments are constant in the inner well and are linearly increasing in the outer well.

Summing up, the neutral-to-ion dipole moments for the ionisation into the bound and repulsive ionic states, which describe well the experimental data and are physically motivated, are:

$$\mu_b = \begin{cases} \mu_0, R < 4.7\text{Å} \\ (0.14\text{Å}^{-1}R + 0.32)\mu_0, R > 4.7\text{Å} \end{cases}$$

$$\mu_r = \begin{cases} 0.59\mu_0, R < 4.7\text{Å} \\ (0.03\text{Å}^{-1}R + 0.43)\mu_0, R > 4.7\text{Å} \end{cases} \qquad (5.4)$$

As the ionisation probability is proportional to the square of the ionisation dipole moment, the dependence of the squared dipole moments on internuclear distance, $(\mu(R))^2$, is shown in Figure 5.26.

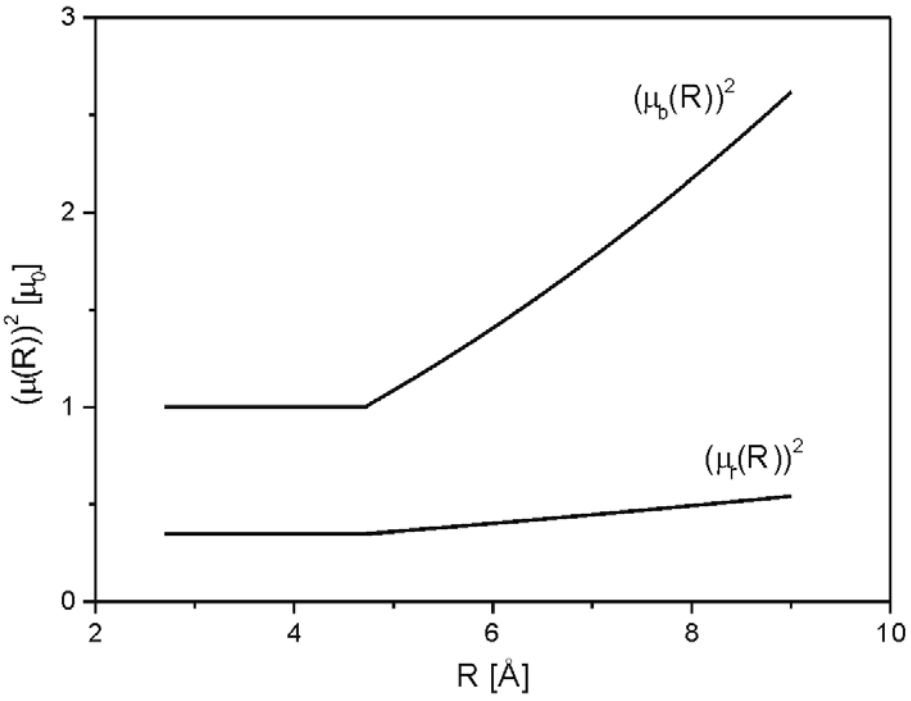

Figure 5.26: Dependence of the squares of the photoionisation dipole moments $(\mu_b(R))^2$ and $(\mu_r(R))^2$ for the ionisation into the bound and into the repulsive ionic states respectively on internuclear distance. The square of the photoionisation dipole moment is proportional to the ionisation probability.

Therefore the ionisation probability at the outer turning point is related to the ionisation probability at the inner turning point as:

$$(\mu_b(8.8\text{Å})/\mu_b(3.1\text{Å}))^2 = 2.5 \pm 0.25$$

$$(\mu_r(8.8\text{Å})/\mu_r(3.1\text{Å}))^2 = 2 \pm 0.2 \qquad (5.5)$$

for ionisation into the bound and the repulsive ionic states respectively. Thus an approximately equal increase of the ionisation probability in the outer well with internuclear distance is seen for ionisation into both ionic states.

The ionisation probability at the outer turning point for the bound ionic state is:

$$(\mu_b(8.8\text{Å})/\mu_r(8.8\text{Å}))^2 = 4 \pm 0.4 \qquad (5.6)$$

times higher than the ionisation probability for the repulsive state.

5.9 Competing ionisation pathways

Photoelectrons from several additional ionisation channels may also contribute to the signal, such as:

a) Other high lying ionic states which are energetically allowed in our excitation scheme;

b) $C^1\Pi_u$ state;

c) Autoionising neutral electronic states, Rydberg or doubly excited autoionising state.

In the second case, excitation into the $C^1\Pi_u$ state may lead to the interference the dynamics with the dynamics on double minimum state. In two other cases the additional ionisation channels may compete with ionisation from the double minimum state.

Below we discuss these additional channels in detail.

a) Figure 5.27a shows the potential scheme of several lowest ionic states of Na_2 molecule. Apart from first two $^2\Sigma_g^+$ and $^2\Sigma_u^+$ states the $2^2\Sigma_g^+$, $2^2\Sigma_u^+$, $1^2\Pi_g^+$ and $1^2\Pi_u^+$ are energetically accessible for the λ_1 = 340 nm excitation and λ_2 = 266 nm ionisation. Figure 5.27b shows the corresponding difference potentials for these ionic states.

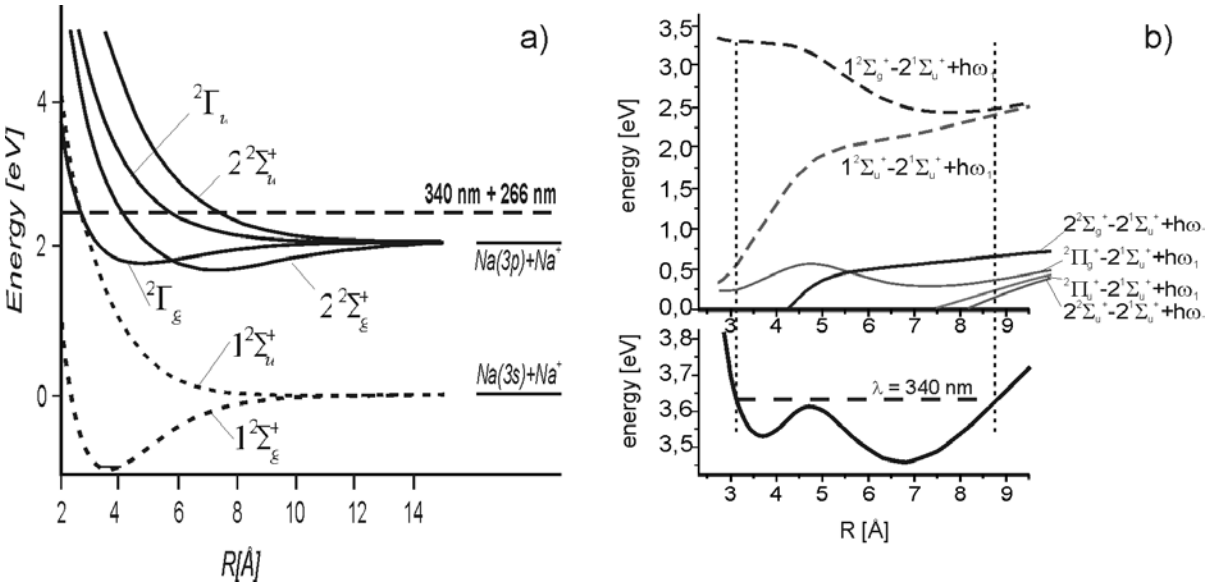

Figure 5.27: a) The scheme of potentials of the Na_2^+ molecule for the excitation with λ_1 = 340 nm and ionisation with λ_2 = 266 nm laser pulses [12]; b) the corresponding different potentials, the dotted lines indicate the range of the wave packet motion in the double minimum well.

The photoelectrons obtained from these states are in the low kinetic energy region i.e. below 0.75 eV, and should predominantly appear at the outer turning point. An example of the calculated photoelectron spectrum for $2^2\Sigma_g^+$ state is shown in Figure 5.28.

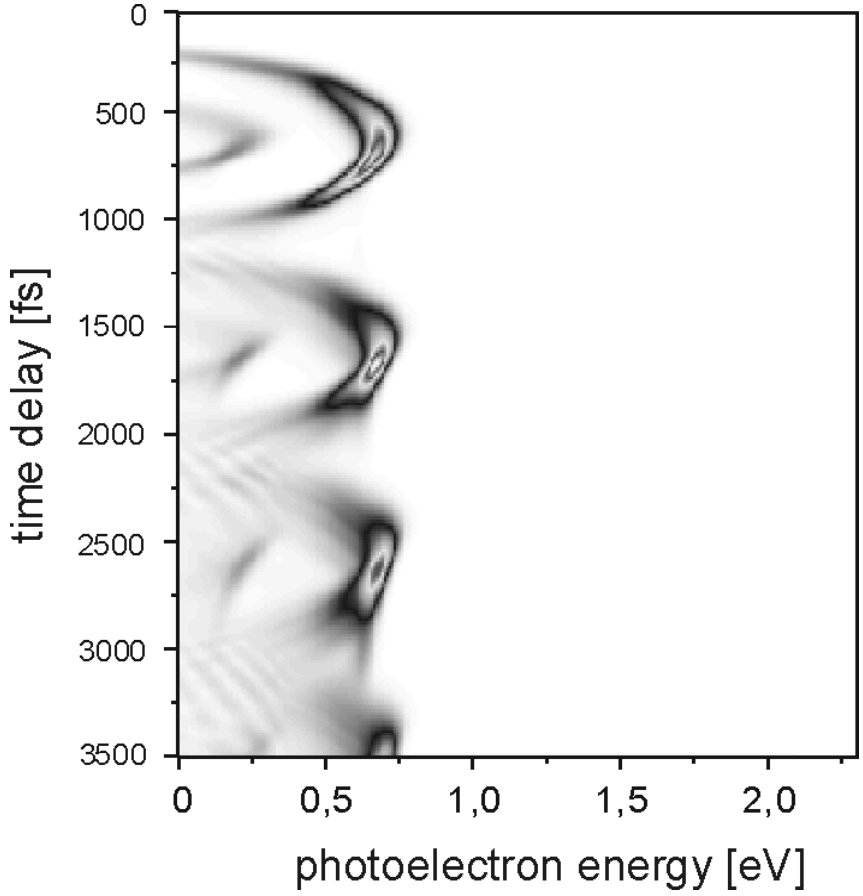

Figure 5.28: Calculated photoelectron signal for the ionisation into $2^2\Sigma_g^+$ state with λ_2 = 265 nm, 40 fs FWHM laser pulse.

The photoelectrons have maxima at a kinetic energy of 0.75 eV at the delay times of 500, 1500 fs and so on, i.e. they are shifted by half a vibrational period with respect to the electrons from the $^2\Sigma_u^+$ repulsive state. Since no such peaks are observed in the signal at these times, we can exclude the overestimation of $\mu(R)$ through photoelectrons from these ionic states. However, we can also exclude underestimation of the photoionisation dipole moment, as in the perturbative regime no population is lost from the double minimum state in the presence of other target ionic states.

b) The $C^1\Pi_u$ state is energetically close, slightly higher with regard to the double minimum state of Na_2. Therefore with 340 nm it could be also excited [63]. The difference potential gives photoelectrons with oscillation period of 114 cm^{-1} at the energies around 0.7, 1.2 and 3.5 eV (see Chapter 4). Indeed, the signal from the $C^1\Pi_u$ state at 0.7 and 1.2 eV was observed in another experiment with slightly different parameters. The experiment is described in the Chapter 4. However, this signal is not observed in the present measurement, therefore the $C^1\Pi_u$ state does not contribute to the measured photoelectron signal.

c) There exists a possibility that highly excited Rydberg states are excited by the second laser pulse which decay via autoionisation. Highly excited Rydberg states are reported in [20,98,113-116]. The states allow to produce highly resolved zero kinetic energy spectra (ZEKE) [117]. The potential curves of the Rydberg states are equal to those of the Na_2^+ ion but slightly shifted towards lower energy. The influence of the states on the measured photoelectron signal can be ruled out, since the autoionised Rydberg states yield photoelectrons with kinetic energies much lower than detected in our experiment. However a bound doubly excited state Na_2^{**} above the ionisation limit is known to exist from previous ultrafast experiments on Na_2 [20] and on K_2 [98] molecules. For autoionising doubly excited states of Na_2 a lifetime of at least half a vibrational period was reported [20]. This leads to a broad photoelectron distribution. Accordingly, stripes in the photoelectron spectrum should be visible at the corresponding Franck-Condon windows due to localised excitation into these states. No such stripes are observed in the experiment, therefore this channel can be also ruled out.

5.10 Conclusion

In this chapter a pump-probe femtosecond experiment with kinetic energy resolved photoelectrons detection is used to map the vibrational and electronic dynamics in the Na_2 molecule. In the experiment the Na_2 $2^1\Sigma_u^+$ double minimum state serves as a model system since the character of the chemical bond changes along the potential well leading to a variation of the photoionisation dipole moment with internuclear distance.

In time domain the motion of the wave packet is followed by the photoelectrons released simultaneously from two ionic potentials. In the frequency domain the direct mapping of the vibrational wave functions with photoelectron signal is performed.

Several models are considered to account for the higher ionisation probability at the outer turning point of the well. The *R*-dependent photoionisation probability is observed such that the photoionisation probability at the outer turning point is 2.5 ± 0.25 and 2 ± 0.2 times higher than that at the inner turning point for ionisation into the bound $^2\Sigma_g^+$ and the repulsive $^2\Sigma_u^+$ ionic states respectively. An increasing ionisation probability at the outer turning point corresponds to the increasing ionic Na^+Na^- character of the double minimum potential. The performed measurement shows discreapancies with the theoretical predictions by Arasaki et al. [99] calculated for different excitation wavelength. A finite non-zero ionisation in the

region of inner well into both ionic states was measured. With the help of energy-resolved photoelectron detection unambiguous identification of the ionisation pathways is achieved and the competing ionisation channels, such as higher lying ionic states, autoionising neutral excited states or close lying $C^1\Pi_u$ state, are ruled out.

The experiment demonstrates the utilization of wave packets as a local probe for the *R*-dependent ionisation probability and in particular the usefulness of energy-resolved photoelectron detection for identification the ionisation pathways.

Chapter 6

Conclusions

The aim of the present thesis is to study the dynamical and structural evolution in atoms and molecules with the pump-probe femtosecond method together with detection of the kinetic energies of photoelectrons.

In a pump-probe laser spectroscopy a first femtosecond laser pulse is applied to initiate a motion in a molecular system and a second time-delayed laser pulse to probe it. Ionisation together with detection of the kinetic energies of the photoelectrons is used. Resolving the kinetic energies of the photoelectrons enables a sub-Ångstrom spatial resolution. Experimentally the set-up combines laser pump-probe technique with atomic and molecular beam technique and electron time of flight measurements.

This method is used to study the dynamics in several systems: vibrational wave packet dynamics in Na_2 $C^1\Pi_u$ and $7^1\Pi_u$ states and electronic structure evolution in $2^1\Sigma_u^+$ state of Na_2 molecule.

The vibrational wave packet evolution in the $C^1\Pi_u$ state is observed in the experiment with λ = 340 nm pump and λ = 266 nm probe laser pulse. The oscillating signal at photoelectron energy of 0.7 and 1.2 eV has the period of 290 fs. The frequency of 114 cm^{-1}, derived using a Fourier analysis, corresponds to a vibrational separation between v' = 0 and v' = 1 levels of the $C^1\Pi_u$ state. A kinetic energy of the released photoelectrons, gives an access to the internuclear distance in the molecule. The difference potential analysis shows that the photoelectrons at 0.7 eV (1.2 eV) map the wave packet at the inner (outer) turning point by projecting into the $^2\Sigma_g^+$ bound ionic state. Thus the analysis of the time behaviour of the photoelectron signal at a certain kinetic energy provides an information about a phase of the wave packet motion, i.e. what particular place of the potential is sampled by the photoelectron signal.

In a pump-probe experiment with λ = 266 nm pump and λ = 340 nm probe laser pulse the vibrational wave packet in the $7^1\Pi_u$ state is studied. A Fourier analysis of the signal at 3.2 eV shows a peak at 97 cm^{-1} which corresponds to a vibrational level separation in the $7^1\Pi_u$ state.

A pump-probe femtosecond technique in combination with the kinetic energy resolved photoelectrons detection is applied to study the electronic dynamics evolution in molecule. The $2^1\Sigma_u^+$ double minimum state of Na_2 molecule serves as a model system for the experiment. The state arises from an avoided crossing of two potentials, therefore the inner well has a Rydberg orbital configuration, the outer well acquires a significant ionic character at large internuclear distance. The change of the chemical bond assumes the variation of the photoionisation dipole moment with internuclear distance.

In a two-color femtosecond pump–probe experiment the pump photon of 3.65 eV excites the the vibrational wave packet in the $2^1\Sigma_u^+$ double-minimum state. The wave packet serves as a local probe for the *R*-dependent ionisation probability. The bound $^2\Sigma_g^+$ and the repulsive $^2\Sigma_u^+$ ionic states are accessible with the probe photon energy of 4.68 eV. Energy-resolved photoelectrons are detected as a function of the pump-probe delay. The oscillating signal in the energy regions of 0.5 – 2.6 eV and 3.3 - 2.4 eV is detected. The oscillation period is found to be 1 ps in accordance of the vibrational level separation of 32 cm^{-1} at v' = 45. By comparing the cuts along the pump-probe axis a clear distinction between ionisation at the inner and outer well from the double minimum state and the corresponding photoelectrons from both the bound and repulsive ionic state is made. The quantum mechanical calculations assuming different *R*-dependencies of the ionisation dipole moment are performed in order to reproduce the experimental data. The variation of the ionisation dipole moment was found to be a constant for the inner well and a linear increasing function of the internuclear distance in the outer well for ionisation into both $^2\Sigma_g^+$ and $^2\Sigma_u^+$ ionic states. The way of the photoionisation dipole moment is confirmed by physical considerations of orbital correlations based on Koopman's theory. The competing processes, such as contributions from other high lying ionic states or doubly excited autoionising neutral states are ruled out as well as the signal from the energetically close lying $C^1\Pi_u$ state.

The experiment shows the utilization of wave packets as a local probe for an *R*-dependent ionisation probability and in particular the usefulness of energy-resolved photoelectron detection to unambiguously identify the ionisation pathways.

Overall the work demonstrates the potential of the ultrafast laser spectroscopy together with photoelectron detection to map both dynamical and electronic evolutions in the molecule for the particular case of the potential avoided crossing involving several states.

This technique therefore provides insight into chemical processes, where the non-adiabaticity plays a great role. With a current development of the ultrafast methods to study big molecules, as DNA or proteins, a photoelectron spectroscopy, as proved tool for effective mapping of the molecular dynamical and electronic evolution in the simple diatomic molecules, opens great perspectives to explore the dynamics in the complex systems.

At the same time the work shows the utility of the wave packet to study quantum mechanical properties of the molecules. The further development of method would allows a detailed investigation of such phenomena as wave function behaviour at the complicated potential surfaces and the tunnel effects in the region of potential barriers.

Appendix A

Magnetic bottle electron spectrometer: calibration and test experiments

The signal obtained at the output of the detector of electron spectrometer is in a time-of-flight form, i.e. the voltage signal from a detector is proportional to a quantity of electrons arriving the detector at a certain flight time *t*. The calibration of the time-of-flight axis into a kinetic electron energy axis is described here. Several calibration methods are suggested which are relevant to the type of substances investigated and to appropriate regions of kinetic energies. Also the kinetic energy resolution of spectrometer is studied. Finally, a number of tests are performed to investigate the influence of different experimental parameters on the performance of the spectrometer and on the kinetic energy resolution.

A.1 Time and energy resolution of magnetic bottle spectrometer

In the magnetic bottle the electrons start their motion in a strong magnetic field of $B_s = 1T$, are parallelized on a distance of few millimetres, and then drift in a weak uniform field of $B_w = 10^{-3}T$ towards a detector. The electrons initially emitted within the solid angle of π sterad end up their motion with angles in the range from 0° to $\Theta_{\max}$ [78,118]:

$$\Theta_{\max} = \arcsin\left(\frac{B_s}{B_w}\right)^{1/2} \approx 1{,}8°. \tag{A.1}$$

The time of flight for the first 30 mm strongly depends on the initial angle of electron motion Θ_i, but the time of flight in the drift tube T_{drift}

$$T_{drift} = \frac{l_{drift}}{v}\left(1 + \frac{B_s \sin^2 \Theta_i}{2B_w}\right) \tag{A.2}$$

is almost independent of Θ_i since the relation $B_s / B_w = 10^{-3}$. In order to calculate the signal broadening arising from parallelizing of electrons in non-uniform magnetic field, a simulation

for electron trajectories was performed by Kruit and Read [78]. For electrons with energies of 1 eV it gives the widths ΔT_c (FWHM) for three angular distributions:

$$\Delta T_c / T = \begin{array}{l} 0.17\ \% \text{ (for electron emission parallel to drift axis)} \\ 0.56\ \% \text{ (for isotropic electron distribution)} \\ 0.89\ \% \text{ (for electron emission perpendicular to drift axis).} \end{array} \quad \text{(A.3)}$$

The major contribution $\Delta T_c / T$ however comes from the region of the strong magnetic field and can be decreased if the length of strong-field region is decreased.

Since the flight time T is proportional to $E^{-1/2}$, where E is the electron energy, the energy resolution is related to the time resolution as

$$\frac{\Delta E}{E} = 2\frac{\Delta T}{T}. \quad \text{(A.4)}$$

Therefore one would expect the minimal theoretical resolution of the spectrometer $\Delta E_c / E$ to be 0.4 % according to (A.3) and (A.4). For the electrons with kinetic energies of 1 eV the minimal energy resolution ΔE_c is 4 meV. Thus, the spectrometer offers the possibility of extremely good photoelectron kinetic energy resolution.

A.2 Experimental energy resolution

In experimental time-of-flight spectra however the observed peak widths are much higher than the calculated ΔT_c. The main contributions to a signal line width ΔT measured in experiment, apart from the ΔT_c, are the following:

- **a.** Because of a finite time width of nanosecond laser pulse the time interval over which electrons are produced is several nanoseconds.
- **b.** The time width of a pulse coming from the MCP detector corresponding to a single electron is a few ns long.
- **c.** The time resolution of electronic measuring system is a limited value, typically 0.5 ns.
- **d.** High particle density in the interaction area (when the alkali metal beams are used) can lead to big space-charge effects. These effects are stronger for higher laser pulse intensities.

In the first mentioned case the width ΔT_c is proportional to $E^{-1/2}$, where E is the photoelectron energy. The effects a – c combine to give a constant which is independent on electron energy contribution of ΔT_l. The last effect gives a broadening ΔT_e which is approximately proportional to $E^{-3/2}$ (considering that the electric potentials cause energy changes that are small compared to photoelectron kinetic energy E). Combining ΔT_c, ΔT_e and ΔT_l in quadrature and assuming $T \sim const / E^{-1/2}$ one receives the relative broadening of a signal in a time-of-flight spectrum:

$$\frac{\Delta T}{T} \approx (c_1 + c_2 E + c_3 E^{-2})^{1/2}. \tag{A.5}$$

The energy width ΔE of the signal can now be derived from (A.4) and (A.5) as:

$$\frac{\Delta E}{E} \approx 2(c_1 E^2 + c_2 E^3 + c_3)^{1/2}. \tag{A.6}$$

According to formula (A.6) the minimum value of ΔE is conditioned by electrical noise broadening. Kruit [78] found the minimal kinetic energy resolution $\Delta E_{\min}$ to be approximately 15 meV (for electron energy 0.62 eV).

In fact, as can be seen from equation (A.6), the energy resolution is dependent on the energy of photoelectrons. A way of improving the resolution is to retard the electrons before they enter the flight tube by applying a negative voltage on a cylindrical grid. Thus, the electrons with high kinetic energies are brought to high-resolution part of spectrum. Therefore the energy resolution ΔE can be always made equal to $\Delta E_{\min}$ for a given energy interval.

A.3 TOF spectra calibration procedure

The experimental results obtained in a measurement represent time-of-flight spectra. In these spectra a voltage signal is recorded for every flight time, the intensity of the signal is proportional to the number of particles, which reach detector at this time. The time-of-flight signal is then converted into electron kinetic energy spectrum. This is done using the procedure described below.

In ideal case the kinetic energies of electrons E_k for the field-free case can be calculated from their flight times in a spectrometer using a formula:

$$E_k = 1/2 m_e \frac{L^2}{T^2}, \tag{A.7}$$

where m_e is the mass of the electron, L the drift length and T the time of flight.

However, in practice the exact drift length cannot be defined precisely because of displacements of the laser focus. This can cause deviations in the drift length of up to ±1 mm. Another uncertainty is introduced by the time T_d between the arrival of the laser pulse at the interaction region and the trigger signal derived from a photodiode. Also, a retardation voltage applied to the flight tube changes the kinetic energies of the photoelectrons. Contact potentials in an apparatus can cause deviations of the time of flights as well.

Taking into account the abovementioned, the electron energies are expected to follow the equation:

$$E_k = \left(\frac{m_e}{2e}\right)\left(\frac{L}{T + T_d}\right)^2 + U_g + U_c, \tag{A.8}$$

where T_d is the trigger delay, U_g the retardation voltage applied to the grid in the flight tube and U_c the measure for possible noise voltages.

In practice deviation from the formula (A.8) can be as large as 0.1 eV. Therefore the following phenomenological expression is used to approximate the previous equation:

$$E_k = \sum_{i=0}^{p} \frac{a_i}{T^i} + U_g \sum_{i=0}^{q} b_i T^i \,, \tag{A.9}$$

which corresponds to

$$E_k = \gamma(T) + U_g \delta(T)\,, \tag{A.10}$$

where $\gamma(T) = \sum_{i=0}^{p} \frac{a_i}{T^i}$ and $\delta(T) = \sum_{i=0}^{q} b_i T^i$.

The first term in equation (A.8) has been replaced by a power series in $1/T$ with coefficients a_i. The possible kinetic energy dependence on U_g and U_c has been taken into account by a power series in T with coefficients b_i.

The calibration procedure is performed as follows. The flight times T associated with at least two electron peaks of a calibration gas whose energies are known from the literature, E_1 and E_2, are measured as a function of the retarding voltages U_1 and U_2. The position of every peak is defined using Gaussian fit of the peak. These two data lists enable the determination of the coefficients a_i and b_i in the following way. Using the abbreviated notation

$$E_1 = \gamma(T) + U_1 \delta(T) \qquad E_2 = \gamma(T) + U_2 \delta(T)\,, \tag{A.11}$$

the expressions for γ and δ are obtained:

$$\gamma(T) = \frac{U_1 E_2 - U_2 E_1}{U_1 - U_2} \quad \delta(T) = \frac{E_1 - E_2}{U_1 - U_2}\,. \tag{A.12}$$

A least-squares fitting procedure for $\gamma(T)$ and $\delta(T)$ is used to calculate the coefficients a_i and b_i. With known coefficients the conversion from the time-of-flight scale into the energy scale according to equation (A.9) is performed. With this equation and the two data lists, E_1 and E_2 can be recalculated in order to determine how well these values are reproduced. The order of both power series (p and q in equation (A.9) can be adjusted to reach a minimal deviation (about 2 meV) from the literature theoretical numbers of energies [119]. We obtain a sufficient good calibration with $p, q = 2$. The least-squares fitting procedure is described in details in [70].

In order to obtain the correct energy spectrum the scale transformation alone is not sufficient, since the energy is a non-linear function of flight time. This means that the signal intensity in the time-of-flight spectrum is not equal to that one in energy spectrum. When performing a time-to-energy transformation of the signal intensity $S(T)$ into an energy-dependent $S'(E)$, the integrated signal is constant:

$$S(T)dT = S'(E)dE\,. \tag{A.13}$$

Therefore the signal intensity in energy spectrum is obtained using the equation:

$$S'(E) = S(T)\left(\frac{dE}{dT}\right)^{-1}\,. \tag{A.14}$$

In practice this means that energy signal intensity from long flight times region becomes much higher in opposite to short times region, as illustrated on a Figure A.1, where a photoelectron kinetic energy spectrum is created from the time-of-flight signal using equations (A.9) and (A.14).

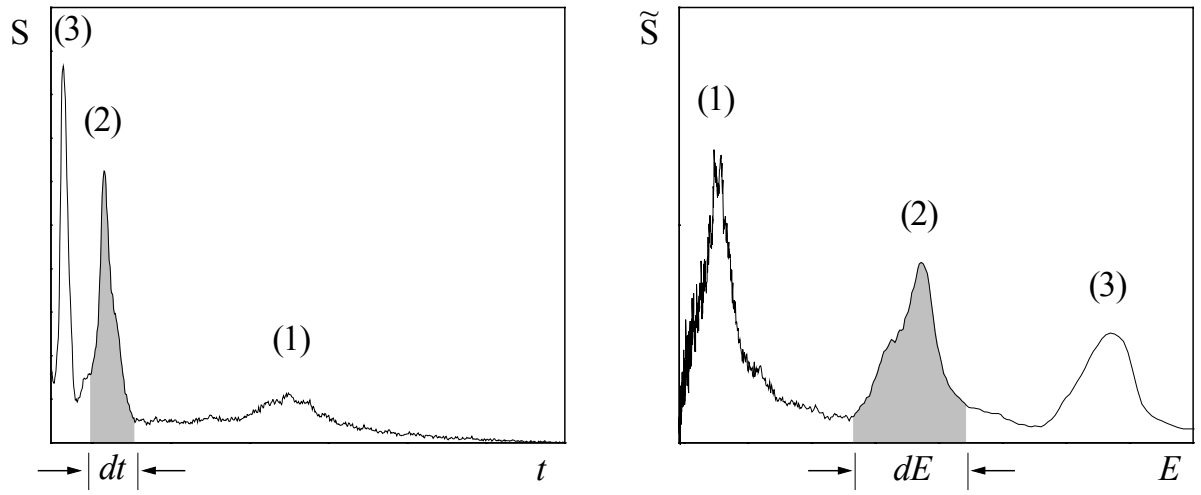

Figure A.1: Time-to-energy transformation of the signal. The energy is a non-linear function of flight time. In order to keep the integrated signal constant upon the transformation the signal height is also recalculated.

The least-square procedure and TOF-to-energy conversion of photoelectron spectra is performed using LabView (version 6.1) software package.

For accomplishing the calibration of the spectrometer, a MPI or REMPI of atoms with laser pulses is used. It can also be appropriate for the determination of the resolution of the spectrometer. The choice of the atomic species for calibration is governed by energy window of the substance to be measured in experiment. In the calibration procedure at least two different known from literature kinetic electron energies are used, which should preferably locate in the energy area, in which the experimental photoelectron signal is expected. The required retardation voltage is increased stepwise, and for each retardation voltage a photoelectron spectrum is recorded. We have found that the calibration procedure is necessary before and after every measurement experiment, since in the experiments with alkali metals space-charge effects and contact potentials on pole-plates change the calibration parameters during the course of the experiment. The photoelectron spectra in this work have been calibrated using known photoelectron signals from multiphoton ionisation of xenon, sodium and potassium atoms.

A.4 Calibration using ionisation of Xe atoms with Nd:YAG laser

A multiphoton non-resonant ionisation of Xe with nanosecond laser pulses of wavelengths λ = 355 nm and 532 nm is used for calibration of magnetic bottle spectrometer in the range of energies between 0.5 and 1.8 eV.

Xe atoms have two ionisation potentials, corresponding to $^2P_{3/2}$ and $^2P_{1/2}$ cores. The ionisation energies are 12.130 eV for $^2P_{3/2}$ and 13.426 eV for $^2P_{1/2}$ potentials. Ionisation of the two Xe cores with 4 photons of λ = 355 nm provides two lines in photoelectron spectra at 1.84 eV and 0.54 eV which are taken for the calibration. The kinetic energies of the photoelectrons obtained from the ionisation with 355 nm and 535 nm wavelengths are summarised in the Table A.1.

Atomic core of ^{54}Xe	Ionisation energy	Ionisation with 355 nm, E_{kin}	Photons	Ionisation with 532 nm, E_{kin}	Photons
$^2P_{3/2}$ orbital	12.130 eV	1.84 eV	4	1.85 eV	6
$^2P_{1/2}$ orbital	13.426 eV	0.54 eV	4	0.56 eV	6

Table A.1: Ionisation energies of Xe atoms and kinetic energies of the photoelectrons from the ionisation with 532 nm second harmonic of Nd:YAG laser and 355 nm third harmonic.

The nanosecond Nd:YAG laser is described in the Chapter 3 of the present work. The Nd:YAG laser provides 10 ns pulses. The 355 nm and 532 nm light pulses have linear polarisation parallel and perpendicular to the axis of the electron spectrometer, respectively. The laser beam is focused into the interaction region between the pole-plates with a 250 mm lens. The lens is installed on a table with micrometer screws for precise adjustment in x, y and z directions. The energy of the laser pulse is 0.50 μJ for 355 nm and 2.0 μJ for 535 nm. Xe gas is supplied to the focal region between the pole-plates using a gas pipe. The Xe pressure during calibration measured in the main chamber is ~$1\text{-}5\cdot10^{-5}$ mbar. At these experimental conditions the signal at 1.8 eV Xe time-of-flight peak is approximately 50 mV. The signal from the electron detector is recorded using a LeCroy oscilloscope and is averaged over 1024 laser shots. The oscilloscope is triggered by a photodiode illuminated with a portion of the reflected laser light. Electrons are accelerated using a voltage range of typically U_g = 0 – 2 V in 0.2 V steps applied to the grid in the flight tube. Data from the oscilloscope are read into a computer and represent a set of time-of-flight versus signal intensity spectra for every voltage U_g.

Figure A.2 shows a typical time-of-flight acceleration series obtained from the ionisation of Xe atoms with 355 nm nanosecond laser pulses with the voltage U_g = 0 - 2 V applied in 0.2 V steps.

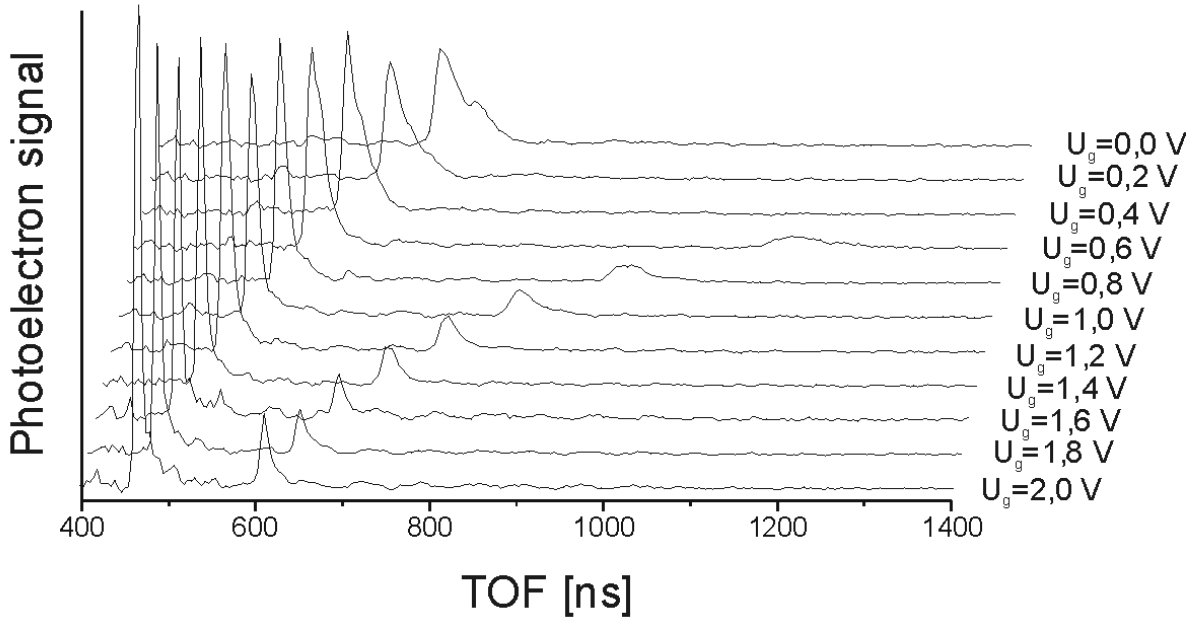

Figure A.2: Retardation series for photoelectron time-of-flight spectra from the ionisation of atomic Xe with λ = 355 nm of the Nd:YAG laser. The applied grid acceleration voltage is U_g = 0 – 2 V.

The calibration procedure as described in section A.4 is performed using the two known kinetic energy values E_1 = 1.84 eV and E_2 = 0.54 eV (see Table A.1) and corresponding time of flights T at each grid voltage U_g. The calibration curve representing time-of-flight versus kinetic energies for grid voltage U_g = 0.4 V is given in Figure A.3. The derived calibration parameters a_i, b_i calculated using least-square fit procedure are also shown on the picture. The typical inaccuracy, i.e. the deviation of the calculated kinetic energy from the theoretical value, in the interval of energies 0.5 – 2 eV is approximately 5 meV.

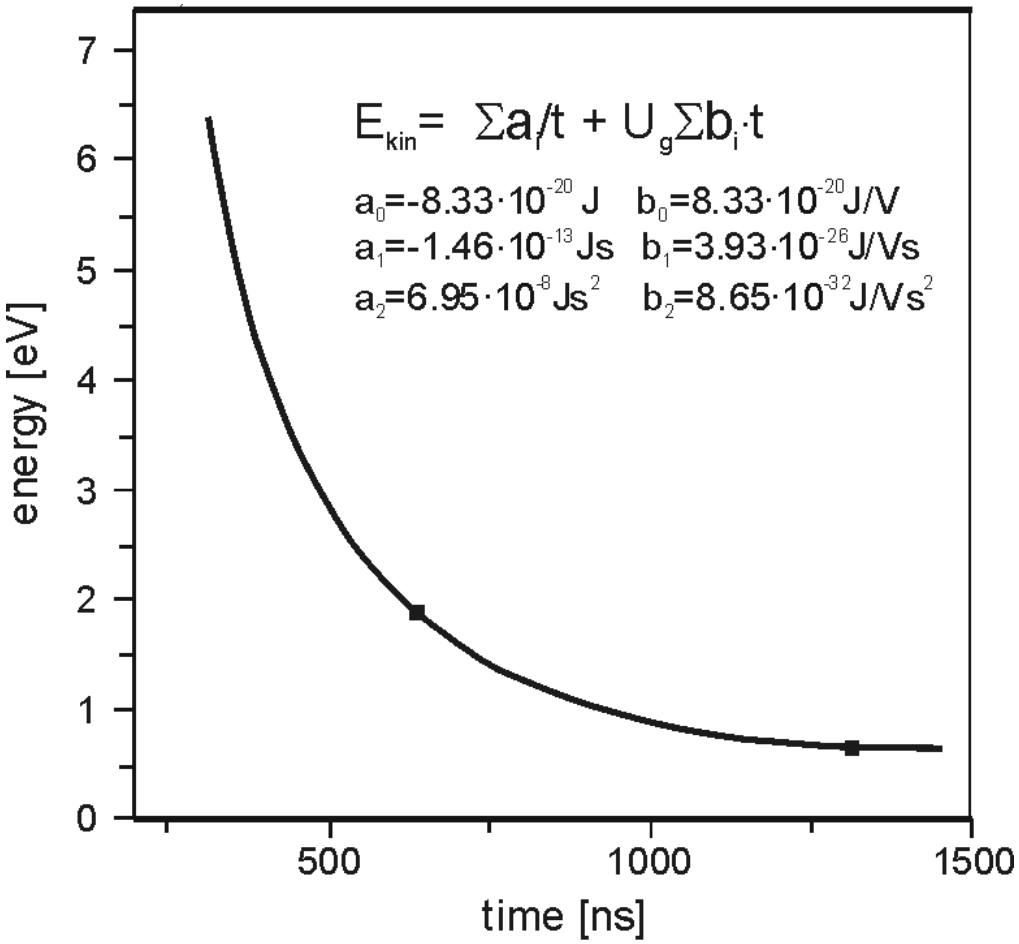

Figure A.3: Typical calibration curve obtained for the retardation voltage U_g = 0.4 V. Also shown are the calibration parameters a_i, b_i defined through the least-square fit procedure.

Given the calibration parameters a_i and b_i, the kinetic energy calculation of the spectrum can be performed for every retardation voltage with equations (A.9) and (A.14). Using the calibration we obtain the photoelectron energy spectrum of Xe shown on Figure A.4.

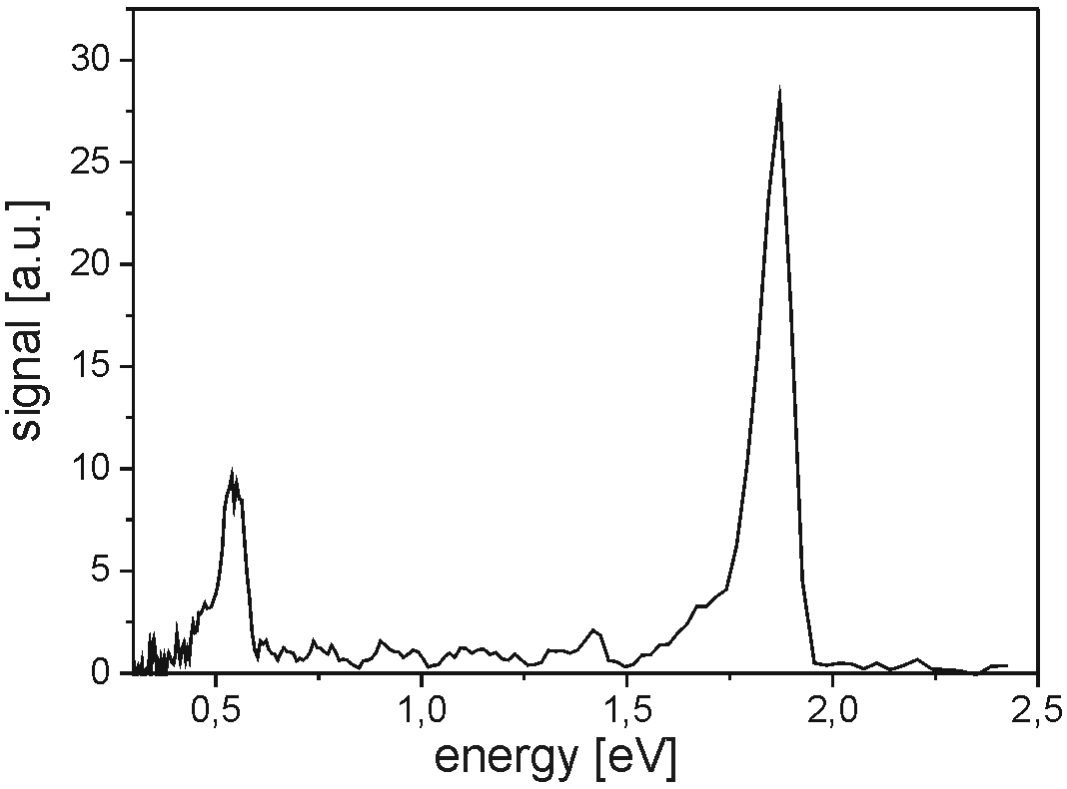

Figure A.4: Photoelectron kinetic energy spectrum of atomic Xe constructed from the TOF spectrum for U_g = 0.4 V at Figure A.2 using the calibration parameters at Figure A.3 and the signal transformation (A.14). Dotted lines show Gaussian fit of the peaks. The FWHM of the 0.54 eV and 1.8 eV peaks, determined as widths of the Gaussian fitting curves at half maximum, are 45 meV and 70 meV respectively.

From these experimental data one can determine also the energy resolution of the spectrometer. As is seen in the Figure A.4, the full width half maximum (FWHM) of the 0.54 eV peak is 45 meV whereas the FWHM of the 1.86 peak is already 70 meV for acceleration voltage U_g = 0.4 V. By applying the retardation voltage, the kinetic energy of the electrons can be reduced in the beginning of the drift tube, thus the effective electron energy can be varied. In this way the electron spectrometer resolution can be defined for different effective photoelectron energies. Figure A.5 shows the FWHM of the 1.8 eV Xe peak for retardation voltages U_g = -1.6 – 0.2 V corresponding to an effective photoelectron energies E_{eff} = 0.2 – 2.0 eV. One can see that, independent of their initial kinetic energies, the electrons can be retarded to the energy of about 0.8 eV to achieve the minimal peak width.

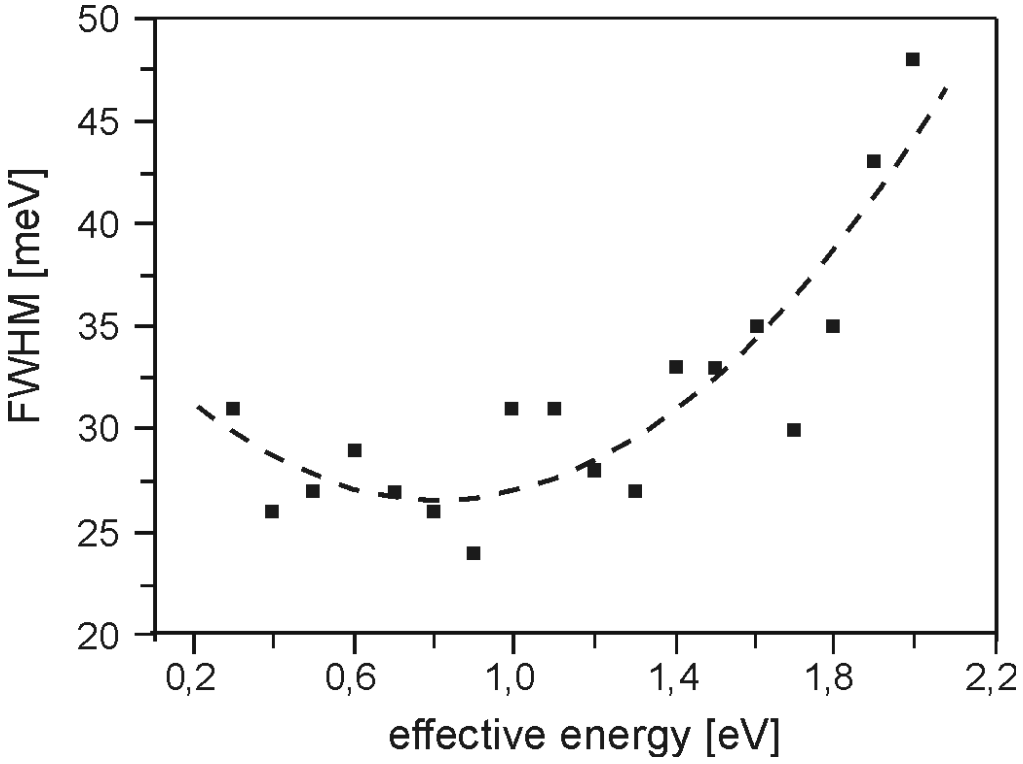

Figure A.5: The FWHM of the 1.8 eV Xe peak taken at different retardation voltages U_g = -1.6 – 0.2 V which corresponds to an effective electron energy E_{eff} = 0.2 – 2 V. Note the improvement of the energy resolution at E_{eff} = 0.8 eV. FWHM(E_{eff}) = 25 meV. The dashed line shows the polynomial fit curve.

The maximal resolution of the spectrometer obtained in experiment at this photoelectron energy is $\Delta E_{\min} \approx 25$ meV. The value is however not the optimal for this type of spectrometer. As was reported by Peter Kruit [120], the optimal resolution of $\Delta E_{\min} = 15$ meV is reached in an experiment with resonant multiphoton ionisation of Xe with $\lambda = 440$ nm. By variation of the wavelength of the laser pulse, ΔE is increasing to $\Delta E = 40$ meV for 355 nm, what agrees very good with our experimental data. The explanation suggested in [120] includes a field gradient, or ponderomotive force, which causes a wavelength dependent line broadening effect, which is stronger for light with longer wavelength.

A.5 Calibration using ionisation of K atoms with dye laser

In order to access small electron kinetic energies up to 0.10 eV as well, we performed the energy calibration using multiphoton non-resonant ionisation of K atom with a dye laser working on Fluorescein 27 pumped by a nanosecond YAG laser of $\lambda = 532$ nm wavelength.

The wavelength range of the dye laser pulses in the configuration described in Chapter 3, Section 3.7 is 545 – 565 nm and is changed in 5 nm steps. The ionisation energies of Xe and K atoms and the photoelectron kinetic energies for every wavelength of a dye and Nd:YAG lasers are given in the Table A.2. Hence we expect 6 calibration points from ionisation of potassium to cover the photoelectron kinetic energy range of 0.05 – 0.35 eV.

Atom	Ionisation energy [121]	Photoelectron kinetic energy, E_{kin}					
		YAG	Dye laser				
		532 nm	545 nm	550 nm	555 nm	560 nm	565 nm
K	3.341 eV	0.32	0.21 eV	0.17 eV	0.13 eV	0.09 eV	0.05 eV

Table A.2: Ionisation energies for K atoms and kinetic energies of photoelectrons for the ionisation with the second harmonic 532 nm of a YAG laser and dye laser (Fluorescein 27 dye).

The dye laser provides pulses in the wavelength range of 540-575 nm with a maximum efficiency at 548 nm. The electrons are produced in a time interval 6 – 8 ns at a repetition rate of 20 Hz. The typical laser pulse energy in experiment measured in front of MaBoS is 1.50 – 1.70 mJ. The light has linear polarisation perpendicular to the axis of the electron spectrometer. To trace the higher energy region also the photoelectron signals from the ionisation of Xe and K atoms with Nd:YAG laser of λ = 532 nm were recorded. The set-up enables fast switching between two lasers. During the calibration two parameters were scanned: (1) the wavelength of dye laser pulses in the range of λ = 545 – 565 nm with 5 nm steps, and (2) the retardation voltage for every wavelength in range of U_g = 0.9 – 1.5 V with 0.2 V steps. The wavelength variation provides the different energies of released photoelectrons in the range of 0.05 – 0.2 eV. The time-of-flight spectra taken at every wavelength and retardation voltage were averaged over several thousand points and then saved into a computer.

Figure A.6 shows the time-of-flight calibration series for ionisation of K atoms with dye laser with wavelength λ = 545 - 565 nm for different U_g. The calibration into a kinetic energy scale is performed using the procedure described in Section A.1.

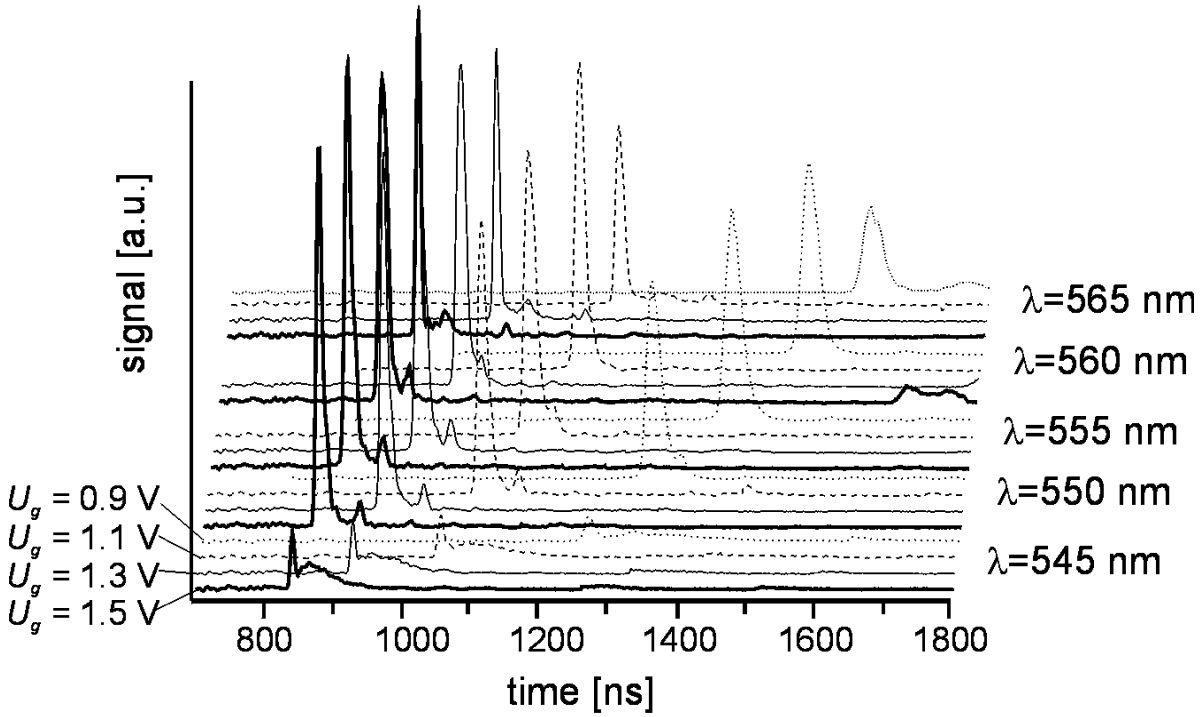

Figure A.6: Retardation series for photoelectrons from the ionisation of atomic K atom with a dye laser. For every dye laser wavelength in the range of λ = 545, 550, 555 and 565 nm a retardation series for grid voltages U_g = 0.9 – 1.5 V is recorded. Spectra are recorded at different wavelengths of the dye laser λ = 545 – 565 nm and different grid voltages U_g = 0.9 – 1.5 V. Bold lines show the spectra for U_g = 1.5 V for every laser wavelength, thin lines – for U_g = 1.3 V, dashed lines – for U_g = 1.1 V and dotted lines – for U_g = 0.9 V.

Figure A.7 shows the calculated photoelectron kinetic energy spectra using formulae (A.9) and (A.14) and the constants a_i, b_i generated in least-squares fit. We found however that the low kinetic energy region is very sensitive with regard to peak positions, so separate calibration procedure should be done for the range of the energies from 0.1 to 0.3 eV. In addition in the area of very small energies (lower 0.1 eV) the inaccuracy in energy is already 0.02 eV which is equal to $dE/E \cong$ 40 % (see Figure A.7), which makes the calibration unacceptable in this region. In the area of 0.1 – 0.3 eV the inaccuracy is of the order of $dE_k/E \approx$ 5 %. Taking into account all abovementioned, the points taken for calibration are: signals from λ = 545, 550, 555 and 565 nm of dye laser and signal from ionisation of K with 532 nm YAG laser.

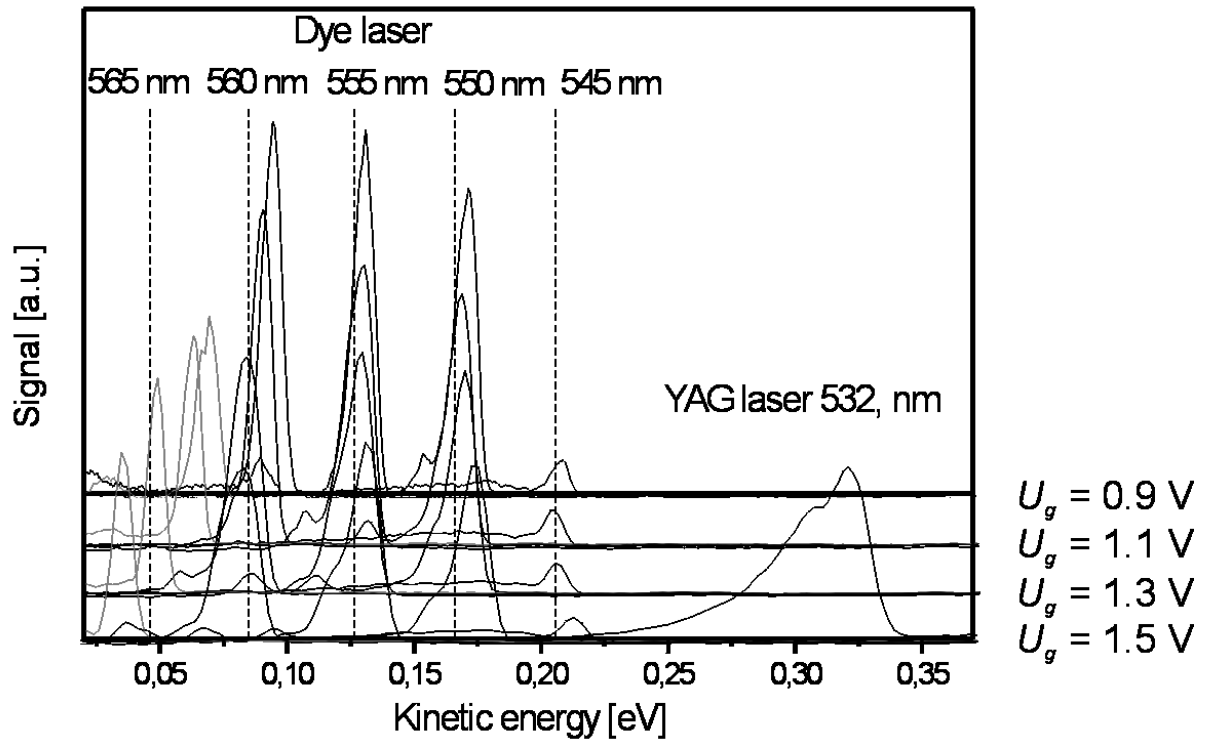

Figure A.7: Calculated photoelectron energy spectra of atomic potassium for different retardation voltages U_g and dye laser wavelengths. The vertical lines show the literature photoelectron energies from the Table A.2 for every dye laser wavelength. There are 4 electron energy spectra corresponding to every wavelength recorded at different grid voltages U_g. Note the increasing calibration inaccuracy for spectra corresponding to λ = 565 nm (spectra are shown in grey color). Also shown is the energy spectrum of atomic K from ionisation with a wavelength of the λ = 532 of Nd:YAG laser for U_g = 1.5 eV.

A.6 Online calibration using Na signal

In experiment with the Na_2 $2^1\Sigma_u^+$ double minimum state the expected photoelectron signal lays in a wide range of kinetic energies from 0.5 to 3.5 eV. The calibration with YAG laser alone is not sufficient because of the following reasons. First, the energy range in the experiment is much bigger than the one in the calibration utilising a Xe or Na atoms ionisation with the Nd:YAG and the dye lasers, and the extrapolation of the calibration curve towards higher kinetic energies gives generally fault values of energies. Second, the times between the arrival of the laser pulse in the interaction region and the trigger signal are often somewhat different for YAG laser and femtosecond laser. The energy shifts due to ponderomotive force play a minor role at the energies used in the experiment, so they are omitted in calculations. Therefore we performed an "online" calibration procedure which takes into account all the abovementioned. The calibration includes signals already present in the measured spectra coming from the multiphoton ionisation of Na atoms with femtosecond laser of the wavelengths involved in the experiment: 267 nm, 340 nm and two-color signal from 267 + 340 nm.

The experimental set-up for the Na_2 $2^1\Sigma_u^+$ double minimum experiment is described in detail in Chapter 3. Briefly, the femtosecond laser probe pulses with λ = 267 nm are obtained by frequency tripling of the 1/3 of 785 nm and 800 μJ output of CPA Ti:Sapphire laser system. The energy of the pulses is 0.4 μJ and FWHM is 3.0 nm. Parametric amplification of the residual light of the amplifier and frequency quadrupling provides the 340 nm, 4.7 nm the

FWHM and 0.6 μJ pump pulses. The repetition rate of laser pulses is 1 kHz. Both laser beams are linearly polarised with polarisation axis parallel to the spectrometer axis. The signal is triggered with the signal coming from the Pockels cell. Na was heated to 870 K in an oven and expanded through a 100 μm nozzle seeded with Ar. The Ar partial pressure in a beam was 1.6 bar. Every TOF photoelectron spectrum was averaged over several thousand laser shots.

A resonant multiphoton ionisation of Na atoms with λ = 340 nm and λ = 267 nm wavelengths of femtosecond laser. Figure A.4 shows the Na energy levels involved in the transitions as well as laser wavelengths.

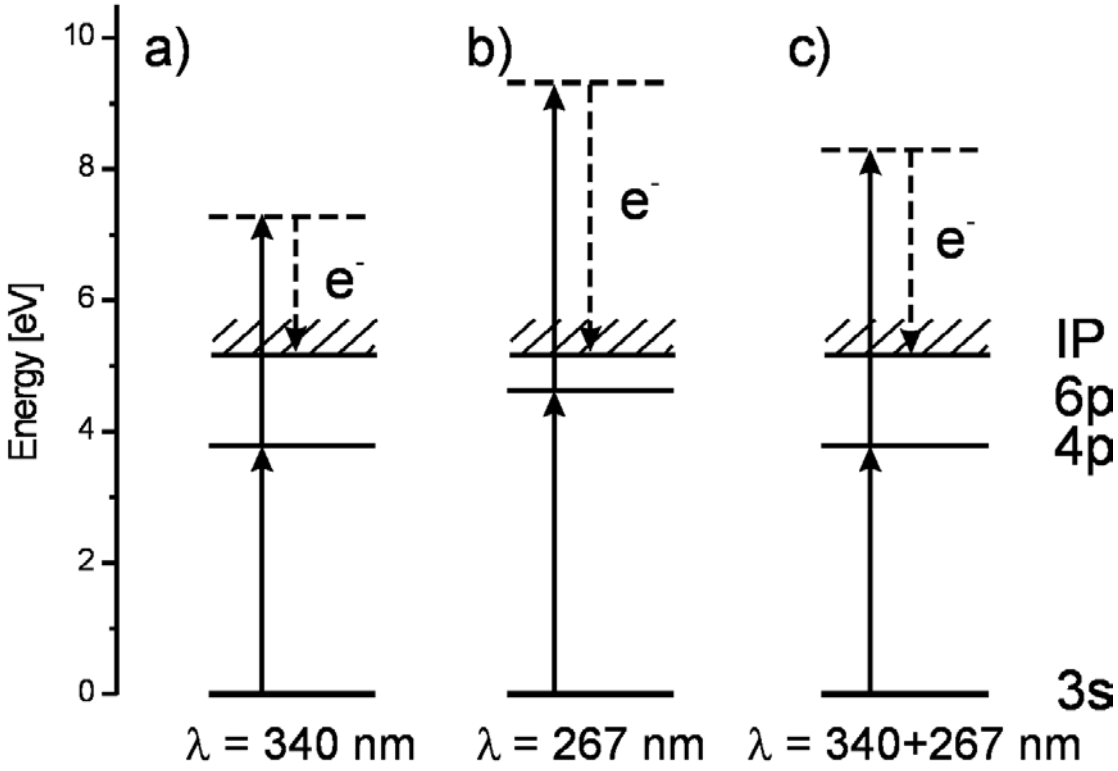

Figure A.4: Scheme of REMPI of Na atom for 267 nm, 340 nm and 267+340 nm wavelengths. a) Two-photon ionisation with λ = 340 nm using 3s – 4p transition of Na atom; b) two-photon ionisation with λ = 267 nm using 3s – 6p transition; c) two-color ionisation scheme with λ = 340 nm excitation (3s – 4p transition) and λ = 267 nm ionisation.

Table A.4 shows the ionisation energy of Na atom and kinetic energies of electrons released from ionisation with two photons of λ = 267 nm, two photons of λ = 340 nm and 267 + 340 nm. The calibration in the high energy range of 1.9 – 4.7 eV in addition to YAG calibration with Xe in the low energy range of 0.5 – 1.9 eV to be sufficient covers the whole energy area of interest.

Atom	Ionisation energy	340 nm, E_{kin}	267 nm, E_{kin}	267+340 nm, E_{kin}
Na I	5.139 eV	2.15 eV	4.21 eV	3.19 eV

Table A.4: Ionisation level of Na atom and kinetic energies of photoelectrons from ionisation with 267 nm, 340 nm and 267 + 340 nm wavelengths.

As opposed to the nanosecond case the photoelectron spectra obtained from ionisation with femtosecond laser pulses have much lower energy resolution. The spectral width of the laser pulse is much higher compared to the nanosecond pulse, thus the width of the lines in the photoelectron spectrum is determined here by the width of laser pulse. Evaluation of the spectrometer resolution in higher kinetic energy area is performed by extrapolation of data obtained in nanosecond calibration.

Time-of-flight femtosecond spectra were taken at one grid voltage used in the experiment (U_g = 1 V). Figure A.8 shows the typical photoelectron time-of-flight spectrum from ionisation of Na with femtosecond laser pulses with λ_{pump} = 340 nm and λ_{probe} = 267 nm. The spectrum is averaged over the pump-probe delay region of 0 till 30 ps.

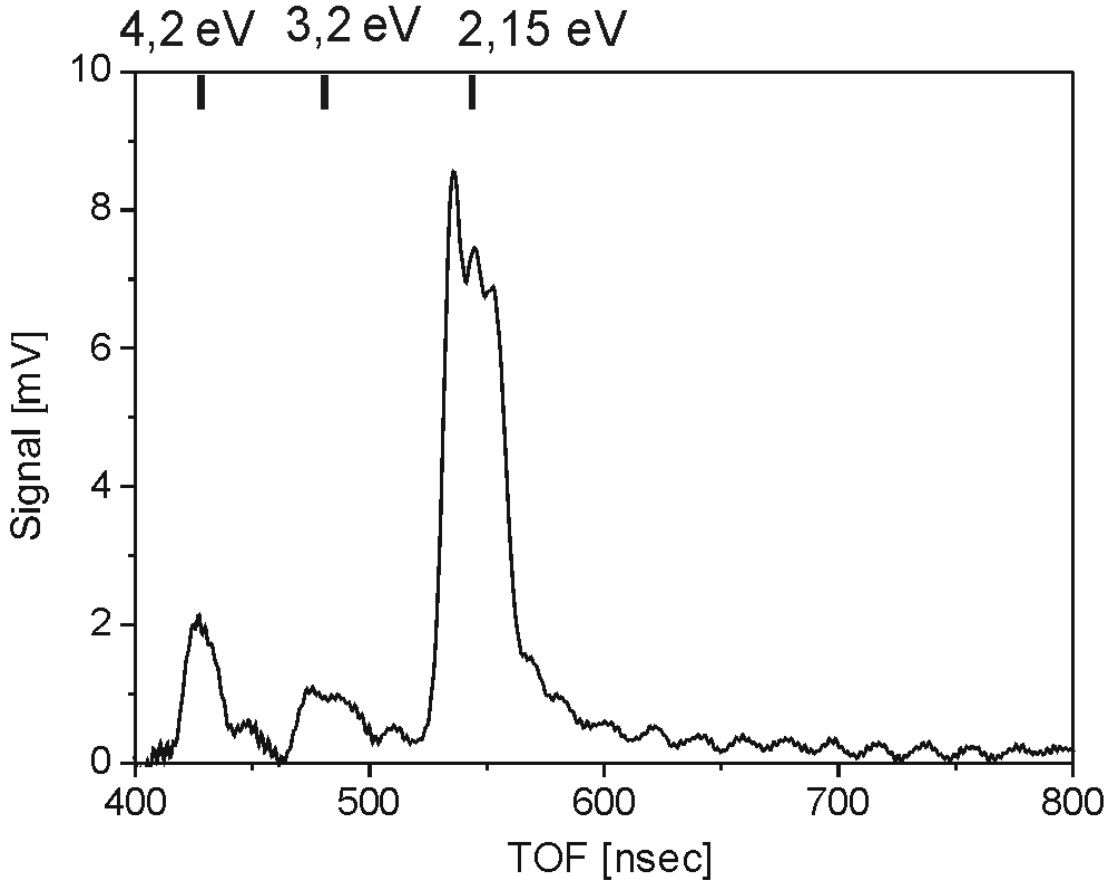

Figure A.8: Photoelectron time-of-flight spectrum from the ionisation of atomic Na with wavelengths λ = 267 and 340 nm of the femtosecond laser. The spectrum is taken at one retardation voltage U_g = 1 V and is averaged over the pump-probe delay region from 0 till 30 ps. Also shown are the corresponding literature kinetic energies of photoelectrons from the Table A.4.

The calibration proceeds normally as follows. The flight times obtained from ionisation of Xe atoms with the Nd:YAG laser at several retardation voltages U_g are added to the 3 points obtained from ionisation of Na atoms with the femtosecond laser at one retardation voltage. These times are inserted into equations (A.11), a least-square-fit procedure generates coefficients a_i, b_i. (Figure A.9 shows the calibration curve obtained from a combination of Xe and Na spectra at a retardation voltage of U_g = 1 V). The energy spectrum of Na obtained with formulae (A.9) and (A.13) is shown on Figure A.9.

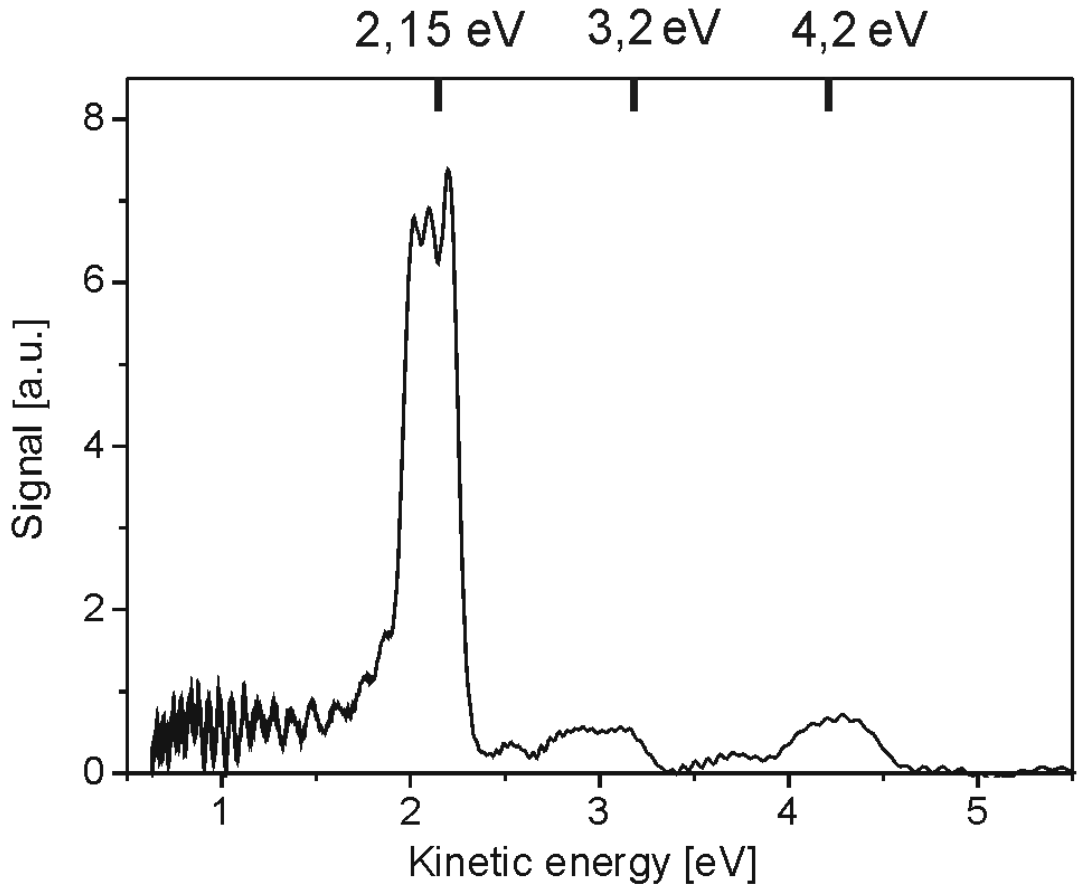

Figure A.9: Photoelectron energy spectrum of atomic Na constructed from the TOF spectrum of Figure A.8 using the calibration procedure.

Since the TOF spectra in experiment were taken at only one U_g the spectrometer resolution here is not constant along the energy scale. The energy resolution for 0.5 eV electrons derived from the nanosecond data consists 40 meV, whereas the resolution at high kinetic energy 4 eV derived by extrapolation of nanosecond data is approximately 200 meV.

A.7 Calibration using Xe ATI photoelectrons

This calibration method is normally used when the energy of the laser pulse used in the experiment is considerably high, so that the ponderomotive forces cannot be neglected. The ponderomotive force leads to broadening and overall shift of the photoelectron energy spectrum, the value of the shift depends on the laser energy in the focus. Thus the exact kinetic electron energies are not known. The calibration now uses Xe ATI peaks appearing in the signal with higher laser energy. In this case not the absolute kinetic energies in photoelectron signal, but the energy separation between them are known. The calibration spectra are taken using different retardation voltage. The spectra should contain at least two ATI signals to obtain the calibration curve. In addition, at a certain U_g an intensity series is taken, in which the intensity of the laser pulse is varied in steps. This enables to obtain the absolute energy offset. The calibration is reasonable when high energy laser pulses are involved in experiment. The procedure is described in details in [70].

A.8 Test experiments with magnetic bottle spectrometer

A series of tests was accomplished to trace the influence of different experimental parameters on the photoelectron signal and on the kinetic energy resolution of the spectrometer. The main parameters varied are the intensity and the polarisation of the nanosecond YAG laser, the magnetic fields of the coils giving the weak 10^{-3} Tesla and strong 1 Tesla fields, the Xe pressure measured in the main chamber, the magnetic fields produced by Helmholtz coils to compensate the Earth field and the voltage at the pole-plates.

A.8.1. Laser intensity

After ionisation with the laser pulse the formed photoelectrons leave the interaction region very fast due to their small masses in comparison to more heavy ions. The ions staying in the ionisation region form a positive charged cloud. This cloud inhibits the photoelectrons formed lately. This space-charge effect leads to broadening the photoelectron signal and its shifting to bigger flight times. This corresponds to an effective decreasing of photoelectron kinetic energies.

The effect and its influence on the resolution of photoelectron spectrometer can be observed in the laser intensity measurements. Figure A.10 shows the photoelectron time-of-flight spectra from ionisation of Xe with nanosecond laser pulses of λ = 355 nm and different intensities from 0.5 mJ to 5.5 mJ measured in front of the MaBoS. One can see that with growing laser intensity the peaks broaden and the signal shifts towards bigger flight times.

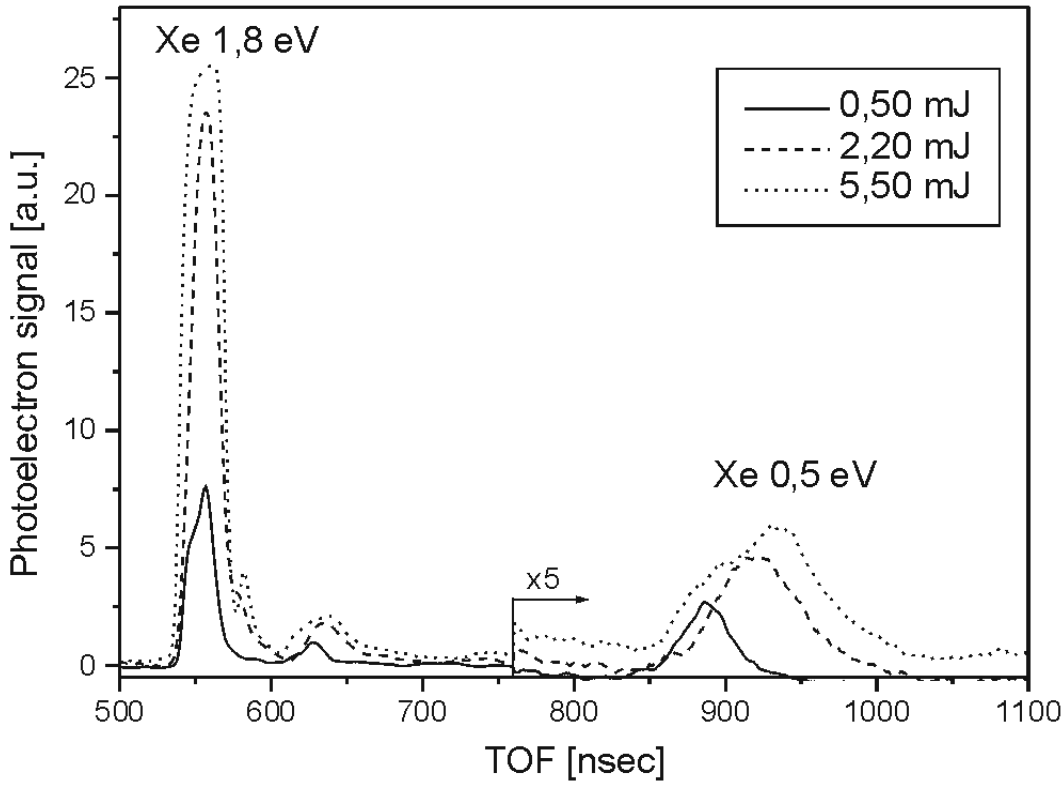

Figure A.10: Photoelectron time-of-flight spectra of Xe recorded at different intensities of λ = 355 nm of YAG laser. With increasing laser intensity the peaks are broadened and shifter towards bigger flight times, the corresponding energies of photoelectrons are decreased. The solid line shows spectrum at routine laser intensity used in experiments of 0.5 mJ. The peak at 630 ns arises from the ionisation of water.

A.8.2 Nd:YAG laser polarisation

Figure A.11 shows the photoelectron kinetic energy spectra of Xe for two polarisations of the nanosecond Nd:YAG laser. The polarisation at the first picture is perpendicular to the axis of the spectrometer, and at the second picture is parallel. The grid and pole-plate voltages are

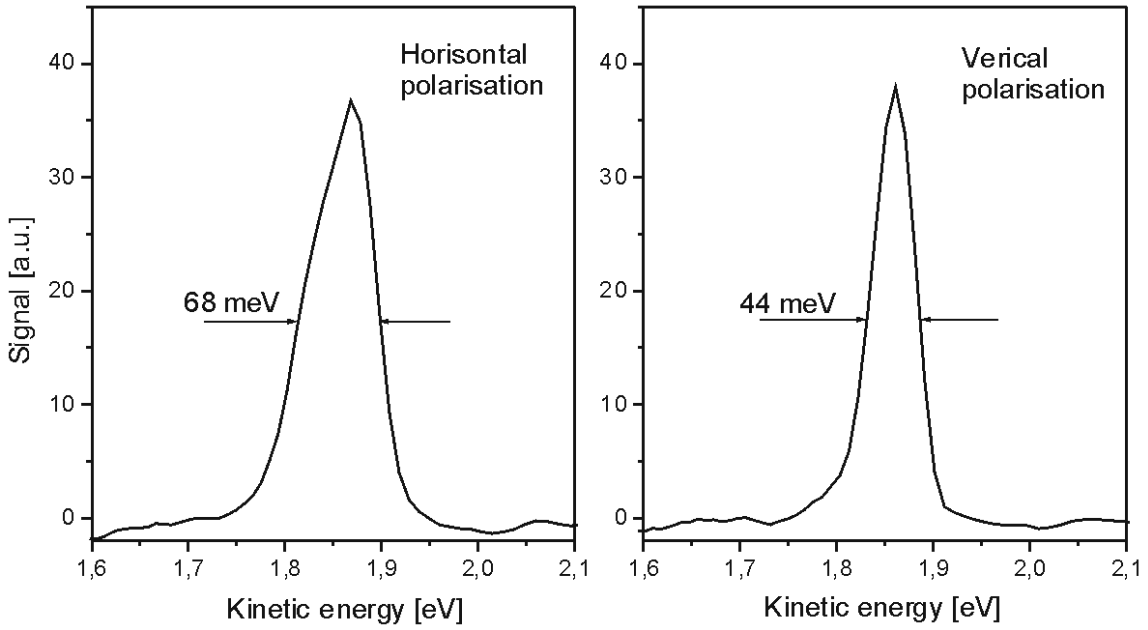

Figure A.11: Photoelectron energy spectra of 1.8 eV Xe peak taken at different polarisations of YAG laser. Left: polarisation is perpendicular to the spectrometer axis; right: parallel to the spectrometer axis.

U_g = 0.4 V and U_{pp} = -0.5 V accordingly. The FWHM of the 1.8 Xe peak for polarisation parallel to the spectrometer axis (corresponds to vertical polarisation of the laser) is almost two times smaller than that for perpendicular. The intensity of the signal remains unchanged.

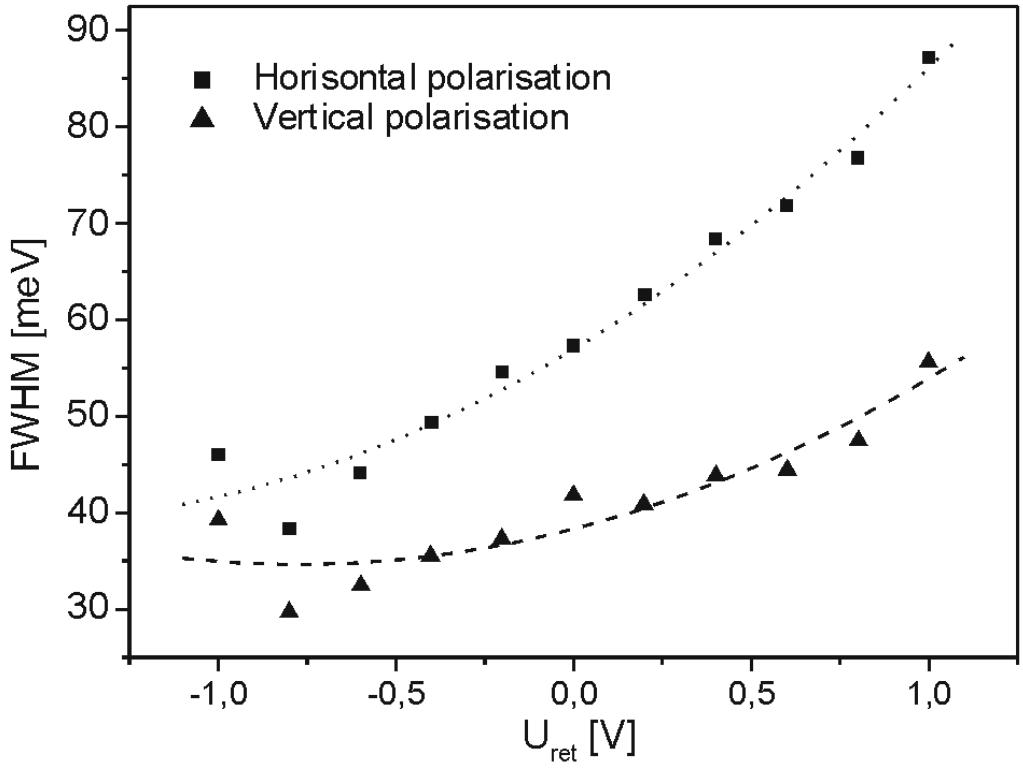

Figure A.12: Dependence of the FWHM of Xe 1.8 eV peak on grid voltage for polarisations of the YAG laser perpendicular (squares) and parallel to the spectrometer axis (triangles).

Figure A.12 shows the dependence of the FWHM of the 1.8 eV Xe peak on the retardation voltage for both polarisations. The resolution for vertical polarisation remains higher at all voltages, however the difference in resolutions tends to decrease at higher retardation voltages.

A.8.3 Xe pressure

Figure A.13 shows the influence of the Xe pressure on the photoelectron kinetic energy resolution. The photoelectron spectra were recorded from ionisation of Xe atoms with nanosecond laser of 355 nm wavelength. The pole-plate voltage is U_{pp} = -0.65 V and the grid voltage is U_g = 0.4 V. The spectra were taken at two Xe pressure measured in the main vacuum chamber: at $p_0 = 3.2 \cdot 10^{-7}$ mbar and $p_1 = 6.5 \cdot 10^{-7}$ mbar = $2 \cdot p_0$.

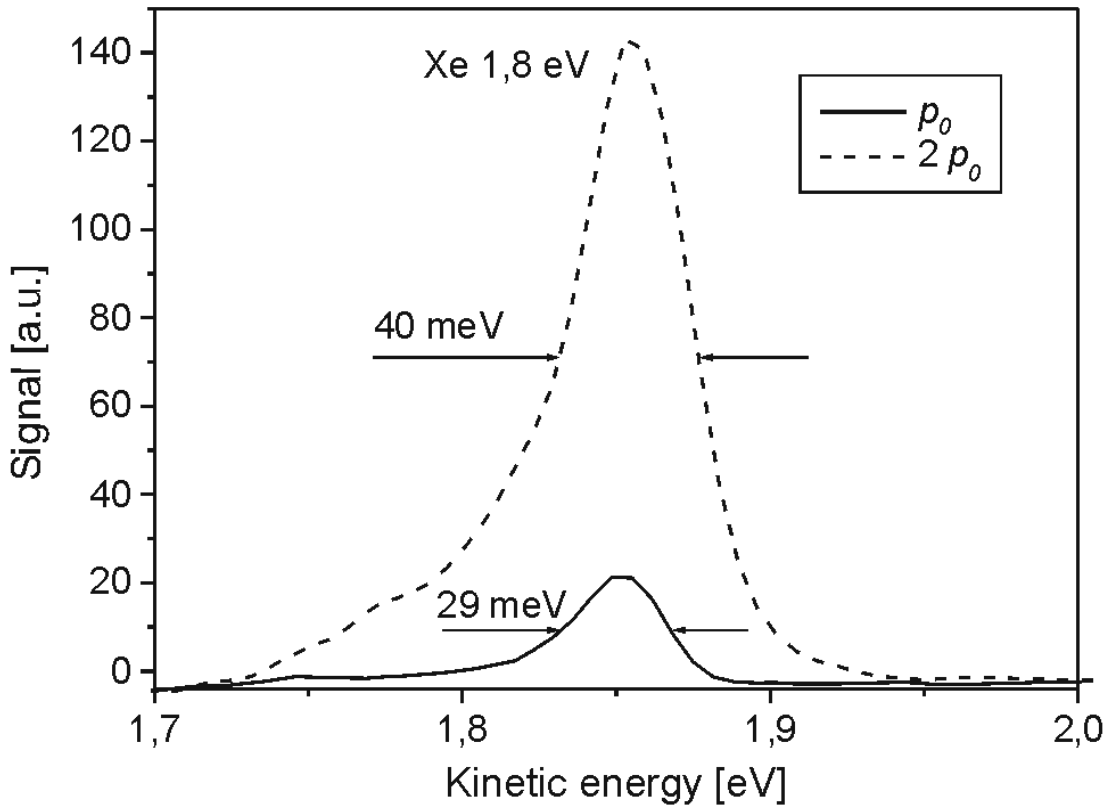

Figure A.13: Photoelectron kinetic energy spectra of 1.8 eV Xe peak for different Xe pressures measured in the main chamber. Also shown are FWHM`s of the peaks.

The 1.8 eV Xe photoelectron peak for higher Xe pressure has 6 times higher intensity and 1.3 times higher full width half maximum (FWHM). In addition the complete photoelectron signal is shifted towards bigger flight times (lower kinetic energies). The relative intensity of the 0.5 eV peak with respect to that of 1.8 eV peak is decreasing for higher Xe pressure, what is however not an instrumental effect [74]. The kinetic energy FWHM`s of 1.8 eV peak after calibration and their dependence on the retardation voltage are given in Figure A.14. Apart from general improvement of the maximal resolution from 40 meV to 30 meV the best resolution for lower Xe pressure is achieved already when acceleration ($U_g \cong 0.4$ eV) voltage is applied to the grid.

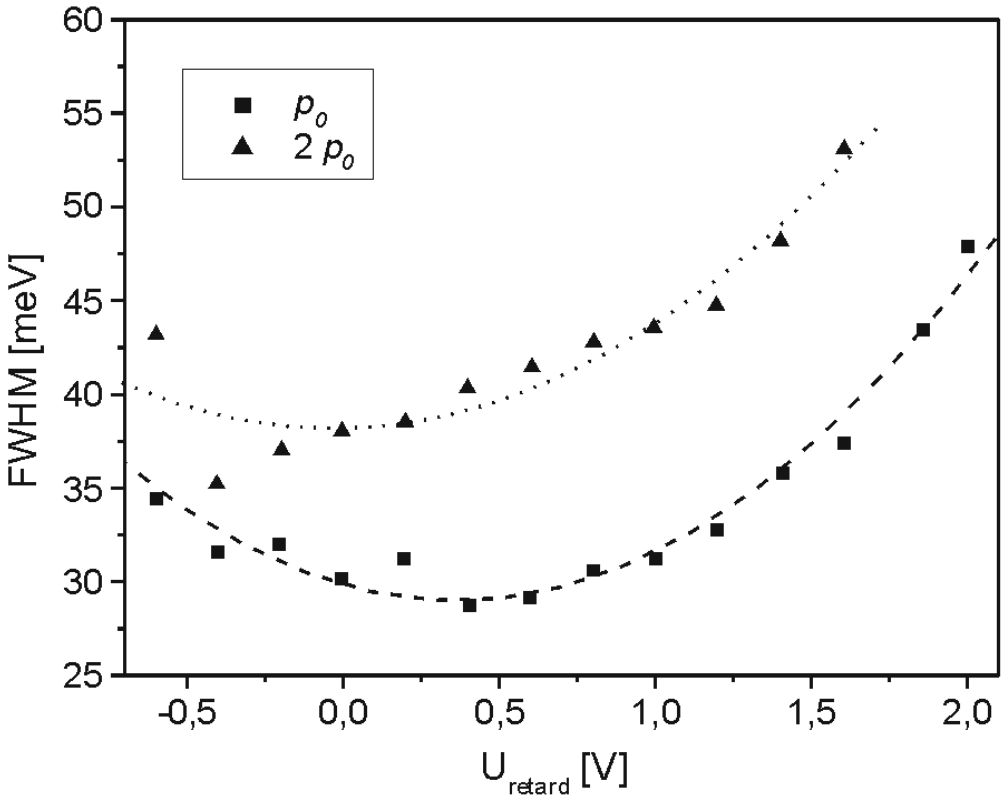

Figure A.14: Dependence of the FWHM of Xe 1.8 eV peak on grid voltage for for different pressures of Xe measured in the main chamber.

One can also define the optimal Xe pressure for the calibration. It is useful to take as a parameter not a pressure in the main chamber, since during experiments with alkali metals the pressure goages are poisoned and show a wrong, usually too high, pressure. In addition, the Xe supply tube position can be changed when cleaning or works are performed at the vacuum machine, thus the actual pressure in the pole-plate area can be somewhat different. We have taken as a parameter the height of the 1.8 eV Xe TOF peak signal. The calibration is performed at the peak height 40 – 50 mV. The laser energy is E_{YAG} = 0.5 mJ.

A.8.4 Magnetic fields

Figure A.15a shows the influence of the strong 1 Tesla magnetic field on the photoelectron time-of-flight signal. The spectra are recorded from ionisation of Xe with YAG laser of the 355 nm wavelength. The grid and pole-plate voltage are U_g = 1.4 V and U_{pp} = -0.5 V accordingly. The magnetic field was changed using different current at the power supply. We have measured photoelectron TOF signal at the current I = 2.5 till 4 A. The value 4 A is a maximal current the power supply gives and corresponds to the field strength 1 Tesla. The photoelectron signal increases with increasing the magnetic field strength, and is maximal for I = 4 A. The fast photoelectrons are especially sensitive to the magnetic field changes. The energy resolution is weakly affected by the strong magnetic field changes and stays almost constant in the region of I = 3.0 – 4.0 A (Figure A.15b). Note that the peak at 580 ns corresponds to the photoelectron kinetic energy of 1.4 eV. It is close to the energy E = 1.37 eV released from the ionisation of water with λ = 355 nm of Nd:YAG laser (the lowest ionisation energy of water corresponding to $1b_1$ orbital is 12.61 eV [121]). Thus it can be referred to water.

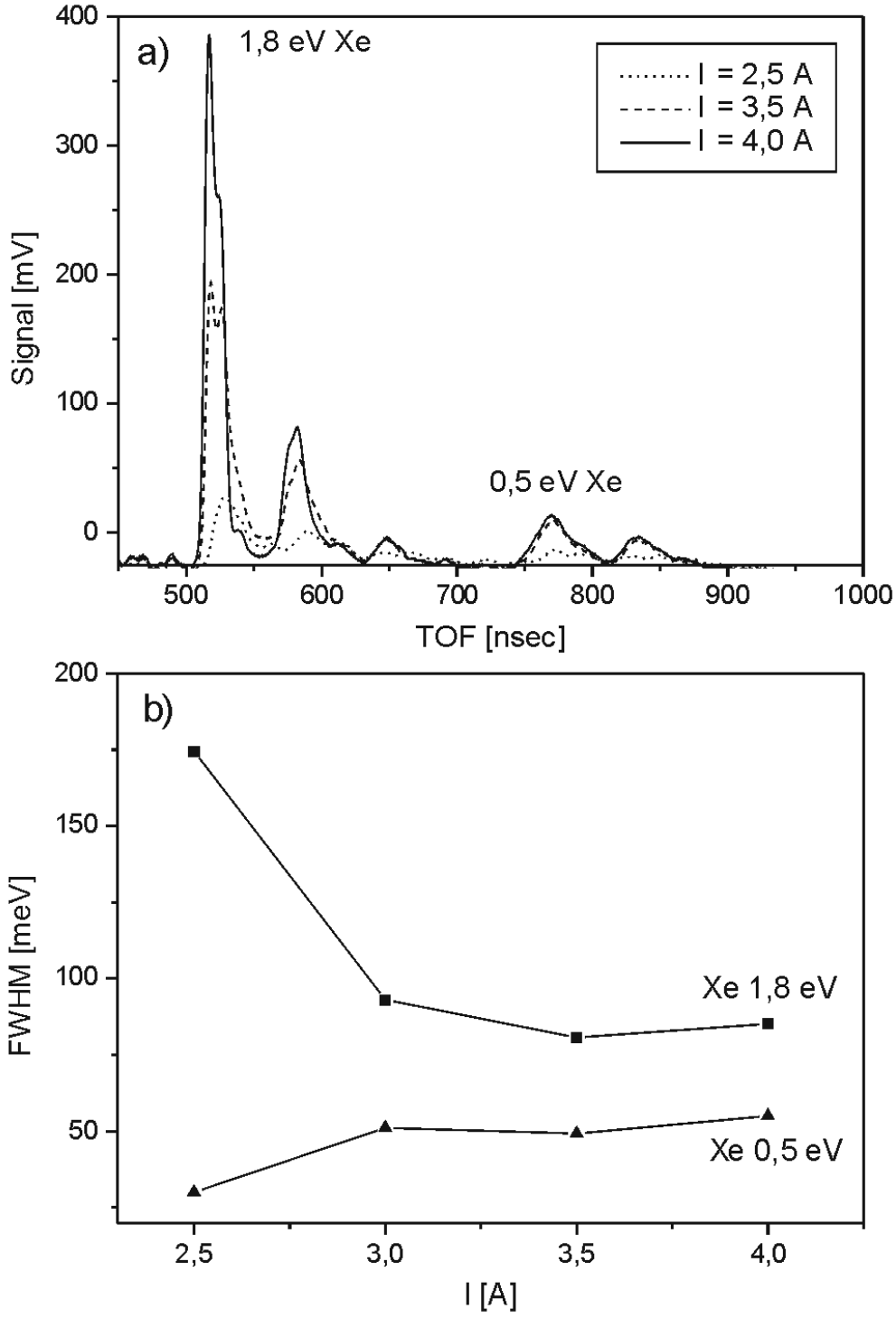

Figure A.15: Dependence of the photoelectron signal on the 1 Tesla magnetic field. a) photoelectron time-of-flight spectra recorded at different currents at the coil creating 1 T field; b) dependence of the FWHM of the 1.8 eV and 0.5 eV Xe peaks on the current at the coil. The routine measurements are made at the current I = 4 A and the voltage $U \approx 55$ V. The peak at 580 ns arises from ionisation of water. Additional peaks in the spectra at 650 ns and 840 ns may be due to impurities in Xe arising, for instance, from improper work of the valve between the Xe bottle and the vacuum chamber.

The influence of the weak magnetic field of 10^{-3} Tesla is shown in Figure A.16a. The field is changed using the current from the power supply in the range of I = 1.35 to 2.60 A, where the value of I = 2.0 A is optimal used routinely. The photoelectron signal increases drastically with increasing the current from 1.35 to 2.0 A, then stays almost constant from 2.0 till 2.60 A.

The effect is also stronger for fast electrons. The energy resolution is independent on the weak field change (Figure A.16b).

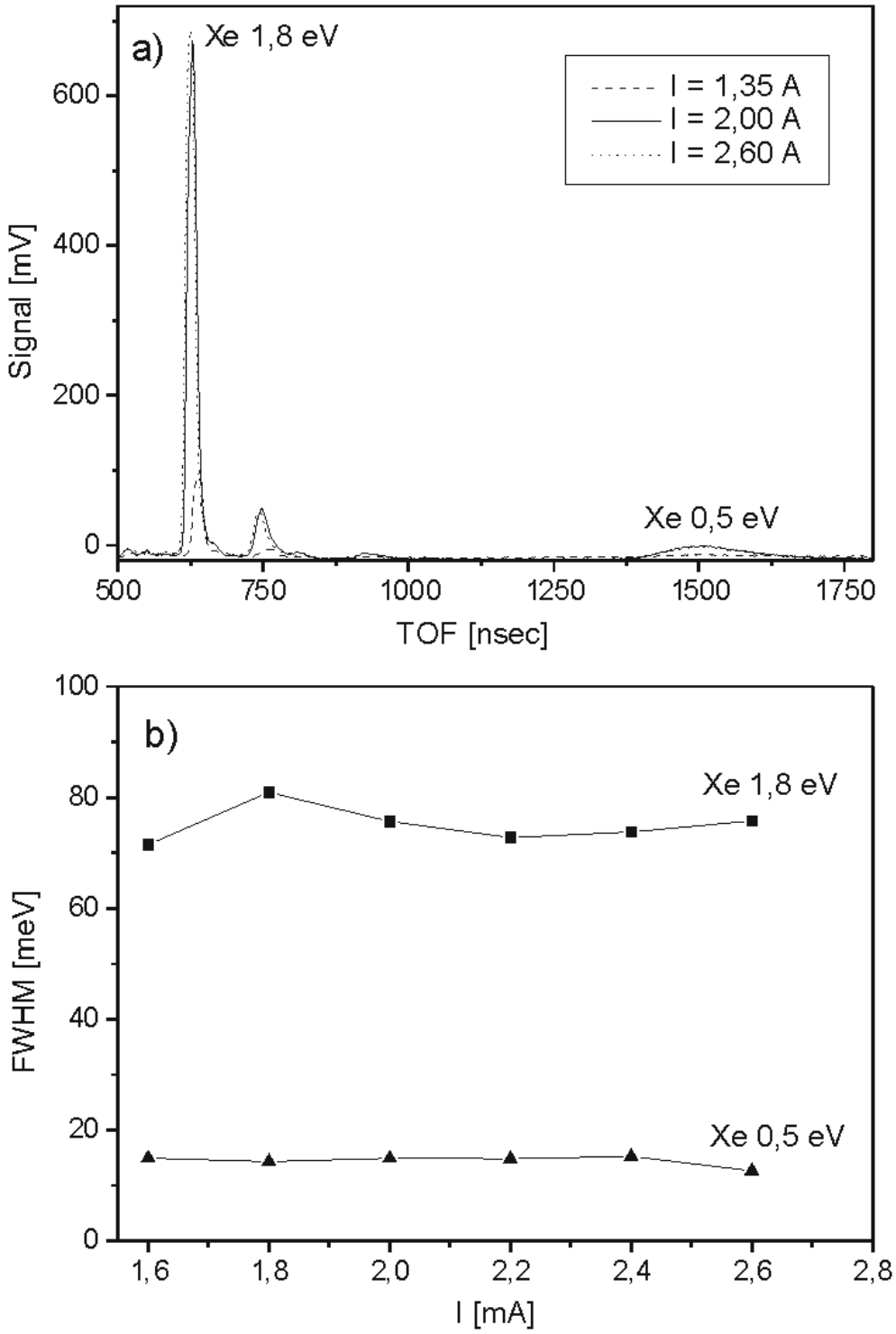

Figure A.16: Dependence of the photoelectron signal on the 1 mT magnetic field. a) photoelectron time-of-flight spectra recorded at different currents at the coil creating 1 mT field; b) dependence of the FWHM of the 1.8 eV and 0.5 eV Xe peak on the current at the coil. The routine parameters used in experiments: I = 2 A at the voltage $U \approx 1$ V. The peak at 750 ns arises from the ionisation of water.

Finally Figure A.17 shows photoelectron signal for different magnetic fields created by Helmholtz coils. The coils are used to compensate the magnetic fields of the Earth. The spectra are taken for different voltages at the power supplies of the coils. With increasing the voltage at the first coil (Figure A.17a) the photoelectron signal slightly increases, reaches its maximum at approximately 6 V and is then suppressed as the voltage increases. The FWHM of both peaks slightly decreases by the value of 10 %.

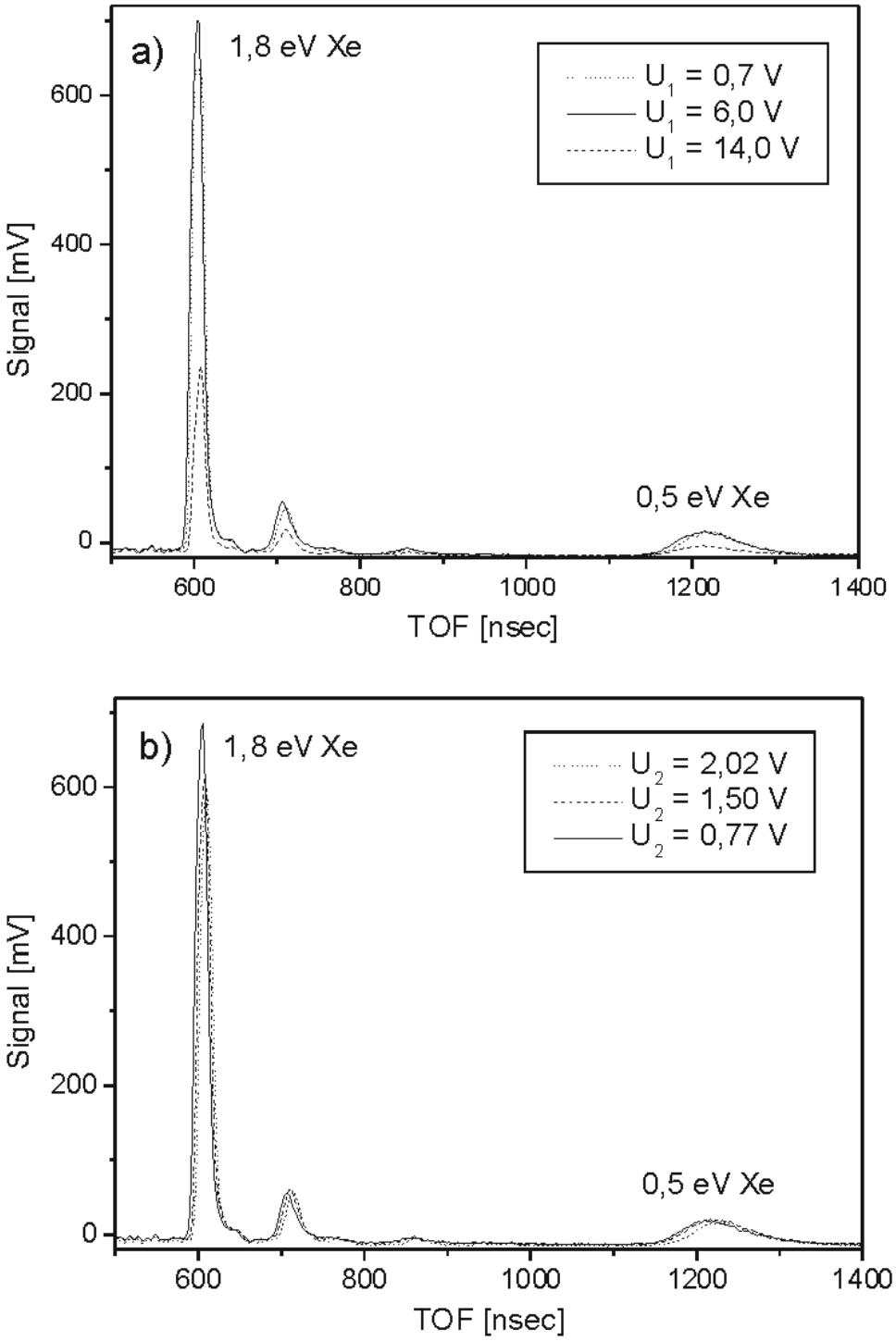

Figure A.17: Photoelectron time-of-flight spectra of Xe recorded at different voltages applied to both Helmholtz coils. The optimal parameters are found to be U_1 = 6.7 V for the first coil and U_2 = 0.77 V for the second coil.

With increasing the voltage at another coil (Figure A.17b)) the photoelectron signal is maximal for the minimal value of voltage (0.77 V), and slightly decreases with increasing voltage. The FWHM of the peaks is not affected. The best voltage for the signal have been found to be 6.7 V for the first coil and 0.77 V for the second one.

A.8.5 Pole-plate voltage

One of the serious problems arising in the experiments with alkali metals is the charges thronging on the pole-plates. These effects arise when the atoms in the beam stick to the pole-plates and influence the spectrum in the case of magnetic bottle spectrometer. We reduced their influence significantly by putting the second skimmer directly in front of the pole-plates. Nevertheless the effect remains and after several days of working with alkali beam becomes observable. We compensate it by applying a significantly higher voltage at the pole-plates. An alternative could be a coating the pole-plates with colloidal carbon [79].

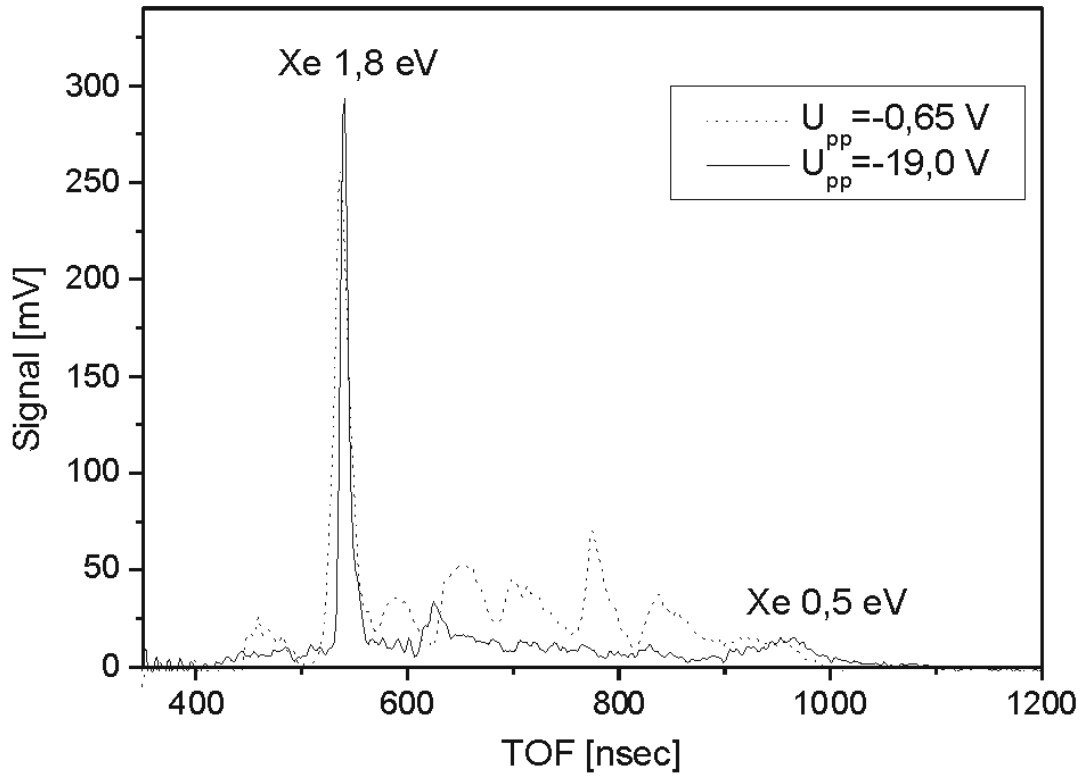

Figure A.18: Photoelectron spectra from ionisation of Xe with nanosecond YAG laser recorded after several days of working with potassium beam. Dotted line: at usual voltage applied on the pole-plates U_{pp} = -0.65 V. The Xe peaks are suppressed and oscillating structure appears in the signal. Solid line: at much higher compensation pole-plate voltage U_{pp} = -19 V; the oscillating structure is mostly gone, the third peak appearing at 620 nsec in the signal coming from ionisation of water.

Figure A.18 shows the photoelectron time-of-flight spectrum from ionisation of Xe with λ = 355 nm of YAG laser after several days of work with potassium beam. The dashed curve corresponds to a voltage at the pole-plates U_{pp} = -0.65 V usually used in measurements. The spectrum reveals an oscillating structure, the Xe signal is supressed and broadened. These charge effects are compensated with the voltage U_{pp} = -19 V (solid curve). The pole-plate voltage, together with the grid voltage, is selected individually to get the reasonable view of the photoelectron signal.

Appendix B

Time-of-flight ion spectrometer: calculation of ion masses and test experiments

The capabilities of the magnetic bottle have been considerably supplemented with time-resolved ion detection [122]. In the present work the mass analysis of the formed ions serves for the identification of species released during photoionisation and for defining the condition of the experimental set-up (i.e. operation of the pumping system, pole-plate area purity, operation of the spectrometer and electronics, condition of a molecular or an atomic beam) before and during the measurement. Below, we demonstrate the calibration procedure using Xe signal for the quantitative mass identification and several spectra appropriate for typical experimental conditions.

B.1 TOF-to-mass calibration procedure

For an ideal Wiley-McLaren time-of-flight spectrometer [80] flight times for different areas depicted in Figure B.1 can be calculated as:

$$
\begin{aligned}
T_s &= c_s m^{1/2}; \qquad & c_s &= \frac{\sqrt{2}}{qE_s}\left(\sqrt{U_0 + qsE_s} \mp \sqrt{U_0}\right) \\
T_d &= c_d m^{1/2}; \qquad & c_d &= \frac{\sqrt{2}}{qE_d}\left(\sqrt{U_0 + qsE_s + qdE_d} - \sqrt{U_0 + qsE_s}\right) \\
T_D &= c_D m^{1/2}; \qquad & c_D &= \frac{D}{\sqrt{2(U_0 + qsE_s + qdE_d)}},
\end{aligned}
\tag{B.1}
$$

where *s, d, D* are the lengths of the extraction area, acceleration area and drift area correspondingly, T_s, T_d, T_D are the flight times in the extraction area, acceleration area and drift area, *m* is the mass of the ion, E_s, E_d, E_D are the electric field strengths, U_0 is the initial energy of the ion, q is the charge of the ion. The "-" sign in c_s corresponds to initial velocities of ions directed towards the detector, the "+" sign to direction away from the detector.

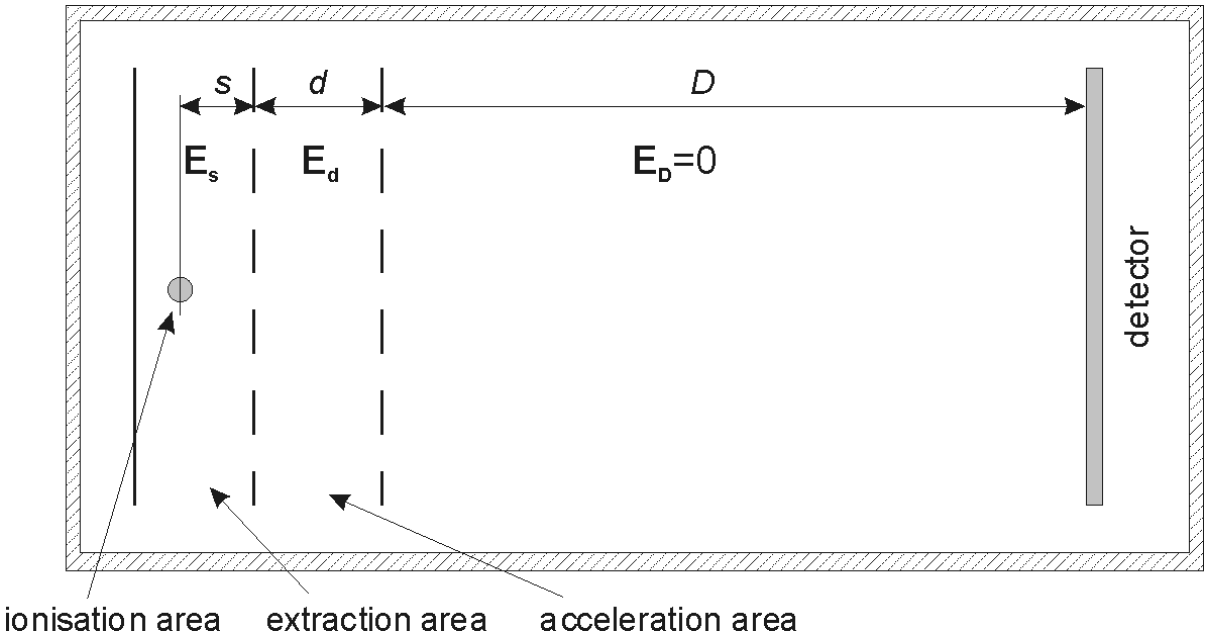

Figure B.1: Principal scheme of Wiley-McLaren time-of-flight spectrometer [80]

The ion masses can be calculated from flight times provided known parameters q, U_o, s, d, D, E_s, E_d, E_D in c_s, c_d, c_D and trigger delay δt (i.e. the time between the trigger and MCP signals):

$$m = \left(\frac{t + \delta t}{c} \right)^2 , \qquad \text{where } c = c_s + c_d + c_D . \tag{B.2}$$

The exact experimental parameters i.e. the ionisation place and trigger delay are not known. Also the grids used in original spectrometer are replaced in our spectrometer by the pole-plates with holes, what leads to inhomogeneous fields in the interaction area. Therefore, as in the case of electron spectrometer, the exact formula for mass (B.2) is replaced by a polynomial series in t:

$$m = \sum_{i=0}^{p} a_i t^i . \tag{B.3}$$

The polynomial degree $p = 2$ gives satisfactory values. In TOF-to-mass calibration the signal height can be transformed using a formula analogous to that for photoelectrons (A.14):

$$S'(m) = S(T) \left(\frac{dm}{dt} \right)^{-1} . \tag{B.4}$$

In our experiment, however, no quantitative information on masses is required, since the ion signal is used for determination of the atomic or molecular beam condition. Therefore only the equation (B.3) is applied to define the masses of species.

B.2 Calibration using ionisation of Xe with Nd:YAG laser

We used Xe atoms for the calibration of our mass spectrometer. In addition other species, like H, C atoms and H_2O which are also present usually in the machine can be taken for calibration. Xe gas consists of several isotopes. The masses and their distribution are shown in the Table B.1 [123]. By comparison of the known relative intensity distribution in mass spectrum to the experimental spectrum the single masses of Xe isotopes can be identified and used as calibration points.

Isotope mass, atomic units	Relative abundance
128	0.0714
129	0.9814
130	0.1487
131	0.7881
132	1.0000
134	0.3903
136	0.3309

Table B.1: Natural isotope distribution of Xe [123].

Xe gas is supplied using the Ø6 mm pipe directly to the interaction area between the pole-plates. The pressure in the main chamber is typically $2\text{-}5\cdot10^{-5}$ mbar, the pressure in the oven chamber is $\sim10^{-7}$ mbar. The nanosecond Nd:YAG laser described in the Chapter 3 provides 355 nm light of E_{YAG} = 0.5 mJ energy. This laser energy is used in all experiments described in this chapter. The laser beam is focused into the interaction chamber with a 250 mm focus lens. The polarisation of laser light is collinear parallel to the spectrometer axis. The front MCP plate voltage is -2.0 kV, the back plate is grounded. The anode is kept at +100 V voltage. The focusing voltage at the middle lens is +160 V. The triggering of the oscilloscope is performed with a photodiode illuminated by a reflected portion of the laser pulse in front of the chamber.

Figure B.2 shows a cut of the time-of-flight spectrum. The signal height is approximately 50 mV at experimental conditions described above. The isotope distribution in Xe plotted according to Table B.1 is shown in the right corner of the picture. The single Xe isotopes are resolved on the spectrum. Provided the relative mass abundances of isotopes, the identification of Xe isotope masses and eventually the calibration using formula (B.3) is performed. We used for calibration also known peaks of H^+, C^+ and H_2O^+. Figure B.3 shows the calibration curve and calibration parameters a_i. The complete time-of-flight spectrum and assigned masses is shown in the Figure B.4. Besides the Xe peaks, a strong peak of water at ~ 5000 nsec is always present in the spectrum. The intensity of water peak reaches values of hundreds of mV every time after opening the vacuum chambers. After several days of pumping the signal is sufficiently reduced to 10 - 20 mV. The peak is also strongly suppressed when an alkali beam is produced in the oven chamber.

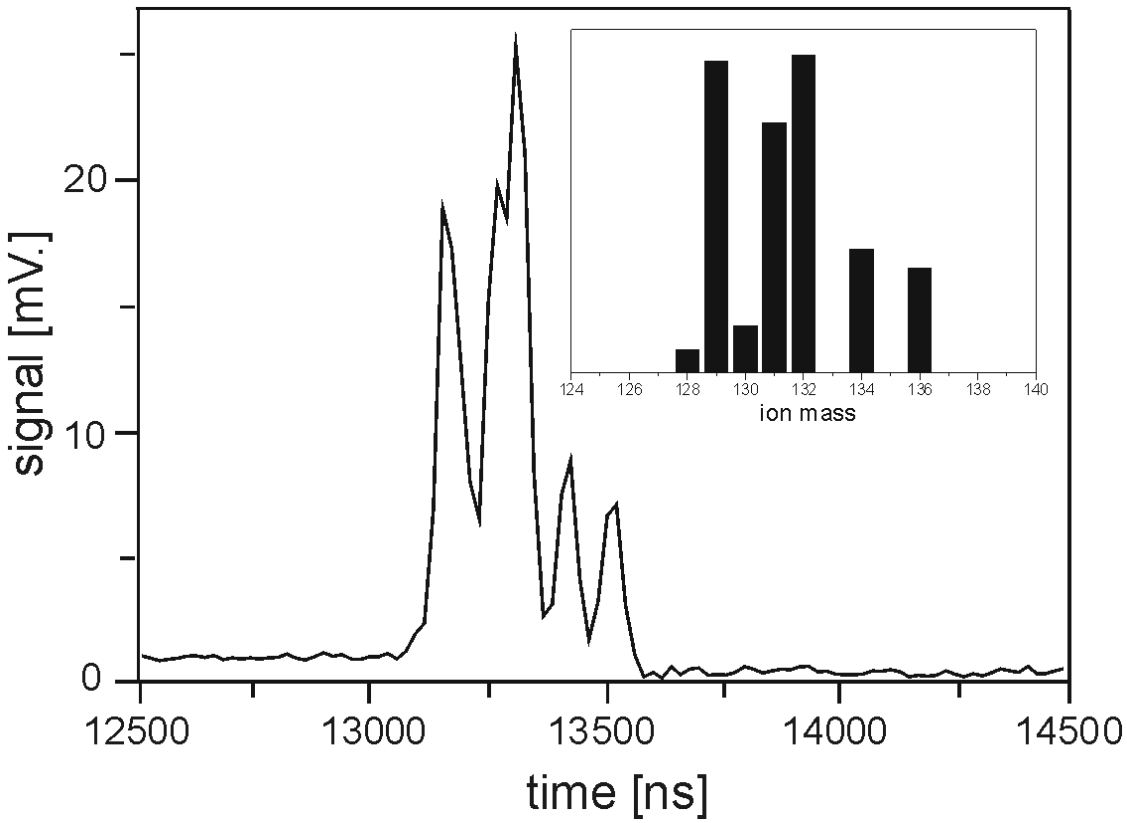

Figure B.2: A cut of the ion time-of-flight spectrum. Single Xe isotopes are resolved. In the right corner Xe isotope mass distribution is shown in accordance with the Table B.1. The correspondence to the measured signal is satisfying.

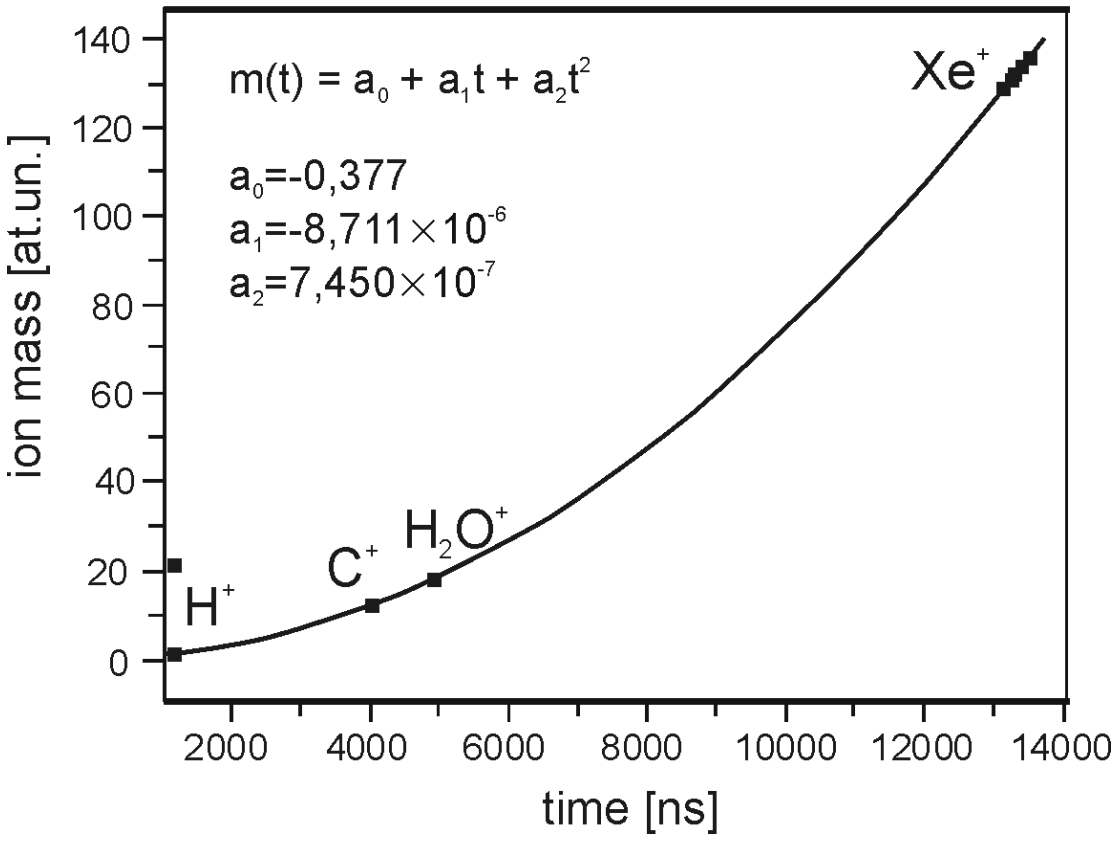

Figure B.3: Calibration TOF-to-mass curve of the ion spectrometer and the parameters a_i. The points taken for calibration are flight times from H^+, C^+ and H_2O^+ ions and Xe^+ isotopes.

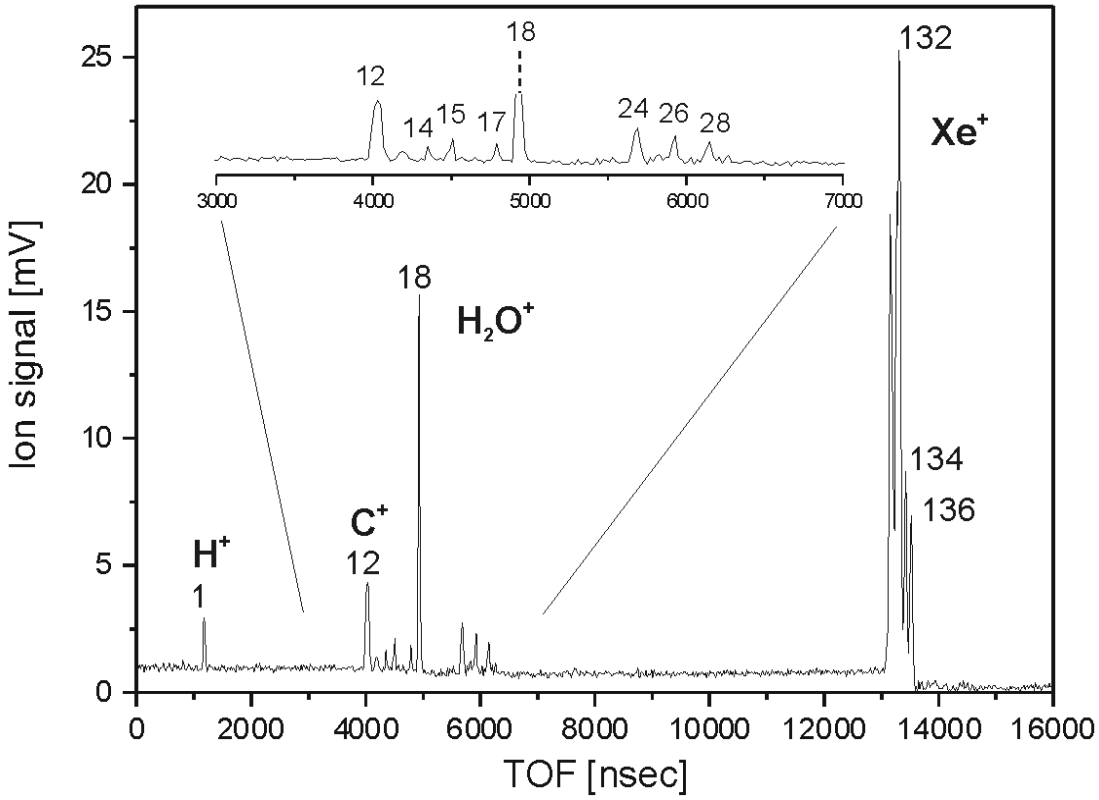

Figure B.4: Typical time-of-flight spectrum together with assigned ion masses. The inset shows a part of the TOF spectrum between 3000 and 7000 ns.

Defined mass	Possible assignment	Defined mass	Possible assignment
1	H^+	24	C_2^+
12	C^+	26	$C_2H_2^+$
13	CH^+	28	$C_2H_4^+$
14	CH_2^+	37	Pump oil
15	CH_3^+	43.5	Pump oil
17	CH_5^+	57	Pump oil
18	H_2O^+		

Table B.2: Assignment of some of the measured ion masses.

B.3 Qualitative observations

The ion time-of-flight spectra are slightly different from day to day, depending on the condition of MABOS machine, and the substances used in the experiment. A several experimental TOF spectra are shown lower relevant for typical experimental conditions.

Figure B.5 shows the influence of the evacuation condition of the vacuum chambers on the ion TOF spectra. The spectrum in Figure B.5a is made under normal pumping conditions, i.e. after 3 – 4 hours of working of the pumps. The spectrum B.5b is recorded after 30 minutes

after switching off the diffusion pump. One can observe the drastically increased signals from radicals $C_nH_n^+$ and their products C_n^+ and H^+. The signals are the products of the pump oil dissociation.

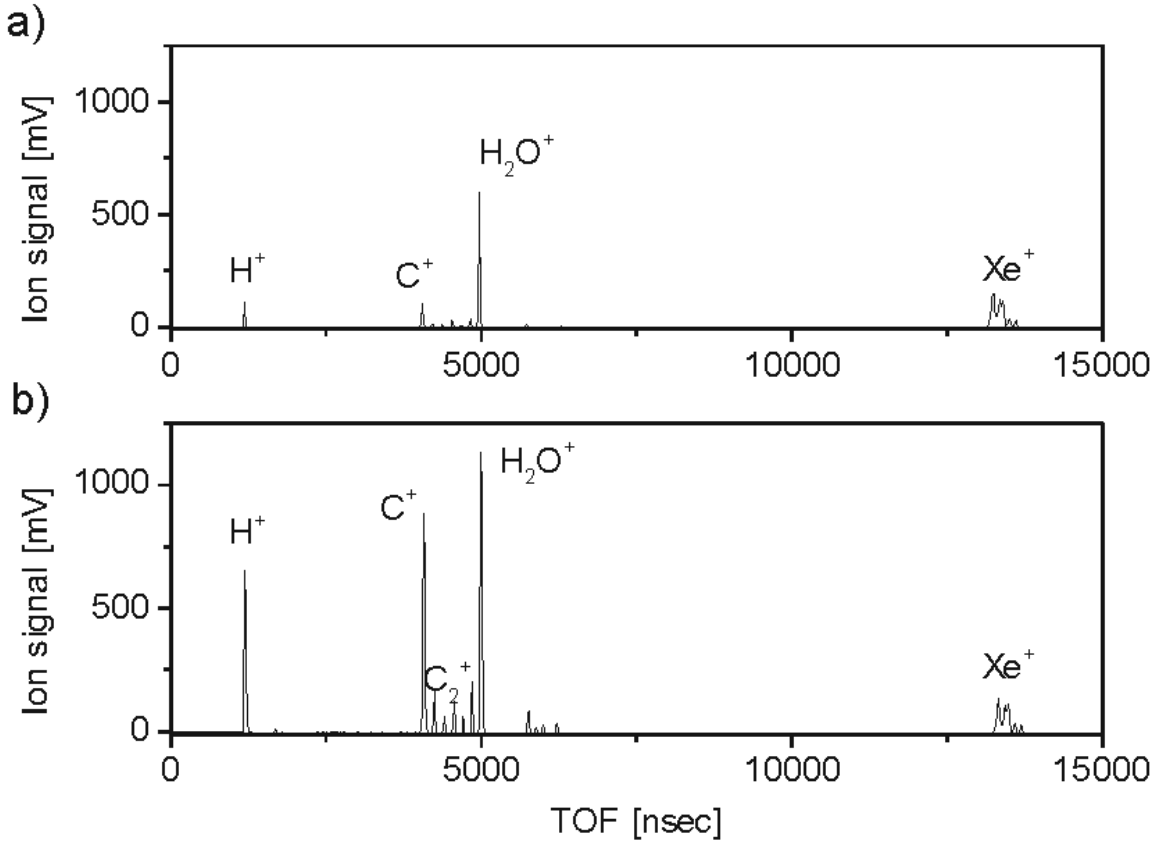

Figure B.5: Ion TOF spectrum from ionisation with λ = 355 nm of Nd:YAG laser at normal pumping conditions (a) and after 30 minutes of switching off the diffusion pump (b). Note the increased H^+, C_n^+ and $C_nH_n^+$ peaks arising from the dissociation of the pump oil.

Figure B.6 shows the ion spectrum during the experiment with unseeded Na beam. The nozzle diameter is 200 μm. The pressures are $p = 3.3 \cdot 10^{-7}$ mbar in the oven chamber and $p = 3.0 \cdot 10^{-7}$ mbar in the main chamber. The Na_2 peak intensity in TOF signal reaches normally 15 – 20 % of the one of Na peak. The ion spectrum for Na seeded beam is depicted in Figure B.7. The nozzle diameter is 100 μm and the pressures are: p = 1.6 bar of Ar seeding gas, $p = 4.5 \cdot 10^{-5}$ mbar in the oven chamber and $p = 1.2 \cdot 10^{-6}$ mbar in the main chamber. The Na_2^+:Na^+ distribution in the spectrum reaches 0.5.

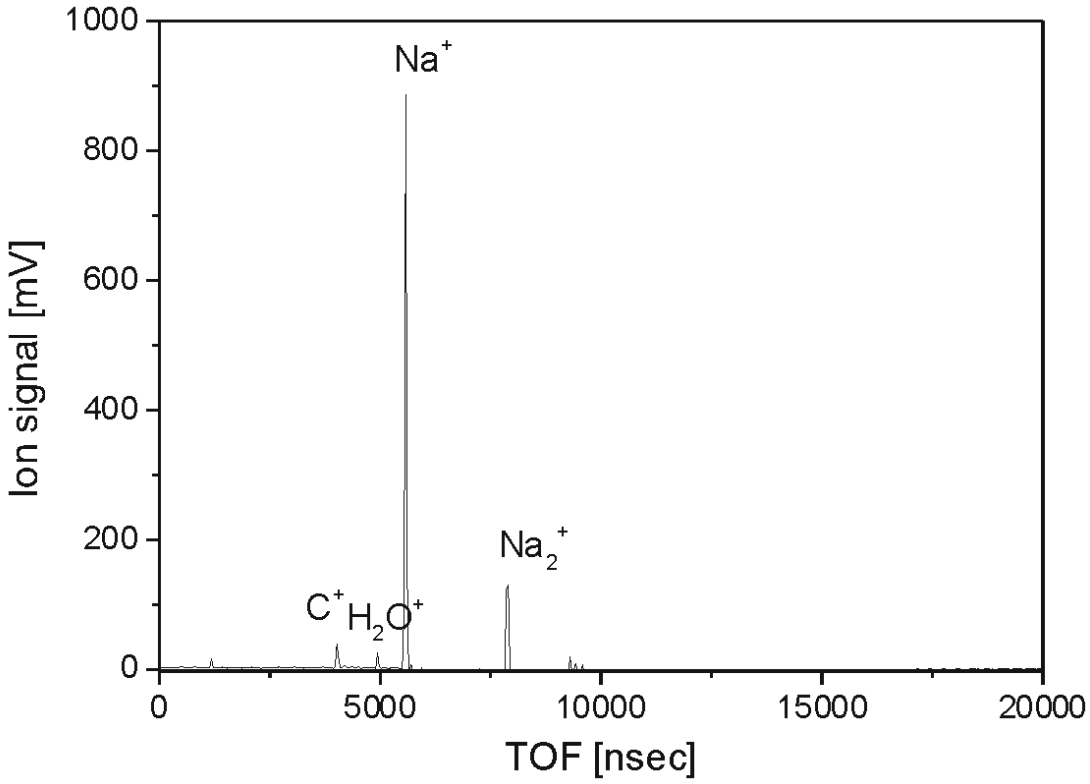

Figure B.6: Ion time-of-flight spectrum from ionisation with λ = 355 nm of Nd:YAG laser during the experiment with Na unseeded beam and 200 μm nozzle diameter.

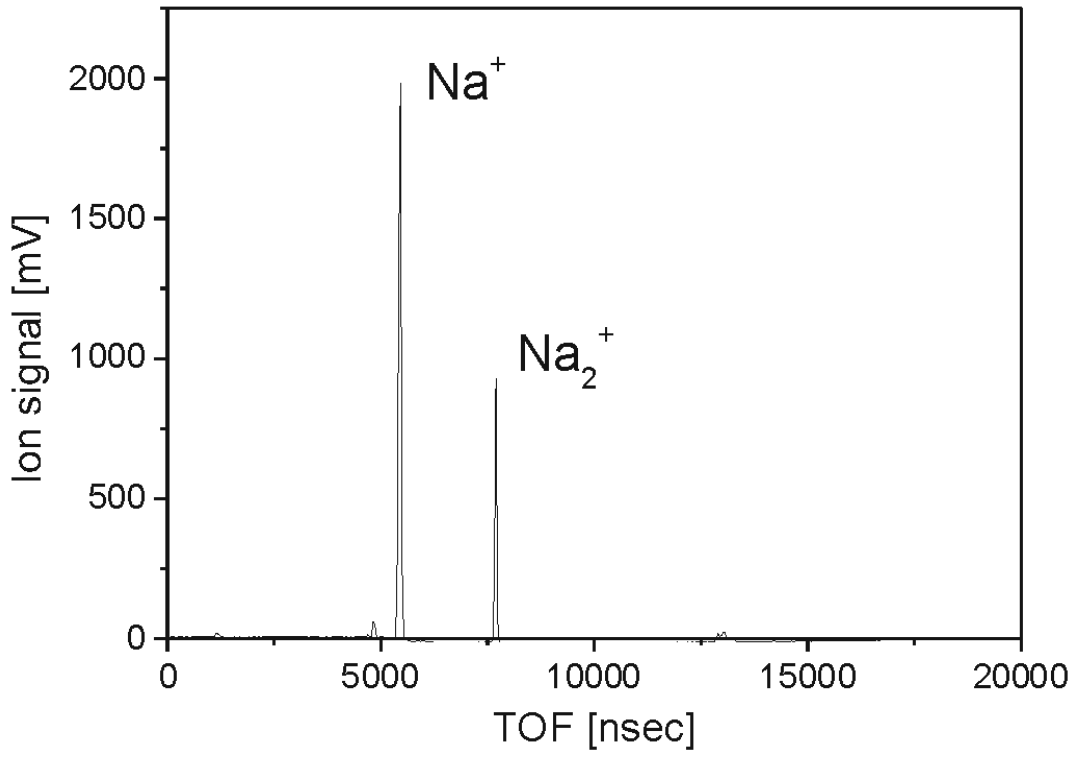

Figure B.7: Ion spectrum during the experiment with a Na beam seeded with Ar and 100 μm nozzle diameter. Ar partial pressure is 1.6 bar.

Appendix C

Pump-probe on Na fine-structure levels

The Chapter presents a pump-probe experiment performed to observe the dynamics in the fine structure levels of the ($3^2S - 4^2P_{1/2,3/2}$) transition in atomic sodium. The experimental results initially aimed on studying the dynamics in Na_2 molecule nevertheless revealed also oscillations in Na atoms fine structure. Such an observation was possible to differentiate from signal originating at other ionisation sources because of principal scheme based on detection of kinetic-energy resolved photoelectrons. The dynamics in the $4^2P_{1/2,3/2}$ doublet, according to the energy splitting, evolves on a picosecond time scale, which enables us to resolve it with our experimental set-up.

C.1 Introduction

With the advent of ultrashort laser pulses it has become possible to study directly dynamical phenomena from atomic and molecular motion to molecular reaction dynamics [1,124-127]. In the simple systems, like atomic fine structure levels, periodic motions can be observed which are in general predicted from the Fourier transform of the absorption lines measured by standard spectroscopy. However time-resolved studies provide a direct insight into the quantum-mechanical processes, with a simple connection to classical interpretations.

Fine and hyperfine structure states in alkali atoms have been widely studied using conventional or quantum beat spectroscopy [128-132]. In quantum beat experiments a laser pulse prepares a coherent superposition of the excited states, and the subsequent fluorescence exhibits modulations at Bohr frequencies corresponding to level separations. Experiments on hyperfine [129] and fine [130] structure levels have been performed by detecting the fluorescence signal. Other detection methods, in which resonant absorption or stimulates emission are used, are described in [131,132]. In [131] a resonance absorption from a laser was used to monitor the evolution of the superposition of hyperfine states in sodium excited by the laser pulses. In [132] a quantum beats method with detection of the stimulated emission is applied to the Zeeman splitting in ytterbium.

Leuchs and Walter have first used laser field ionisation to observe fine-structure beats in higher n states of sodium [133]. In [134] a wave packet interferometry method together with

associative ionisation mechanism is applied to $np^2P_{1/2,3/2}$ fine-structure levels of rubidium atom. In this method interferences result from the wave packet created by two identical laser pulses which reflect the time evolution of the system. These interferences are then probed by photoionisation for fine-structure states. Fine structure states have also been studied on the femtosecond scale using the technique of wave packet interference by the group of Gerard [135-137].

First femtosecond pump-probe experiments on observation of wave packets in the fine-structure states have been performed in [138] on potassium atoms. In this work the evolution of the wave packet corresponding to a precession of spin and orbital angular momentum around the total angular momentum is probed via photoionisation and by observation the K^+ ion signal. The theoretical description using dark-bright states formalism, alternative to the commonly used stationary basis state description is suggested [137,138]. In [139,140] there was shown how this scheme can be applied to produce highly spin-polarised free electrons on the femtosecond time scale.

In this chapter the pump-probe technique is applied to directly observe the precession of the orbital and spin angular momentum vectors in the $4^2P_{1/2,3/2}$ fine structure states of Na atoms. A first femtosecond laser pulse with wavelength λ_1 prepares a coherent superposition of the two fine-structure levels. The evolution of the wave packet is then probed by the second laser pulse λ_2 via ionisation. Detection of kinetic-energy resolved photoelectron signal has advantages with regard to the conventional ion detection in which the total ion yield is usually detected. Resolving the kinetic energy of photoelectrons enables to unambiguously identify and differentiate between the channels giving the input into the overall ionisation process.

C.2 Scheme of the pump-probe experiment

A pump-probe experiment is performed on the fine structure levels of the (3S – 4P) transition in atomic sodium. Figure C.1 shows the relevant levels. The 4P doublet can be excited with the wavelength of λ = 330.3 nm. The fine-structure states in doublet (J = 1/2 and J = 3/2) are split by an energy 5.59 cm^{-1} [128].

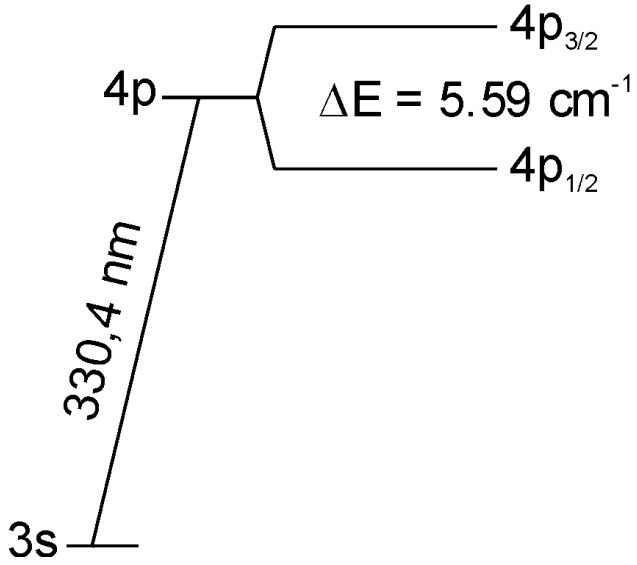

Figure C.1: Scheme of the 3^2S - 4^2P transition in Na atom. The 4P level is split into two states with total angular momentum J = 1/2 and J = 3/2.

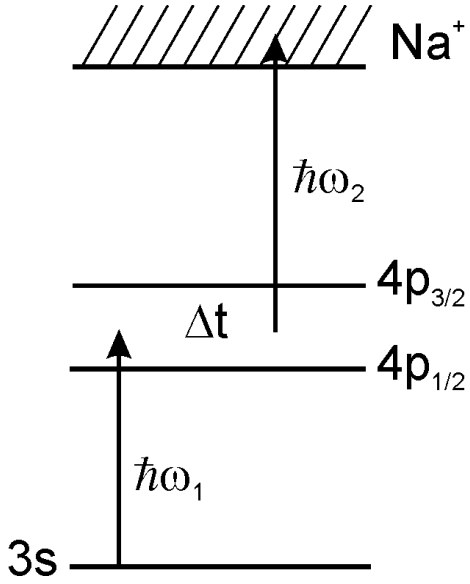

Figure C.2: Scheme of the pump-probe experiment. First laser pulse excites a coherent superposition of $4P_{1/2}$ and $4P_{3/2}$ levels. Second pulse ionises it. The population of electrons is measured as a function of pump-probe delay.

The scheme of experiment is presented in Figure C.2. The pump-probe set-up combines two ultrashort laser pulses which interact with the atomic system being in the ground state $|g\rangle$. The pump pulse is used to excite several adjacent states. The spectral width of the pulse, $\Delta\omega_1$, is sufficiently broad to excite both involved fine-structure levels, $4P_{1/2}$ and $4P_{3/2}$. The wave packet in the excited state is given by the formula [138]:

$$|\psi(t)\rangle = \sum_k e_1(\omega_k)\mu_{kg} e^{-i\omega_k t}|k\rangle, \qquad \text{(C.1)}$$

where $|k\rangle = |J = 1/2\rangle, |J = 3/2\rangle$ are the levels of the doublet; μ_{kg} represents the matrix element of the dipole moment operator $|g\rangle \to |k\rangle$, ω_k is the frequency of the $|g\rangle \to |k\rangle$ transition, $e_1(\omega_k)$ is the pump laser electric field.

The wave packet consisting of a coherent superposition of the excited levels evolves freely after the excitation. The second pulse after the time delay transfers the wave packet towards the final state $|f\rangle$. One can choose as a final state the ionisation continuum. In this case the ionisation probability oscillates as a function of a time delay t at the relative frequency $\omega_{kk'} = \omega_k - \omega_{k'}$. The oscillations result from the quantum beats between two parts the same initial and final states, and different intermediate states $|J = 1/2\rangle$ and $|J = 3/2\rangle$ (see Figure C.2). The population of ionisation products, electrons, recorded as a function of a time delay, reveals the dynamics.

The initial phase of the oscillation for a two state system depends on the sign of the ionisation dipole moments product $\mu_{kg}\mu^*_{k'g}\mu_{fk}\mu^*_{fk'}$ [138]. If $\mu_{kg}\mu^*_{k'g}\mu_{fk}\mu^*_{fk'}$ is positive, then the interference will be constructive for delay time t = 0 and for multiples of oscillation period, hence, for these times a maximum in the photoelectron signal will be observed. In the case of negative value of $\mu_{kg}\mu^*_{k'g}\mu_{fk}\mu^*_{fk'}$ a first maximum appears at half an oscillation period.

C.3 Experimental results and discussion

The experimental arrangement includes a sodium supersonic beam, a Ti:sapphire femtosecond oscillator and a magnetic bottle time-of-flight electron spectrometer. The 341 nm and 0.6 μJ pump pulses were generated by parametric amplification of 2/3 of the energy of the 1kHz, 785 nm and 800 μJ output of CPA Ti:Sapphire laser system and subsequent frequency quadrupling. Figure C.3 shows the spectral distribution of the 341 nm pulse. The FWHM of the pulse of 5.7 nm was broad enough to excite both fine-structure levels of the 3s – 4p transition. Frequency tripling of the residual light of the amplifier provided the 265 nm, 0.4 μJ and 3.8 nm FWHM probe pulses. Both light pulses were polarised collinear to the axis of the TOF spectrometer. The delay between the pump and the probe laser pulses was set by a stepper motor driven delay line in a range of several picoseconds in 50 and 100 fs steps. With a f = 200 nm lens both laser beams were focussed into a vacuum chamber to intersect an atomic beam. Na was heated to 875 K in an oven and expanded through a 200 mm nozzle. The released photoelectrons were detected with a magnetic bottle spectrometer as a function of a pump-probe delay. For each delay spectra were averaged over several thousand laser pulses.

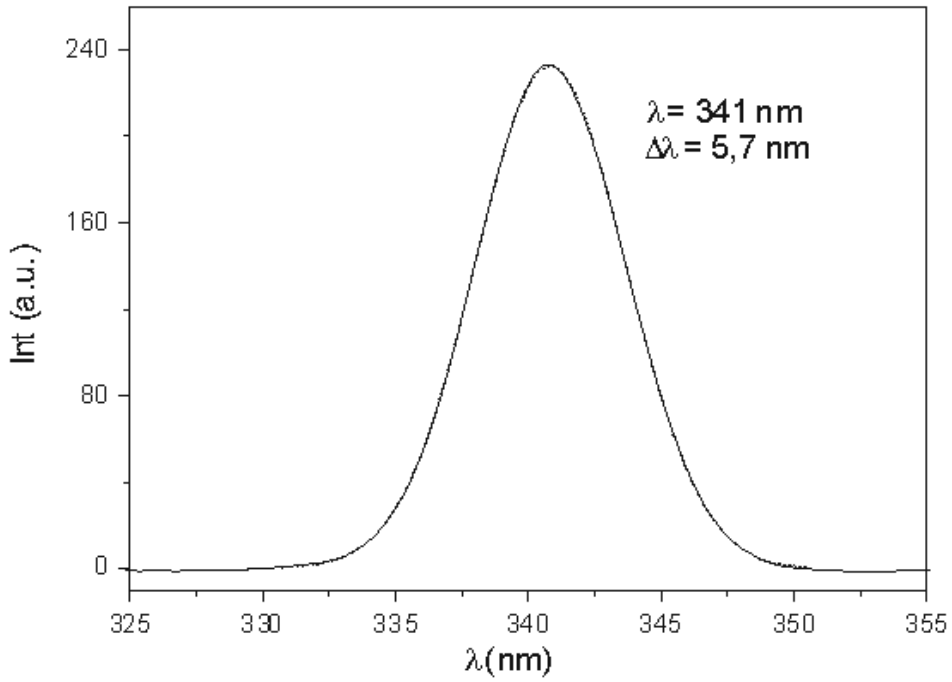

Figure C.3: Spectrum of the pump pulse. The pulse has a central wavelength λ = 341 nm and a FWHM $\Delta\lambda$ = 5.7 nm.

The experimental spectrum represents a 2D scan, with a flight time along abscissa axis and delay between pump and probe pulses along ordinate axis. For each pump-probe delay a photoelectron time-of-flight spectrum in the range of 0 to 1600 ns was recorded and averaged. Figure C.4 shows a part of the experimental spectrum for the flight times from 350 to 550 nanoseconds. The delay time ranged from -2 to 26 picoseconds.

One can differentiate the contributions from sodium atomic and molecular signals at different photoelectron energies, and hence, different flight times. A stationary signal, i.e. independent on the pump-probe delay, at 500 ns corresponds to the one-colour signal from the atomic near resonance transition 3s – 4p at 2.15 eV from 2 photons of λ = 341 nm. The signal at 395 ns

corresponds to one-colour signal from 3s – 6p transition at 4.2 eV from 2 photons of λ = 265 nm. The contribution from the molecular signal, which can overlap with the fine-structure signal, especially at time zero, can be varied by changing the parameters of the sodium beam. This contribution shown up as a weak modulation of the atomic signal, since only a small part of the molecules is measured to be present in a not seeded Na beam.

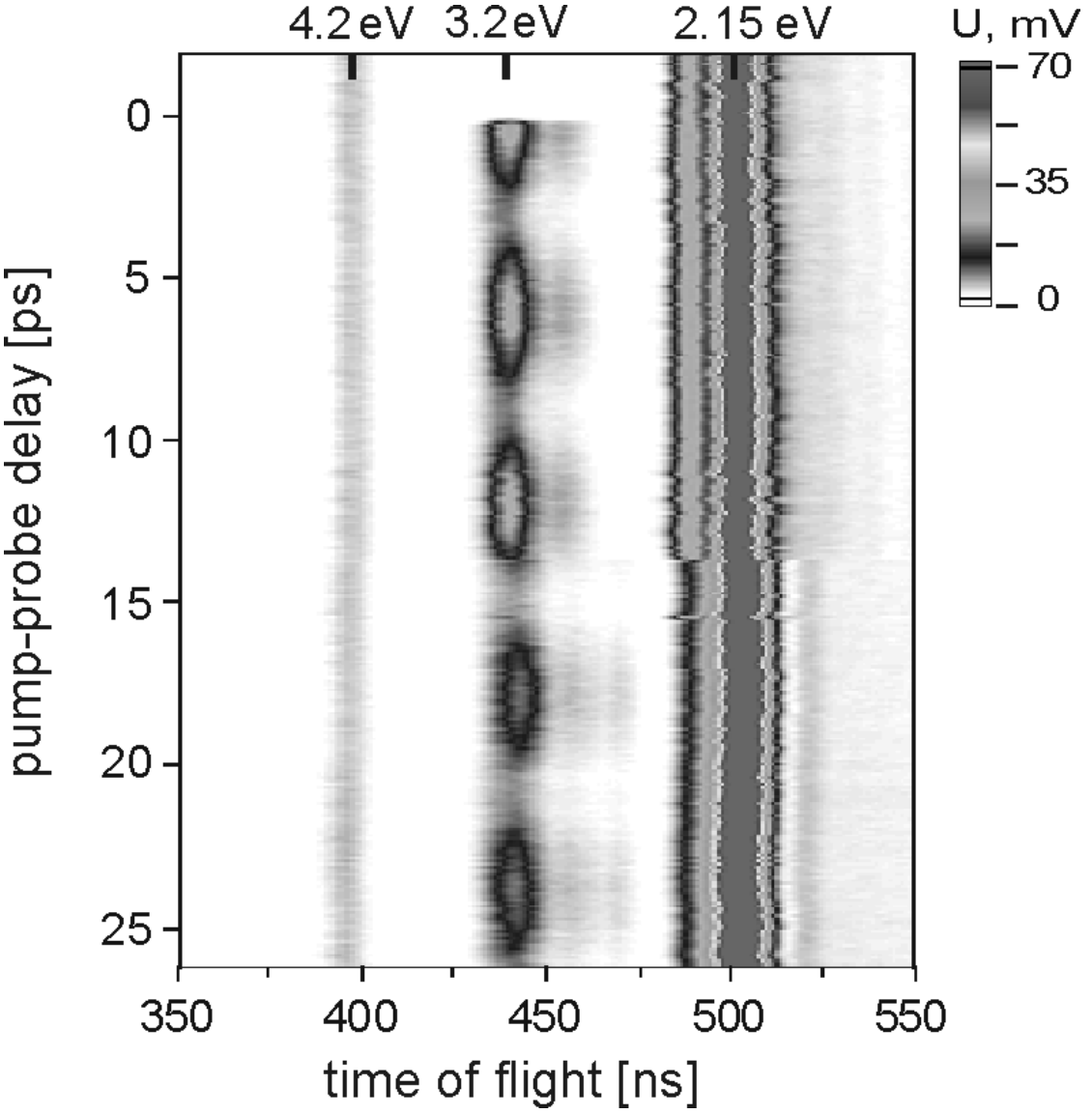

Figure C.4: Time-of-flight photoelectron spectrum as a function of pump-probe delay. The one-colour signals from near resonance Na 3s – 4p transition with λ = 341 nm and 3s – 6p transition with λ = 265 nm are seen at 395 ns and 500 ns respectively. Fine-structure oscillations from 3s-4s transition are observed at 440 ns.

The signal from the Na fine structure splitting is expected at the photoelectron energy E_{kin} = 3.2 eV. The calibration of the TOF axis is performed as described in the Appendix E. The signals taken for the calibration are one-colour lines from Na atoms in femtosecond spectra and peaks from ionisation of Xe atoms with λ = 355 nm of the nanosecond YAG laser pulses. We observe indeed the oscillatory signal at a time t = 440 ns which corresponds after calibration to the photoelectron kinetic energy E_{kin} = 3.2 eV, what agrees with the expected value.

At negative pump-probe delays (t < 0 ns) the probe pulse with a wavelength of λ = 265 nm comes first, which corresponds to the excitation with λ = 265 nm and ionisation with λ = 341 nm laser pulses. In this case no excitation of the 4p levels of Na occurs as the pump pulse wavelength is not resonant. Therefore no signal is observed at 440 ns at negative delay times. However, at this time-of-flight there is a weak contribution in the signal at $t < 0$ coming from $7^1\Pi_u$ state which is discussed in the Chapter 4 of the present work. At $t = 0$ ns the pump and the probe pulses overlap and times $t > 0$ correspond to the excitation with λ = 341 nm and ionisation with λ = 265 nm.

Figure C.5 shows a cut along the time axis performed at the time-of-flight centred at 440 ns and averaged over 9 ns. The signal consists of an oscillatory component superimposed on a featureless background arising at positive delay times. The oscillations have a period of 5900 fs. The first sharp maximum appears at time zero. Thus the signal represents a cosine function with a part at negative pump-probe delay suppressed.

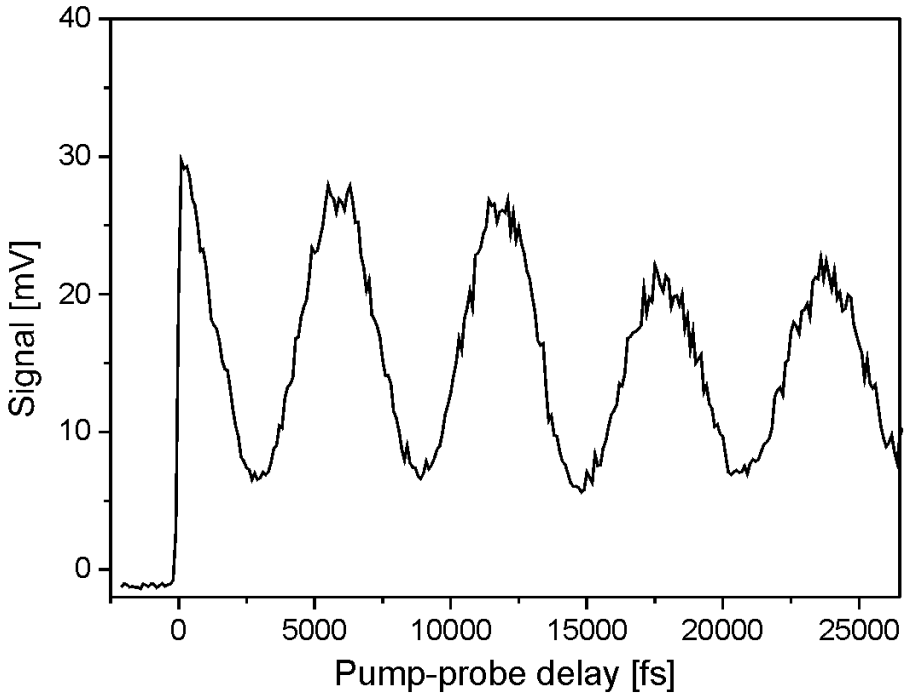

Figure C.5: A cut of the photoelectron measured spectrum along the time delay axis made at the time-of-flight 440 ns, that is at the photoelectron energy E_{kin} = 3.2 eV. The signal consists of the featureless background and the oscillating part. The oscillation period is 5900 fs. At negative times the 265 nm pulse comes first, so no pump-probe signal is observed.

The fast Fourier transform of the signal is shown at the Figure C.6. The oscillation period of 5900 fs is determined by the fine-structure splitting as $t = 2\pi\hbar / \Delta E$, where ΔE is the energy splitting. The oscillation period corresponds to the splitting of 5.66 cm^{-1}, which is in a good agreement with the value of ΔE = 5.59 cm^{-1} in the fine-structure doublet [128] measured with the methods of conventional spectroscopy.

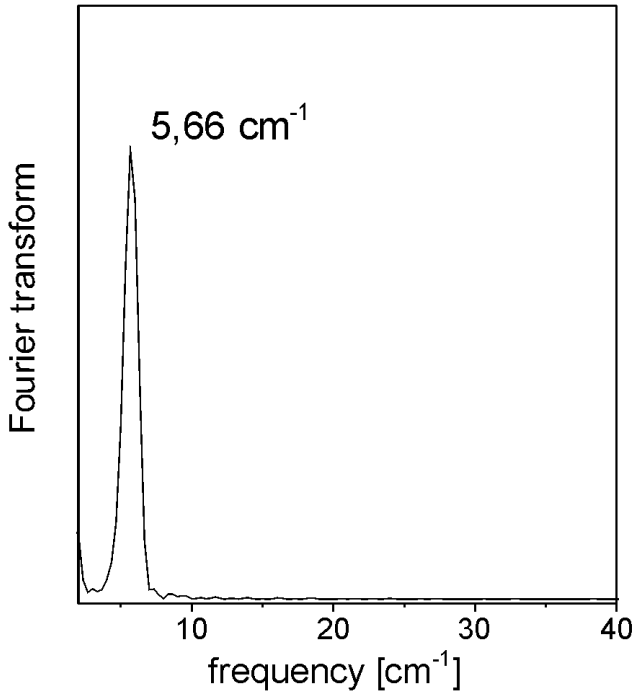

Figure C.6: The Fast Fourier Transform spectrum of the signal at 440 ns. The oscillation period corresponds to the energy splitting in a doublet of ΔE = 5.66 cm^{-1}, which is in a good agreement with the literature value of 5.59 cm^{-1} [128].

In order to elucidate the origin of the oscillations the application of the ionisation scheme to the Na $4^2P_{1/2}$, $4^2P_{3/2}$ fine structure is shown in Figure C.7. According to the transition selection rules, two states are accessible in the ionisation continuum from $^2P_{1/2}$ state: the $^2S_{1/2}$ state and $^2D_{3/2}$ state. From the $^2P_{3/2}$ three states in the continuum states can be reached: the $^2S_{1/2}$, $^2D_{3/2}$ and $^2D_{5/2}$ states. The oscillations arise only when both $^2P_{1/2}$ and $^2P_{3/2}$ fine-structure levels can be excited into the same ion state. This is valid for the $^2S_{1/2}$ and $^2D_{3/2}$ states. These oscillations with the period corresponding to the fine-structure level separation are thus visible in the photoelectron signal. Further, the calculation of the product of the matrix elements of the ionisation dipole moments $\mu_{kg}\mu^*_{k'g}\mu_{fk}\mu^*_{fk'}$ would enable to interpret the phase of the oscillations. A higher ionisation probability from the $^2P_{3/2}$ state in comparison to the $^2P_{1/2}$ state leads to a featureless, time-independent background in the photoelectron signal at flight time 440 ns at t >0 [138].

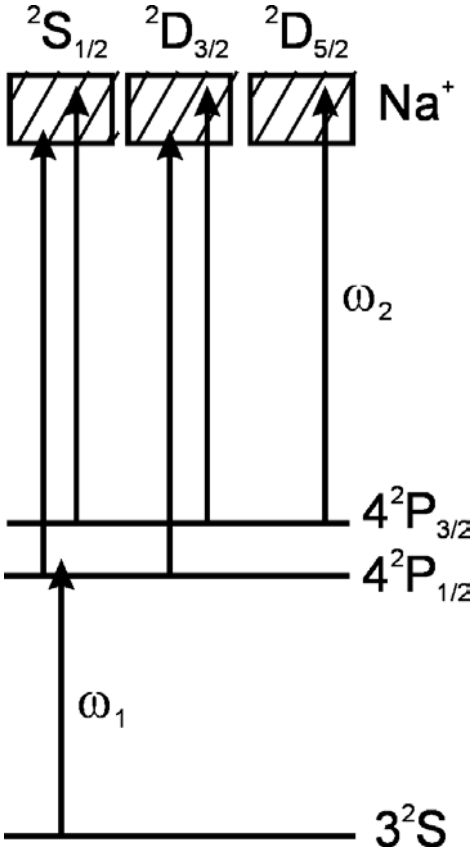

Figure C.6: The scheme of ionisation of Na. The $^2S_{1/2}$ and $^2D_{3/2}$ states of Na^+ ion can be reached from both $4^2P_{1/2,3/2}$ fine-structure states thus leading to oscillations in photoelectron signal.

The contrast of the oscillations can be calculated as [138]:

$$C = 2\frac{I_{\max} - I_{\min}}{I_{\max} + I_{\min}}, \tag{C.2}$$

where I_{max} is the intensity at maxima of the oscillations, I_{min} is the signal intensity at minima of the oscillations. The experimental value derived from the Figure C.5 consists 1.24. This value is higher than the analogous value of 0.34 defined in the experiment on potassium atoms performed with ion yield detection [138]. The calculated theoretical value of the oscillation contrast for the experiment on potassium atoms is 0.56 [138]. The low experimental value of the oscillation contrast, according to authors [138], could be due to apparatus reason. The higher contrast of the oscillations in our experiment can be due to the scheme with photoelectron detection. The ion yield signal is an average over several ionisation channels which can contribute to the signal, whereas the photoelectron detection enables to differentiate between the ionisation channels by resolving the kinetic energy of photoelectrons. However our value of 1.24 is approximately two times higher then the theoretical value of 0.56 derived for the potassium atom, whereas we believe that they should be nearly equal because of the similiarity of both Na and K atoms.

C.3 Conclusions and outlook

A direct observation of fine-structure structure splitting in $4^2P_{1/2,3/2}$ doublet of Na atoms is performed. The method used in our experiment is a pump-probe scheme with a photoelectron detection. In a scheme a first femtosecond laser pulse excites the wave packet as a sum of the

close lying doublet states, which is then evolved freely and is probed by the second, time-delayed pulse via ionisation. The measured level splittings are in good agreement with the literature values. Detection of the photoelectron signal is advantageous in comparison with the ions as it supresses background from two-photon ionisation. The experiment demonstrated the applicability of pump-probe femtosecond method to observe the quantum mechanic dynamics in simple systems, such as Na atoms. Extension to more than two excited states leads to new features, including the appearance of several frequencies in the oscillation pattern. This situation is encountered with the vibrational wave packets described in the Chapter 5.

Once the spin angular momentum is identified as a quantity which changes its direction during the wave packet evolution, the wave packets can be produced with a controlled spin-polarisation rate [141]. Using the of such spin-polarised electrons on a femtosecond timescale combined with ultrafast diffraction technique may be a promising way to probe the molecular dynamics during chemical reactions [142].

Appendix D

Applied voltages and currents

The appendix shows the required values of voltage and current used during the experiments with the electron spectrometer and the ion spectrometer.

The typical values for the *electron spectrometer*:

MCP-Input:	+ 2100 V
MCP-Output:	Ground
Grid:	Voltage in stepwise manner for calibration (typically U_g = -1 … +2 V); Constant voltage during the measurement
Pole-plates (upper and lower):	U_{pp} = -0.6 … -0.8 V, when clean; up to -25 V, when covered with alkali metal layer
1 T-coil:	4 A at about 60 V (current is stabilised)
1 mT-coil:	2 A at about 0.8 V (current is stabilised)
Inner Helmholtz coil:	10-15 V at ~ 0,3 A (voltage is stabilised)
Outer Helmholtz coil:	5 V at ~ 0.1 A (voltage is stabilised)

The typical values for the *ion spectrometer*:

MCP-Input:	Ground
MCP-Output:	- 2000 V
MCP-Anode:	+ 100 V
Ion optics lens (Input, Output):	Ground
Ion optics lens (Mitte):	+ 160 V
Upper pole-plate:	+ 409 V
Lower pole-plate:	+ 390 V

Appendix E

Calibration procedure of the electron spectrometer

The procedure of calibration of the magnetic bottle spectrometer is presented here together with the programs needed for the calibration and the data treatment. All the programs described here are created using the National Instruments LabVIEW programming, versions 5.1/6.1. The programs are located in the directory *\\physpdc\exp3-all\Lab-View*.

In order to perform a calibration, one should perform the following steps:

E.1 *Read_osci.vi*

- Objective: saves the time of flight spectra corresponding to the different grid voltages U_g. The program is in the directory *exp3-all\Lab-View\Lecroy\Photoelectrons.*
- Input data: "Source": indicates the channel of the LeCroy oscilloscope;

  "File Path": indicates the directory to save the measurement file. Normally it is *exp3-all\Projects\Mabos\Data\yymmdd*, where *yymmdd* are the year, months and day of the current measurement;

"Dot"-"Komma": the button saves the numbers either with commas or dots, the default is "Dot".

- Output data: the spectrum from the LeCroy is saved as a file with extension .dat in the directory mentioned in the file path.

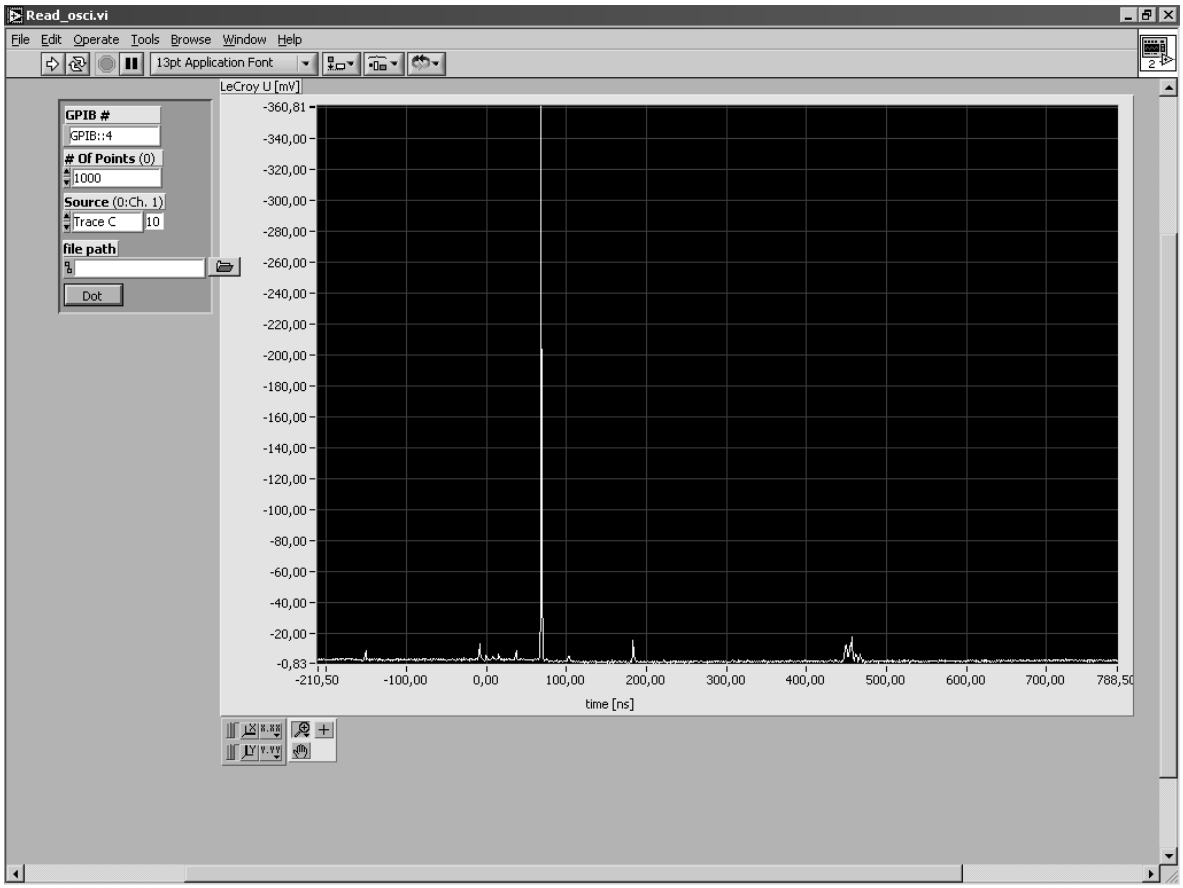

The program saves a measured TOF spectrum as dat-file. Usually several (5 – 10) spectra are saved for U_g changing in 0.2 V steps. The grid voltage U_g used in experiment at the same day must be within the range of U_g applied for the calibration.

E.1a *PowerMeterSaveLoadNewLeCroy.vi*

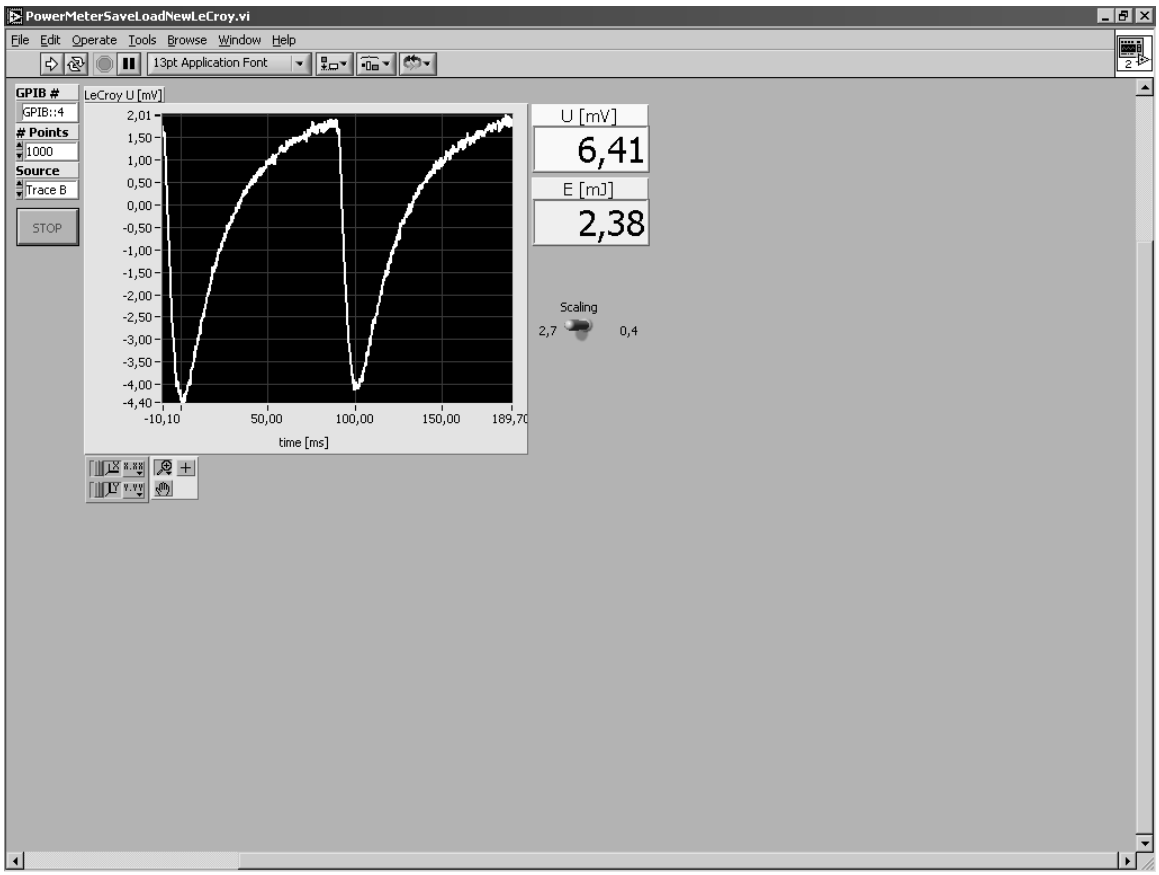

- Objective: Measures the energy of the YAG or dye laser pulses. The program is placed in the directory *exp3-all\Lab-View\Lecroy\PowerMeter*.
- Input data: "Source": Trace B of LeCroy oscilloscope by default;

  "Scaling": on 0.4 for for the 3rd harmonic of the YAG laser and on 2.7 for the 2nd harmonics of the YAG and the day laser.
- Output data: The energy of the laser is read in the window "E[mJ].

The measurement is started with pressing the "Run" button. The energy of the laser pulse is read as a value in mJ in the window "E, mJ". It is important to press the "STOP" button in the program window after the measurement, so that the program could restore the previous settings of the LeCroy. The measurement of the laser pulse energy is performed before and after every calibration series.

E.2 *FitPhotoelectronsSave_All.vi*.

- Objective: fits the Gausian of the calibration measurement profiles of lines in the measured photoelectron spectra as functions of time. As a result the time of flights of the photoelectrons resulting from ionisation of different states of Xe, Na atoms are obtained from spectra taken with different voltages U_g. The file is located in *exp3-all\Lab-View\Photoelectrons*.

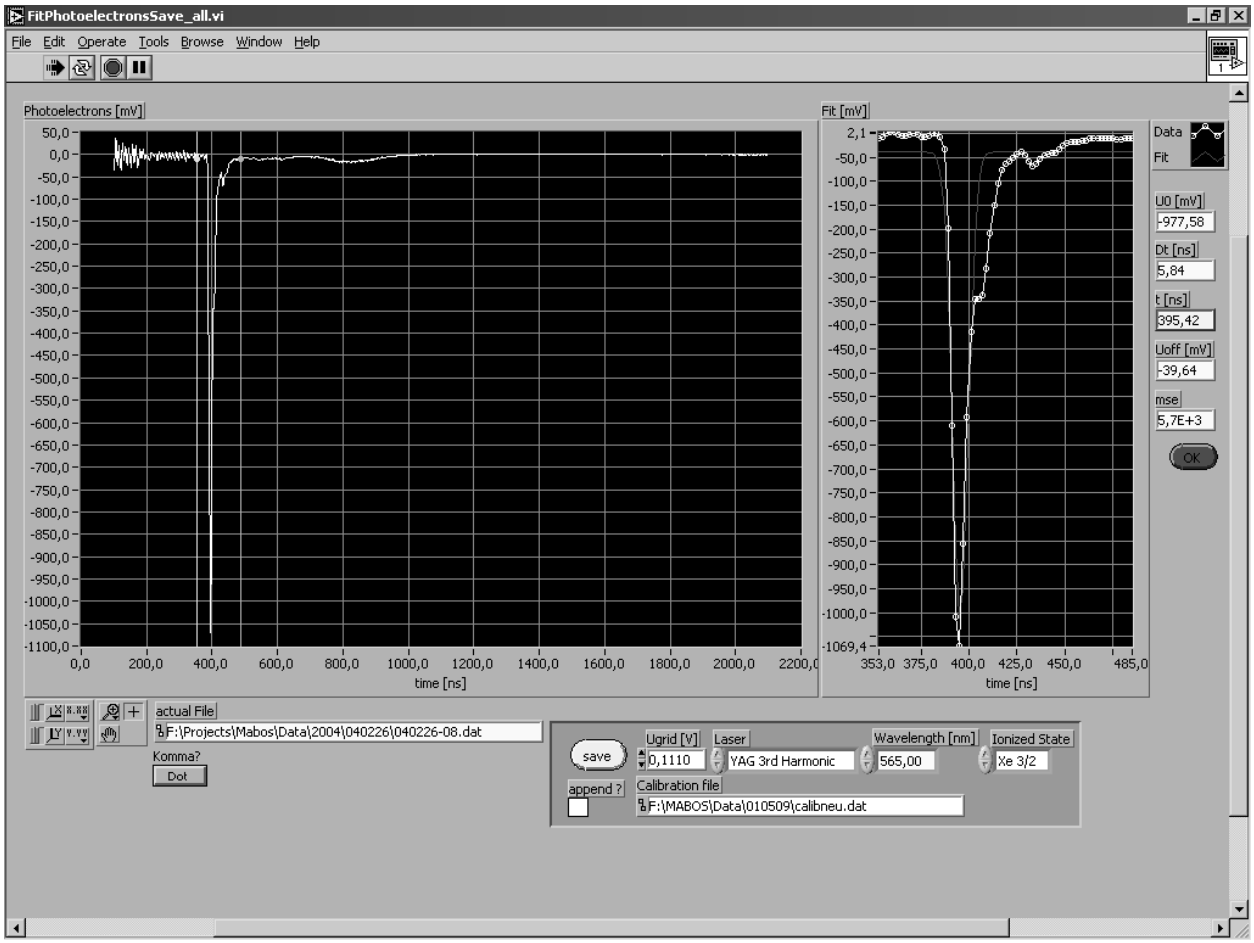

- Input data: "Actual file": reads the time of flight file to be evaluated;

  "Ugrid[mV]": a value of U_g corresponding to the current file;

  "Laser": the laser type and harmonics used in measurement;

  "Wavelength [nm]": only in the case of dye laser one should input the laser wavelength;

  "Ionized State": input the identified ionised state (Xe1/2, Xe3/2, Na or K) corresponding to the line in the spectrum;

  "Calibration file": input the name of the file with output data;

  "append?": check every time after the first time, then the data will be appended to the existing file.

- Output data: Calibration file with the name written in the field "Calibration file".

After the filling the above data, the program is started with the pressing of "Run" button. The loaded spectrum will appear in the window "Photoelectrons [mV]".

In order to save the parameters of the needed line in the spectrum, one should separate with two cursors the line in the window "Photoelectrons [mV]" (the Gaussian fit appears as a red line in the window "Fit [mV]"), fill in the "Ionized State" field corresponding to the line of the spectrum, then press the "save" button, and repeat this procedure for the next lines in the spectrum. When the work with this spectrum is finished, press the "OK" button, then the program is ready to work with the next file. Repeat with all the files saved for different U_g.

The program generates the "calibration file" with extension "*dat*", where the parameters are stored in the form:

| level | Energy of Photons [eV] | Grid Voltage [V] | TOF (centre of Gaussian) [ns] | dt width of Gaussian [ns] | height of Gaussian [mV]

These values are appended for every line. The example of the calibration file is shown below:

1,00000000 1,85618174 2,00399995 480,44287109 -8,50495148 -962,71838379 20,00000000

0,00000000 0,54317999 2,00399995 640,51788330 7,48939180 -56,33808136 20,00000000

1,00000000 1,85618174 1,80100000 492,67178345 7,39432621 -1232,21704102 21,00000000

0,00000000 0,54317999 1,80100000 676,41699219 15,92933559 -49,64966965 21,00000000

E.3 ***Measured Data Save_all.vi***.

- Objective: The program uses the calibration file as the input and generates the file with coefficients a_n and b_n of the fit. The coefficients a_n and b_n are determined using the formula (see also Appendix A):

$$E_k = \sum_{i=0}^{p} \frac{a_i}{T^i} + U_g \sum_{i=0}^{q} b_i T^i , \qquad p,q = 2.$$

- Input data: "calibration file (read)": input the name of the calibration file generated above; "calibration constants file (write)": input the name of the file with coefficients.
- Output: The coefficients are stored in the "calibration constants file" with the format:

a_0 | a_1 | a_2

b_0 | b_1 | b_2

The example of the constants file is shown below:

-2,14981809E-1 1,39708618E+3 1,22689359E+5

3,24935913E-1 -2,88941618E-3 1,63076288E-6

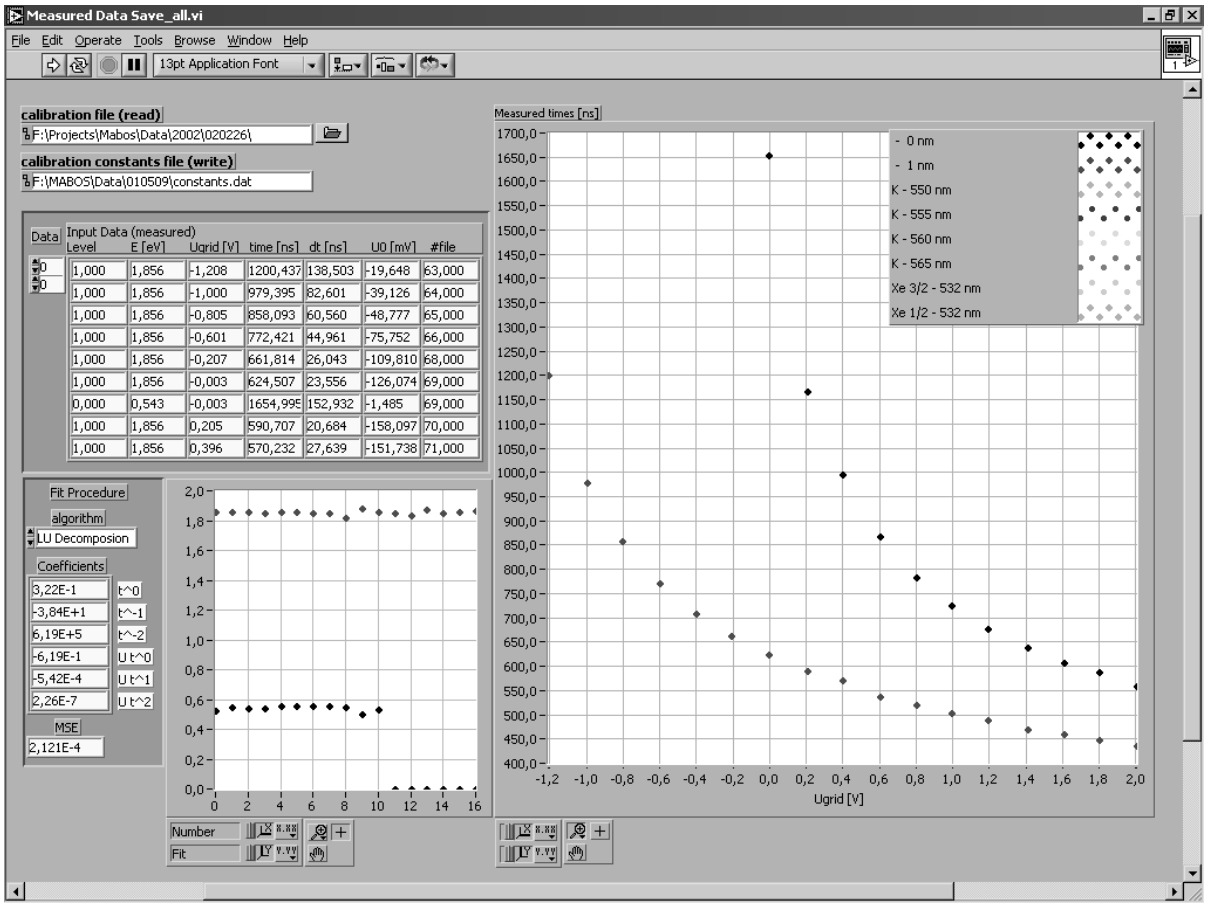
Measured Data Save_all.vi
File Edit Operate Tools Browse Window Help
13pt Application Font
calibration file (read)
F:\Projects\Mabos\Data\2002\020226\
calibration constants file (write)
F:\MABOS\Data\010509\constants.dat
Data
Input Data (measured)
Level E [eV] Ugrid [V] time [ns] dt [ns] U0 [mV] #file
1,000 1,856 -1,208 1200,437 138,503 -19,648 63,000
1,000 1,856 -1,000 979,395 82,601 -39,126 64,000
1,000 1,856 -0,805 858,093 60,560 -48,777 65,000
1,000 1,856 -0,601 772,421 44,961 -75,752 66,000
1,000 1,856 -0,207 661,814 26,043 -109,810 68,000
1,000 1,856 -0,003 624,507 23,556 -126,074 69,000
0,000 0,543 -0,003 1654,995 152,932 -1,485 69,000
1,000 1,856 0,205 590,707 20,684 -158,097 70,000
1,000 1,856 0,396 570,232 27,639 -151,738 71,000
Fit Procedure
algorithm
LU Decomposion
Coefficients
3,22E-1 t^0
-3,84E+1 t^-1
6,19E+5 t^-2
-6,19E-1 U t^0
-5,42E-4 U t^1
2,26E-7 U t^2
MSE
2,121E-4
Number
Fit
Measured times [ns]
- 0 nm
- 1 nm
K - 550 nm
K - 555 nm
K - 560 nm
K - 565 nm
Xe 3/2 - 532 nm
Xe 1/2 - 532 nm
Ugrid [V]

E.4 *TimeToEnergyCurve.vi*

- Objective: Evaluates the time versus kinetic energy curve. It can be found in the directory *exp3-all\Lab-View\Na2Analysis\Photoelectrons*.

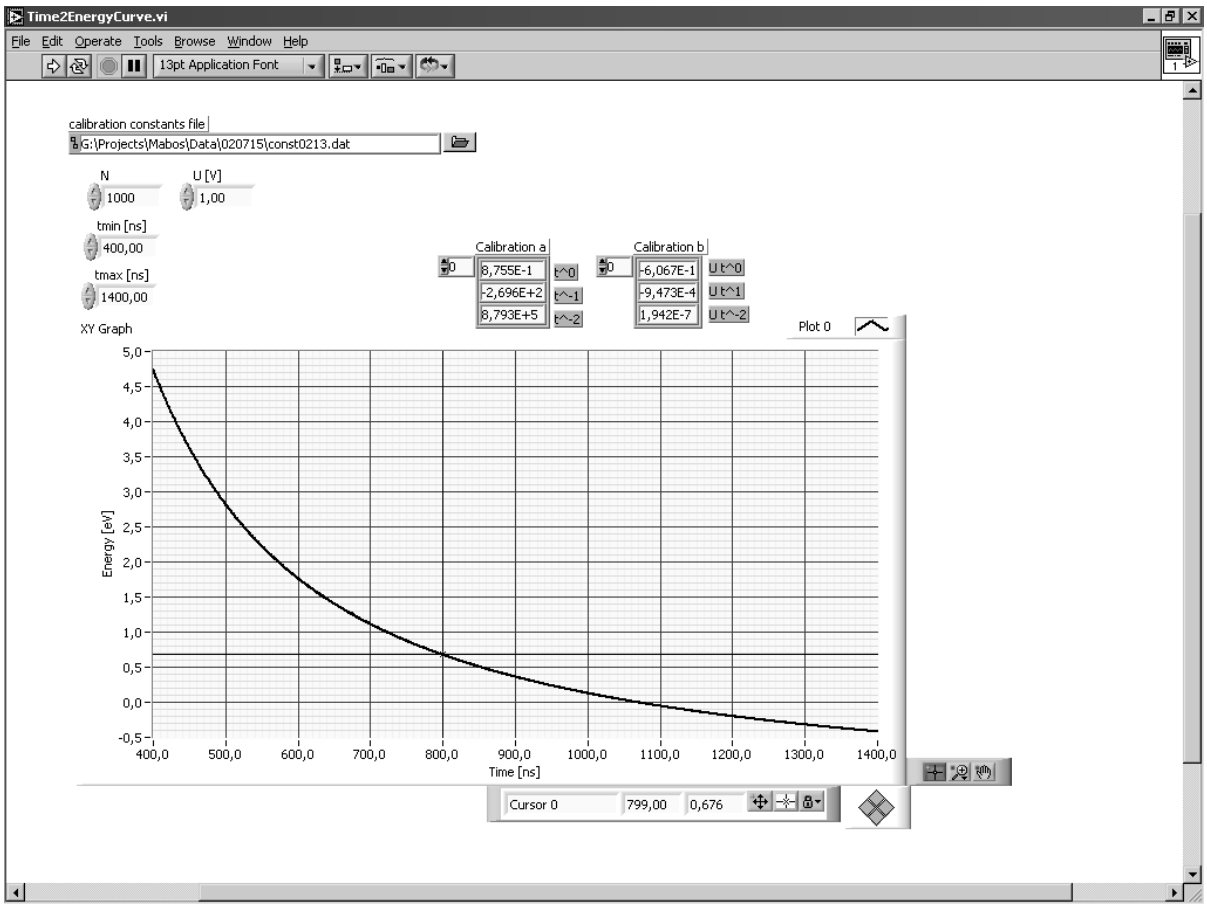

- Input data: "calibration constants file" is the name of the file with calibration constants generated in the E.3;

  "N" is the number of points of the curve, 1000 by default;

  "U [V]" is the grid voltage U_g at which the actual data are taken;

  "tmin [ns]" and "tmax [ns]" are the time intervals for which the curve is calculated.

- Output data: the calibration curve appears in the graph of kinetic energy as a function of time of flight.

This step is not necessary for the calibration, it is used to visualise the calibration curve.

E.5 *Time2Energy Load Data Save E.vi*

- Objective: Converts the photoelectron time of flight spectra into the photoelectron energy spectra. The program is located in *exp3-all\Lab-View\Photoelectrons*.
- Input data: "Photoelectrons (t) file": input the TOF measured file (saved with *Read_osci.vi*) to be calibrated;

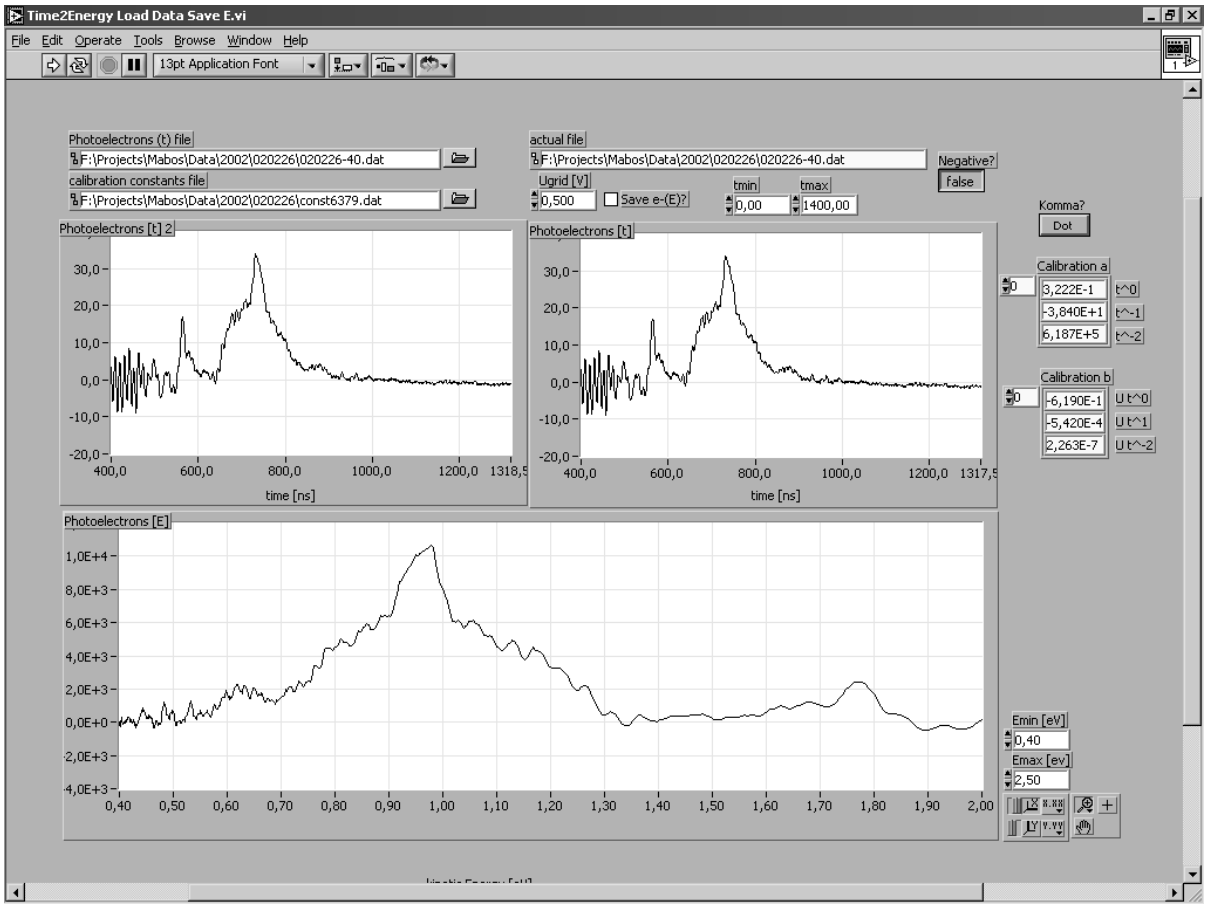

- Input data: "Photoelectrons (t) file": input the TOF measured file (saved with *Read_osci.vi*) to be calibrated,

  "calibration constants file": input the calibration constants file, generated in **E**.3;

  "Ugrid [V]": input the grid voltage U_g of the measured spectrum;

  "tmin" and "tmax": input the TOF segment of the spectrum to be calibrated;

  "Negative?": input "true" if the TOF file have negative ordinate scale;

  "Komma?": input "komma" or "dot" dependent on the wished TOF file data format;

  "Emin [eV]" and "Emax [eV]": input the energy segment;

  "Save e-(E)?": check to save the calibrated energy file.

- Output data: calibrated *dat*-file of photoelectron energy versus signal.

To run the program fill in the above mentioned fields, then press the "Run" button. The initial TOF spectrum appears in the upper left window "Photoelectrons [t] 2". The selected segment of the spectrum defined by "tmin" and "tmax" placed is in the upper right window called "Photoelectrons [t]" will be calibrated. The resulting energy spectrum appears in the window "Photoelectrons [E]". This photoelectron energy spectrum can be stored in a file with the same name as the loaded one and additional extension "*_e"*.

E.6 ***FitPhotoelectrons Energy.vi***.

- Objective: the centre and the FWHM of the lines in the photoelectron energy distribution are evaluated. The program fits a Gaussian to the photoelectron distribution as a function of energy.
- Input data: "actual file": the name of the file to be evaluated.
- Output data: "E,[eV]" reads the central energy of the line; "FWHM [meV]" reads the halfwidth of the line.

The two cursors in the spectrum window serve for selection of the needed line in the spectrum. The centre of Gaussian fitted to the line is shown in the "E [eV]" window, and the halfwidth is in the "FWHM [meV]" window. Pressing the "OK" button finishes the work with the file and the program is ready to read the next file.

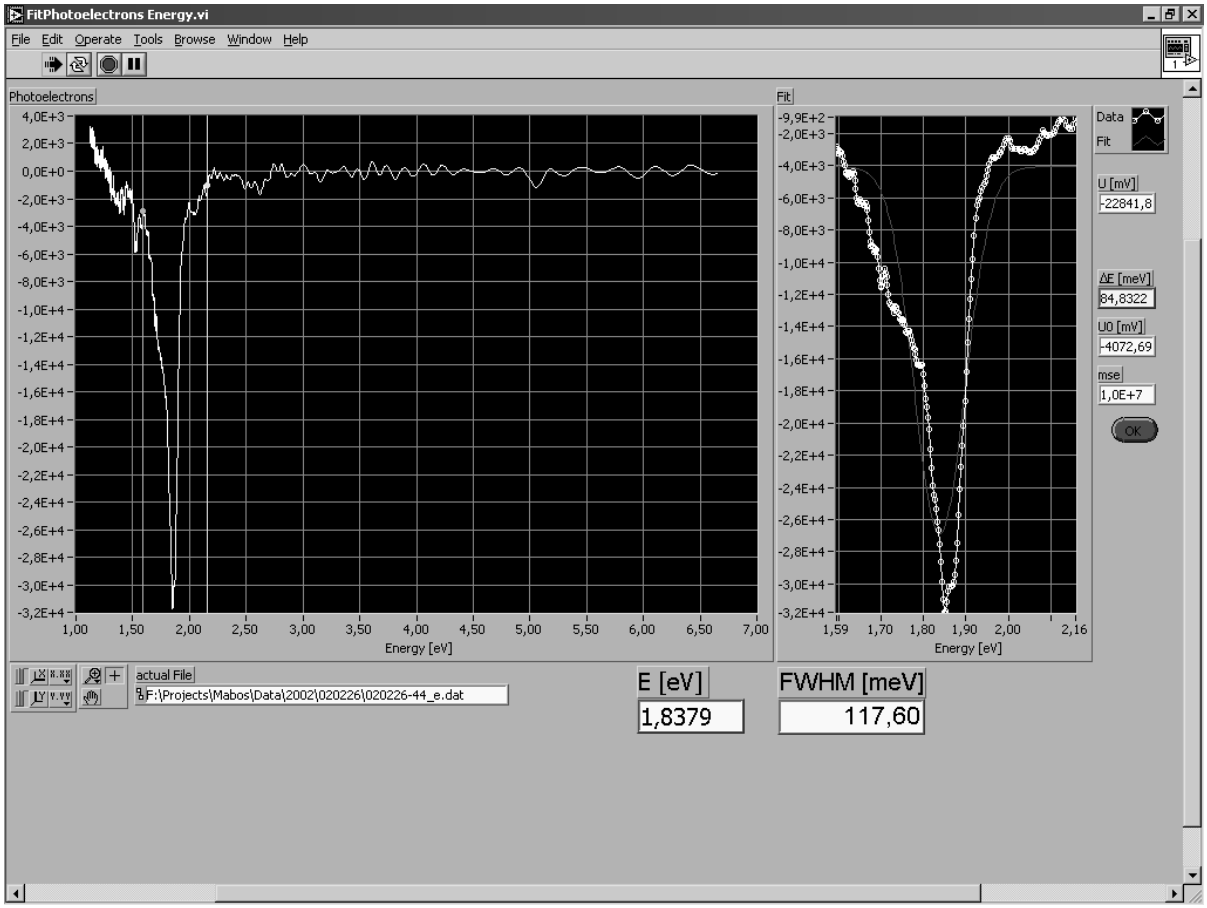

Alternatively, for calibration of the *scanned* two-dimentional (time of flight versus delay between laser pulses) photoelectron spectra, saved with the program *MM-O_v3.vi* [83] first steps 1 – 4 are performed and then the steps 5 and 6 are substituted by the following procedure:

E.1-4 Like in the calibration procedure above.

E.7 *CalibrateImage.vi*

- Objective: The program for calibration of the scanned time of flight photoelectron spectra. located in *exp3-all\Lab-View\Na2Analysis\Photoelectrons\ConvertImages* is applied.
- Input data: "Photoelectrons (start path)": input the directory of the file to be calibrated. The program calibrates only the files with the extension "*lcs"*.

  "calibration constants file": input the (exact!) name of the file generated in E.3;

  "Ugrid [V]": input the grid voltage U_g corresponding to the actual file;

  "N": the number of points to split the energy spectrum, is 1000 by definition;

  "save?": check to save the calibrated image.
- Output data: the calibrated file is saved into the same directory with the same name and an additional extension "*_cal*".

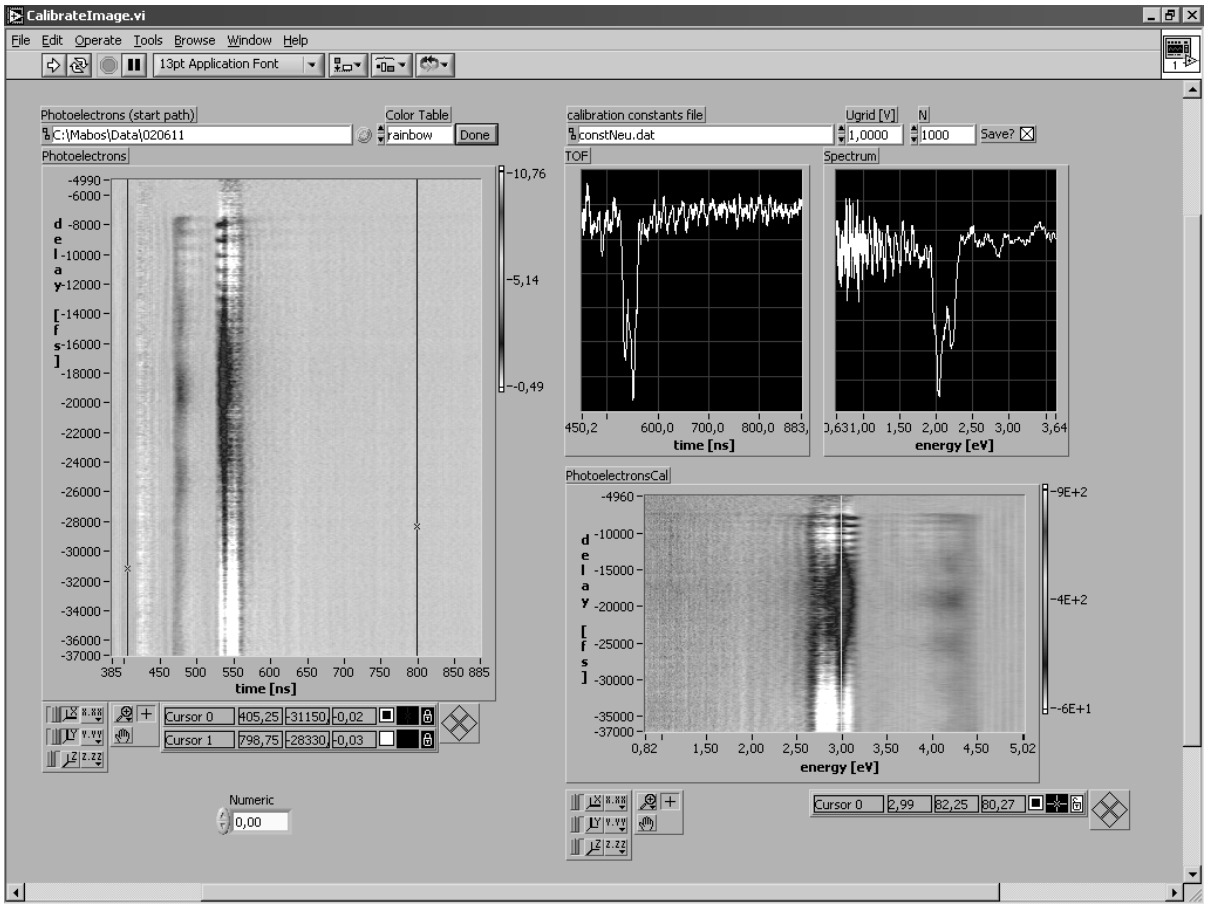

The input file, a scan performed with the program *MM-O_v3.vi* and saved with the extension "*lcs*" represents the 2D plot of the time of flight along the abscissa and the pump-probe delay time in femtoseconds along ordinate. The generated calibrated file is also a 2D plot of the kinetic energies along abscissa and the delay time along the ordinate.

Before (!) starting the program the fields "calibration constants file", "Ugrid [V]" and "save?" should be filled. After loading of the file the segment of the time of flight spectrum needed to be calibrated is selected with two cursors. (Important: it is necessary to check carefully this

interval before the calibration!) After that pressing the button “Done” starts the calibrating procedure. If the field “save?” was checked, then the program saves the calibrated file into the same directory with the additional extension “*_cal*”.

Appendix F

Programs to work with pump-probe photoelectron spectra

The programs for processing the measured photoelectron signal, for calculation of the photoelectron spectra and for comparison of the measured and the calculated spectra are presented here. The programs described here are created using the National Instruments LabVIEW programming, versions 5.1/6.1. The programs are located in the directory *\\physpdc\exp3-all\Lab-View*.

The next four programs are used for the experimental data treatment:

F.1 *ShowDataColorBC.vi*

- Objective: The program to visualise the pump-probe files. It can be found in the directory *exp3-all\Lab-View\Na2Analysis\FourierAnalysis*.
- The input data: "start path" and "file path": input the directory and the name of the file to view. The extension of the file could be "lcs" or " spc".

The program starts with asking for the name of the measured file. The loaded file appears in the window "Photoelectrons". The parameters of the experiment appear in the window "Parameter File". After that one can start to manipulate with the appearance of the data. One can choose the color palette representation with "Color Table" option. Usually "f rainbow" or "lt rainbow" are used. When necessary, the averaging method and the degree of averaging can be chosen in "D-Matrix" and "# Avg" fields. Pressing the button "AVG" executes the averaging of the spectrum.

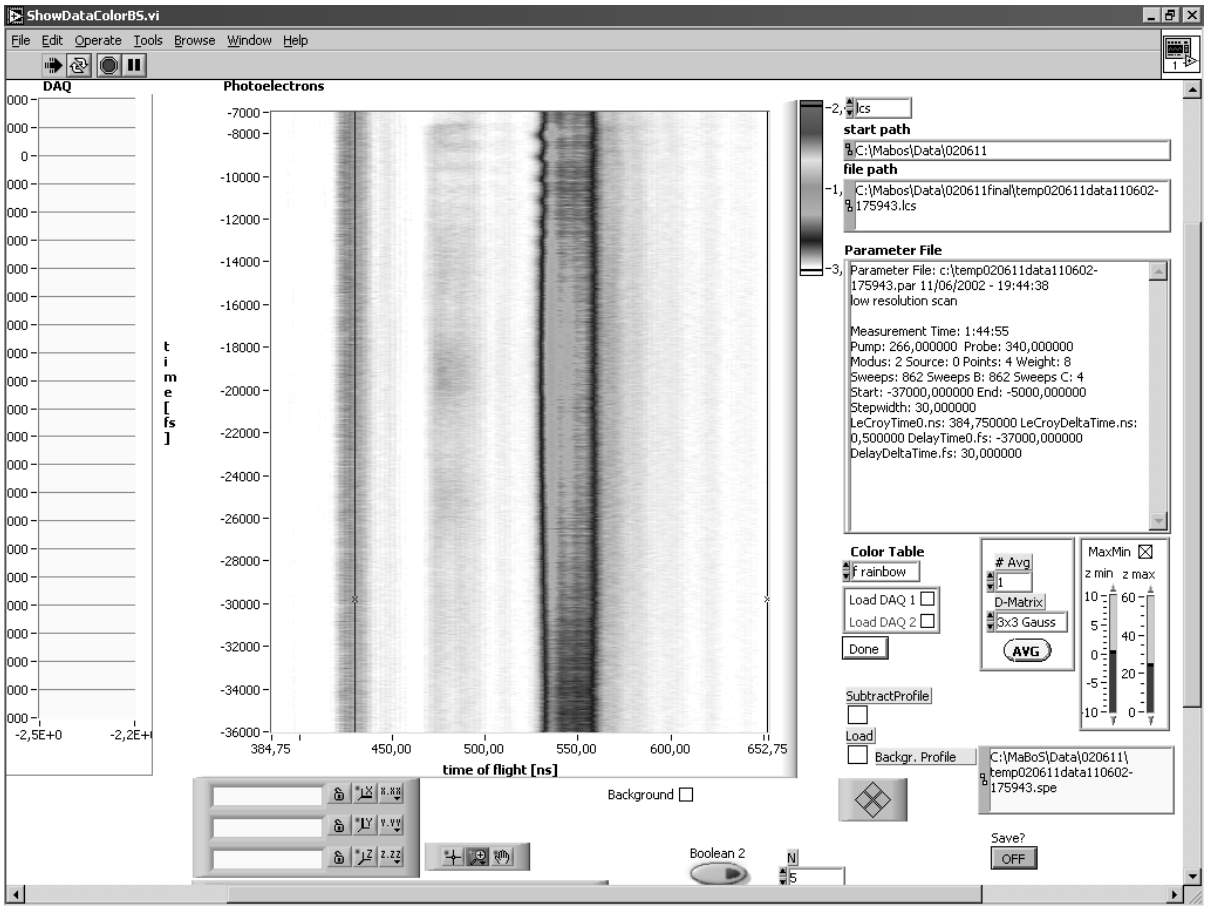

The option "MaxMin" enables to find an optimal contrast of the spectrum, one should play with "z min" and "z max" to achieve an optimal appearance. After that the file can be saved if the field "save?" was checked.

F.2 *QAnalyzeProfi.vi*

- Objective: The program performs the following:
  - Subtracts the background
  - Averages the spectra
  - Smoothes the spectra along abscissa and ordinate
  - Saves the final spectrum
  - Takes cuts of the spectrum along the y-axis (time profiles)

  The program is in the directory *exp3-all\Lab-View\Na2Analysis\FourierAnalysis*.
- Input data: "start path" and "file path": input the directory and the name of the initial file.

  The extension of the file could be "lcs" or " spe".

The program starts with loading the file. The loaded file appears in the window "photoelectrons". In order to subtract the background, one chooses the spectrum to be subtracted in this window with ordinates of two cursors. Additionally, the spectrum to be subtracted can be smoothed along energy axis with the option "smooth spectra" and along time axis with the option "smooth time spectra".

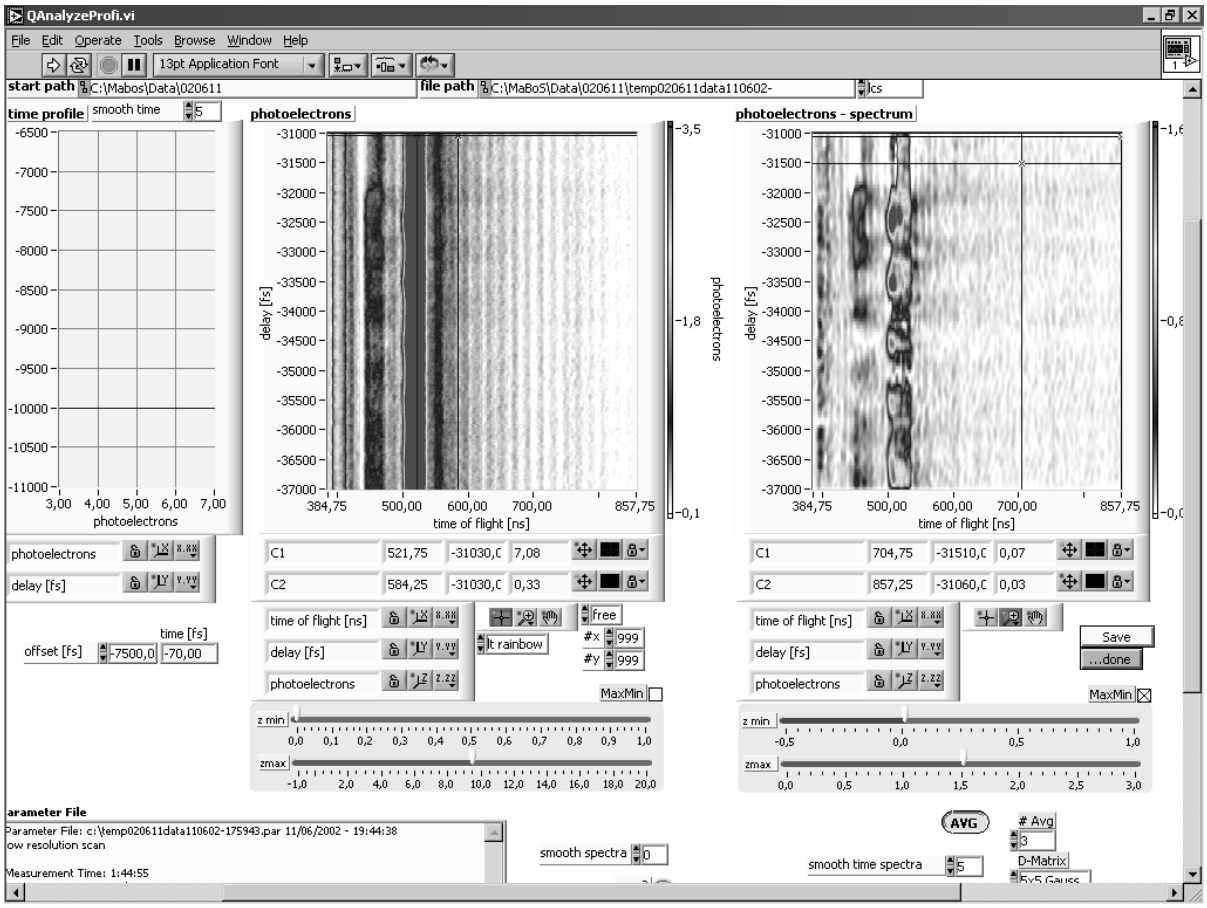

The time profile of the initial spectrum can be extracted with two cursors in the "photoelectrons" window. The abscissas of the cursors give the area to average. The spectrum can be controlled in the field "time profile", it can be additionally averaged in the field "smooth time". The spectrum can be saved with pressing the button "save?".

The resulting photoelectron spectrum obtained by the subtracting the background appears in the window "photoelectrons – spectrum" online, i.e. in a few seconds after the manipulating with subtraction file parameters. It can be averaged using the fields "D-Matrix" and "# Avg". It can be additionally smoothed along the x-axis with field "smooth spectra 2". Pressing the "Save" button saves the resulting spectrum with the extension "lcs".

F.3 *PhotoelectronSpectra.vi*

- Objective: The programs performs cuts of the photoelectron scans along the x-axis (giving the photoelectron spectra at certain time delay) and their subsequent averaging.
- Input data: "start path" and "file path": input the directory and the name of the initial file. The extension of the file is "lcs".

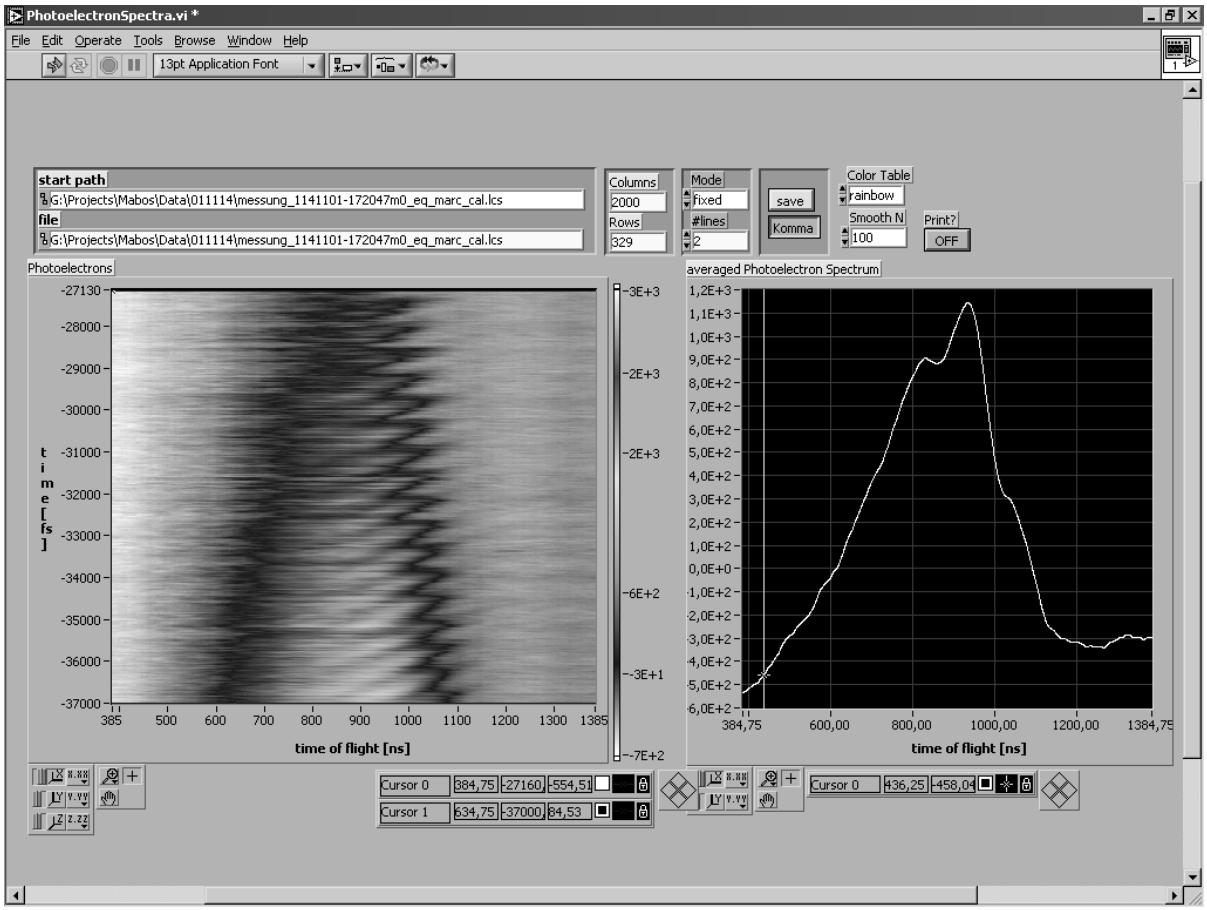

The program starts with loading the scan. The scan appears in the window “Photoelectrons”. The y-region for the photoelectron spectrum is chosen by the ordinate of two cursors. The resulting photoelectron spectrum appears in the field “averaged Photoelectron Spectrum”. It can be additionally smoothed with the field “Smooth N”. The spectrum can be then saved by pressing the button “Save” with the parameters “Dot”-“Komma” (default is Dot). The files are saved with the same name as original file and extension “spe”.

F.4 *FourierAnalysis3.vi*

- Objective: The program performs the following:
  - Subtracts up to two background files from the scanned spectrum
  - Averages the spectrum (duplicates the program *QAnalyzeProfi.vi*)
  - Takes cuts along the time axis (duplicates the program *QAnalyzeProfi.vi*)
  - Performs the FFT spectrum of the scan
  - Performs a cut of the FFT spectrum along the frequency axis

  The program is in the directory F:\Lab-View\Na2Analysis.
- Input data: “start path” and “file path”: input the directory and the name of the initial file.

  The extension of the file is “lcs”.

  “1st Backgr. File” and “2nd Backgr. File”: input the (exact!) names of the background files or one of them. This option is switched on when the field “Load” is checked. (Attention! Even if the option “Load” is not checked, in both fields “1st Backgr. File”

and "2nd Backgr. File" there should be the names of the existing files. Otherwise the program may not work!).

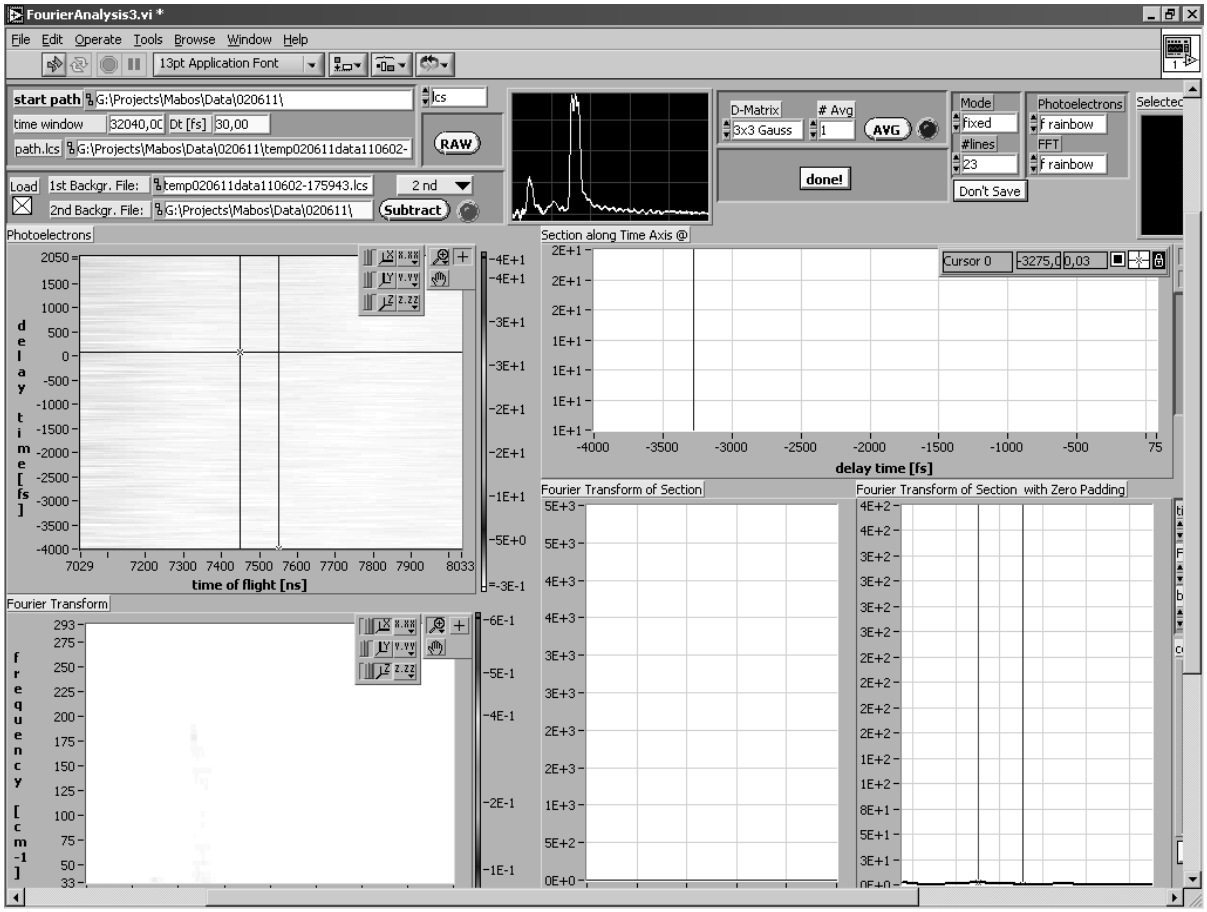

"D-Matrix", "# Avg": should be filled in before running the program if averaging is required. The button "AVG" should be also pressed (indicated by pink color).

The program starts with loading the file (and, if needed, the background files). The background can be subtracted by pressing "Subtract" button. The loaded, as well as the resulting, spectrum appears in the window "Photoelectrons". The area for the cuts along the time delay axis is selected with two cursors. The time profile spectrum appears in the window "Section along Time Axis @". Additionally, it can be smoothed using the field "Smooth" and saved. The Fourier spectrum for the selected area along ordinate axis appears in "Fourier Transform" window. Its cut along the frequency axis is shown in the window "Fourier Transform of Section with Zero Padding". It can be also saved with pressing the "Save?" button.

The two next programs are used for calculation of the photoelectron spectrum and the FFT of the spectrum.

F.5 *FastPhotoelectronsμ(R)2.vi*

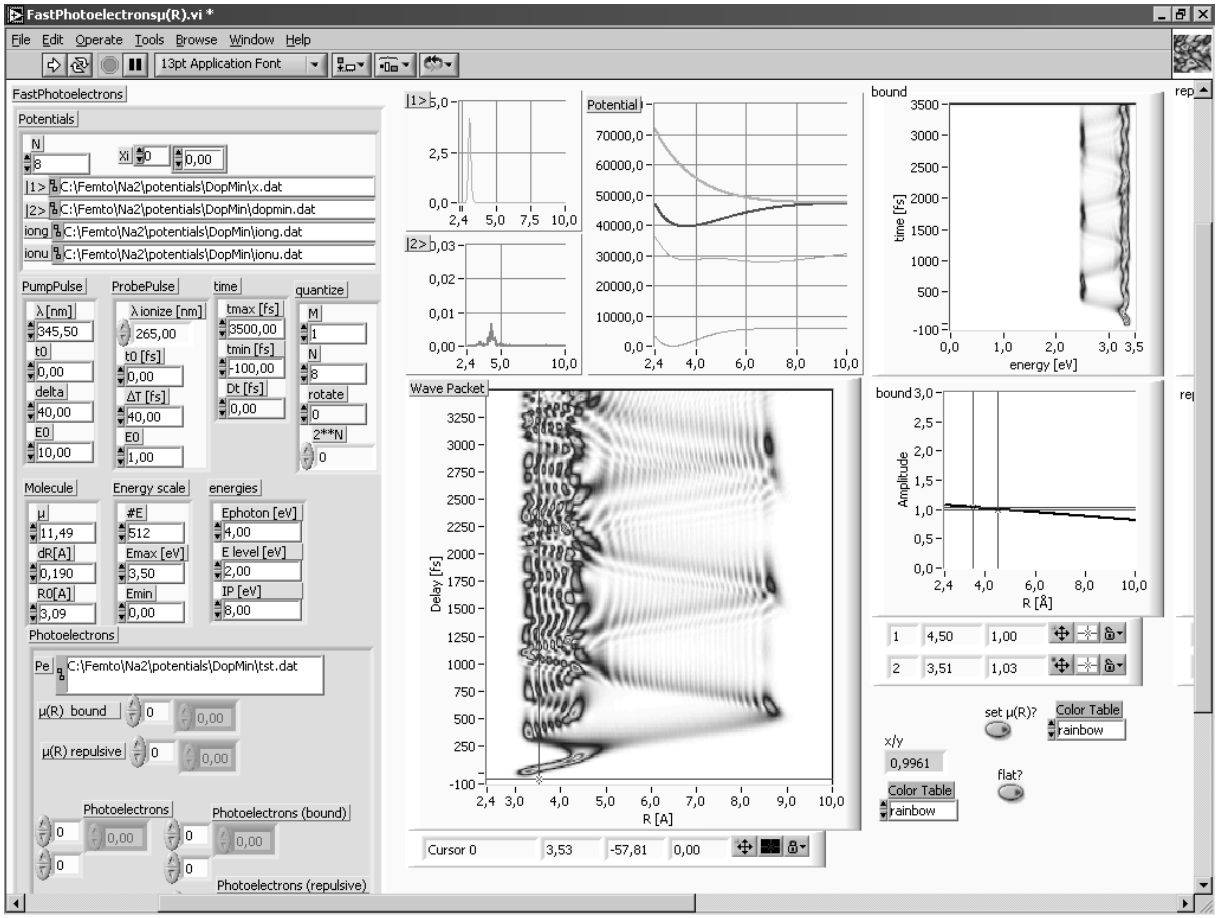

- Objective: The program calculates the photoelectron spectrum assuming the dipole moments for ionisation into the bound and the repulsive ionic states as functions of internuclear distance R. The program is in the directory F:\Lab-View\Na2Analysis\2level.

- Input data:

  The group "Potentials" is related to the potential states of the investigated molecule. "N": input the level of quantising the wave packet evolution calculation, 8 is for fast calculations, the precise calculation require level 10. "I1>", "I2>", "iong", ionu": input the potentials data for the ground state, excited state, first (where "g" means "gerade") and second (where "u" means "ungerade") ionic states of the molecule respectively.

  The groups "Pump pulse" and "Probe pulse" are related to the parameters of the laser pulses. "λ [nm]" and ""λ ionize [nm]": input the central wavelength of the pump and the probe pulse. "Delta [fs]" and "DT [fs]": the durations of the pump and the probe pulses.

  The group "time" is related to the time range for the calculation. "tmax [fs]: input the maximal time for the calculation. "tmin [fs]": input the minimal time.

  The group "Energy scale" is related to the kinetic energy range for the calculation. "Emax [eV]: input the maximal kinetic energy for the calculation. "Emin": input the minimal energy.

The field "Pe": input the path and the name of the file with the calculated photoelectron spectrum.

Other parameters can remain their default values.

The program is started by the pressing "Run" button. After that the input of the $\mu(R)$ is performed. It is important to press the "set μ(R)?" button before starting the program, so the button should have green color. The functions of the $\mu(R)$ are shown in the graphics "bound amplitude" and "repulsive amplitude". There could be three functions, and therefore three regimes of the $\mu(R)$ input:

- For zero or linear functions $\mu(R)$ change the view of the $\mu(R)$ functions by the two cursors in the graphics "bound amplitude" and "repulsive amplitude"
- For Heaviside functions check the "flat?" before the starting of the program and change the height of the step by one cursor.
- For $\mu(R)$ functions representing a combination of a constant and a linear function input values of the constant in the fields "Offset bound" and "Offset repul" and then change the view of the function with two cursors.

Pressing the button "set μ(R)?" will start the calculations. The quota of the performed calculations can be seen in the field "x/y". The calculated wave packet appears in the graphic "Wave Packet", the calculated photoelectron signal for the bound ionic state in "bound" and for the repulsive ionic state in "repulsive" graphics separately and the combined (incoherently added) photoelectron spectrum – in the graphic "Merged Photoelectrons". The spectrum is saved automatically under the name in the field "Pe".

F.6 *FastPhotoelectronsμ(R)f1.vi*

- Objective: The program calculates the FFT spectrum of the pump-probe measurement file as a function of the pump-probe delay and a photoelectron kinetic energy assuming the dipole moments for ionisation into the bound and the repulsive ionic states as functions of internuclear distance R. The program is in the directory F:\Lab-View\Na2Analysis\2level.
- Input data of the program are the same as for the program *FastPhotoelectronsμ(R)2.vi.* The calculated FFT spectrum is shown in the graphic "Merged Photoelectrons 2".

The following two programs perform the comparison of the calculated and the measured data.

F.7 *CompareMeasuredCalculated.vi*

- Objective: The program compares the cuts along the pump-probe axis for the calculated and the measured photoelectron spectra and saves the resulting calculated and measured cuts.

  The program is in the directory F:\Lab-View\Na2Analysis\FourierAnalysis.

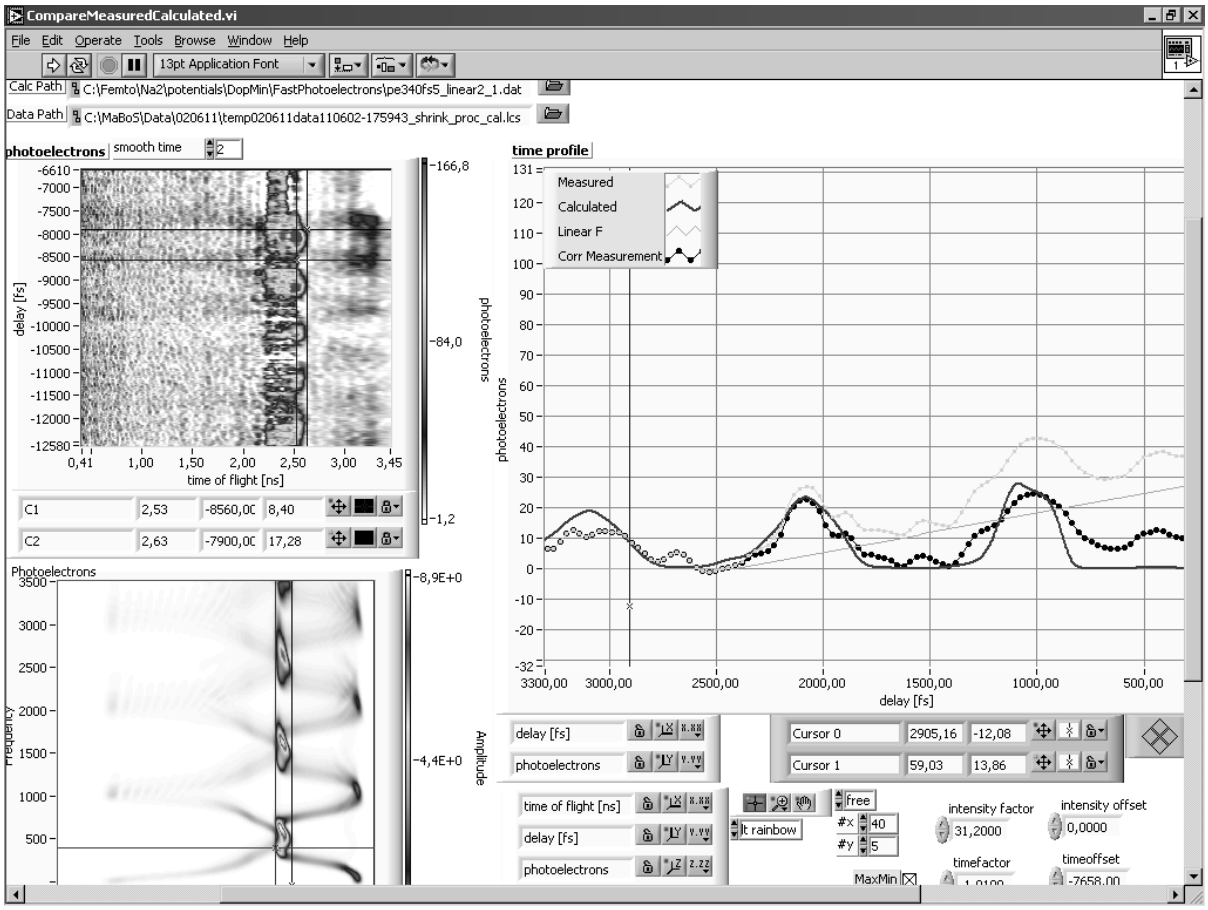

- Input data: "Calc Path": input the name of the file with calculated photoelectron spectrum, generated, for instance, by the program *FastPhotoelectronsμ(R)2.vi.* "Data Path": input the measured signal file.

The measured photoelectron spectrum appears in the graphic "photoelectrons", additionally smoothing along the time axis can be applied, the rate of smoothing is changed in the window "smooth time". The calculated spectrum is seen in the window "Photoelectrons" below. In order to select the time intervals to compare, one uses two cursors in both graphs. The cuts along the delay axis selected appear in the window "time profile". One can use scaling of the calculated spectrum, the intensity can be changed in the window "intensity factor" and the time scale in the window "timefactor". The corresponding offsets to the axes can be changed in windows "intensity offset" and "timeoffset". The background of the measured spectrum can be subtracted using two cursors in the graph. The button "Zero" can be checked if one wants to allow negative intensity values. Checking the button "Save?" saves the both the calculated and the measured timecuts.

F.8 *CompareMeasuredCalculateEnergyd.vi*

- Objective: The program compares the cuts along the energy axis for the calculated and the measured photoelectron spectra and saves the resulting calculated and measured cuts.

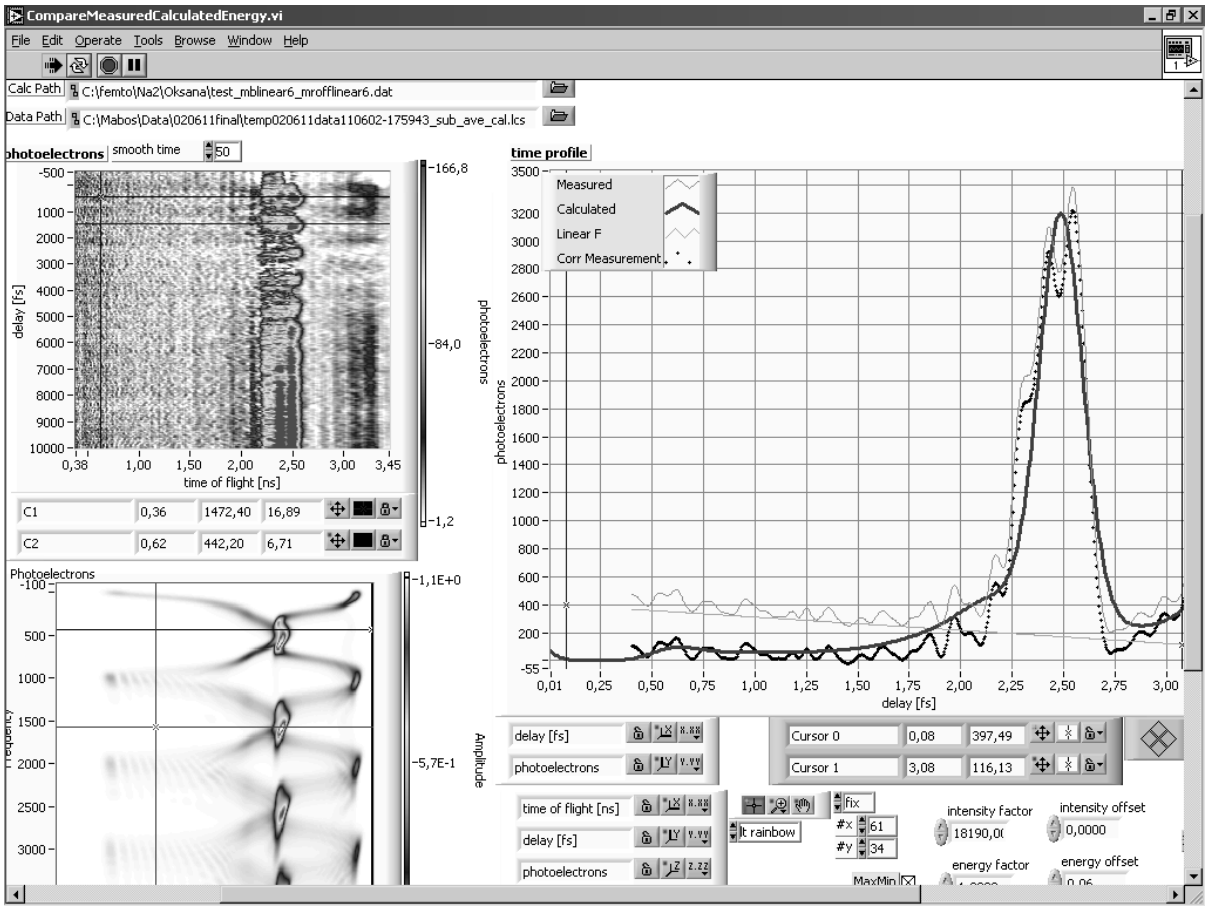

The program is in the directory F:\Lab-View\Na2Analysis\FourierAnalysis.

- Input data: "Calc Path": input the name of the file with calculated photoelectron spectrum. "Data Path": input the measured signal file.

The measured photoelectron spectrum appears in the graphic "photoelectrons", additionally the smoothing along the time axis can be used, the rate of smoothing is changed in the window "smooth time". The calculated spectrum is seen in the window "Photoelectrons" below. In order to select the energy intervals to be compared, one uses two cursors in both graphs. The cuts along the energy axis are shown in the window "time profile". One can scale of the calculated spectrum, the intensity can be changed in the window "intensity factor", the energy scale in the window "energy factor" and the time scale in the window "timefactor". The corresponding offsets to the axes can be changed in windows "intensity offset", "energy offset" and "timeoffset". The background of the measured spectrum can be subtracted using two cursors in the graph. Checking the button "Save?" saves the both the calculated and the measured energy cuts.

Appendix G

List of publications

1. Ultrafast Molecular Events in Chemistry and Biology, Chapter “Quantum control beyond spectral interference and population control: can resonant intense laser pulses freeze the population?”.

M.Wollenhaupt, A. Assion, O. Graefe, Ch. Horn, D. Liese, C. Sarpe-Tudoran, M. Winter, and T. Baumert. Elsevier, in press (2004).

2. Quantum control by ultrafast polarization shaping.

T. Brixner, G. Krampert, T. Pfeifer, R. Selle, G. Gerber, M. Wollenhaupt, O. Graefe, C. Horn, D. Liese, and T. Baumert. Phys. Rev. Lett., accepted (2004).

3. Changes of the electronic structure along the internuclear coordinate studied by ultrafast photoelectron spectroscopy: the $2^1\Sigma_u^+$ Na_2 double-minimum state.

M. Wollenhaupt, A. Assion, O. Graefe, D. Liese, C. Sarpe-Tudoran, M. Winter, and T. Baumert. Chem. Phys. Lett. **376**, 457–464, (2003).

4. Control of interferences in an Autler-Townes doublet: Symmetry of control parameters.

M. Wollenhaupt, A. Assion, O. Bazhan, Ch. Horn, D. Liese, Ch. Sarpe-Tudoran, M. Winter, and T. Baumert. Phys. Rev. A **68**, 015401 (2003).

5. One-parameter control of quantum dynamics using femtosecond pump-probe photoelectron spectroscopy on a model system.

M. Wollenhaupt, A. Assion, O. Bazhan, D. Liese, C. Sarpe-Tudoran, and T. Baumert. Appl. Phys. B **74(1)**, 121–125 (2002).

6. Femtochemistry and Femtobiology, Chapter “Femtosecond Pump-Probe Photoelectron-Spectroscopy on Electronic States of Na_2: A Tool To Study Ultrafast Control of Chemical Reactions”.

M. Wollenhaupt, A. Assion, O. Bazhan, D. Liese, C. Sarpe-Tudoran, and T. Baumert., pages 568–575. World Scientific Publishing (2002).

Bibliography

[1] A.H. Zewail: *Femtochemistry – Ultrafast Dynamics of the Chemical Bond I & II.* World Scientific, New Jersey, Singapore, 1994.

[2] A.H. Zewail, Femtochemistry: *Atomic-Scale Dynamics of the Chemical Bond.* J. Phys. Chem. A 104:5660-5694, 2000.

[3] J. Manz and L. Wöste: *Femtosecond Chemistry.* VCH Weinheim, 1995.

[4] W. Demtröder: *Laser Spectroscopy.* Springer Verlag, Berlin/Heidelberg, 1995.

[5] T. S. Rose, M. J. Rosker, and A. H. Zewail: *Femtosecond real-time probing of reactions. IV. The reactions of alkali halides.* J. Chem. Phys., 91:7415-7436, 1989.

[6] A. Mokhtari, P. Cong, J. L. Herek and A. H. Zewail: *Direct femtosecond mapping of trajectories in a chemical reaction.* Nature, 348:225-227, 1990.

[7] P. Cong, G. Roberts, J. L. Herek, A. Mohktari, and A. H. Zewail: *Femtosecond Real-Time Probing of Reactions. 18. Experimental and Theoretical Mapping of Trajectories and Potentials in the NaI Dissociation Reaction.* J. Phys. Chem., 100:7832-7848, 1996.

[8] R. Andersson, M. Kadi, J. Davidsson, T. Hansson: *Photoionisation of molecular wavepackets – the NaK ($C^1\Sigma^+$) state.* Chem. Phys. Lett., 352:106-112, 2002.

[9] V. Blanchet and A. Stolow: *Nonadiabatic dynamics in polyatomic systems studied by femtosecond time-resolved photoelectron spectroscopy.* J. Chem. Phys., 108:4371-4374, 1998.

[10] V. Blanchet, S. Lochbrunner, M. Schmitt, J.P. Shaffer, J.J. Larsen, M.Z. Zgierski, T. Seideman, A. Stolow: *Towards discentangling coupled electronic-vibrational dynamics in ultrafast non-adiabatic processes.* Faraday Discuss., 115:33-53, 2000.

[11] V. Blanchet, M.Z. Zgierski, A. Stolow: *Electronic continua in time-resolved photoelectron spectroscopy. I. Complementary ionization correlations.* J. Chem. Phys., 114:1194-1205, 2001.

[12] A. Assion, T. Baumert, J. Helbing, V. Seyfried, and G. Gerber: *Femtosecond time-resolved observation of above-threshold ionization in Na_2.* Phys. Rev. A, 55:1899-1902, 1997.

[13] A. Valance and Q.N. Tuan*: The molecular electronic structure of the lowest $^{1,3}\Sigma_{g,u}$ states of Na_2 and K_2.* J. Phys. B, 15:17-33, 1982.

[14] G. Herzberg. *Molecular spectra and molecular structure. Volume I. Spectra of diatomic molecules.* Krieger publishing company. Malabar, Florida, 1989.

[15] R. Schinke. *Photodissociation Dynamics.* Cambridge University Press, 1993.

[16] H. Köppel, W. Domcke and L.S. Cederbaum: *Multimode molecular dynamics beyond the Born-Oppenheimer approximation.* Adv. Chem. Phys., 57:59-246, 1984.

[17] M. Born and J.R. Oppenheimer: *Zur quantentheorie der molekeln.* Ann. Phys., 84:457-484, 1927.

[18] M.J. Rosker, M. Dantus and A.H. Zewail: *Femtosecond real-time probing of reactions. I. The technique.* J. Chem. Phys., 89:6113-6127, 1988.

[19] M. Dantus, M.H.M. Janssen, and A.H. Zewail: *Femtosecond probing of molecular dynamics by mass-spectrometry in a molecular beam.* Chem. Phys. Lett., 181:281-287, 1991.

[20] T. Baumert, M. Grosser, R. Thalweiser, and G. Gerber: *Femtosecond Time-Resolved Molecular Multiphoton Ionization: The Na_2 System.* Phys. Rev. Lett., 67:3753-3756, 1991.

[21] B.J. Greenblatt, M.T. Zanni and D.M. Neumark: *Photodissociation dynamics of the I_2^- anion using femtosecond photoelectron spectroscopy.* Chem. Phys. Lett., 258:523-529, 1996.

[22] V. Stert, W. Radloff, C.P. Schulz and I.V. Hertel: *Ultrafast photoelectron spectroscopy: Femtosecond pump-probe coincidence detection of ammonia cluster ions and electrons.* Eur. Phys. J. D, 5 :97-106, 1999.

[23] P. Farmanara, W. Radloff, V. Stert, H.-H. Ritze and I.V. Hertel: *Real time observation of hydrogen transfer: Femtosecond time-resolved photoelectron spectroscopy in the excited ammonia dimer.* J. Chem. Phys.; 111:633-642, 1999.

[24] L.R. Khundkar and A.H. Zewail: *Ultrafast molecular reaction dynamics in real-time: Progress over a decade.* Annu. Rev. Phys. Chem., 41:15-60, 1990.

[25] G. R. Fleming. *Chemical applications of ultrafast spectroscopy.* Oxford University Press New York, 1986.

[26] C.E. Hamilton, J.L. Kinsey and R.W. Field: *Stimulated Emission Pumping: New Methods in Spectroscopy and Molecular Dynamics.* Ann. Rev. Phys. Chem., 37:493-524, 1986.

[27] D.M. Jonas, X. Yang and A.M. Wodtke: *Axis-switching transitions and the stimulated emission pumping spectrum of HCN.* J. Chem. Phys., 97:2284-2298, 1992.

[28] T. Baumert, R. Thalweiser, V. Weiss, and G. Gerber, in: *Femtosecond Chemistry,* edited by J. Manz and L. Wöste. VCH Verlagsgesellschaft, Weinheim, 1995.

[29] C.C. Hayden and A. Stolow*: Non-Adiabatic Dynamics Studied by Femtosecond Time-Resolved Photoelectron Spectroscopy.* In: Photoionization, and Photodetachment, edited by C. Y. Ng. World Scientific, Singapore 1999

[30] T. Baumert, R. Thalweiser, and G. Gerber: *Femtosecond two-photon ionization spectroscopy of the B state of Na_3 clusters.* Chem. Phys. Lett., 209:29-34, 1993.

[31] A. Assion, M. Geisler, J. Hebling, V. Seifried, and T. Baumert: *Femtosecond pump-probe photoelectron spectroscopy: Mapping of vibrational wave-packet motion.* Phys. Rev. Lett. A, 54:R4605-R4608, 1996.

[32] P. Ludowise, M. Blackwell, and Y. Chen: *Perturbation of electronic potentials by femtosecond pulses – time resolved photoelectron spectroscopic study of NO multiphoton ionisation.* Chem. Phys. Lett., 258:530-539, 1996.

[33] I. Fischer, M.J.J. Vrakking, D.M. Villeneuve, and A. Stolow: *Femtosecond time-resolved zero kinetic energy photoelectron and photoionization spectroscopy studies of I_2 wavepacket dynamics.* Chem. Phys., 207 :331-354, 1996.

[34] T. Seideman : *Time-resolved photoelectron angular distributions : A nonperturbative theory.* J. Chem. Phys., 107:7859-7868, 1997.

[35] V. Engel*: Femtosecond pump-probe experiments and ionization: the time dependence of the total ion signal.* Chem. Phys. Lett., 178:130-134, 1991.

[36] Ch. Meier, V. Engel: *Electron kinetic energy distributions from multiphoton ionization of Na_2 with femtosecond laser pulses.* Chem. Phys. Lett., 212:691-696. 1993.

[37] Ch. Meier, V. Engel: Mapping of wave-packet dynamics in a double-well potential via femtosecond photolectron spectroscopy. J. Chem. Phys. **101**, 2673-2677 1994.

[38] R.S. Mulliken: *Role of Kinetic Energy in the Franck-Condon Principle.* J. Chem. Phys., 55:309-314, 1971.

[39] R. Loudon. *The Quantum Theory of Light.* Oxford University Press, Oxford, 1983.

[40] L.D. Landau und E.M. Lifschitz. *Quantenmechanik. Lehrbuch der Theoretischen Physik* Bd. 3, 8. Aufl. AkademieVerlag, Berlin, 1988.

[41] I. S. Averbukh and N. F. Perelman*: Fractional revivals: universality in the long-term evolution of quantum wave packets beyond the correspondence principle dynamics.* Phys. Lett. A, 139:449-453, 1989.

[42] T. Baumert, V. Engel, C. Röttgermann, W.T. Strunz, G. Gerber: *Femtosecond pump-probe study of the spreading and reccurence of a vibrational wave packet in Na_2.* Chem. Phys. Lett., 191:639-644, 1992.

[43] T. Lohmüller, M. Erdmann, O. Rubner, and V. Engel: *Determination of transition dipole moments from time-resolved photoelectron spectroscopy.* Eur. Phys. J. D, 25 :95-99, 2003.

[44] M. Seel, W. Domcke: *Model studies on femtosecond time-resolved ionisation spectroscopy of excited-state vibrational dynamics and vibronic coupling.* Chem. Phys., 151:59-72, 1991.

[45] M. Seel, W. Domcke: *Femtosecond time-resolved ionisation spectroscopy of ultrafast internal-conversion dynamics in polyatomic molecules: Theory and computational studies.* J. Chem. Phys., 95:7806-7822, 1991.

[46] J.H.D. Eland. *Photoelectron spectroscopy.* Butterworths, London, 1974.

[47] K.K. Verma, J.T. Bahns, A.R. Rajaei-Rizi, W.C. Stwalley, and W.T. Zemke: *First observation of bound-continuum transitions in the laser-induced $A^1\Sigma_u^+$ - $X^1\Sigma_g^+$ fluorescence of Na_2.* J. Chem. Phys., 78:3599-3613, 1983.

[48] M.A. Henesian, R.L. Herbst, and R.L. Byer: *Optically pumped superfluorescent Na_2 molecular laser.* J. Appl. Phys., 47, 1515-1518, 1976.

[49] M.E. Kaminsky, R.T. Hawkins, F.V. Kowalski, and A.L. Shawlow: *Identification of Absorption Lines by Modulated Lower-Level Population: Spectrum of Na_2.* Phys. Rev. Lett., 36:671-673, 1976.

[50] M.E. Kaminski: *New spectroscopic constants and RKR potential for the $A^1\Sigma_u^+$ state of Na_2^*.* J. Chem. Phys., 66:4951-4953, 1977.

[51] P. Kusch and M.M. Hessel: *Perturbations in the $A^1\Sigma_u^+$ state of Na_2^*.* J. Chem. Phys., 63:4087-4088, 1975.

[52] W. Demtröder and M. Stock: *Molecular Constants and Potential Curves Of Na_2 from Laser-Induced Fluorescence.* J. Mol. Spectrosc., 55:476-486, 1975.

[53] K.K. Verma, T.H. Vu, and W.C. Stwalley: *Reanalysis of the $C^1\Pi_u$ State of Na_2 Based on Ultraviolet Argon Ion Laser Fluorescence.* J. Mol. Spectrosc., 91:325-347, 1982.

[54] C. Effantin, J. d'Incan, A.J. Ross, R.F. Barrow, and J. Verges: *Laser-induced fluorescence spectra of Na_2: the $(3s,3p)^1\Sigma_g^+$, $(3s,3p)^1\Pi_g$ and $(3s,4s)^1\Sigma_g^+$ states.* J. Phys. B 17:1515-1523, 1984.

[55] J. Verges, C. Effantin, J. d'Incan, D.L. Cooper, and R.F. Barrow: *Double-minimum (2) $^1\Sigma_u$ State of Na_2.* Phys. Rev. Lett., 53:46-47, 1984.

[56] D.L. Cooper, R.F. Barrow, J. Verges, C. Effantin, and J. d'Incan: *Laser-induced fluorescence of the (2) $^1\Sigma_u$ double-minimum state of Na_2 studied by Fourier transform spectrometry.* Can. J. Phys. 62:1543-1562, 1984.

[57] D.D. Konowalow, M.E. Rosenkrantz, and M.L. Olson: *The molecular electronic structure of the lowest $^1\Sigma_g^+$, $^3\Sigma_u^+$, $^1\Sigma_u^+$, $^3\Sigma_g^+$, $^1\Pi_u$, $^1\Pi_g$, $^3\Pi_u$, and $^3\Pi_u$ states of Na_2.* J. Chem. Phys., 72:2612-2615, 1980.

[58] W.J. Stevens, M.M. Hessel, P.J. Bertoncini, and A.C. Wahl: *Theoretical transition dipole moments and lifetimes for the $A^1\Sigma_u^+ \rightarrow X^1\Sigma_g^+$ system of Na_2^*.* J. Chem. Phys., 66:1477-1482, 1977.

[59] G. Jeung: *Theoretical study of low-lying electronic states of Na_2.* J. Phys. B: At. Mol. Phys., 16:4289-4297, 1983.

[60] A.C. Wahl: *Chemistry by computer*. Scientific American, 322:54-58, 1970.

[61] J. M. Tedder, A. Nechvatal. *Pictorial Orbital Theory.* Pittman Publishing Limited. London, GB, 1985.

[62] G. Delakretaz and L. Wöste: *Two-photon ionisation spectroscopy of the (2) $^1\Sigma_u$ double-minimum state of Na_2.* Chem. Phys. Lett., 120:342-348, 1985.

[63] R. Haugstätter, A. Goerke, and I.V. Hertel*: Case studies in multiphoton ionisation and dissociation of Na_2. I. The (2) $^1\Sigma_u$ pathway.* Z. Phys. D, 9:153-166, 1988.

[64] D.D. Konowalow and J.L. Fisch: *The molecular electronic structure of the twenty-six lowest lying states of Li2 at short and intermediate internuclear separations.* Chem. Phys., 84:463-475, 1984.

[65] L. Wolniewicz and K. Dressler: *The EF and GK $^1\Sigma_g^+$ States of Hydrogen. Adiabatic calculation of Vibronic States in H_2, HD, and D_2.* J. Mol. Spectrosc., 67:416-439, 1977.

[66] K.P. Huber and G. Herzberg. *Molecular spectra and molecular structure IV. Constants of diatomic molecules.* D van Nostrand – Reinhold, New York, NY, 1979.

[67] K. Dressler, R. Gallusser, P. Quadrelli, and L. Wolniewicz: *The EF and GK $^1\Sigma_g^+$ States of Hydrogen.* J. Mol. Spectrosc., 75:205-219, 1979.

[68] C.-N. Liu and A.F. Starace: *Photodetachment of Na^-*. Physical Review A, 59:3643-3654, 1999.

[69] Volker Weiß. *Merhphotonen-Ionisations- und Photofragmentationsspektroskopie von Natriomklastern mit Femtosekunden-Laserpulsen.* Dissertation, Albert-Ludwigs-Universität Freiburg, 1996.

[70] Dirk Wößner. *Femtosekundenzeitaufgelöste Photoelektronenspektroskopie am Natrium-Dimer und aufbau einer molekularstrahlapparatur.* Diplomarbeit, Physikalisches Institut der Julius-Maximilians-Universitaet Wuerzburg, 1997.

[71] G. Scoles (editor). *Atomic and molecular beam methods. Vol. 1.* Oxford University Press, 1988.

[72] Landolt-Börnstein. *Zahlenwerte und Funktionenaus Physik, Chamie, Astronomie, Geophysik und Technik.* II. Band, Ed. J. Bartels, P. Ten Bruggencate, H. Hausen, K.H. Hellwege, Kl. Schäfer, E Schmidt. Springer-Verlag, 1960.

[73] H. Pauly. *Atom, Molecule, and Cluster Beams.* Springer-Verlag, 2000; R. Thalweiser. *Femtosekunden-Zeitaufgelöste-Experimente und ZEKE-Photoelektronen-Spektroskopie an Nan-Clustern.* Dissertation, Albert-Ludwigs-Universität Freiburg, 1992; S. Rosin and I.I. Rabi: *Effective Collision Cross Sections of the Alkali Atoms in Various Gases.* Phys. Rev., 48:373-379, 1935.

[74] M. Hofmann. *Femtosekundenzeitaufgelöste Photoelektronenspektroskopie am Na_2 in intensiven Laserfeldern.* Diplomarbeit, Physikalisches Institut der Julius-Maximilians-Universität Würzburg, 1998.

[75] R.J. Gordon, Y.T. Lee and D. Herschbach: *Supersonic Molecular Beams of Alkali Dimers.* J. Chem. Phys., 54:2393-2409, 1971.

[76] K. Bergmann, U. Hefter and P. Hering: *Quantum dependent velocity distribution in Na_2 molecular beams.* J. Chem. Phys., 65:488-490, 1976.

[77] R. Möller. *Photofragmentspektroskopie an Na_2.* Dissertation, Universität Freiburg i.B., 1985

[78] P. Kruit. *Photoionisation of atoms in strong laser fields; an electron spectroscopy study.* Doctor thesis, University of Amsterdam, 1982.

[79] Koenders B.G. PhD Thesis, University of Amsterdam, 1990.

[80] W.C. Wiley and I.H. McLaren: *Time-of-Flight Mass Spectrometer with Improved Resolution.* Rev. Sci. Instrum., 26:1150-1157, 1955.

[81] Femtolasers Produktions GmbH, Wien: *User's Manual for Mirror-Dispersion-Controlled Ti:Sapphire Oscillator:* Femtosource Scientic Spro, 2000.

[82] Coherent Inc. *Operator's Manual Verdi V-2/V-5 Diode-Pumped Lasers*, 1999.

[83] Femtolasers Produktions GmbH, Wien: *User's Manual for Femtosecond Multipass Amplifer.* Femtopower Pro, 2000.

[84] B.M. Industries*: 621-D CW pumped doubled Multi-kHz Nd:YLF Laser,* Users Manual.

[85] A.Assion: *Ultrakurzzeitspektroskopie: Beobachtung von Licht-induzierten Primärprozessen und Anwendungen in der Analytik.* Habilitationsschrift, Universität Kassel, 2004.

[86] Marc Winter. *Charakterisierung von Femtosekundenlaserpulsen.* Diplomarbeit, Universität Kassel, 2002.

[87] M. Braun, Ch. Meier, V. Engel: *The reflection of predissociation dynamics in pump-probe photoelectron distributions.* J. Chem. Phys., 105:530-534, 1996.

[88] C. Jouvet, S. Martrenchard, D. Solgadi, Dedonder-Lardeux, M. Mons, G. Gregoire, I. Dimicoli, F. Piuzzi, J.P. Visticot, J.M. Mestdagh, P. D'Oliveira, P. Meynadier, M. Perdrix: *Experimental Femtosecond Photoionization of NaI.* J. Phys. Chem. A, 101:2555-2560, 1997

[89] P. W. Atkins: *Physical Chemistry.* Oxford University Press Oxford, 1997.

[90] S. Magnier. *Determination der etats electroniques excites desmolecules Na_2 et K_2. Application aux collisions entre atomes excites par laser.* Dissertation, Universite de Paris-Sud, 1993.

[91] A. H. Zewail: *Femtochemistry. Feature Article.* J. Phys. Chem., 97:12427-12446, 1993.

[92] E. Charron and A. Suzor-Weiner: *Femtosecond dynamics of NaI ionisation and dissociative ionisation.* J. Chem. Phys., 108:3922-3931, 1988.

[93] V. Engel and H. Metiu: *The study of NaI predissociation with pump-probe femtosecond laser pulses: the use of an ionising probe pulse to obtain more detailed dynamic information.* Chem. Phys. Lett., 155:77-82, 1989.

[94] G. Gregoire, M. Mons, I. Dimicoli, F. Puizzi, E. Charron, C. Dedonder-Lardeux, C. Jouvet, S. Martrenchard, D. Solgadi, A. Suzor-Weiner: *Photoionization of NaI: inward-outward asymmetry in the wave packet detection.* Eur. Phys. J. D, 1 :187-192, 1998.

[95] S. Gräfe, V. Engel: *Indirect versus direct photoionization with ultrashort pulses: interferences and time-resolved bond-length changes.* Chem. Phys. Lett., 385:60-65, 2004.

[96] Y. Arasaki, K. Takatsuka, K. Wang, V. McKoy: *Studies of electron transfer in NaI with pump-probe femtosecond photoelectron spectroscopy.* J. Chem. Phys., 119:7913-7923, 2003.

[97] H. Schwoerer, R. Pausch, M. Held, V. Engel, W. Kiefer: *Femtosecond time-resolved two-photon ionization spectroscopy of K_2.* J. Chem. Phys., 107:9749-9754, 1997.

[98] C. Nicole, M.A. Bouchene, C. Meier, S. Magnier, E. Schreiber, B. Girard: *Competition of different ionization pathways in K_2 studied by ultrafast pump-probe spectroscopy: A comparison between theory and experiment.* J. Chem. Phys., 111:7857-7864, 1999.

[99] Y. Arasaki, K. Takatsuka, K. Wang, V. McKoy: *Femtosecond energy- and angle-resolved photoelectron spectra.* Chem. Phys. Lett., 302:363-374, 1999.

[100] Y. Arasaki, K. Takatsuka, K. Wang, V. McKoy: *Femtosecond energy- and angle-resolved photoelectron spectroscopy.* J. Chem. Phys., 112:8871-8884, 2000.

[101] Y. Arasaki, K. Takatsuka, K. Wang, V. McKoy: *Energy- and angle-resolved pump-probe femtosecond photoelectron spectroscopy: Molecular rotation.* J. Chem. Phys., 114:7941-7950, 2000.

[102] K. Takatsuka, Y. Arasaki, K. Wang, V. McKoy: *Probing wavepacket dynamics with femtosecond energy- and angle-resolved photoelectron spectroscopy. Introductory Lecture.* Faraday Discuss., 115:1-15, 2000.

[103] A. Assion, T. Baumert, V. Seifried, V. Weiss, E. Wiedenmann, G. Gerber: *Femtosecond spectroscopy of the (2) $^1\Sigma_u^+$ double minimum state of Na_2: time domain and frequency spectroscopy.* Z. Phys. D, 36:265-271, 1996.

[104] A. Assion, T. Baumert, M. Geisler, V. Seyfried, G. Gerber: *Mapping of vibrational wave-packet motion by femtosecond time-resolved kinetic energy time-of-flight mass spectroscopy.* Eur. Phys. J. D, 4 :145-149, 1998.

[105] M. Wollenhaupt, A. Assion, O. Bazhan, D. Liese, C. Sarpe-Tudoran, T. Baumert: *One-parameter control of quantum dynamics using femtosecond pump-probe photoelectron spectroscopy on a model system.* Appl. Phys. B, 74:S121-S125, 2002.

[106] S. Meyer, C. Meier, V. Engel: *Photoelectron distributions from femtosecond pump-probe esxitation with chirped probe pulses.* J. Chem. Phys., 108:7631-7636, 1998.

[107] Matthias Wollenhaupt. *Observation and Coherent Control of Atomic and Molecular Dynamics.* Habilitationsschrift, Universität Kassel, 2004.

[108] M. D. Feit and J. A. Fleck Jr.: *Solution of the Schrödinger equation by a spectral method II: Vibrational energy levels of triatomic molecules.* J. Chem. Phys., 78:301-308, 1983; B. M. Garraway and K. A. Suominen: *Wave-packet dynamics: new physics and chemistry in femto-time.* Rep. Prog. Phys., 58:365-419, 1995.

[109] M. Wollenhaupt, A. Assion, O. Graefe, D. Liese, C. Sarpe-Tudoran, M. Winter, T. Baumert: *Changes of the electronic structure along the internuclear coordinate studied by ultrafas photoelectron spectroscopy: the $2^1\Sigma_u^+$ Na_2 double-minimum state.* Chem. Phys. Lett. **376**, 457-464, 2003.

[110] M. Aymar: *Influence of Core-polarisation effects on the photoionisation cross section of the ground level and excited ns levels of neutral sodium.* J. Phys. B: At. Mol. Phys., 11:1413-1423, 1978.

[111] W. Kolos, L. Wolniewicz: *Theoretical Investigation of the Lowest Double-Minimum State E,F $^1\Sigma_g^+$ of the Hydrogen Molecule.* J. Chem. Phys., 50 :3228-3240, 1969.

[112] W. Meyer (private communication).

[113] J. Davidsson, T. Hansson, E. Mukhtar: *Ultrafast multiphoton ionization dynamics and control of NaK molecules.* J. Chem. Phys., 109:10740-10753, 1998.

[114] R. Andersson, J. Davidsson, T. Hansson: *Rydberg state-mediated photoionisation of dissociating NaK wave packets in the $B^1\Pi$ state.* Chem. Phys. Lett., 322:439-446, 2000.

[115] R. Uberna, Z. Amitay, C.X.W. Qian, S.R. Leone : *Ultrafast spectroscopy of wavelength-dependent coherent photoionization cross-section of Li_2 wave packets in the $E^1\Sigma_g^+$ state: The role of Rydberg states.* J. Chem. Phys., 114:10311-10320, 2001.

[116] L. Pesce, Z. Amitay, R. Uberna, S.R. Leone, M. Ratner, R. Kosloff: *Quantum dynamics simulation of the ultrafast photoionization of Li_2.* J. Chem. Phys., 114:1259-1271, 2001.

[117] K. Müller-Dethlefs and E. W. Schlag: *High-resolution zero kinetic energy (ZEKE) photoelectron spectroscopy of molecular systems.* Annu. Rev. Phys. Chem., 42:109-136, 1991.

[118] P. Kruit and F.H. Read: *Magnetic field paralleliser for 2π electron-spectrometer and electron-image.* J. Phys. E, 16:313-324, 1983.

[119] I. Powis, T. Baer and C.Y. Ng (editors). *High Resolution Laser Photoionisation and Photoelectron Studies.* Chapter 6 by C.A. de Lange. Wiley & Sons Ltd, 1995.

[120] P. Kruit, J. Kimman, H.G. Muller and M.J. Van der Wiel, Phys. Rev. A. 28, 248 1983.

[121] NIST Atomic Spectra Database.

[122] M.R. Dobber, W.J. Buma, and C.A. de Lange: *Resonance enhanced multiphoton ionisation spectroscopy on nanosecond and picosecond time scales of Rydberg states of methyl iodide.* J. Chem. Phys., 99:836-853, 1993.

[123] Horst Kuchling. *Taschenbuch der Physik.* Verlag Harri Deutsch, Thun & Frankfurt / Main, 1978.

[124] G. Alber, H. Ritsch and P. Zoller: *Generation and direction of Rydberg wave packets by short laser pulses.* Phys. Rev. A, 34:1058-1064, 1986.

[125] A. ten Wolde, L.D. Noordam, A. Lagendijk and H.B. van Linden van den Heuvell: *Observation of Radially Localised Atomic Electron Wave Packets.* Phys. Rev. Lett., 61:2099-2101, 1988.

[126] V. Engel und H. Metiu: *Two-photon wave-packet interferometry.* J. Chem. Phys., 100:5448-5458, 1994.

[127] M. Nauenberg, C. Stroud and J. Yeazell: *The Classical Limit of an Atom.* Sci.Am., 270:6, 2294-2297, 1994.

[128] A.A. Radzig, B.M. Smirnov. *Reference Data on Atoms, Molecules, and Ions.* Springer, Berlin, 1985.

[129] S. Haroche, J.A. Paisner, and A.L. Schawlow: *Hyperfine Quantum Beats Observed in Cs Vapor under Pulsed Dye Laser Excitation.* Phys. Rev. Lett., 30:948-951, 1973.

[130] S. Haroche, M. Gross, and M.P. Silverman: *Observation of Fine-Structure Quantum beats Following Stepwise Excitation in Sodium D states.* Phys. Rev. Lett., 33:1063-1066, 1974.

[131] T.W. Ducas, M.G. Littman and M.L. Zimmerman: *Observation of Oscillations in Resonance Absorption from a Coherent Superposition of Atomic States.* Phys. Rev. Lett., 35:1752-1754, 1975.

[132] W. Lange and J. Mlynek: *Quantum Beats in Transmission by Time-Resolved Polarization Spectroscopy.* Phys. Rev. Lett., 40:1373-1375, 1978.

[133] G. Leuchs and H. Walther: *Quantum Interference Effects in Field Ionization Application to the Measurement of the Fine Structure Splitting of Highly Excited Na ^2D States.* Z. Phys. D, 293:93-101, 1979.

[134] J.F. Christian, L.C. Snoek, S.G. Clement, W.J. van der Zande*: Application of associative ionisation to the observation of quantum beats in low-lying atomic resonances.* Phys. Rev. A, 53:1894-1899, 1996.

[135] V. Blanchet, C. Nicole, M.A. Bouchene and B. Girard: *Temporal Coherent Control in Two-Photon Transitions: From Optical Interferences to Quantum Interferences.* Phys. Rev. Lett., 78:2716-2719, 1997.

[136] M.A. Bouchene, V. Blanchet, C. Nicole, N. Melikechi, B. Girard, H. Ruppe, S. Rutz, E. Schreiber and L. Wöste: *Temporal coherent control induced by wave packet interferences in one and two photon atomic transitions.* Eur. Phys. J. D, 2 :131-141, 1998.

[137] C. Nicole, M.A. Bouchene, S. Zamith, N. Melikechi, B. Girard: *Saturation of wave-packet interferences: Direct observation of spin precession in potassium atoms.* Phys. Rev. A, 60:R1755-R1758, 1999.

[138] S. Zamith, M.A. Bouchene, E. Sokell, C. Nicole, V. Blanchet and B. Girard: *Pump probe experiment in atomic fine structure levels: Observation of the oscillation of an angular wavepacket.* Eur. Phys. J. D, 12 :255-261, 2000.

[139] E. Sokell, S. Zamith, M.A. Bouchene and B. Girard: *Polarization-dependent pump-probe studies in atomic fine-structure levels: Towards the production of spin-polarized electrons.* J. Phys. B, 33:2005-2015, 2000.

[140] M.A. Bouchene, S. Zamith and B. Girard: *Spin-polarized electrons produced by a sequence of two femtosecond pulses. Calculation of differential and global polarization rates.* J. Phys. B, 34:1497-1512, 2001.

[141] J. Cao, C.J. Bardeen and K.R. Wilson: *Molecular "π Pulse" for Total Inversion of Electronic State Population.* Phys. Rev. Lett., 80:1406-1409, 1998.

[142] J.C. Williamson, M. Dantus, S.B. Kim and A.H. Zewail: Ultrafast diffraction and molecular structure. Chem. Phys. Lett. **196**, 529-534 1992.

Acknowledgement

I would like to acknowledge all people who helped me with this doctor studies.

First, I would like to express my sincere gratitude to Prof. Baumert for giving me the opportunity to study and work in the Experimentalphysik III. Over the years his encouragement, continual willingless to discussions and numerous ideas have helped in my work. Without his support I won't be able to pursue this doctor studies.

I want to take the chance to thank Dr. Matthias Wollenhaupt for his intensive support and lots of constructive discussions and suggestions. These discussion and suggestions help me solve the problems I have encountered in my research work these years and lead my thesis work to proceed forward. I also want to thank Dr Andreas Assion for his support and stimulating discussions.

Another big regard to Dirk Liese for help with experiments. I won't forget the long evenings that we spent in the lab in fighting through the experiments, and of course a lot of fun too. I want to thank Cristian Sarpe-Tudoran not only for helping me with experiments and valuable discussions but also for being a friend.

I would also like to thank all members, past and present, at Experimentalphysik III for their help and the warm and friendly atmosphere over the years: Tim Bayer, Ronja Bäumner, Edith Brühl, Lars Englert, Lars Haag, Christian Horn, Petra Kasper, Jens Koehler, Marc Krug, Fedor Maiorov, Ute Meier-Diedrich, Andreas Präkelt, Elma Weber, Marc Winter.

Finally I would like to thank my mother for her continuous support and encouragement. I am gratefull to my husband, Martin, for his support and his patience through all these years.

Erklärung

Hiermit versichere ich, dass ich die vorliegende Dissertation selbständig und ohne unerlaubte Hilfe angefertigt und andere als die in der Dissertation angegebenen Hilfsmittel nicht benutzt habe. Alle Stellen, die wörtlich oder sinngemäß aus veröffentlichten oder unveröffentlichten Schriften entnommen sind, habe ich als solche kenntlich gemacht. Kein Teil dieser Arbeit ist in einem anderen Promotions- oder Habilitationsverfahren verwendet worden.